The Effects of Load History and Design Variables on Performance Limit States of Circular Bridge Columns Volume 1

Prepared By:
Jason Chad Goodnight
Yuhao Feng
Mervyn J. Kowalsky
James M. Nau
North Carolina State University

January 2015

REPORT DOCUMENTATION PAGE		Form approved OMB No. 298

Public reporting for this collection of information is estimated to average 1 hour per response, including the time for reviewing instructions, searching existing data sources, gathering and maintaining the data needed, and completing and reviewing the collection of information. Send comments regarding this burden estimate or any other aspect of this collection of information, including suggestion for reducing this burden to Washington Headquarters Services, Directorate for Information Operations and Reports, 1215 Jefferson Davis Highway, Suite 1204, Arlington, VA 22202-4302, and to the Office of Management and Budget, Paperwork Reduction Project (0704-1833), Washington, DC 20503

1. AGENCY USE ONLY (LEAVE BLANK) 4000(72)	2. REPORT DATE January 2015	3. REPORT TYPE AND DATES COVERED FINAL, November 2008 through January 2015

4. TITLE AND SUBTITLE The Effects of Load History and Design Variables on Performance Limit States of Circular Bridge Columns – Volume 1	5. FUNDING NUMBERS AKSAS #60855/T2-08-02 Federal # HPR-4000(72)

6. AUTHOR(S) Jason Chad Goodnight Yuhao Feng Mervyn J. Kowalsky James M. Nau	

7. PERFORMING ORGANIZATION NAME(S) AND ADDRESS(ES) North Carolina State University	8. PERFORMING ORGANIZATION REPORT NUMBER 4000(72)

9. SPONSORING/MONITORING AGENCY NAME(S) AND ADDRESS(ES) Alaska Department of Transportation and Public Facilities Research, Development &Technology Transfer P.O. Box 112500 3132 Channel Drive Juneau, AK 99811-2500	10. SPONSORING/MONITORING AGENCY REPORT NUMBER 4000(72)

11. SUPPLEMENTARY NOTES

12a. DISTRIBUTION / AVAILABILITY STATEMENT No restrictions.	12b. DISTRIBUTION CODE

13. ABSTRACT (Maximum 200 words)

This report is the first of three volumes and presents interpretation of all experimental and numerical data and recommendations. In total, 30 large scale reinforced concrete columns tests were conducted under a variety of loading conditions. Using advanced instrumentation methods, strain levels for multiple performance limit states were established, including reinforcing bar buckling. A new model for plastic hinge lengths has been proposed as well.

14. KEYWORDS : Seismic, reinforced concrete, strain limits, buckling, performance-based design, bridge design, plastic hinge lengths	15. NUMBER OF PAGES 278
	16. PRICE CODE N/A

17. SECURITY CLASSIFICATION OF REPORT Unclassified	18. SECURITY CLASSIFICATION OF THIS PAGE Unclassified	19. SECURITY CLASSIFICATION OF ABSTRACT Unclassified	20. LIMITATION OF ABSTRACT N/A

NSN 7540-01-280-5500

STANDARD FORM 298 (Rev. 2-98)
Prescribed by ANSI Std. 239-18 298-1

SI* (MODERN METRIC) CONVERSION FACTORS

APPROXIMATE CONVERSIONS TO SI UNITS

Symbol	When You Know	Multiply By	To Find	Symbol
LENGTH				
in	inches	25.4	millimeters	mm
ft	feet	0.305	meters	m
yd	yards	0.914	meters	m
mi	miles	1.61	kilometers	km
AREA				
in^2	square inches	645.2	square millimeters	mm^2
ft^2	square feet	0.093	square meters	m^2
yd^2	square yard	0.836	square meters	m^2
ac	acres	0.405	hectares	ha
mi^2	square miles	2.59	square kilometers	km^2
VOLUME				
fl oz	fluid ounces	29.57	milliliters	mL
gal	gallons	3.785	liters	L
ft^3	cubic feet	0.028	cubic meters	m^3
yd^3	cubic yards	0.765	cubic meters	m^3
		NOTE: volumes greater than 1000 L shall be shown in m^3		
MASS				
oz	ounces	28.35	grams	g
lb	pounds	0.454	kilograms	kg
T	short tons (2000 lb)	0.907	megagrams (or "metric ton")	Mg (or "t")
TEMPERATURE (exact degrees)				
^{o}F	Fahrenheit	5 (F-32)/9 or (F-32)/1.8	Celsius	^{o}C
ILLUMINATION				
fc	foot-candles	10.76	lux	lx
fl	foot-Lamberts	3.426	candela/m^2	cd/m^2
FORCE and PRESSURE or STRESS				
lbf	poundforce	4.45	newtons	N
lbf/in^2	poundforce per square inch	6.89	kilopascals	kPa

APPROXIMATE CONVERSIONS FROM SI UNITS

Symbol	When You Know	Multiply By	To Find	Symbol
LENGTH				
mm	millimeters	0.039	inches	in
m	meters	3.28	feet	ft
m	meters	1.09	yards	yd
km	kilometers	0.621	miles	mi
AREA				
mm^2	square millimeters	0.0016	square inches	in^2
m^2	square meters	10.764	square feet	ft^2
m^2	square meters	1.195	square yards	yd^2
ha	hectares	2.47	acres	ac
km^2	square kilometers	0.386	square miles	mi^2
VOLUME				
mL	milliliters	0.034	fluid ounces	fl oz
L	liters	0.264	gallons	gal
m^3	cubic meters	35.314	cubic feet	ft^3 m^3
	cubic meters	1.307	cubic yards	yd^3
MASS				
g	grams	0.035	ounces	oz
kg	kilograms	2.202	pounds	lb
Mg (or "t")	megagrams (or "metric ton")	1.103	short tons (2000 lb)	T
TEMPERATURE (exact degrees)				
^{o}C	Celsius	1.8C+32	Fahrenheit	^{o}F
ILLUMINATION				
lx	lux	0.0929	foot-candles	fc
cd/m^2	candela/m^2	0.2919	foot-Lamberts	fl
FORCE and PRESSURE or STRESS				
N	newtons	0.225	poundforce	lbf
kPa	kilopascals	0.145	poundforce per square inch	lbf/in^2

*SI is the symbol for the International System of Units. Appropriate rounding should be made to comply with Section 4 of ASTM E380.
(Revised March 2003)

ABSTRACT

This report discusses a research program aimed at defining accurate limit state displacements which relate to specific levels of damage in reinforced concrete bridge columns subjected to seismic hazards. Bridge columns are designed as ductile elements which form plastic hinges to dissipate energy in a seismic event. To satisfy the aims of performance based design, levels of damage which interrupt the serviceability of the structure or require more invasive repair techniques must be related to engineering criteria. For reinforced concrete flexural members such as bridge columns, concrete compressive and steel tensile strain limits are very good indicators of damage.

Serviceability limit states such as concrete cover crushing or residual crack widths exceeding 1mm may occur during smaller, more frequent earthquakes. While the serviceability limit states do not pose a safety concern, the hinge regions must be repaired to prevent corrosion of internal reinforcing steel. At higher ductility demands produced by larger less frequent earthquakes, reinforcing bar buckling may lead to permanent elongation in the transverse steel, which diminishes its effectiveness in confining the concrete core. Bar buckling and significant damage to the core concrete represent the damage control limit states, which when exceeded lead to significant repair costs. Furthermore, rupture of previously buckled bars during subsequent cycles of loading leads to rapid strength loss. The life safety or collapse prevention limit state is characterized by fracture of previously buckled bars.

The goal of the experimental program is to investigate the impact of load history and other design variables on the relationship between strain and displacement, performance strain limits, and the spread of plasticity. The main variables for the thirty circular bridge column tests included: lateral displacement history, axial load, longitudinal steel content, aspect ratio, and transverse steel detailing. A key feature of the experiments is the high fidelity strain data obtained through the use of an optical 3D position measurement system.

Column curvature distributions and fixed-end rotations attributable to strain penetration of reinforcement into the footing were quantified.

The following sequence of damage was observed in all of the cyclically loaded experiments: concrete cracking, longitudinal steel yielding, cover concrete crushing, confinement steel yielding, longitudinal bar buckling, and fracture of previously buckled reinforcement. The first significant loss in strength occurred when previously buckled reinforcement fractured. The measured data was used to refine strain limit recommendations. Particular attention was paid to the limit state of longitudinal bar buckling, since it limited the deformation capacity of all of the cyclically loaded specimens. Empirical expression were developed to predict the compressive strain at cover crushing, the compressive strain at spiral yielding, and the peak tensile strain prior to visible buckling after reversal of loading.

In design, limit state curvatures are converted to target displacements using an equivalent curvature distribution. The Modified Plastic Hinge Method was developed to improve the accuracy of strain-displacement predictions. Key aspects of the proposed model which differentiate it from the current method include: (1) a decoupling of column flexure and strain penetration deformation components, (2) a linear plastic curvature distribution which emulates the measured curvature profiles, and (3) separate plastic hinge lengths for tensile and compressive strain-displacement predictions.

In the experiments, the measured extent of plasticity was found to increase due to the combined effects of moment gradient and tension shift. The proposed tension hinge length was calibrated to match the upper bound of the measured spread of palsticity. The proposed compressive hinge length only contains a term related to the moment gradient effect. Expressions which describe the additional column deformation due to strain penetration of reinforcement into the adjoining member were developed. When compared to the current technique, the Modified Plastic Hinge Method improved the accuracy of both tensile and compressive strain-displacement predictions.

ORGANIZATION OF THE MULTI-VOLUME REPORT

There are three volumes which comprise this report. Volume 1 contains commentary, conclusions, and design recommendations from the experimental portion of the research program. An overview of the contents Volume 1 appears in the preceding abstract. Volume 2 contains a summary of experimental observations and data analysis for each column test. The material and geometric properties of each experiment are documented, and the sequence of observed and measured damage is presented.

Volume 3 presents the numerical portion of the research project on the impacts of loading history on the behavior of reinforced concrete bridge columns. Two independent finite element methods were utilized to accomplish the goal of this research work. First, fiber-based analysis was utilized which employed the Open System for Earthquake Engineering Simulation (OpenSees). The second model uses solid elements to predict bar buckling. The model included a segment of reinforcing bar and its surrounding elements, such as spiral turns and concrete. A series of strain histories from the experimental tests and fiber-based analyses were applied to the finite element model to study their impacts on the strain limit for reinforcing bar buckling.

Initial analytical investigations have shown significant impact of load history on the strain demand to lead to reinforcing bar buckling in the plastic hinge region. The parametric study extended the range of load history types and also studied the effect of reinforcement detailing on bar buckling. A design approach was developed to include the load history effect on the strain limit state of bar buckling.

ACKNOWLEDGMENTS

TABLE OF CONTENTS

LIST OF TABLES

LIST OF FIGURES

LIST OF SELECTED NOTATIONS

A_{st} = Total Area of Longitudinal Steel in the Column Cross Section

A_g = Gross Area of the Column Cross Section

$\rho_l = A_{st}/A_g$ = Longituidnal Reinforcement Ratio

P = Compressive Axial Load Applied to the Specimen

f_c' = Measured Column Concrete Strength at the Day of Testing

f_{cf}' = Meausred Footing Concrete Strength at the Day of Testing

$P/(f_c'A_g)$ = Column Axial Load Ratio

L = Column Length from the Top of the Footing to the Center of the Applied Lateral Load

L_c = Column Cantilever Length, $L_c = L$ for Single Benidng, $L_c = L/2$ for Double Bending

D = Column Diameter

M = Moment in the Column, Specifically the Maximum Value at the Base Section

V = Shear Force in the Column

L/D = Column Aspect Ratio, Equivalent to $M/(VD)$

f_y and ε_y = Yield Stress and Strain of Longituidnal Reinforcement

E_s = Elastic Modulus of Longitudinal Reinforcement

f_h and ε_h = Stress and Strain at Strain Hardening of Longitudinal Reinforcement

f_u and ε_u = Stress and Strain at Maximum Stress of Longituidnal Reinforcement

$d_{bl} \; and \; A_{bl}$ = Diameter and Area of the Longitudinal Bar

A_{sp} = Cross Sectional Area of a Single Spiral Trnasverse Steel Bar

s = Centerline Spacing between Transverse Steel Layers

D' = Diameter of the Confined Core Measured Between Spiral Centerlines

$\rho_s = \left(4A_{sp}\right)/(D's)$ = Transverse Volumetric Steel Ratio

$\rho_{eff} = \rho_s f_{yh}/f'_c$ = Effective Confinement Ratio

Δ = Column Displacement at the Center of the Applied Lateral Load

Δ'_y = Column Displacement at First Yield of Longitudinal Reinforcement

ϕ'_y = Base Section Curvature at First Yield of Longitudinal Reinforcement

$F'_y \; and \; M'_y$ = Shear Force and Moment at First Yield of Longitudinal Reinforcement

L_{sp} = Equivalent Strain Penetration Length

L_{eff} = Effective Column Length

k = Moment Gradient Component of Plastic Hinge Length Expression

ε_s = Extreme Fiber Bar Longitudinal Steel Strain

ε_c = Extreme Fiber Cover Concrete Strain

ε_{core} = Core Concrete Strain Measured at the Centerline of the Transverse Steel

M_n = Nominal Moment Capacity Defined by First Occurance of Either $\varepsilon_s = 0.015$ or $\varepsilon_c = -0.004$

$\phi_y = \phi'_y M_n/M'_y$ = Equivalent Yield Curvature at the Base Section

$\Delta_y = \Delta'_y M_n / M'_y =$ Equivalent Yield Displacement of the Column

$\mu_\Delta =$ Displacement Ductility

$\mu_\phi =$ Curvature Ductility

$\phi_p = \phi - \phi'_y M / M'_y =$ Plastic Curvature at the base Section

$\Delta_p =$ Column Plastic Displacement

$L_p =$ Equivalent Plastic Hinge Length from Priestley, Calvi, and Kowaksy (2007)

$\Delta_e =$ Elastic Column Displacement

$Lpr =$ Extent of Plasticity, Measured at Intersection of Elastic and Plastic Curvature Profiles

$Lpr_t =$ Tension Hinge Length Based on Triangular Distribution

$Lpr_c =$ Compression Hinge Length Based on Triangular Distribution

$Lp_t =$ Tension Hinge Length Based on Rectangular Distribution

$Lp_c =$ Compression Hinge Length Based on Rectangular Distribution

Chapter 1: Introduction

1.1   Background – Performance Limit States

Bridge columns are designed as ductile elements which form plastic hinges to dissipate energy in a seismic event. The goal of performance based seismic engineering is to design structures to achieve a predictable level of performance under a specific earthquake hazard within definable levels of reliability, as defined by the Structural Engineering Association of California (SEAOC 1999). To satisfy the aims of performance based design, levels of damage which interrupt the serviceability of the structure or require more invasive repair techniques must be related to engineering criteria.

For reinforced concrete flexural members such as bridge columns, concrete compressive and steel tensile strain limits are good indicators of damage. Serviceability limit states such as concrete cover crushing or residual crack widths exceeding 1mm may occur during smaller, more frequent earthquakes (Priestley et al. 1996). While the serviceability limit states do not pose a safety concern, the hinge regions must be repaired to prevent corrosion of internal reinforcing steel. This repair is typically accomplished through removal of damaged concrete, epoxy injection of cracks, and subsequent patching to restore the damaged concrete.

At higher ductility demands produced by larger less frequent earthquakes, reinforcing bar buckling may lead to permanent elongation in the transverse steel, which diminishes its effectiveness in confining the concrete core. Bar buckling and significant damage to the core concrete represent the damage control limit states, which when exceeded lead to significant repair costs (Priestley et al. 1996). The damage control limit states of reinforcement bar buckling and significant damage to the core concrete represent the limit of economical repair. This being said, (Rutledge et al. 2013) demonstrated that the displacement capacity of columns with buckled reinforcement could be rehabilitated through plastic hinge relocation.

This procedure involved capacity protection of damaged column regions through FRP wraps and anchors to relocate of the new plastic hinge to an undamaged section of the column.

Rupture of previously buckled bars or confining steel during subsequent cycles of loading leads to rapid strength loss. The life safety or collapse prevention limit state is characterized by fracture of previously buckled bars or confining steel. A summary of damage observations from a reinforced concrete bridge column tested at NCSU as part of this research appears in Figure 1.1. Stable hysteretic response was observed until the first fracture of a previously buckled longitudinal bar.
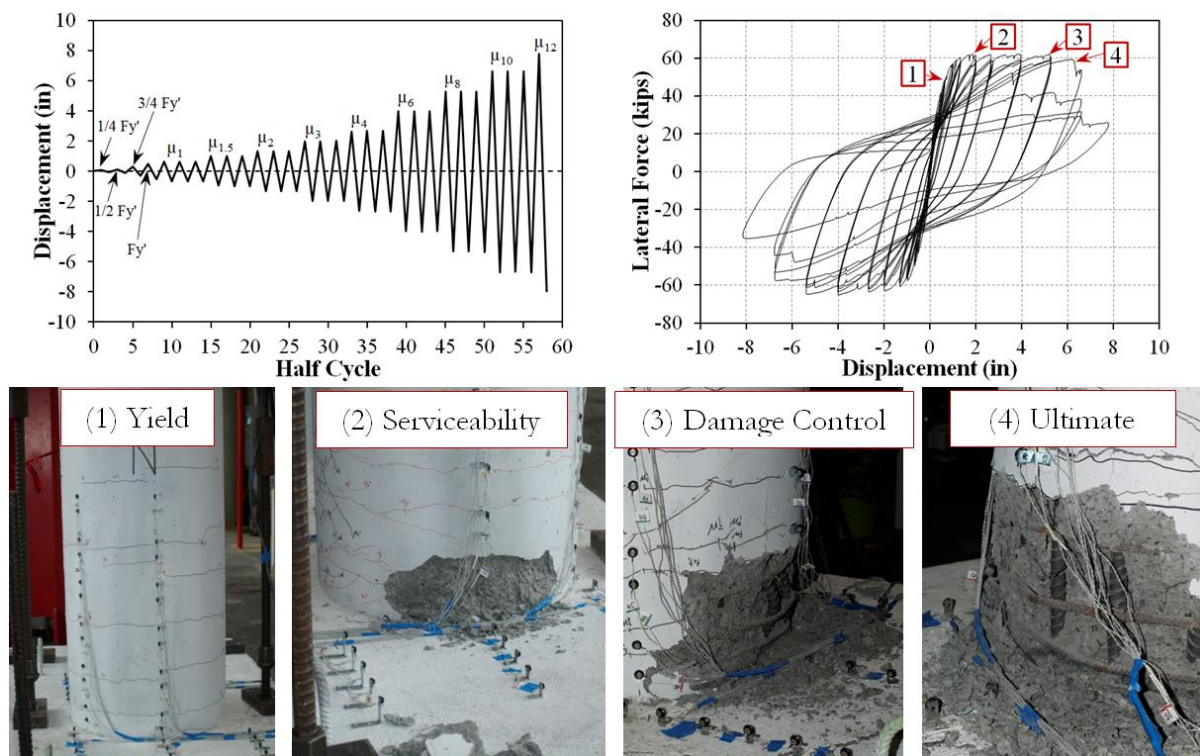
Figure 1.1 Displacement History, Hysteretic Response, and Performance Limit States

1.2   The Need for Research

While the progression of damage in flexural bridge columns has been investigated in the past for both uniaxial and biaxial deformation demands, traditional methods of deriving material strains from measured curvatures do not asses strains at the locations of interest, namely the longitudinal reinforcement and core concrete. These methods utilize an array of linear potentiometers placed on the ends of threaded rods embedded in the core concrete to calculate changes in displacement outside of the cover concrete. An example of this instrumentation technique from experiments by (Hose et al. 1997) appears in Figure 1.2. The instrumentation diagram for the test conducted by (Hose et al. 1997) appeared in a report by (Hines et al. 2003).

These linear potentiometer displacement readings, and their associated location within the cross section, are used to compute the cross-section curvature and neutral axis depth. Material strains at locations of interests are then calculated based on this strain profile. The accuracy of computed strain histories are influenced by rotations in the curvature rods themselves. It is for this reason that the current performance strain limit recommendations, summarized in Table 1.1 from (Kowalsky 2000), lack adequate experimental basis.
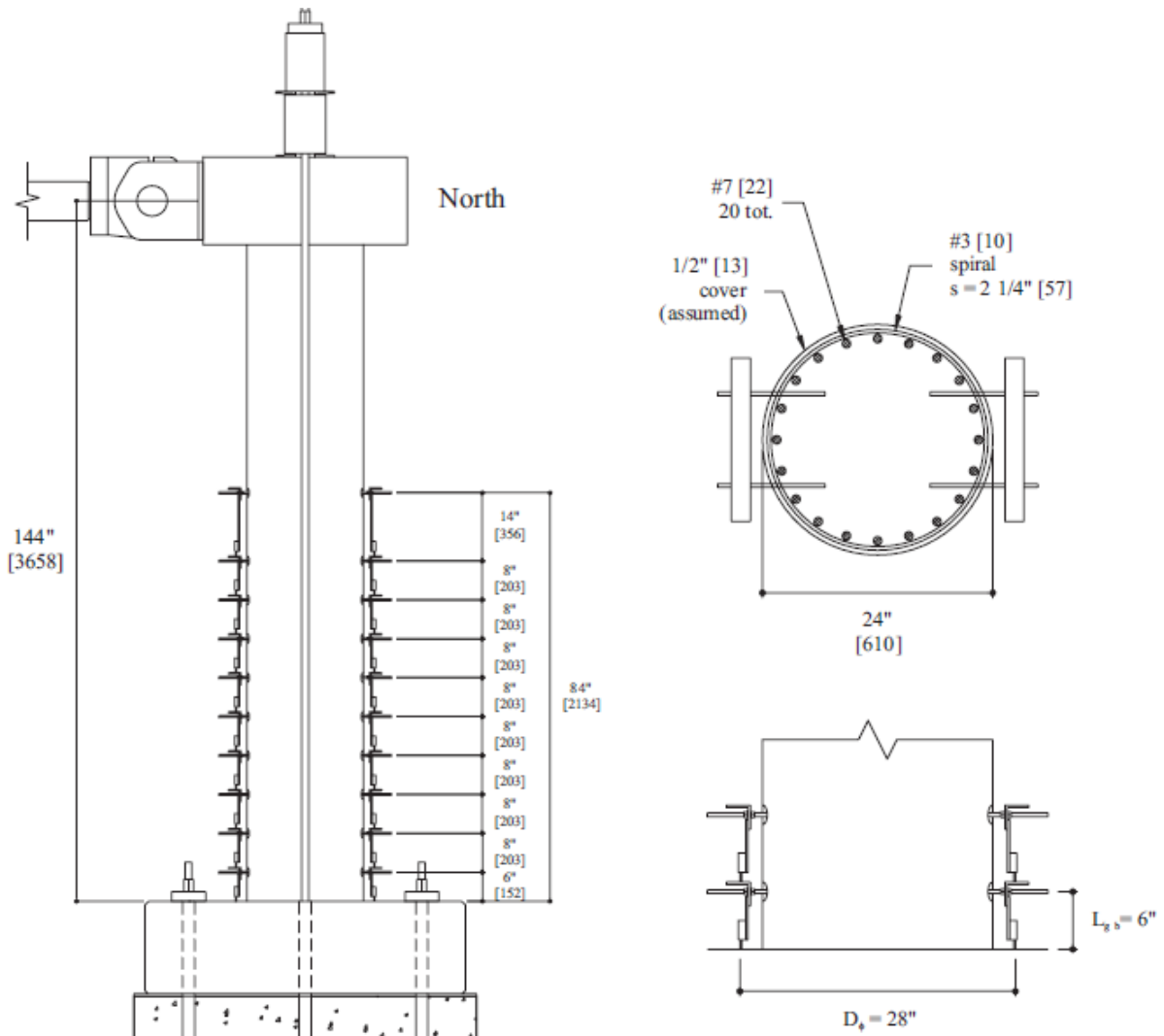
Figure 1.2 Curvature Rod and Linear Potentiometer Instrumentation from Tests by (Hose et al. 1997), Figure appears in (Hines et al. 2003)

Table 1.1 Performance Strain Limits from (Kowalsky 2000)

Limit State	Concrete Compressive Strain Limit	Steel Tensile Strain Limit
Serviceability	0.004 Cover Concrete Crushing	0.015 Residual Crack Widths Exceed 1mm
Damage Control	0.018 (Mander et al. 1988), ε_{cu} Limit of Economical Concrete Repair	0.060 Tension Based Bar Buckling

1.3   Research Goals and Scope

The 2009 AASHTO Seismic provisions are a displacement-based document and as a consequence, accurate estimates of displacement at key performance limit states are essential. The current code provisions are focused on life safety or collapse prevention under the ultimate limit state defined by loss or significant reductions to the lateral or axial capacity of the columns. The scope of the research presented in this dissertation aims to identify engineering demand parameters which can be used to predict the occurrence of key limit states, and provide engineers with an accurate method of relating these parameters to column deformations needed in design. Particular focus is given to the damage control limit states which lack adequate experimental basis. This includes yielding of confinement steel, significant damage to the core concrete, and buckling of longitudinal reinforcement.

An experimental program was devised to assess the performance of thirty circular well-confined bridge columns. A key feature of the experiments is the high fidelity strain data obtained using an optical 3D position measurement system. The goal of the experimental program is to investigate the impact of load history and other design variables on the relationship between strain and displacement, performance strain limits, and the spread of plasticity. The main variables for the thirty tests include: (1) lateral displacement history, (2) axial load, (3) longitudinal steel content, (4) aspect ratio, and (5) transverse steel detailing.

Chapter 2: Test Setup, Instrumentation, Construction, and Text Matrix

2.1 Test Setup

The specimen was designed to represent a single degree of freedom bridge column subjected to lateral and axial load. The test specimen consists of a footing, column, and loading cap, Figure 2.1 and Figure 2.2. The footing is a capacity protected member which secures the specimen to the lab strong floor using post tensioned bars placed through four perimeter holes. The footing was elevated above the lab floor by ½" black board pads placed under the six floor holes. Gypsum cement was poured in the gap between the specimen and the lab floor to create a level bonded connection surface.

A 200kip hydraulic actuator, with a 40in stroke capacity, applies lateral load to the loading cap of the specimen, Figure 2.3 and Figure 2.8. The actuator was connected to the lab strong wall through a wall plate with hole patterns customized for various column lengths. The actuator end connections allow for rotation about the horizontal axis, which places the column under single bending.

A spreader beam, two hydraulic jacks, and a load cell are placed above the loading cap to apply a constant axial compressive load, Figure 2.7. Rectangular ducts near in the middle of the footing allowed for movement of the axial post tensioning bars. A self-regulating axial load system was utilized with a third hydraulic jack in a force controlled uniaxial testing machine to regulate the pressure, and thus the load, of two jacks on top of the specimen to maintain a constant axial load throughout testing. This technique of axial load application does not replicate true P-Δ effects induced by a vertical gravity load. Instead, the axial force follows the direction of the post tensioning bar which is hinged at the floor and centered above the column. Examples of test setups which recreate P-Δ effects may be found in (Dutta et. al. 1999) and (Esmaeily and Xiao 2002).

The procedure used to setup the self-regulating axial load system is described below. The two hydraulic jacks at the top of the specimen and the third jack placed into the uniaxial testing machine were elongated to half of their total stroke capacity. The locking nuts on the post tensioning bars were tightened beneath the lab floor. Under displacement control, the platens for the universal testing machine were brought into contact with both ends of the jack. A hydraulic pump was added to the closed hydraulic system connecting the three jacks to increase the pressure, and thus the load, until each jack reached half of the target column axial load. The two jacks placed above the column apply the total column axial load. The valve for the hydraulic pump was then closed creating an initially pressurized, but locked off system between the three hydraulic jacks. At this point, the MTS platens under displacement control have not moved. The universal testing machine was then placed into force control to maintain that prescribed level of axial load in the three jack system as the column undergoes lateral displacements. This process was done in reverse to remove the axial load from the column. The technique can be done with both single acting and double acting jacks. For specimens subjected to the highest axial loads double acting jacks were utilized, and a separate hydraulic reservoir was placed above the column and the MTS machine, Figure 2.7.
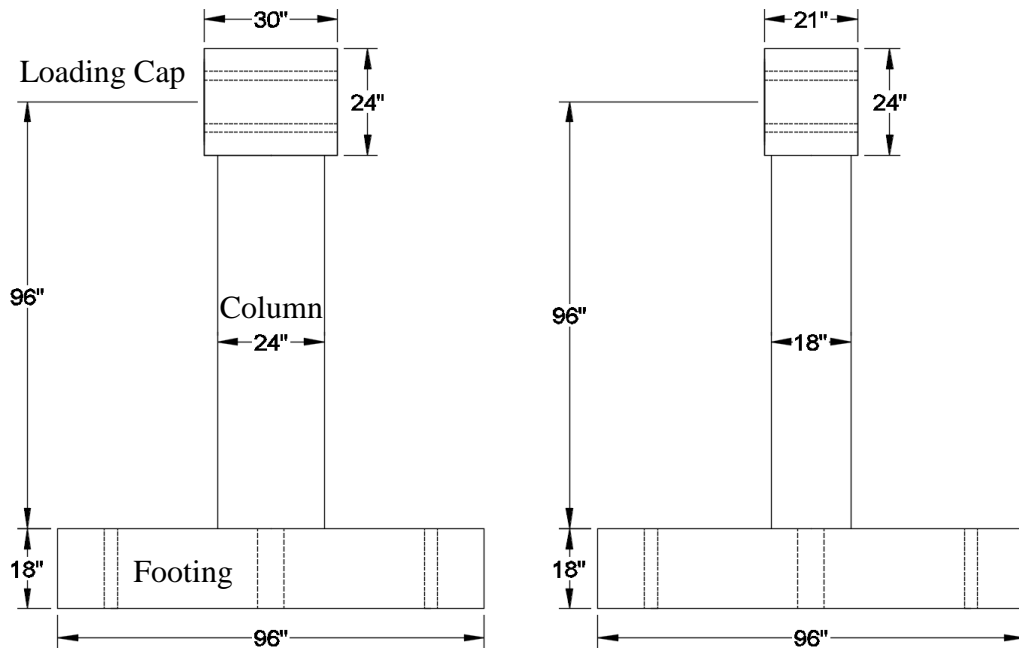
Figure 2.1 General Dimensions for 24" and 18" Specimens with 8ft Cantilever Lengths
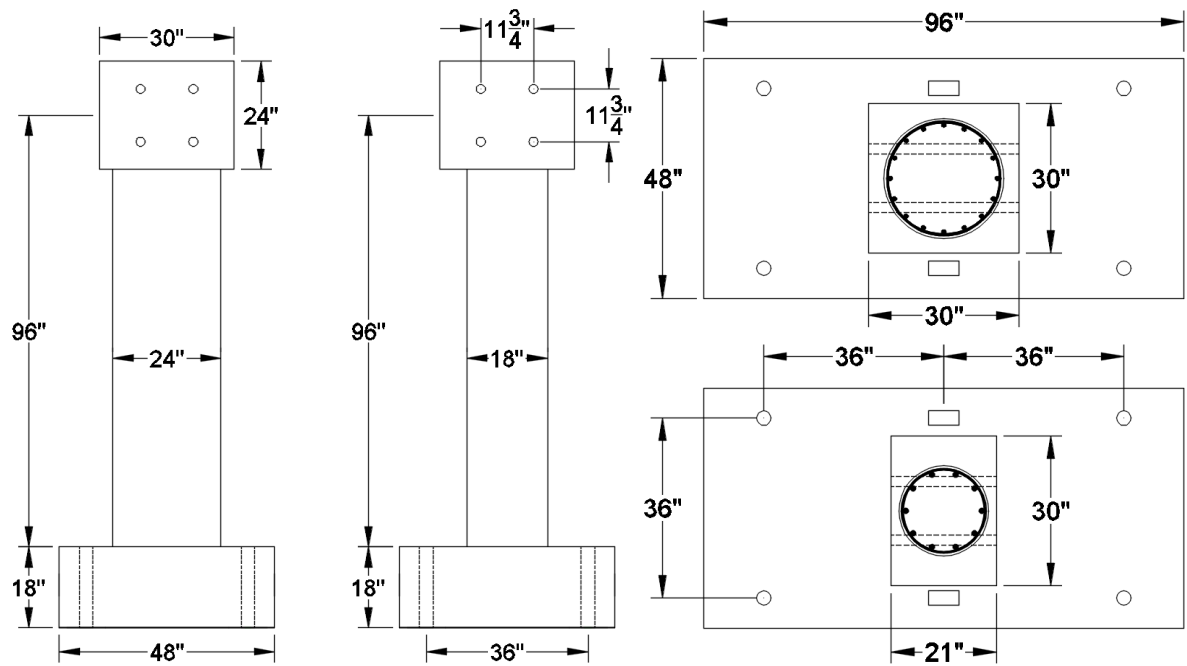
Figure 2.2 General Dimensions for 24" and 18" Specimens with 8ft Cantilever Lengths

Instrumentation Column

Optotrak Position Monitor #2

Main and Backup String Potentiometers

Long. and Transverse Inclinometers

Hydraulic Jacks

Axial Load Cell

Spreader Beam

1 3/8" Dywidag for Axial Load

1 3/8" Dywidag PT Corner Tie Downs

220kip Actuator

Steel Wall Plate

Optotrak Position Monitor #1

Strong Floor

Strong Wall
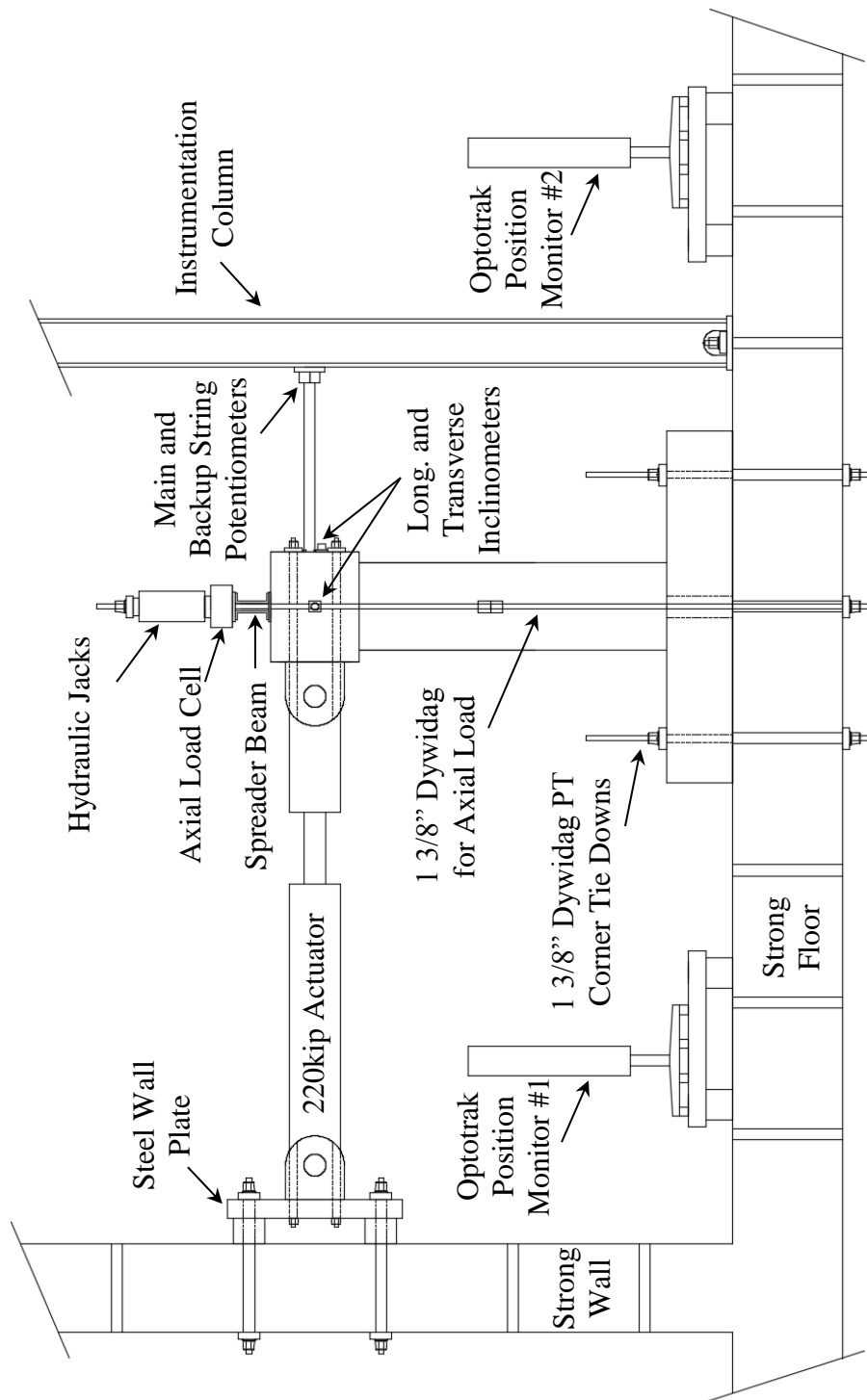
Figure 2.3 Front View of Test Specimen

Hydraulic
Jacks

Axial
Load Cell

Spreader Beam

Strong
Wall

Steel Wall
Plate

Main and
Backup String
Potentiometers

Long. and
Transverse
Inclinometers

1 3/8" Dywidag
for Axial Load

220kip
Actuator

Dywidag
Coupler

Spreader
Beam

Hydraulic
Jacks

Strong
Floor

1 3/8"
Dywidag PT
Corner Tie
Downs
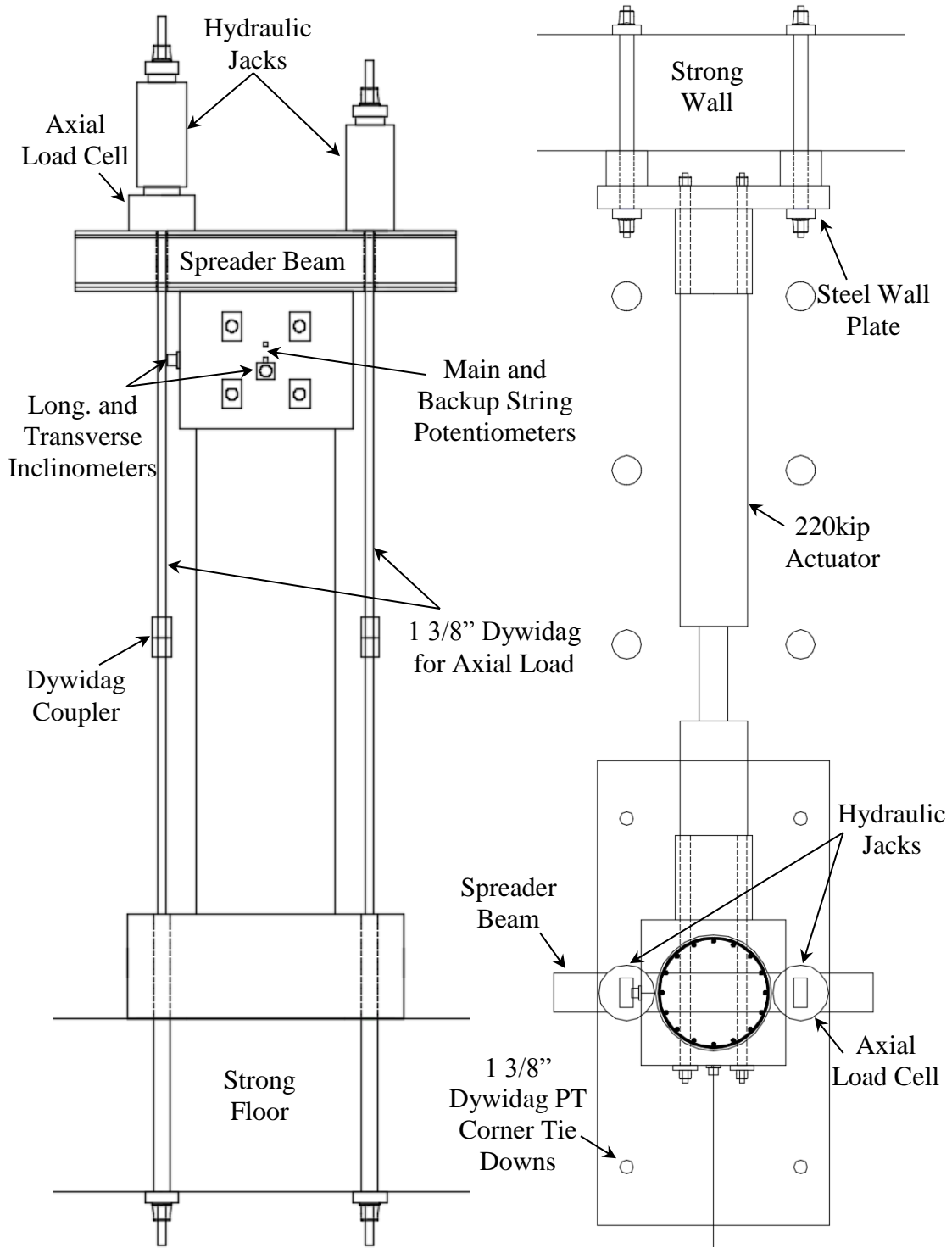
Axial
Load Cell

Figure 2.4 Side and Top Views of the Test Setup

Figure 2.5 Test Setup Overview

Figure 2.6 Specimen Under Lateral Deformation

Figure 2.7 Self-Regulating Axial Load with 3rd Jack in Force Controlled MTS Machine

Figure 2.8 Test Setup for 11' and 13' Cantilever Length Specimens

2.2   Test Matrix

The main variables for the thirty tests include: (1) lateral displacement history, (2) axial load, (3) longitudinal steel content, (4) aspect ratio, and (5) transverse steel detailing. The specimens were constructed in sets of six columns. The first six specimens, which are excluded from the body of this report and design recommendations, were constructed by a local contractor. The standards of detailing were not sufficient to isolate the impact of individual variables. The transverse steel spacing was not uniform, which influenced the restraint of longitudinal bars and subsequent bar buckling. A brief review of the first six tests is included in Volume 2. To improve the quality of construction, all subsequent specimens were constructed at NCSU by the research team. Test 7 used the same instrumentation technique as the first six experiments. This technique involved tack welding steel post extensions to longitudinal reinforcement, Figure 2.13. Test 7 was ultimately excluded from design recommendations, because the A706 steel was influenced by the surface tack welds. The strain at maximum stress was reduced, and this shifted the failure mechanism for the column to brittle fracture of reinforcement without prior bar buckling. The results for Test 7 and a discussion of weldability if A706 reinforcing steel is included in Volume 2 of this report.

An improved instrumentation system was devised in which instrumentation was directly applied to the reinforcing steel. All design recommendations and strain data presented in this report come from Tests 8-30 which utilized the direct application instrumentation method. This technique is discussed in greater detail in the following section. Nominally identical Specimens 8-12 investigated the impact of lateral displacement history on column performance. The test matrix for these experiments appears in Table 2.1, while a full observation summary appears in Volume 2. Specimens 13-18, in Table 2.2, investigated the transverse steel detailing and lateral displacement history. Specimens 19-24, in Table 2.3, had axial load and aspect ratio as the primary variable. The final test series, Specimens 25-30 in Table 2.4, investigated the impact of longitudinal steel content and axial load on column performance.

Table 2.1 Column Property Summary for Load History Variable Tests 8-12

Test	Load History	D (in)	L/D	Long. Steel (ρ_l)	Spiral Detailing (ρ_s)	f'c (psi)	P/f'c*Ag
8	Chile 2010	24	4	16 #6 bars (1.6%)	#3 at 2" (1%)	6988	5.4%
8b	Cyclic Aftershock	24	4	16 #6 bars (1.6%)	#3 at 2" (1%)	6988	5.4%
9	Three Cycle Set	24	4	16 #6 bars (1.6%)	#3 at 2" (1%)	6813	5.5%
10	Chichi 1999	24	4	16 #6 bars (1.6%)	#3 at 2" (1%)	5263	7.1%
10b	Cyclic Aftershock	24	4	16 #6 bars (1.6%)	#3 at 2" (1%)	5263	7.1%
11	Kobe 1995	24	4	16 #6 bars (1.6%)	#3 at 2" (1%)	6070	6.2%
12	Japan 2011	24	4	16 #6 bars (1.6%)	#3 at 2" (1%)	6100	6.2%

Table 2.2 Column Property Summary for Load History Variable Tests 13-18

Test	Load History	D (in)	L/D	Long. Steel (ρ_l)	Spiral Detailing (ρ_s)	f'c (psi)	P/f'c*Ag
13	Three Cycle Set	24	4	16 #6 bars (1.6%)	#4 at 2.75" (1.3%)	6097	6.2%
14	Three Cycle Set	24	4	16 #6 bars (1.6%)	#3 at 4" (0.5%)	6641	5.7%
15	Three Cycle Set	24	4	16 #6 bars (1.6%)	#3 at 2.75" (0.7%)	7232	5.2%
16	Three Cycle Set	24	4	16 #6 bars (1.6%)	#3 at 1.5" (1.3%)	6711	5.6%
17	Llolleo 1985	24	4	16 #6 bars (1.6%)	#3 at 1.5" (1.3%)	7590	5.0%
17b	Cyclic Aftershock	24	4	16 #6 bars (1.6%)	#3 at 1.5" (1.3%)	7590	5.0%
18	Darfield 2010	24	4	16 #6 bars (1.6%)	#3 at 1.5" (1.3%)	7807	4.8%
18b	Cyclic Aftershock	24	4	16 #6 bars (1.6%)	#3 at 1.5" (1.3%)	7807	4.8%

Table 2.3 Column Summary for Aspect Ratio and Axial Load Variable Tests 19-24

Test	Load History	D (in)	L/D	Long. Steel (ρ_l)	Spiral Detailing (ρ_s)	f'c (psi)	P/f'c*Ag
19	Three Cycle Set	18	5.33	10 #6 bars (1.7%)	#3 at 2" (1.3%)	6334	10%
20	Three Cycle Set	18	5.33	10 #6 bars (1.7%)	#3 at 2" (1.3%)	6467	5%
21	Three Cycle Set	18	7.33	10 #6 bars (1.7%)	#3 at 2" (1.3%)	6390	5%
22	Three Cycle Set	18	7.33	10 #6 bars (1.7%)	#3 at 2" (1.3%)	6530	10%
23	Three Cycle Set	18	8.67	10 #6 bars (1.7%)	#3 at 2" (1.3%)	6606	5%
24	Three Cycle Set	18	8.67	10 #6 bars (1.7%)	#3 at 2" (1.3%)	6473	10%

Table 2.4 Column Summary for Steel Content and Axial Load Variable Tests 25-30

Test	Load History	D (in)	L/D	Long. Steel (ρ_l)	Spiral Detailing (ρ_s)	f'c (psi)	P/f'c*Ag
25	Three Cycle Set	24	4	16 #7 bars (2.1%)	#3 at 2" (1%)	6289	5%
26	Three Cycle Set	24	4	16 #7 bars (2.1%)	#3 at 2" (1%)	5890	10%
27	Three Cycle Set	24	4	16 #6 bars (1.6%)	#3 at 2" (1%)	6149	10%
28	Three Cycle Set	18	5.33	10 #6 bars (1.7%)	#3 at 2" (1.3%)	6239	15%
29	Three Cycle Set	18	5.33	10 #6 bars (1.7%)	#3 at 2" (1.3%)	5912	20%
30	Three Cycle Set	18	5.33	10 #8 bars (3.1%)	#3 at 2" (1.3%)	6050	15%

2.3 Instrumentation

Instrumentation diagrams for the specimen appear in Figure 2.9 and Figure 2.10. A string potentiometer, placed at the center of the applied lateral load, was used to monitor the column displacement. The longitudinal and transverse rotations of the cap were monitored with inclinometers. The lateral load and stroke of the 200kip MTS hydraulic actuator were measured through an integrated load cell and temposonic. An axial load cell monitored the contribution of a single jack to the total compressive axial load of the column.

The experimental program utilized an innovative technique of applying a commercially available instrumentation system to measure large strains at the level of the reinforcement with multiple Optotrak Certus HD 3D position sensors produced by Northern Digital Inc. The Optotrak position monitoring system can read the location of target markers placed on the specimen in three dimensional space during a test, Figure 2.11 and Figure 2.12. By calculating the change in three dimensional distance between adjacent target markers, strains can be determined with respect to their original unloaded gage lengths. The 3D accuracy of the Optotrak Certus system reported by Northern Digital Inc. is 0.1mm with a resolution of 0.01mm.

Over the course of the study three different techniques were used to monitor material strains with the Optotrak system: (1) a single positon monitor with post extensions, (2) two position monitors with vertical cover concrete blockouts, and (3) three position monitors with a complete cover blockout. The single position monitor method was utilized in the first seven specimens, which were ultimately excluded from design recommendations in this report. The single positon monitor technique, Figure 2.13, had target markers applied to the ends of tack welded steel posts. Vertical cover concrete blockout strips over six extreme fiber bars were created by blocking out the cover concrete with insulation foam during casting. The measured strains from the target markers at the ends of the post extensions suffer from the same issues of the traditional curvature rod method. Strains are not measured

at the location of interest; therefore the recorded values are influenced by rotations of the rods themselves.

The second method utilized two Optotrak position monitors facing extreme fiber regions of the specimen and direct application of target markers to six reinforcing bars, Figure 2.11. The same technique of blocking out vertical strips of cover concrete to the outside surface of the longitudinal bars was utilized, Figure 2.11. Target markers were applied directly to longitudinal bars in the extreme fiber regions of the column to obtain strain hysteresis, vertical strain profiles, cross section curvatures, curvature distributions, and fixed-end rotations attributable to strain penetration.

The third method used three Optotrak position monitors and a complete cover concrete blockout to the depth of the outside surface of the longitudinal reinforcement. Spiral layers were always in complete contact with the core, as shown in Figure 2.12. Target markers were applied to longitudinal and transverse reinforcement on the two extreme fiber regions and on a shear face. The additional target markers on the transverse steel were used to compute spiral strains based on the change in arc-length between adjacent target markers. This technique allowed for strain measurements in ten reinforcing bars at different depths within the cross section to analyze the plane sections hypothesis.

Strain gages were applied to layers of transverse steel overlaying the extreme fiber longitudinal reinforcement to observe the interaction between compressive demand, transverse steel strain, and buckling restraint. An illustration of the accuracy of the Optotrak system compared to traditional measurement techniques appears in Figure 2.14. A tensile test on a reinforcing bar was conducted with a 2" Optotrak gage length, a 2" extensometer gage length, and a centrally placed strain gage. Closer inspection demonstrates that the Optotrak strains oscillate around the measurements predicted by the conventional instrumentation, but the general trend is captured throughout the entire tensile test. Electrical resistance strain gages fail to remain attached at large inelastic strain levels, which are of interest to this study.
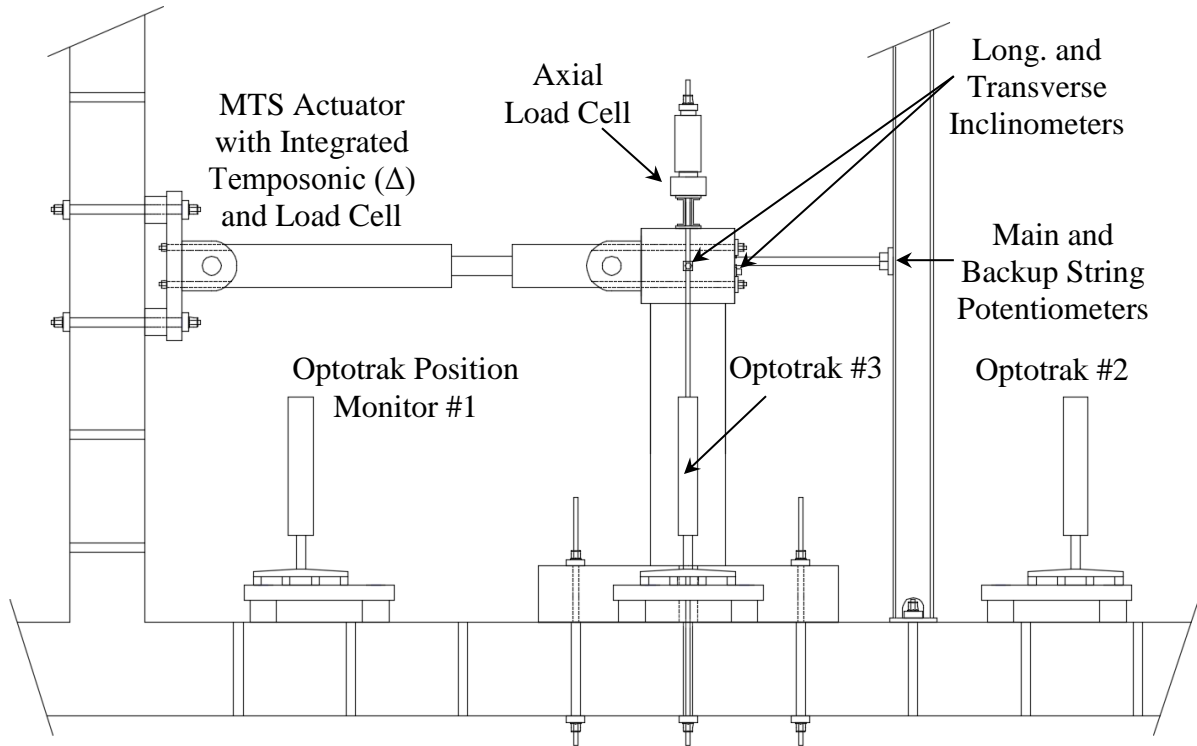
Figure 2.9 Instrumentation Placement on Test Setup
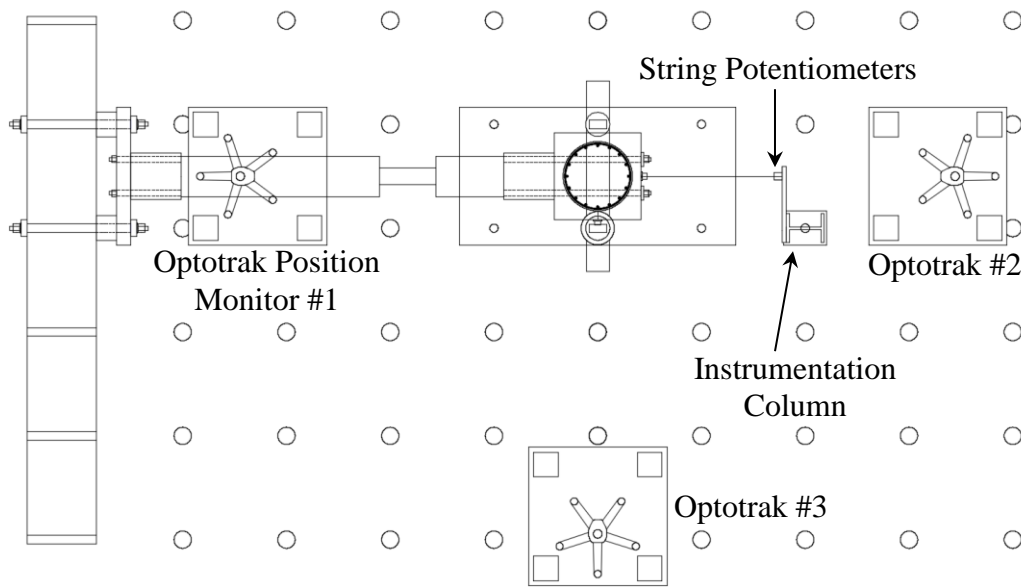
Figure 2.10 Overlapping Measurement Volume for the Optotrak Position Monitors
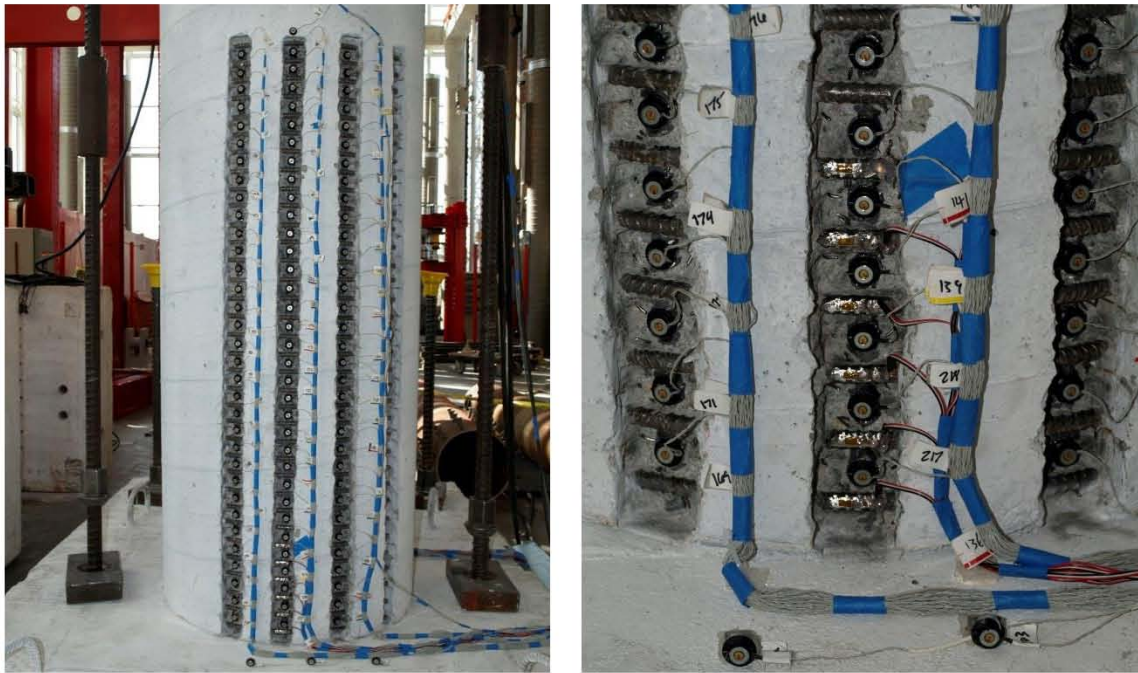
Name	x [mm]	y [mm]	z [mm]
Marker_1	243.342	-775.449	-3468.849
Marker_2	242.805	-738.987	-3468.806
Marker_3	240.540	-700.665	-3469.522
Marker_4	240.220	-663.994	-3469.319
Marker_5	238.663	-626.652	-3469.705
Marker_6	238.487	-591.017	-3469.443
Marker_7	237.847	-554.487	-3469.455
Marker_8	238.294	-521.629	-3469.352
Marker_9	236.335	-484.682	-3469.819
Marker_10	237.127	-449.465	-3469.560
Marker_11	236.254	-415.474	-3469.817
Marker_12	235.905	-380.216	-3470.093
Marker_13	235.622	-343.807	-3470.186
Marker_14	235.178	-309.686	-3470.715
Marker_15	233.959	-274.697	-3471.321
Marker_16	234.297	-237.406	-3471.108
Marker_17	234.856	-203.623	-3471.170
Marker_18	234.953	-166.232	-3471.027
Marker_19	234.559	-133.283	-3471.502
Marker_20	233.714	-97.790	-3472.006
Marker_21	233.148	-63.162	-3472.391
Marker_22	233.241	-26.371	-3472.452
Marker_23	233.296	9.834	-3472.859
Marker_24	233.881	43.727	-3472.463
Marker_25	231.191	79.206	-3474.050
Marker_26	231.247	113.540	-3474.491
Marker_27	231.251	151.705	-3474.842
Marker_28	231.040	186.054	-3475.058
Marker_29	231.481	220.929	-3475.127
Marker_30	231.686	257.761	-3475.166
Marker_31	231.667	293.566	-3476.817
Marker_32	230.904	326.309	-3475.969
Marker_33	232.543	363.480	-3475.408
Marker_34	230.225	398.459	-3476.678
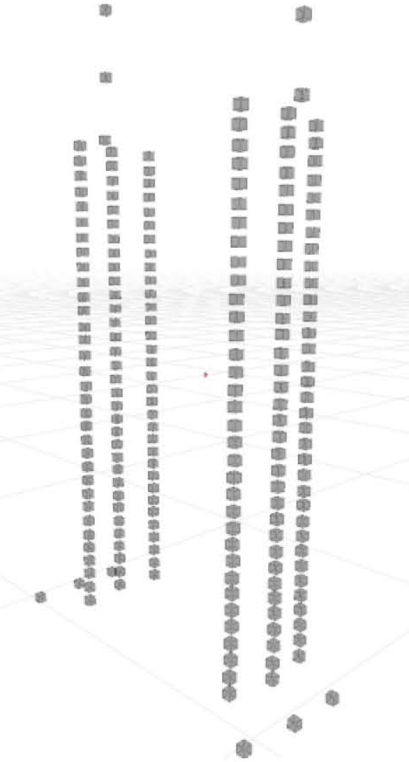
Figure 2.11 Dual Optotrak Method with Vertical Cover Concrete Blockout Strips
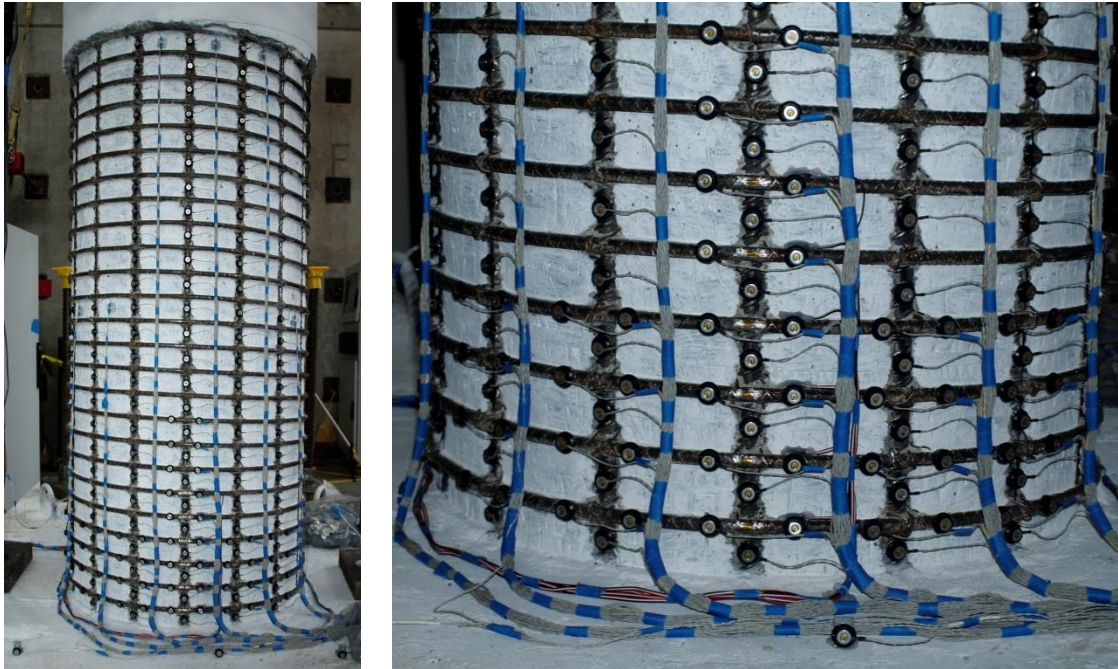
Name	x [mm]	y [mm]	z [mm]
Marker_56	22.605	-768.878	-2823.420
Marker_57	22.023	-723.502	-2823.224
Marker_58	23.611	-675.963	-2823.620
Marker_59	22.914	-627.713	-2823.769
Marker_60	22.309	-578.423	-2823.920
Marker_61	22.457	-530.064	-2824.156
Marker_62	22.898	-481.580	-2824.496
Marker_63	23.570	-429.917	-2824.482
Marker_64	24.335	-381.253	-2824.373
Marker_65	24.346	-332.084	-2824.542
Marker_66	22.813	-283.271	-2824.657
Marker_67	23.262	-234.317	-2824.772
Marker_68	23.264	-183.634	-2825.202
Marker_69	23.365	-134.318	-2825.322
Marker_70	22.845	-86.205	-2825.807
Marker_71	24.211	-35.837	-2825.957
Marker_72	23.834	12.833	-2825.893
Marker_73	24.170	59.599	-2826.011
Marker_74	24.888	108.682	-2825.957
Marker_75	24.585	158.003	-2825.720
Marker_76	24.183	208.389	-2825.508
Marker_77	23.858	256.409	-2825.454
Marker_78	25.731	306.625	-2825.952
Marker_79	26.656	354.616	-2826.074
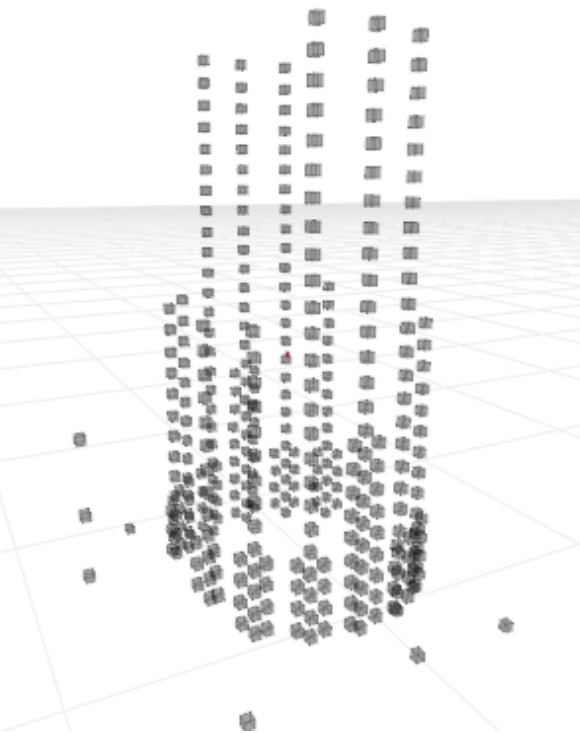
Figure 2.12 Triple Optotrak Method with Complete Cover Concrete Blockout
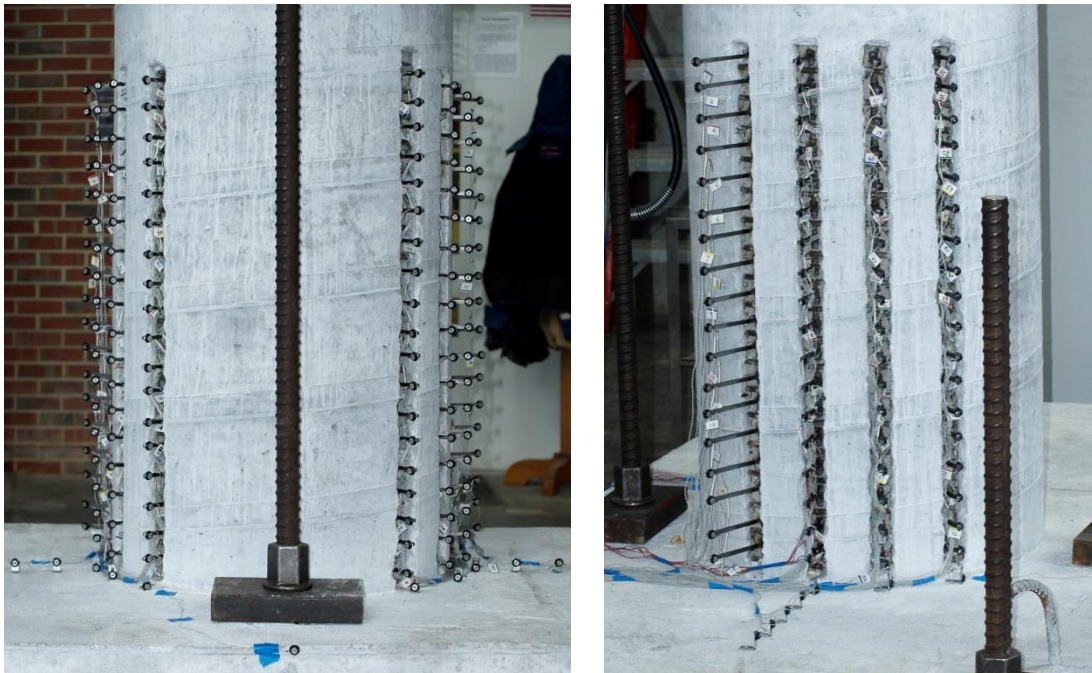
Figure 2.13 Single Optotrak Method Utilizing Post Extensions (Ultimately Abandoned)
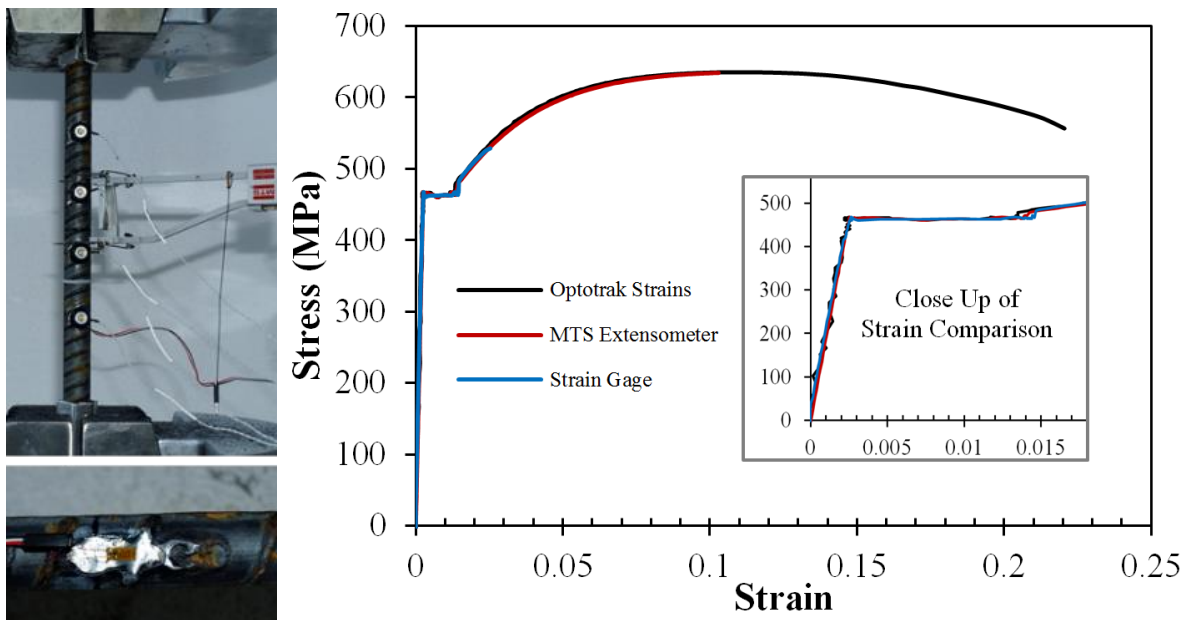
Figure 2.14 Comparison of Measurement Techniques for Tensile Rebar Test

2.4   Construction Process

The first six specimens, which are excluded from the body of this report and design recommendations, were constructed by a local contractor. The standards of detailing were not sufficient to isolate the impact of individual variables. The transverse steel spacing was not uniform, which influenced the restraint of longitudinal bars and subsequent observations of bar buckling. A brief review of the first six tests is included in the Volume 2 of this report, but the data is excluded from design recommendations because the direct application instrumentation method produced superior strain measurements. To improve the quality of construction, all subsequent specimens were constructed at NCSU by the research team. The process through which these specimens were constructed is described below, along with the method of preparing the specimens for instrumentation with the Optotrak position monitoring system.

The general reinforcement layout for the footing, column, and cap appear in Figure 2.15 through Figure 2.19. Two column variants were utilized in the study, (1) a 24" diameter column with 16 longitudinal bars and ½" cover the outside of the transverse steel and (2) a 18" diameter column with 10 longitudinal bars and ½" cover the outside of the transverse steel. The longitudinal bar sizes, transverse steel detailing, and column lengths varied depending on the test series. The test variables and detailing for individual specimens is addressed in Volume 2 of this report. The footing is a capacity protected member designed to remain elastic while the full flexural capacity of the column was developed at the footing-column interface. Specifically, the required footing steel was allocated based on the maximum flexural overstrength of the column plastic hinge. The same transverse steel spacing was utilized over the entire column length. Longitudinal reinforcement was inclined through the footing-column joint to provide joint shear resistance. Additional vertical J-hooks were provided outside the joint for shear resistance. The column reinforcement had ninety degree end bends in which extreme fiber bars turned inside the joint to take advantage of the additional support provided by the inclined compression strut. Individual horizontal

hoops were provided in the footing joint for additional confinement and joint shear resistance.

2.4.1 Construction Sequence

The first step in the column construction process was to tie the column reinforcing cages. Wooden support templates with the specific locations of longitudinal bars in the cross section were created to maintain consistent reinforcement placement throughout the column length, Figure 2.20 through Figure 2.22. Individual longitudinal bars were tied in their proper location to the wooden exterior support templates, while interior templates maintained the correct bar placement over the column length. An interior support was provided to minimize the sag created by self-weight of the column cage. The column reinforcement had ninety degree end bends in which extreme fiber bars turned inside the joint to take advantage of the additional support provided by the inclined compression strut, Figure 2.22. The footing and cap locations of the column were left untied with a double overlapping ring of transverse steel at the termination points, Figure 2.20. A constant transverse steel spacing was utilized over the column length, and temporary diagonal supporting bars were added to provide stability until the cage was placed into the footing.

For the second stage of construction, the column cage was placed horizontally onto supports, and the inclined footing longitudinal steel was added to the joint, Figure 2.23 and Figure 2.24 Once the footing longitudinal steel was in place, individual 2/3 circumference overlapping transverse steel hoops were tied over column reinforcement in the footing joint, Figure 2.25. Once the additional joint hoop steel was added, individual J-hooks were tied over the side-by-side footing longitudinal steel outside of the joint, Figure 2.26.

The horizontal column and joint steel assemblages were picked up by a crane, rotated vertically, and placed into the footing formwork. Additional inclined and straight footing longitudinal reinforcement was placed outside of the joint, and later secured using transverse bars, Figure 2.17, Figure 2.18, Figure 2.27, and Figure 2.28. The reinforcement diagram and photos are shown for the most congested 24" and 18" configurations. These columns had the

largest steel content and axial load ratio, increasing the demands on the footing. For many of the test series, the size of the footing inclined longitudinal steel was decreased and the number of J-hooks was reduced. End-capped PVC tubes were used to block out the footing concrete in the four perimeter holes. The two rectangular axial load ducts near the middle of the footing were created using insulation foam.

A concrete mix with a target 28-day strength of 5ksi and a ½" maximum aggregate size was utilized for the footing concrete. Columns were constructed in sets of six, one concrete truck was used to pour three of the footings and a second truck poured the remaining three specimens. Cylinders for the separate trucks were kept separate so that they could be attributed to the correct columns. A seven day covered cure with damp burlap was utilized before removing the footing formwork. The excess concrete which covered some of the lower column reinforcement was removed, and the surface of the footing to column joint was roughened using an air needle scaler, Figure 2.29.

The second instrumentation technique using the Optotrak position monitoring system had vertical strips of cover concrete which were blocked out during construction. This was accomplished using two layers of ½" thick insulation foam over seven extreme fiber bars, Figure 2.31. The first layer was made from individual squares cut and placed directly over the longitudinal bar between each spiral layer. The second layer was a single vertical strip which was adhered to the first layer using construction adhesive. Tie wire was placed between each transverse steel spacing to prevent either layer from slipping during construction. Using this technique, the foam never shifted during casting.

The third method Optotrak instrumentation method required a complete cover concrete blockout to the depth of the outside surface of the longitudinal steel. Strips of ½" insulation foam were cut to match the clear spacing between spiral layers. After wrapping the strips in clear packaging tape to minimize the bond to the core concrete, the strips were wound around the column. At every intersection of the strip with a longitudinal bar tie wire was used to prevent the foam from shifting, Figure 2.30. An outside layer of ¼" thick insulation foam was wound tightly around the column to block out the region outside of the spiral.

A sonotube was placed over the foam blockout and column cage before being wrapped with plastic to keep it dry prior to casting. Formwork was erected to level and stabilize the column and cap as shown in Figure 2.32 and Figure 2.33. The column formwork was freestanding; scaffolding was only used as a work platform. Three panels of the cap formwork were erected before placing the cap reinforcement, Figure 2.19. The rectangular cap ties were fit above and below each of the four actuator attachment holes formed using PVC pipe. The ends of the PVC were fit over circular disks drilled into the formwork panels to prevent movement during casting.

For the 8ft cantilever length columns a forklift and 1/3 cubic yard concrete hopper was used to cast the specimen. A 13ft attachment for a concrete vibrator was used to consolidate individual lifts. Each column consisted of around four lifts, where each lift was connected to the prior lift by consolidating the interface with the concrete vibrator. A crane was used to pour lifts with the concrete hopper for the 11ft and 13ft cantilever length columns. After removing the formwork and sonotube, the insulation foam which was used to block out the cover concrete was left in place to prevent corrosion of the internal reinforcing steel.
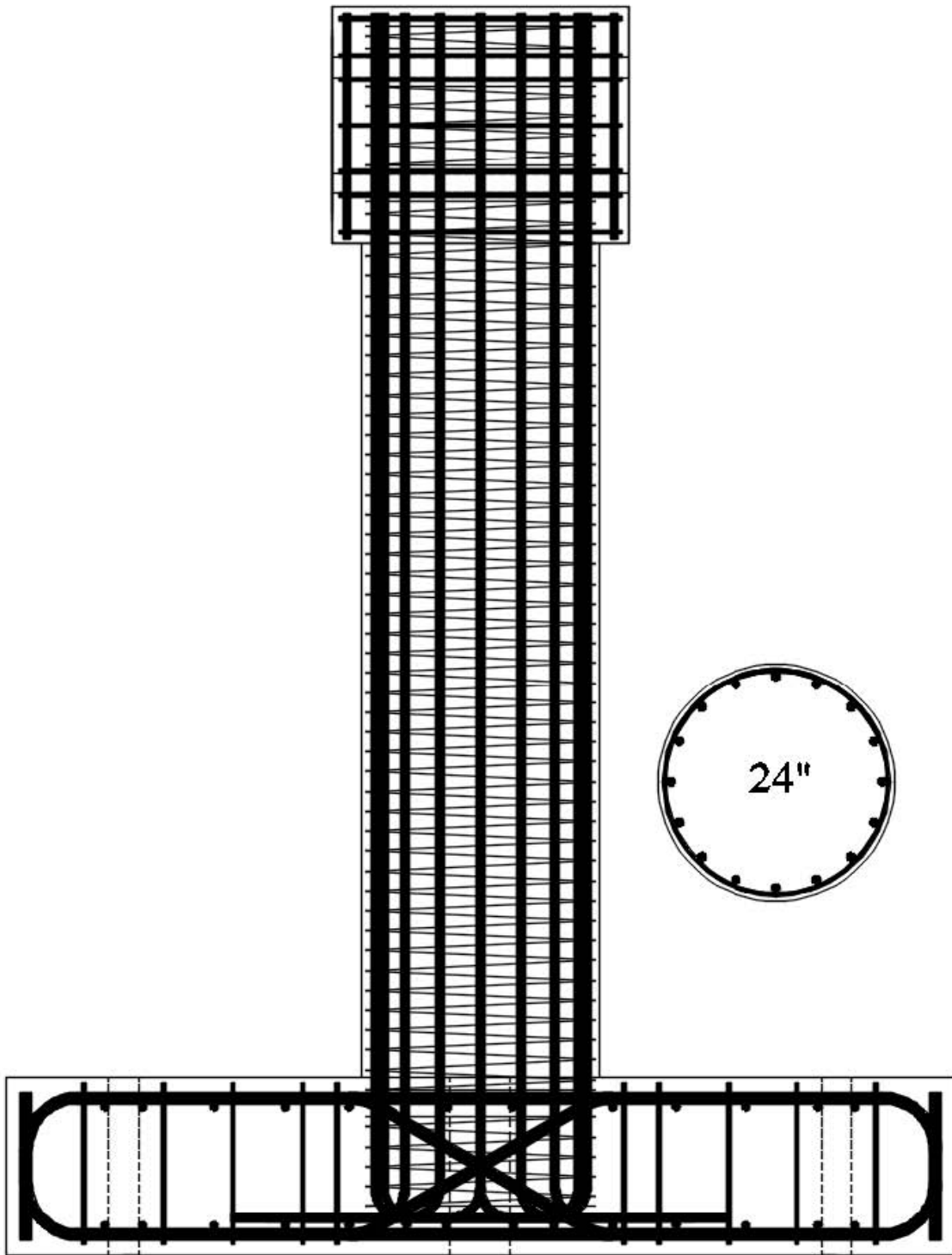
Figure 2.15 General Reinforcement Details for 24" Diameter Specimens
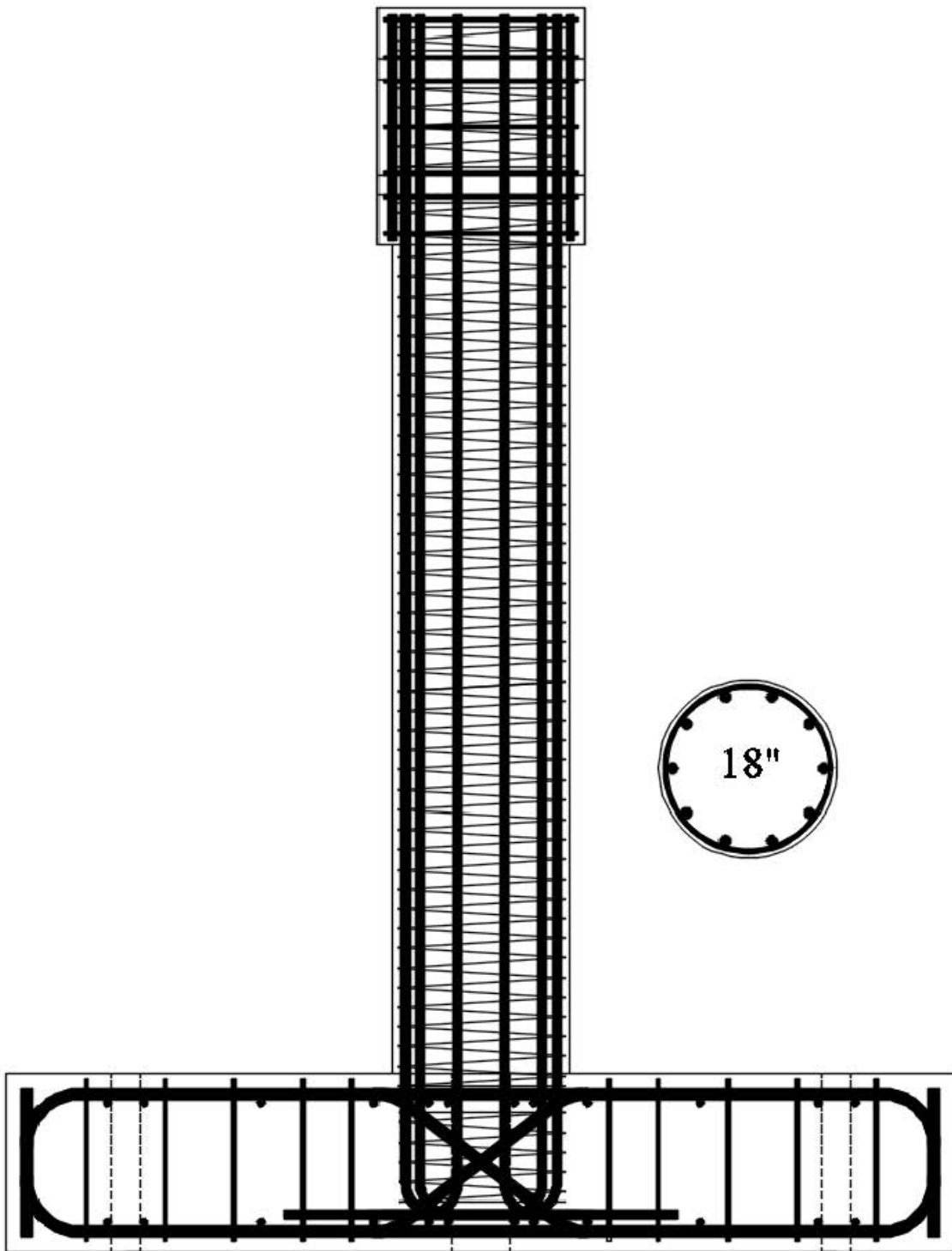
Figure 2.16 General Reinforcement Details for 18" Diameter Specimens
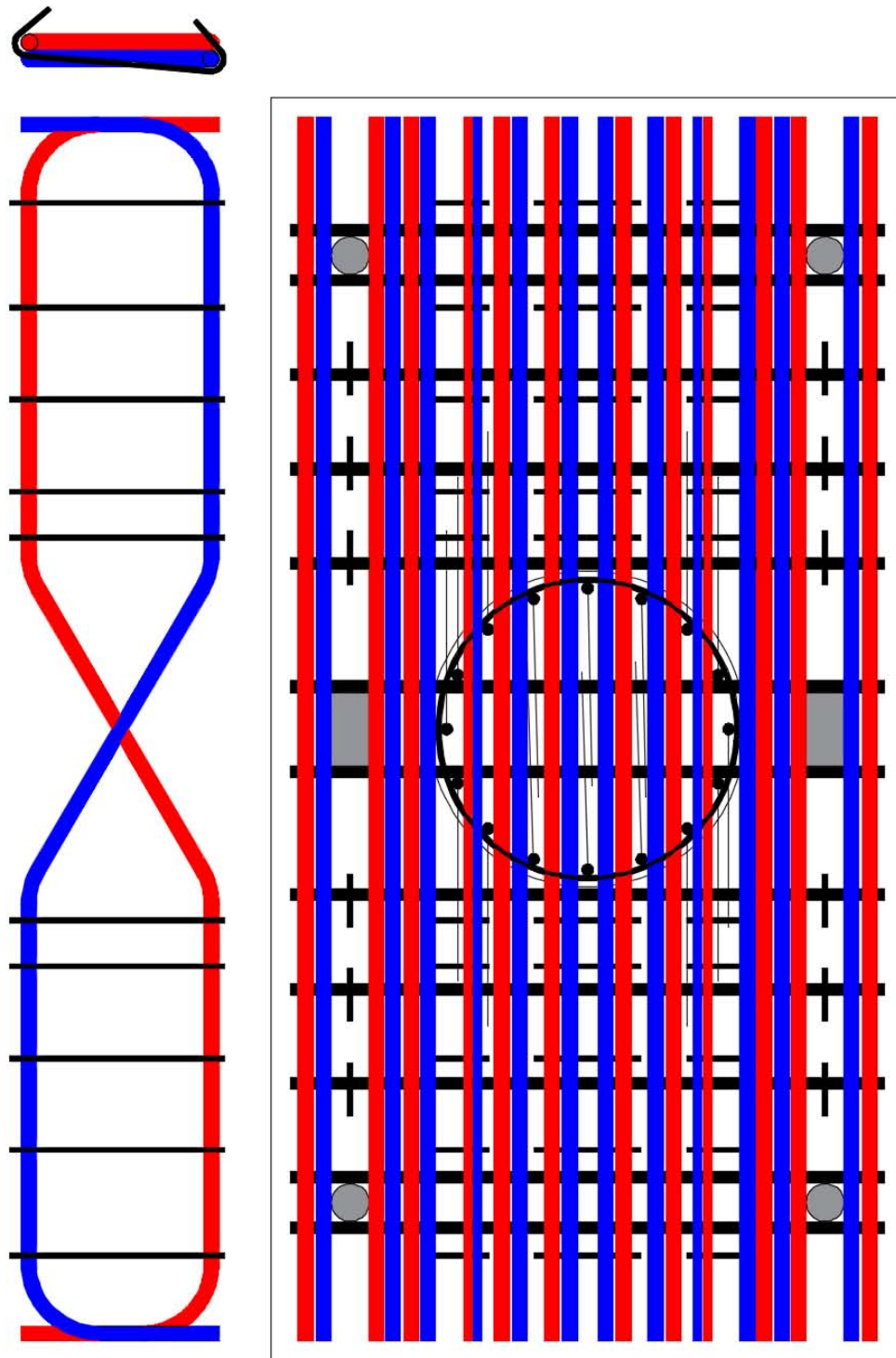
Figure 2.17 Footing Reinforcement Details for 24" Diameter Specimens
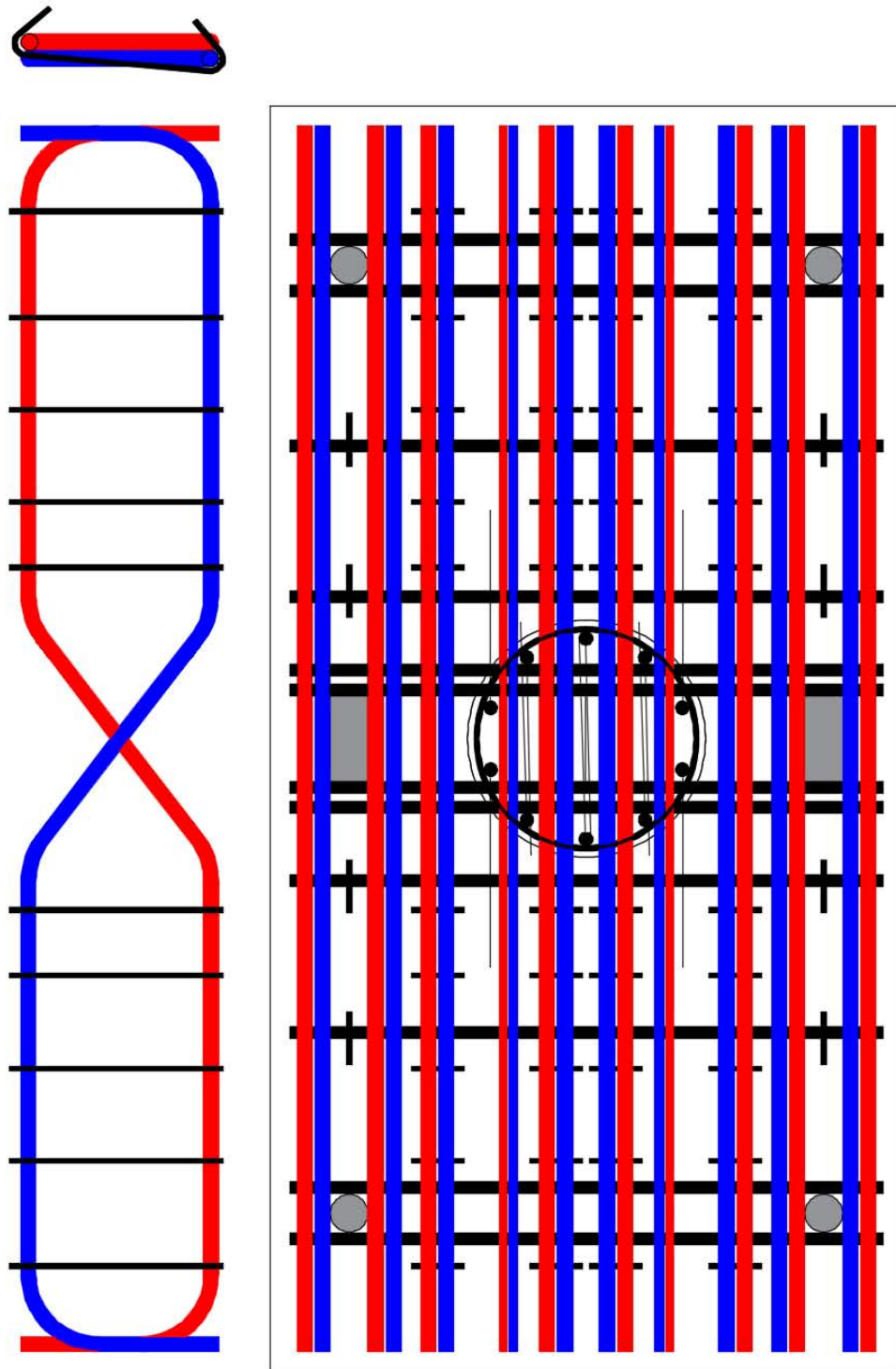
Figure 2.18 Footing Reinforcement Details for 18" Diameter Specimens
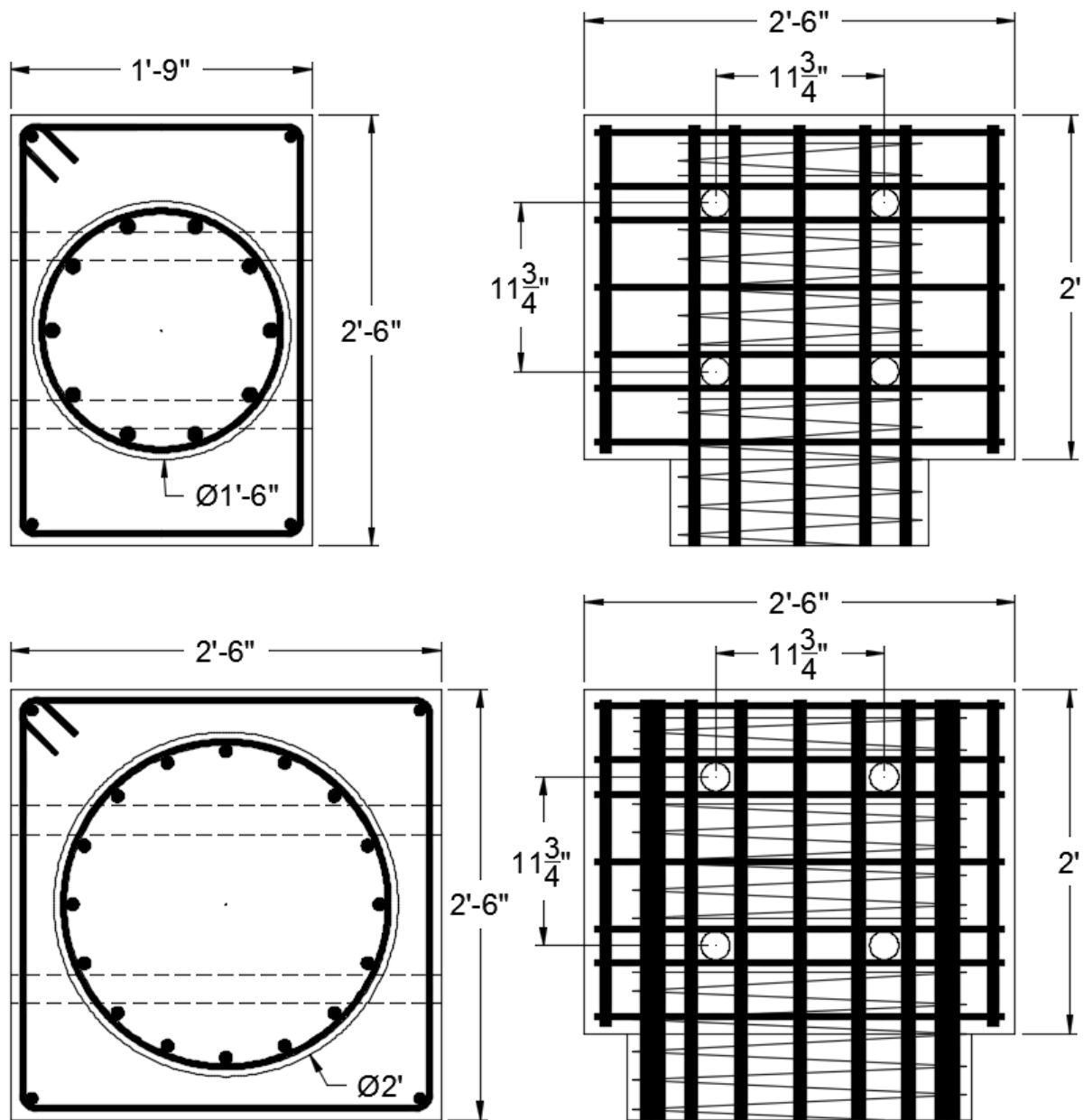
Figure 2.19 Column Cap Reinforcing Details for 18" and 24" Diameter Specimens
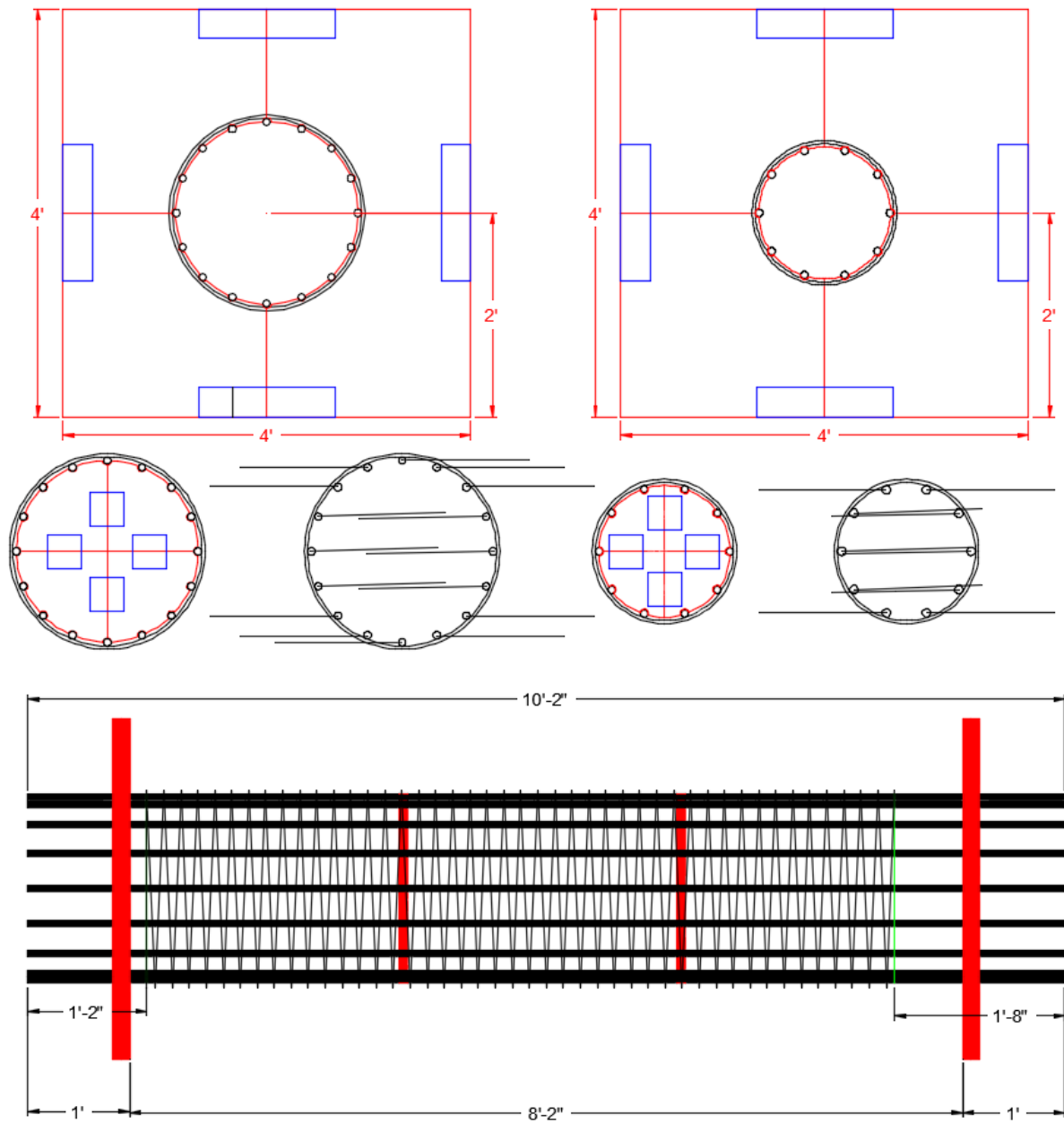
Figure 2.20 Column Reinforcing Cage Construction Method with Rebar Templates

Figure 2.21 External and Internal Column Reinforcement Cage Templates

Figure 2.22 Longitudinal Column Rebar Bends in the Footing
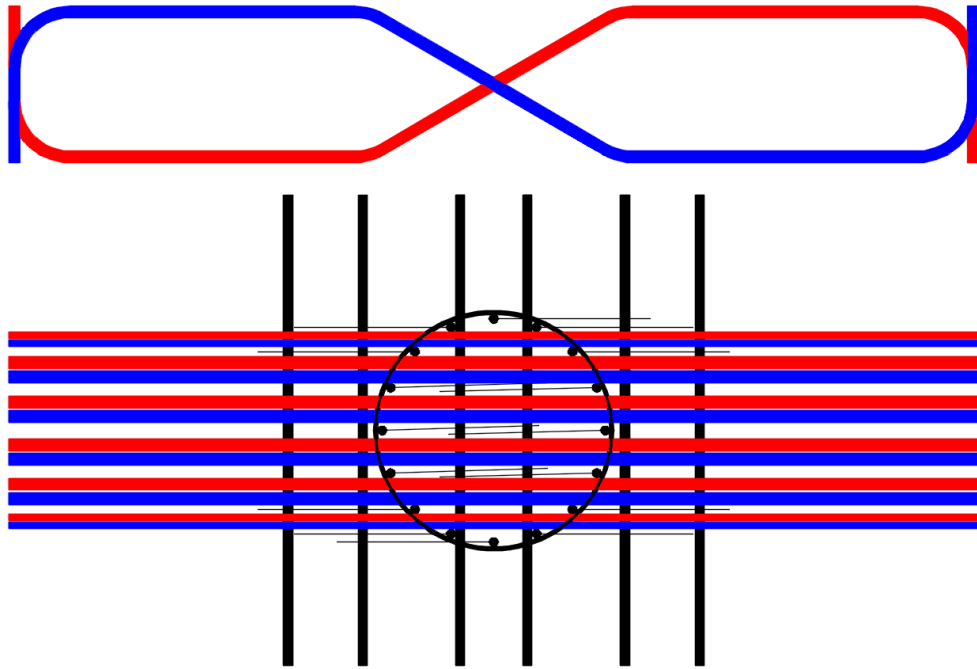
Figure 2.23 Footing Longitudinal and Joint Shear Z-Bar Installation

Figure 2.24 Install Footing Longitudinal and Inclined Joint Shear Steel

Figure 2.25 Individual 2/3 Circumference Overlapping Single Hoops in Footing Joint
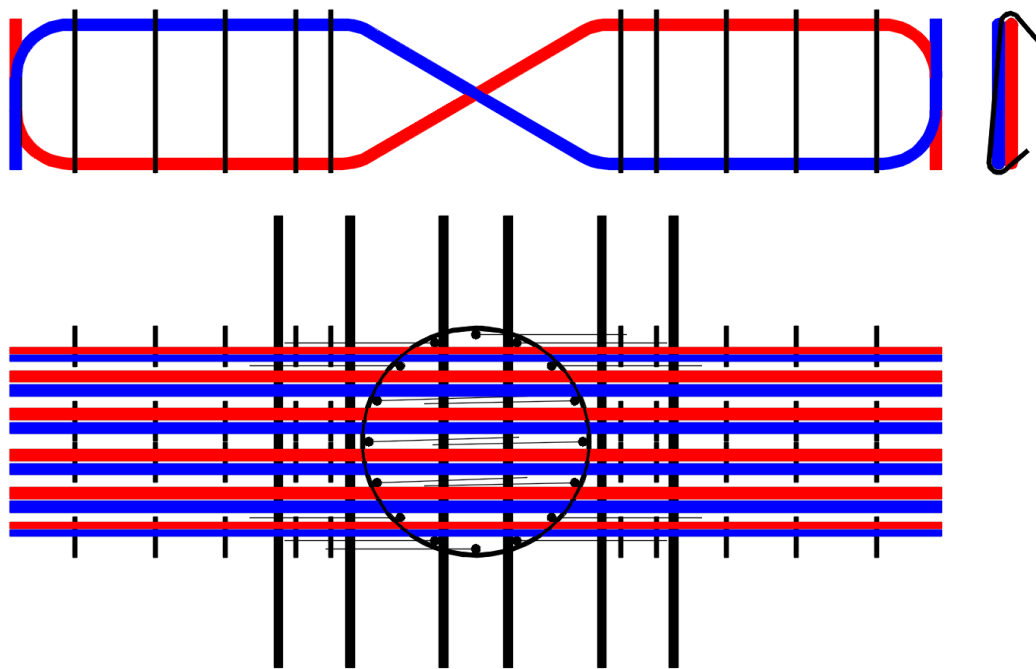
Figure 2.26 Install Individual J-Hooks over the Back-to-Back Z-Bars

Figure 2.27 Footing Formwork, Reinforcement, Tie Down PVC, and Axial Blockouts

Figure 2.28 Footing Formwork, Reinforcement, Tie Down PVC, and Axial Blockouts
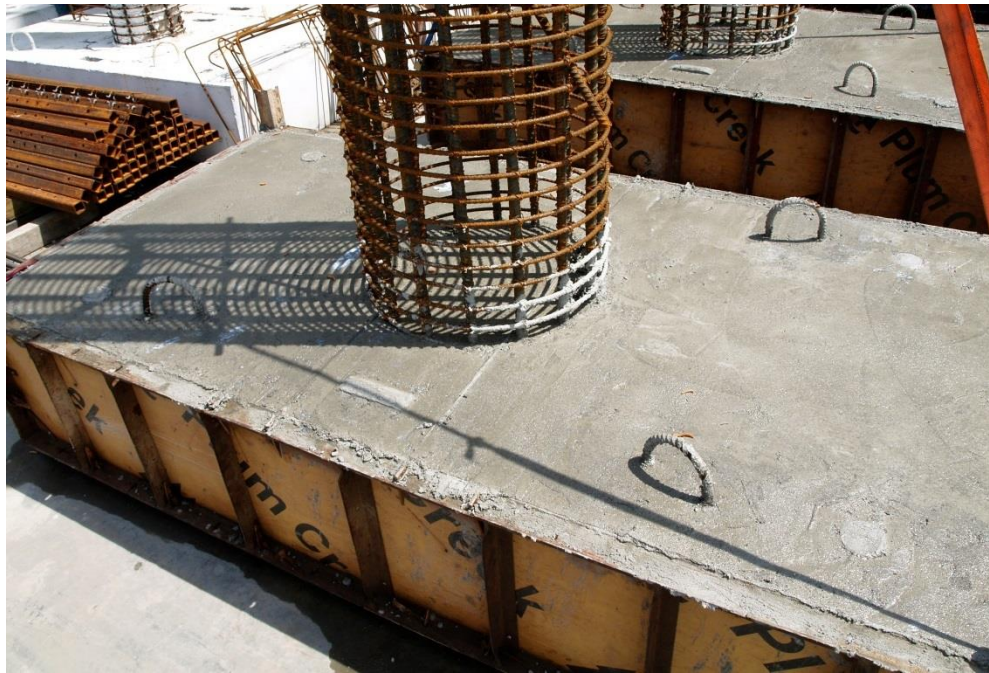
Figure 2.29 Casting of the Footing Concrete with Rented Formwork

Figure 2.30 Installation of 2-Layer Full Cover Concrete Blockout

Figure 2.31 After Casting, 2-Layer Longitudinal Cover Concrete Blockout Strips

Figure 2.32 Column Stabilization and Cap Formwork
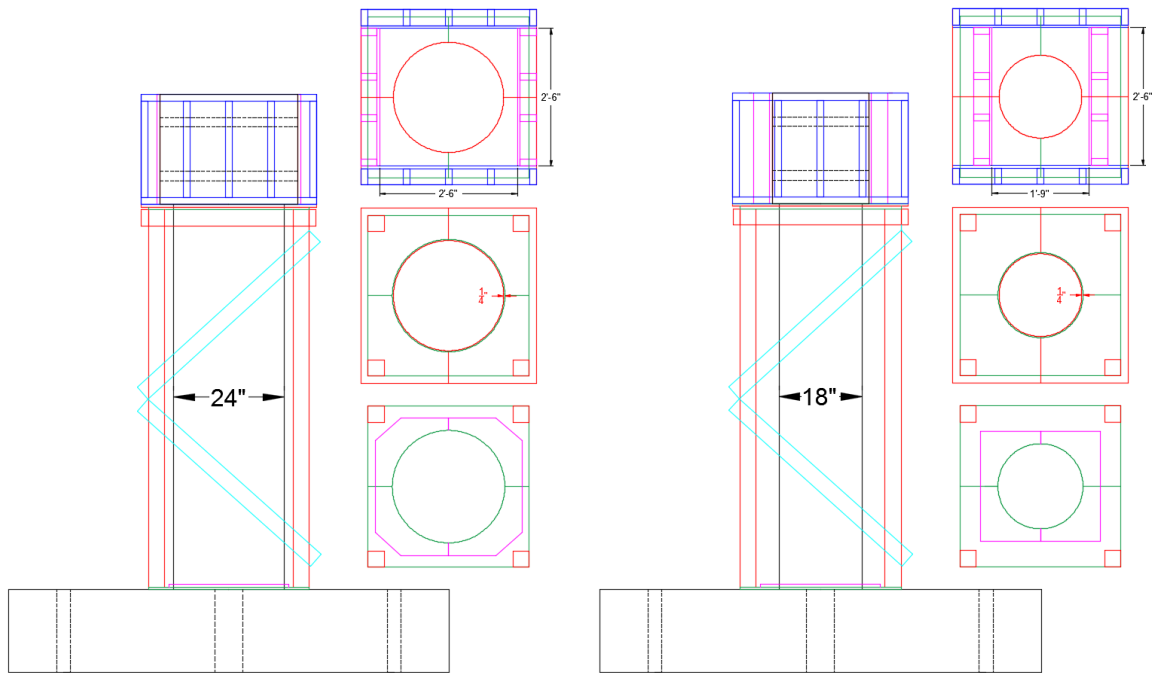
Figure 2.33 Details for Column Stabilization and Cap Formwork

Figure 2.34 Casting with Fork Lift, 1/3 Cubic Yard Hopper, and 13' Concrete Vibrator

2.4.2   Optotrak Target Marker Application Method

Now that the method of blocking out cover concrete during construction has been reviewed for both instrumentation techniques, Figure 2.30 and Figure 2.31, the method of surface preparation and application of Optotrak target markers deserves some discussion. After casting the columns, a small layer of concrete formed over the outside surface of the longitudinal reinforcement since the foam is compressible. An air needle scaler was used to remove this small layer of concrete over the reinforcing steel since the procedure is non-invasive and does not damage the underlying concrete. The remaining concrete debris was removed using a wire brush drill attachment.

Uniaxial tests on reinforcing steel bars were used to identify the best surface preparation technique and adhesive. The first step involved removing the layer of mill scale over the longitudinal reinforcement by polishing the bar with a wire brush. This layer of mill scale would otherwise flake off at high strains, debonding the instrumentation. The surface of the reinforcement was then cleaned with a degreaser. Disposable plastic caps which house the Optotrak target markers were adhered to the reinforcement using several different adhesives. Instrumentation adhered with hot glue and five minute epoxy failed to remain attached at large inelastic strain levels. A flexible silicone-based RTV adhesive provided the best results since it could accommodate the large strains in the steel while retaining strength.

The plastic caps had a center hole which filled with adhesive forming a shear key. A photo of a specimen with the disposable caps applied appears in Figure 2.35. The tape plugging the hole in the plastic cap was removed and the reusable target markers were snapped into place. Tape was used to route wires away from the field of view of the positon monitor. The wire management technique needs to accommodate deformation during the test and allow for the underlying concrete material to crush. The technique ultimately proved successful, and instrumentation remained attached to the latest stages of damage where previously buckled reinforcement fractured, Figure 2.36.
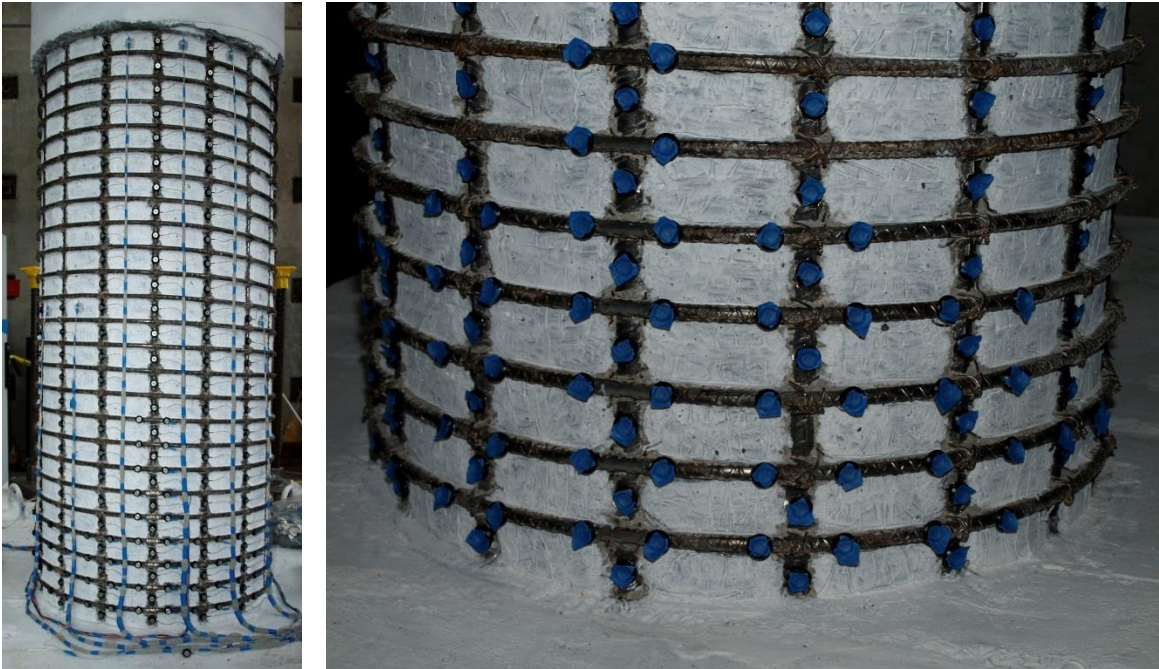
Figure 2.35 Surface Preparation and Target Marker Plastic Cap Application

Figure 2.36 Instrumentation Remained Attached to the Latest Stages of Damage

Chapter 3: Experimental Observations

3.1   Contents of Report Volume 2

Volume 2 contains a summary of experimental observations and data analysis for each column test. The material and geometric properties of each experiment are documented, and the sequence of observed and measured damage is presented. Volume 2 is broken up into three separate chapters based on the method of construction and instrumentation technique utilized in the experiments. The differences in the test series is discussed below, since design recommendations from Volume 1 of this report come from only Experiments 8-30, which utilized an improved instrumentation technique.

The initial six columns for the Load History research program were constructed by a local contractor. Although the need for accurate detailing was expressed and tolerances were specified, the resulting specimens had discrepancies in transverse steel spacings in the plastic hinge region. This influenced the restraint of longitudinal reinforcing bars and significantly impacted the performance of these specimens. Furthermore, these tests utilized the single position monitor and welded steel post extension instrumentation technique discussed in Chapter 2. The strain capacity reinforcing steel from Tests 1-6 was not influenced by the surface tack welded posts, but the technique produced less reliable strains when compared to the use of multiple position monitors and direct application of target markers to the longitudinal reinforcement.

To ensure proper detailing, Tests 7-30 were constructed by the research team at NCSU utilizing the procedure summarized in Chapter 2. Test 7 utilized the same steel post instrumentation as the previous six tests. The batch of A706 reinforcing steel had reduced strain at maximum stress when compared in the presence of small surface tack-welds. This shifted the failure mechanism of the column to brittle fracture of longitudinal reinforcement without prior bar buckling, resulting in a reduced deformation capacity. For this reason, as

well as the detailing errors mentioned, the occurrence of limit states in Tests 1-7 were not included in the formulation of design recommendations. Observational summaries for Tests 1-6 and separately Test 7 are included in Volume 2, along with a discussion of the impact of welding on the longitudinal steel from the two test series.

Since design recommendations from Volume 1 arise from only Experiments 8-30, additional care was taken when describing the observed and measured sequence of damage. For each experiment, the process through which the measured strain data was used to quantify deformation components is presented. This information although summarized in subsequent chapters, can be explored in greater detail in Volume 2 of this report.

Chapter 4: The Effect of Load History on Column Performance

In this section, the importance of displacement history and its effects on performance limit states, the relationship between strain and displacement, and the spread of plasticity in reinforced concrete structures is explored. An experimental study was carried out to assess the performance of thirty circular, well-confined, bridge columns with varying lateral displacement history, transverse reinforcement detailing, axial load, aspect ratio, and longitudinal steel content. Eight of these columns, with similar geometry and detailing, were subjected to various unidirectional displacement histories including standardized laboratory reversed cyclic loading and recreations of the displacement responses obtained from non-linear time history analysis of multiple earthquakes with distinct characteristics. Longitudinal reinforcing bars were instrumented to obtain strain hysteresis, vertical strain profiles, cross section curvatures, curvature distributions, and fixed-end rotations attributable to strain penetration. Results have shown that the limit state of reinforcement bar buckling was influenced by load history, but the relationship between strain and displacement along the envelope curve was not. The main impact of load history on bar buckling is its influence on accumulated strains within the longitudinal reinforcement and transverse steel.

4.1 Introduction

The goal of performance based seismic engineering is to design structures to achieve a predictable level of performance under a specific earthquake hazard within definable levels of reliability, as defined by the Structural Engineering Association of California, (SEAOC 1999). To satisfy the aims of performance based design, levels of damage which interrupt the serviceability of the structure or require more invasive repair techniques must be related to engineering criteria. For reinforced concrete flexural members such as bridge columns, concrete compressive and steel tensile strain limits are very good indicators of damage.

Closely spaced transverse steel hoops or spirals provide adequate confinement and shear resistance to produce a flexural mode of failure for columns without detailing deficiencies. The displacement capacity of these columns is limited by buckling and subsequent fracture of longitudinal reinforcement or rupture of confinement steel. An understanding of the spread of plasticity in reinforced concrete structures is required to determine the deformation at damage limit states for design.

A summary of the performance strain limits from (Kowalsky 2000) appear in Table 4.1. Serviceability limit states such as concrete cover crushing or residual crack widths exceeding 1mm may occur during smaller, more frequent earthquakes, (Priestley et. al. 1996). While the serviceability limit states do not pose a safety concern, the hinge regions must be repaired to prevent corrosion of internal reinforcing steel. At higher ductility demands produced by larger less frequent earthquakes, reinforcing bar buckling may lead to permanent elongation in the transverse steel, which diminishes its effectiveness in confining the concrete core. Bar buckling and significant damage to the core concrete represent the damage control limit states, which lead to significant repair costs. Furthermore, rupture of previously buckled bars during subsequent cycles of loading leads to strength loss. The life safety or collapse prevention limit state is characterized by fracture of previously buckled bars or rupture of confinement steel under displacements exceeding those required to initiate bar buckling.

Table 4.1 Performance Strain Limits from (Kowalsky 2000)

Limit State	Concrete Compressive Strain Limit	Steel Tensile Strain Limit
Serviceability	0.004 Cover Concrete Crushing	0.015 Residual Crack Widths Exceed 1mm
Damage Control	0.018 Mander et al. (1988), ε_{cu} Limit of Economical Concrete Repair	0.060 Tension Based Bar Buckling

Previous experimental studies on circular bridge columns with constant axial loads have shown that reinforcing bar buckling is influenced by unidirectional lateral displacement history: (Moyer and Kowalsky 2003), (Kunnath et al. 1997), and (Freytag 2006). Tests by Moyer and Kowalsky (2003) utilized fabricated load histories to investigate the influence of previous tensile strains on buckling of longitudinal reinforcement under compressive stress. Their results suggest that reinforcement buckling occurs after reversal from a peak tensile strain, while the bar is still under net elongation but compressive stress. After reversal from the peak displacement, the cracks on the tensile side begin to close, and before the column reaches zero displacement the reinforcement enters a state of compressive stress but net elongation. It is during this time, while the cracks are still open, that the reinforcement is the sole source of compression zone stability and the bars are prone to buckling. According to Kunnath et al. (1997), random displacement cycles provide a better means for understanding the effects of cumulative damage and assessing the performance of structures subjected to low-cycle fatigue. Freytag (2006) utilized instrumentation to detect lateral displacements of buckled bars in column tests with fabricated lateral displacement histories before the event could be visibly observed. The tests conducted by Freytag (2006) supported the tension based bar buckling mechanism, and suggested that bar buckling may be gradual phenomenon occurring over multiple cycles. Analytical studies by Syntzirma et. al. (2010) concluded that when flexural members are controlled by bar buckling, the deformation capacity cannot be defined uniquely since it is a function of the applied cyclic deformation history.

Tests by Wong et. al. (1993) focused on the effect of bidirectional lateral displacement history for squat circular columns with various levels of constant axial load. Their results indicated that bidirectional load path led to additional degradation in strength and stiffness, and a reduction in the deformation capacity when compared to nominally identical columns subjected to unidirectional load histories. Additionally, they found that the shape of the bidirectional load path did not significantly affect the displacement capacity of the columns. Experiments conducted by Bousias et al. (1995) investigated the influence of bidirectional load path and variable axial load history. They observed a significant coupling between the three loading directions, and found that the magnitude and history of the axial load

influenced the axial expansion and shortening of the column. Experiments by Esmaeily and Xiao (2005) demonstrated importance of considering axial load history when predicting the response of bridge columns. They concluded, "At a certain displacement and axial load level, the flexural capacity is significantly different depending on the history of axial loading path, from the flexural capacity at the same displacement and the same level but constant axial load."

4.1.1 Test Setup

While the progression of damage in flexural bridge columns has been thoroughly investigated in the past, to the author's knowledge, none of the previous studies had the ability to measure large strains at the level of the longitudinal reinforcement up to bar buckling. The goal of the experimental program is to investigate the impact of load history and design variables on the relationship between strain and displacement, performance strain limits, and the spread of plasticity. In total, the thirty specimens of the research program focus on the effects of load history, axial load, aspect ratio, transverse reinforcement, and longitudinal steel content. All of the variables found to be statistically significant towards describing bar buckling in an experimental dataset by Berry and Eberhard (2005) appear in the test matrix. This section focuses on eight specimens which had unidirectional lateral displacement history as the primary variable.

The specimen was designed to represent a single degree of freedom bridge column subjected to lateral and axial load, Figure 4.1. The test specimen consists of a footing, column, and loading cap. The footing is a capacity protected member which secures the specimen to the lab strong floor using post tensioned bars. A 220kip (980kN) hydraulic actuator, with a 40" (1016mm) stroke capacity, applies lateral load to the loading cap of the specimen. A spreader beam, two hydraulic jacks, and a load cell are placed above the loading cap to apply a constant axial compressive load through post tensioning bars which run beneath the lab strong floor. A self-regulating axial load system was utilized with a third hydraulic jack in a force controlled uniaxial testing machine to regulate the pressure, and thus

the load, of two jacks on top of the specimen to maintain a constant axial load throughout testing. This technique of axial load application does not replicate true P-Δ effects induced by a vertical gravity load. Instead, the axial force follows the direction of the post tensioning bar which is hinged at the floor and centered above the column. Examples of test setups which recreate P-Δ effects may be found in (Dutta et. al. 1999) and (Esmaeily and Xiao 2002).

The load history variable specimens had nominally identical geometry and longitudinal steel content, and were subjected to different quasi-static unidirectional lateral displacement histories. The 24" (610mm) diameter bridge columns, Figure 4.2, contained 16 #6 (19mm) A706 bars for longitudinal reinforcement ($A_{st}/A_g = 1.6\%$) and a #3 (9.5mm) A706 spiral at either 2" (51mm) ($4A_{sp}/(D's) = 1\%$) or 1.5" (38mm) (1.3%) on center. The shear span for the cantilever columns was 8ft (244cm), and they had a moment to shear ratio of ($M/VD = 4$). The specimens were subjected to a constant axial load of 170kips (756kN), ($P/(f_c'A_g) \approx 5\%$) depending on the concrete compressive strength. The test matrix for the eight columns is shown in Table 4.2, and the material properties of the longitudinal and transverse reinforcement appear in Table 4.3.
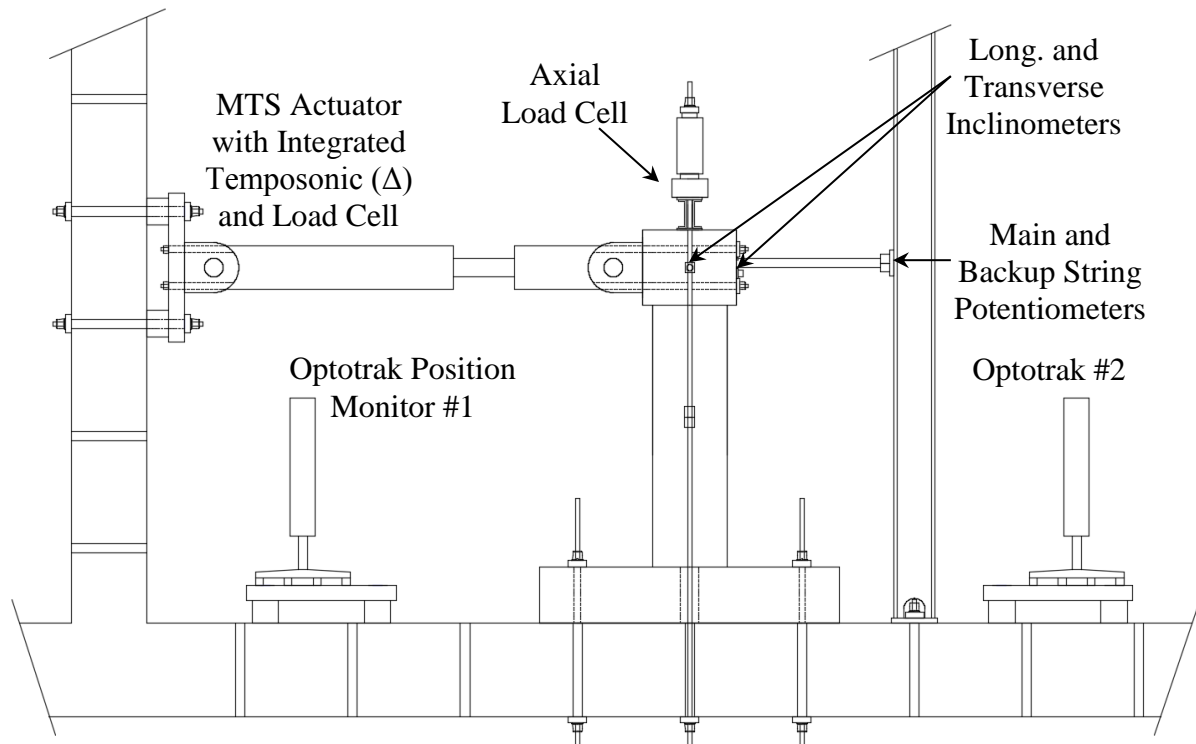
Figure 4.1 Test Setup for Load History Tests (Two Optotrak Position Monitors)
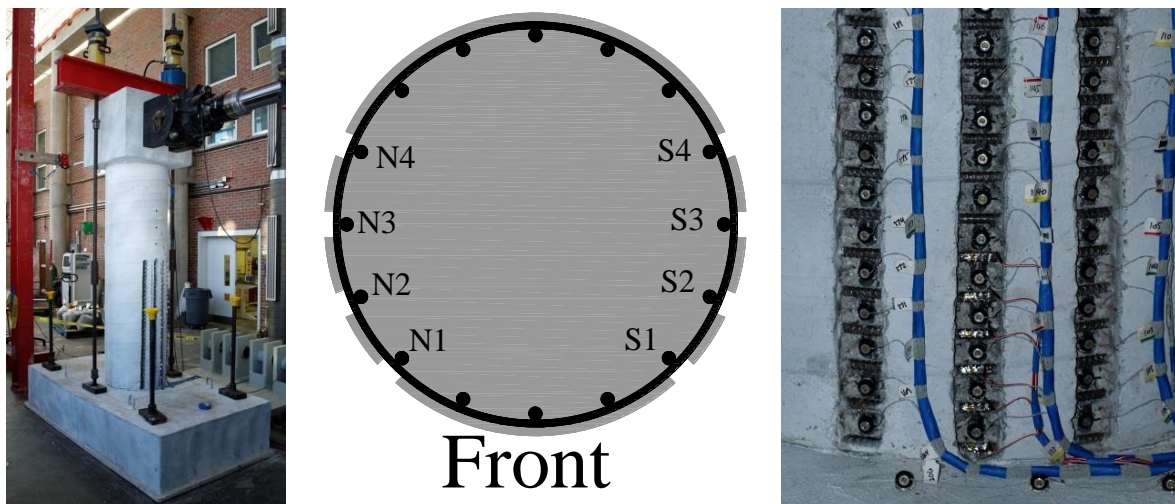
Figure 4.2 Column Cross Section for Load History Tests

Name	x [mm]	y [mm]	z [mm]
Marker_1	32.622	-726.444	-2930.306
Marker_2	32.496	-687.185	-2931.137
Marker_3	33.461	-645.676	-2932.094
Marker_4	34.025	-608.345	-2932.906
Marker_5	34.337	-572.444	-2933.642
Marker_6	34.567	-535.868	-2934.635
Marker_7	35.034	-497.412	-2934.922
Marker_8	36.253	-457.184	-2935.375
Marker_9	36.811	-420.613	-2936.034
Marker_10	36.651	-382.274	-2936.742
Marker_11	37.194	-347.498	-2937.788
Marker_12	36.057	-311.491	-2938.482
Marker_13	37.745	-276.437	-2938.848
Marker_14	38.088	-239.135	-2939.463
Marker_15	39.179	-199.496	-2940.132
Marker_16	38.289	-162.678	-2941.334
Marker_17	37.925	-126.207	-2941.940
Marker_18	38.382	-92.501	-2942.708
Marker_19	38.387	-52.669	-2943.177
Marker_20	37.914	-19.704	-2944.086
Marker_21	38.282	16.432	-2944.563
Marker_22	37.883	53.179	-2945.331
Marker_23	37.021	92.056	-2946.380
Marker_24	37.401	128.900	-2947.265

Figure 4.3 (Left) Optotrak Spatial Coordinate Output and (Right) Comparison of Optotrak Strains to Traditional Measurements

Table 4.2 Test Matrix for Load History Variable Columns

Test	Load History	Spiral Detailing (ρ_s)	f'c (ksi, MPa)	P/f'c*Ag
T9	Three-Cycle-Set	#3 at 2" (51mm) (1%)	6.81, 46.97	5.5%
T8	Chile 2010	#3 at 2" (51mm) (1%)	6.99, 48.18	5.4%
T8b	Three-Cycle-Set	#3 at 2" (51mm) (1%)	6.99, 48.18	5.4%
T10	Chichi 1999	#3 at 2" (51mm) (1%)	5.26, 36.29	7.1%
T10b	Three-Cycle-Set	#3 at 2" (51mm) (1%)	5.26, 36.29	7.1%
T11	Kobe 1995	#3 at 2" (51mm) (1%)	6.18, 41.85	6.2%
T12	Japan 2011	#3 at 2" (51mm) (1%)	6.10, 42.06	6.2%
T16	Three-Cycle-Set	#3 at 1.5" (38mm) (1.3%)	6.71, 46.27	5.6%
T17	Llolleo 1985	#3 at 1.5" (38mm) (1.3%)	7.59, 52.33	5.0%
T17b	Three-Cycle-Set	#3 at 1.5" (38mm) (1.3%)	7.59, 52.33	5.0%
T18	Darfield NZ 2010	#3 at 1.5" (38mm) (1.3%)	7.80, 53.83	4.8%
T18b	Three-Cycle-Set	#3 at 1.5" (38mm) (1.3%)	7.80, 53.83	4.8%

Table 4.3 Reinforcement Material Properties

Longitudinal Reinforcement	ε_y	f_y (ksi)	ε_h (hardening)	f_h (ksi)	ε_u (max stress)	f_u (ksi)	Transverse Steel	fy (ksi)
T8 – T12	0.00235	68.1	0.0131	68.2	0.1189	92.8	T8 – T12	74.1
T16 – T18	0.00235	68.1	0.0146	68.2	0.1331	94.8	T16 – T18	64.6

Longitudinal Reinforcement	ε_y	f_y (MPa)	ε_h (hardening)	f_h (MPa)	ε_u (max stress)	f_u (MPa)	Transverse Steel	fy (MPa)
T8 – T12	0.00235	470	0.0131	470	0.1189	640	T8 – T12	511
T16 – T18	0.00235	470	0.0146	470	0.1331	654	T16 – T18	445

4.1.2 Instrumentation

Numerous experimental studies in the past, for example (Moyer and Kowalsky 2003) and (Hines et. al. 2004), utilized an array of linear potentiometers to measure cross section curvatures in the column hinge regions. These potentiometers were attached to the ends of imbedded threaded rods to measure the average strain in the tensile and compressive extreme fiber regions of the column. Since the potentiometers are placed at the ends of the rods, their measurements are affected by rotations of the rods themselves.

The experimental program presented in this paper utilized an innovative technique of applying a commercially available instrumentation system to measure large strains at the level of the reinforcement with multiple Optotrak Certus HD 3D position sensors produced by Northern Digital Inc. The Optotrak position monitoring system can read the location of target markers placed on the specimen in three dimensional space during a test, Figure 4.3. By calculating the change in three dimensional distances between target markers, strains can be determined with respect to the original unloaded gage lengths. The 3D accuracy of the Optotrak Certus system reported by Northern Digital Inc. is 0.1mm with a resolution of 0.01mm. Target markers were applied directly to six longitudinal bars in the extreme fiber regions of the column to obtain strain hysteresis, vertical strain profiles, cross section curvatures, curvature distributions, and fixed-end rotations attributable to strain penetration. To accomplish this, vertical strips of cover concrete overlaying the extreme fiber bars were

blocked out over the instrumented region as shown in Figure 4.2. Strain gages were applied to layers of transverse steel overlaying the longitudinal reinforcement to observe the interaction between compressive demand, transverse steel strain, and buckling restraint. An illustration of the accuracy of the Optotrak system compared to traditional measurement techniques appears in Figure 4.3. A tensile test on a reinforcing bar was conducted with a 51mm Optotrak gage length, a 51mm extensometer gage length, and a centrally placed strain gage.   Closer inspection demonstrates that the Optotrak strains oscillate around the measurements predicted by the conventional instrumentation, but the general trend is captured throughout the entire tensile test. Electrical resistance strain gages fail to remain attached at large inelastic strain levels, which are of interest to this study.

The top column displacement was obtained through a string potentiometer placed at the center of the lateral load. The lateral load and stroke of the 220kip (980kN) hydraulic actuator were measured through an integrated load cell and linear variable differential transformer (LVDT). An axial load cell monitored the contribution of one hydraulic jack to the total axial load of the column, the total axial load double the recorded value.

4.1.3 Loading Protocol

The specimens were subjected to various unidirectional top-column displacement histories including standardized laboratory reversed cyclic loading, and recreations of the displacement responses obtained from non-linear time history analysis of multiple earthquakes with distinct characteristics. The top-column displacement histories used in the tests are shown in Figure 4.4 through Figure 4.9. The experiments utilized a quasi-static displacement controlled loading procedure. The symmetric three-cycle-set load history is commonly used to evaluate the seismic performance of structural components. The load history begins with elastic cycles to the following increments of the analytically predicted first yield force: ¼ F_y', ½ F_y', ¾ F_y', and F_y'. The experimental first yield displacement is then determined by taking the average of the recorded displacements during the first yield push and pulls cycles. The equivalent yield displacement, used to determine the displacement

ductility levels ($\mu_{\Delta 1} = (1 * \Delta_y)$), is then calculated as $\Delta_y = \Delta'_y \, (M_n/M'_y)$. The symmetric three-cycle-set load history resumes with three balanced cycles at each of the following displacement ductility levels: 1, 1.5, 2, 3, 4, 6, 8, 10, 12, etc.

For earthquake time-history tests, the analytical top column displacement history is determined using non-linear time history analysis (NLTHA). The original acceleration input of the earthquake record is multiplied by a constant scale factor to produce a peak displacement response suitable for the experimental test. This is necessary because the amplitude of peak response is an important variable when comparing the performance of the columns subjected to different load histories. The goal of the experimental load history is not to re-produce the exact displacement response which the specific acceleration record may have created, but rather to compare the performance of columns subjected to specific characteristics in the displacement histories obtained from NLTHA. Specific earthquake top-column displacement response characteristics were chosen including: the number and amplitude of cycles prior to the peak, degree of symmetry, and peak displacement in each direction of loading. The symmetric three-cycle-set experiments (T9 and T16) were conducted prior to earthquake tests to establish the displacement ductility levels. The scaling factors of the acceleration input used in NLTHA of the earthquake load histories were determined based on the displacement capacities of T9 and T16, which had bar buckling during displacement ductility eight. Four earthquake records were scaled approximately displacement ductility nine while two records were scaled to ductility ten. The strains at the first yield displacement of each earthquake test were verified to confirm that the ductility levels from T9 and T16 remained appropriate. Specimens which had un-buckled reinforcement during the earthquake load histories were subjected to a symmetric three-cycle-set displacement history to evaluate the columns post-earthquake performance (T8b, T10b, T17b, T18b).
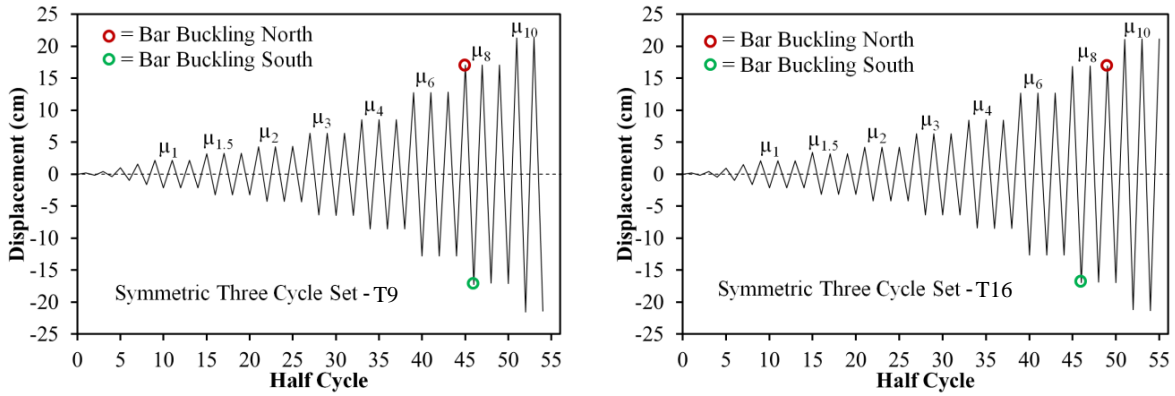
Figure 4.4 Control Specimen Load Histories (Left) T9 and (Right) T16
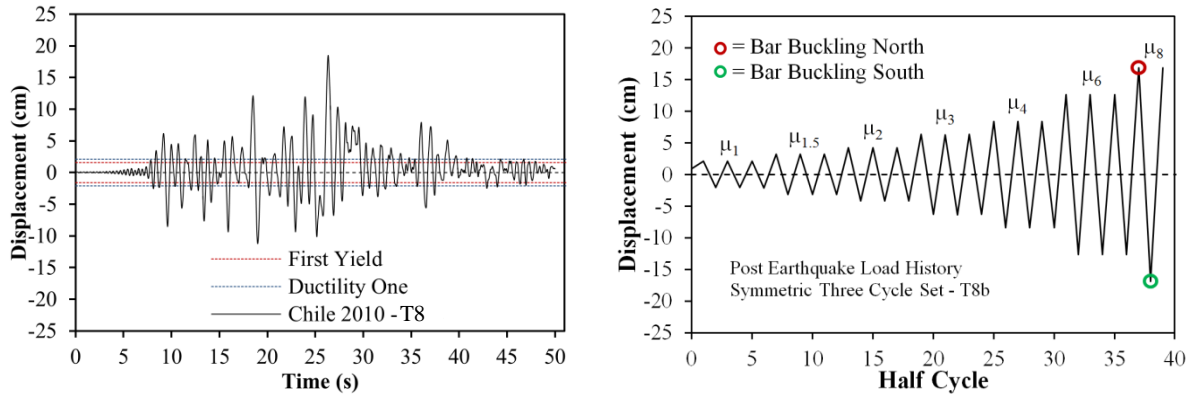
Figure 4.5 Test 8 Chile 2010 Load History and Post EQ Three Cycle Set
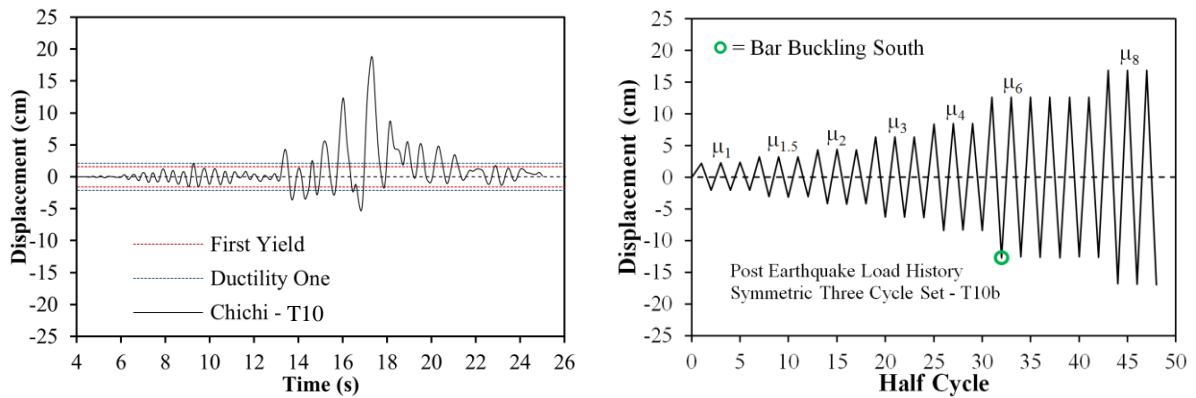
Figure 4.6 Test 10 Chichi Load History and Post EQ Three Cycle Set
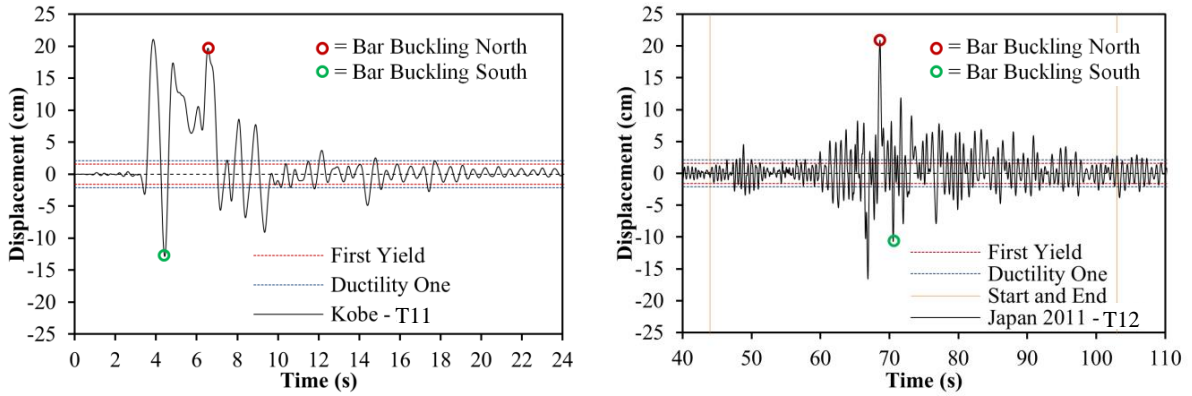
Figure 4.7 (Left) T11 Kobe 1995 Load History and (Right) T12 Japan 2011 LH
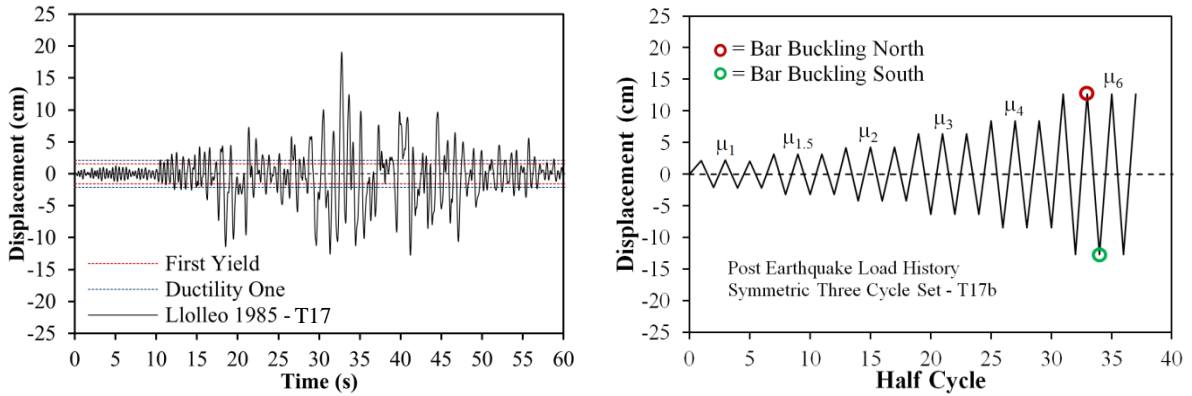
Figure 4.8 Test 17 Llolleo 1985 Load History and Post EQ Three Cycle Set
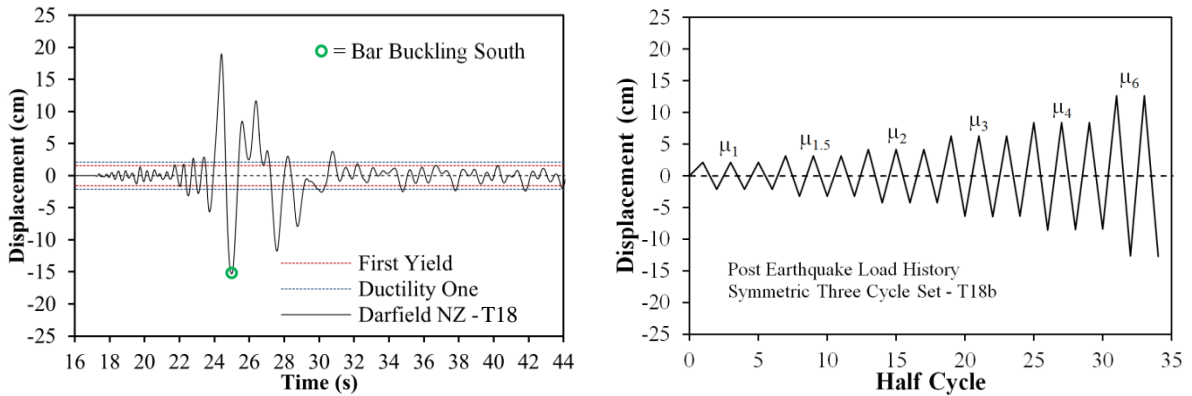
Figure 4.9 Test 18 Darfield NZ Load History and Post EQ Three Cycle Set

4.2 Experimental Results

4.2.1 Damage Observations

The deformation capacity of all of the cyclically loaded specimens was limited by longitudinal bar buckling and subsequent rupture during later cycles of the load history. The following sequence of damage was observed: cracking, longitudinal reinforcement yield, cover concrete crushing, yielding of transverse steel, bar buckling, and then reinforcement rupture. Rupture of transverse steel was never observed. The first significant loss of strength occurred when previously buckled reinforcement ruptured in tension.

For the load history variable tests, cover concrete crushing occurred at an average compressive strain of 0.0045, when the compressive demand exceeded the unconfined concrete compressive strength. The average compressive strain measured at spiral yield in the confinement region was 0.015. As a reference, the Mander et. al. (1988) ultimate concrete compressive strain of specimens T8-T12 is equal to 0.0185 and 0.0183 for tests T16-T18. On average, spiral yielding in the confinement region occurred at approximately 80% of the Mander et. al. (1988) ultimate concrete compressive strain. Noticeable influences of displacement history on cover concrete crushing on spiral yielding were not discernible based on the test results.

4.2.2 Test 11 – Response to the Kobe 1995 Earthquake

Sample results from test unit LH4 are presented to explain the influence of load history on accumulated strains in the longitudinal and transverse steel. The acceleration input of the Kobe 1995 earthquake record was multiplied by 1.13 to produce an analytical top column response equivalent to displacement ductility 9.9, as shown in Figure 4.7. A 24" (610mm) diameter bridge column with a constant axial load equivalent to $(P/(f_c'A_g) = 6.2\%)$, confined with a #3 (9.5mm) spiral at 2" (51mm) on center, was subjected to a quasi-static loading procedure which recreated the analytical Kobe displacement history obtained from NLTHA. The test began with a small pull cycle followed by a near monotonic push to the

peak displacement ductility of 9.9. The North longitudinal reinforcement, shown in Figure 4.11, is placed into tension during push cycles while the South side is subjected to compression, refer to Figure 4.12. The push cycle to displacement ductility 9.9 resulted in a peak tensile strain of 0.059 in the North extreme fiber bar, a peak compressive strain of -0.037 in the South extreme fiber bar, and two layers of inelastic transverse steel in the compression zone (Figure 4.12). The particular longitudinal reinforcement gage lengths depicted in Figure 4.11 and Figure 4.12 do not align with the peak tensile and compressive strains, but rather with the location which later outwardly buckled. This region is presented because it provides a clear representation of when buckling occurred, since strains measured by target markers on the convex side of a buckled bar increase under compressive demand. The peak tensile strain of 0.059 was not sufficient to buckle the North bar during the subsequent reversal to displacement ductility -6.1.

   At displacement ductility -6.1, tensile strains in the South bar reached 0.033, compressive strains in the North bar measured -0.0119, and the transverse steel on the North side of the specimen remained elastic (Figure 4.11). This peak tensile strain, combined with multiple layers of inelastic transverse steel, was sufficient to buckle the South extreme fiber bar after reversal of loading. At this time, the measured strains in the South bar no longer represent engineering strains due to the outward buckled deformation between target markers. As the South bar buckles outwards, the strain in the transverse steel begins to rapidly increase as shown in Figure 4.12. A peak tensile strain of 0.053 was measured in the North extreme fiber bar at the end of the push cycle to displacement ductility 9.3. Again, note that this peak tensile strain occurred over an adjacent gage length to that shown in Figure 4.11 which depicts outward buckled region. It was during the following reversal from displacement ductility 9.3 that the North extreme fiber bar visually buckled under compressive stress. The outward buckled deformation in the North bar caused measured strains in the transverse steel to sharply increase as shown in Figure 4.11. Prior to buckling of the North extreme fiber bar, the transverse steel remained elastic.
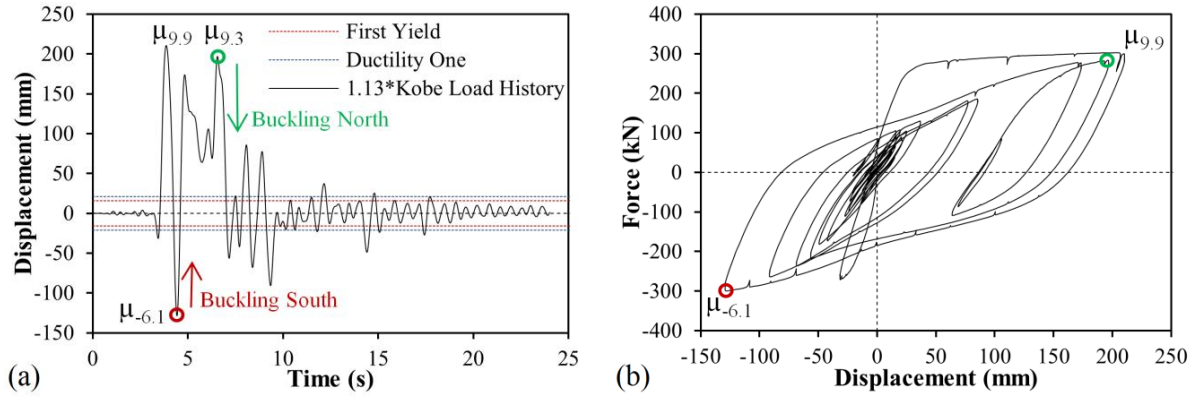
Figure 4.10 (Left) Kobe 1995 EQ Load History and (Right) Hysteretic Response
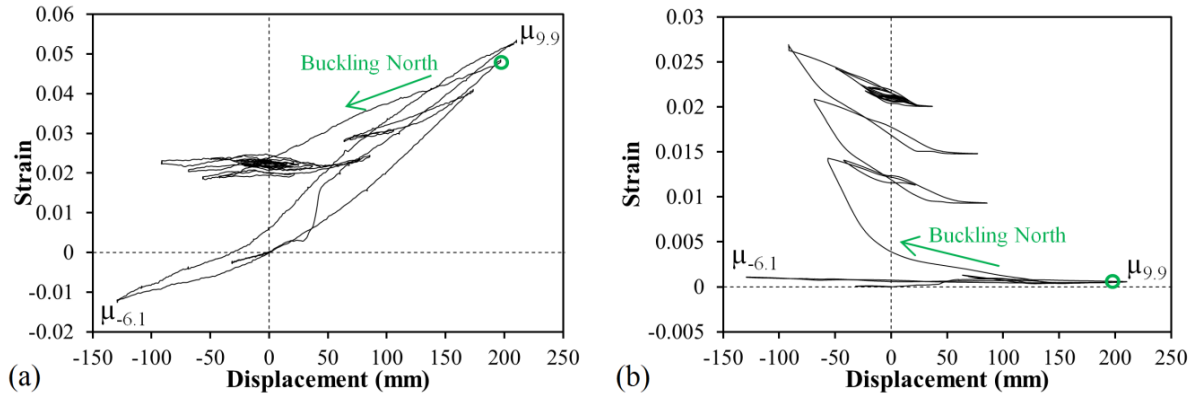
Figure 4.11 (Left) North Bar Strain History (Right) Overlying Spiral Strain History
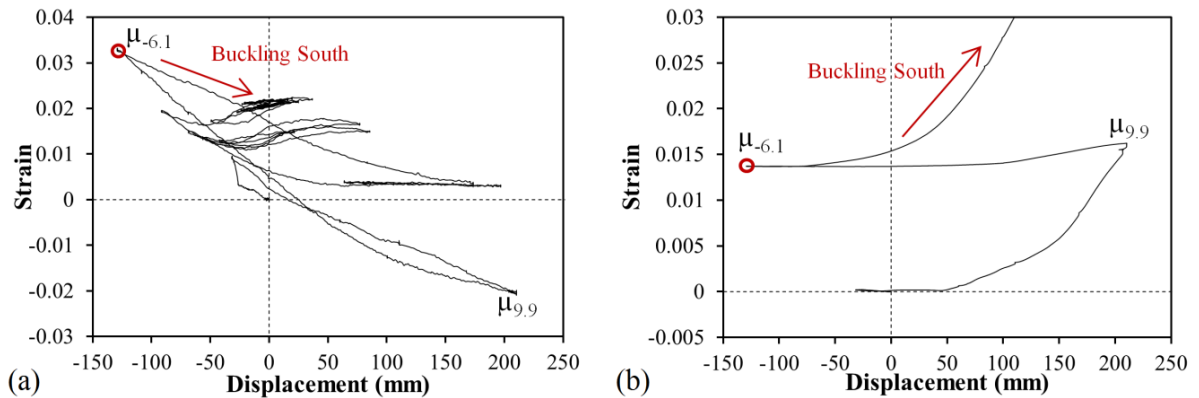
Figure 4.12 (Left) South Bar Strain History (Right) Overlying Spiral Strain History

4.2.3   The Effect of Load History on Reinforcement Bar Buckling

The main impact of load history on column behavior is its effect on accumulated strains within the longitudinal and transverse reinforcement. Large concrete compressive demand results in inelastic strains in the transverse steel, which reduces its effectiveness in restraining the longitudinal bars from buckling. Load histories with compressive demand sufficient to produce inelastic transverse steel may require lower values of peak tensile strain to initiate bar buckling after reversal of load. The symmetric three-cycle-set load history is more severe than the load histories produced by actual earthquakes, when evaluated to the same peak displacement, due to the balanced repeated cycles at each ductility level. Multiple cycles at the same amplitude allow each side of the specimen to be subjected to the peak compressive and tensile cycles, creating the worst situation for bar buckling a given peak displacement.

The relationship between strain and displacement during the largest push and pull cycles of each load history variable test appear in Figure 4.14 and Figure 4.15. Not all of the peak excursions produced bar buckling after reversal from the peak tensile strains shown, for instance the Kobe 1995 record (LH4) did not buckle the North bar until the second peak as discussed in the previous section. An extreme fiber bar buckling summary is shown in Table 4.4 and Table 4.5. The 24" (610mm) diameter bridge columns contained a #3 (9.5mm) spiral at either 2" (51mm) or 1.5" (38mm) on center. A specimen with each transverse steel detailing was subjected to a symmetric three-cycle-set load history (T9 and T16) which produced bar buckling during cycles at displacement ductility eight. For the specimen subjected to T9, fracture of previously buckled reinforcement occurred during repeated cycles at displacement levels equal to those necessary to initially produce bar buckling. The following four earthquake load histories: Chichi 1999 (T10), Chile 2010 (T8), Llolleo 1985 (T17), and Darfield 2010 (T18) were scaled to produce peak response displacement ductility of 8.8, 8.7, 9.0, and 9.0 respectively. The longitudinal steel placed into tension during the peak push cycles of these four load histories did not buckle during the earthquake record.

For the case of the Darfield 2010 load history (T18), the peak push displacement led to inelastic layers of transverse steel, and the following pull cycle to displacement ductility -7.3 had sufficient tensile demand to buckle a single bar during the subsequent reversal of load. The four specimens were then subjected to symmetric three-cycle-set load histories (T10b, T8b, T17b, and T18b) to determine the post-earthquake performance of the columns. Reinforcement buckling occurred during cycles at displacement ductility six of the cyclic load histories after the Chichi 1999 (T10b) and Llolleo 1985 (T17b) records. This indicates that the earthquake load histories led to a reduction in the displacement capacity at bar buckling of two ductility levels during tests T10b and T17b when compared to initially undamaged specimens T9 and T16. This is a potential issue for post-earthquake inspection because there was no visible indication of the reduced ductility capacity after T10 and T17.

Bar buckling occurred during ductility eight of the cyclic load history conducted after the Chile 2010 earthquake (T8b). The cyclic load history after the Darfield 2010 record (T18b) ruptured the previously buckled bar during ductility six. This shows that increases in displacement demands beyond those which were initially required buckle a reinforcing bar (displacement ductility -7.3 with inelastic spiral restraint) are not required to rupture the previously buckled bar. A dependable level of displacement at which fracture of a previously buckled bar would occur cannot be reliably developed because it is dependent on the severity of the buckled deformation. Since bar buckling permanently deforms the spiral restraint, even smaller cycles after the initiation of buckling degrade the core concrete and increase the buckled deformation. Uniaxial bar tests by Restrepo-Posada et. al. (1994) showed that micro-cracks develop at the locations of ribs on the compression side of a severely buckled bar, Figure 4.13. Once these micro-cracks develop, the future tensile capacity of the bar is compromised.

To produce buckling after reversal from the peak displacement response of earthquake load histories, the Kobe 1995 (T11) and Japan 2011 (T12) records were scaled to displacement ductility 9.9 and 10 respectively. As discussed previously, bar buckling did not

occur until reversal from the second peak cycle to displacement ductility 9.3 of the Kobe record (LH4).

The relationship between strain and displacement along the envelope curve of cyclic response does not appear to be affected by seismic load history. Since the curves shown in Figure 4.14 and Figure 4.15 are from the peak cycles of their respective load histories, only portions of the curve lie upon the envelope of cyclic response. At low ductility levels the measured tensile strains during the Kobe 1995 (T11) and Darfield 2010 (T12) peak cycles are larger than the other records because these were near monotonic push cycles to the peak displacement while the crack distribution was still forming.
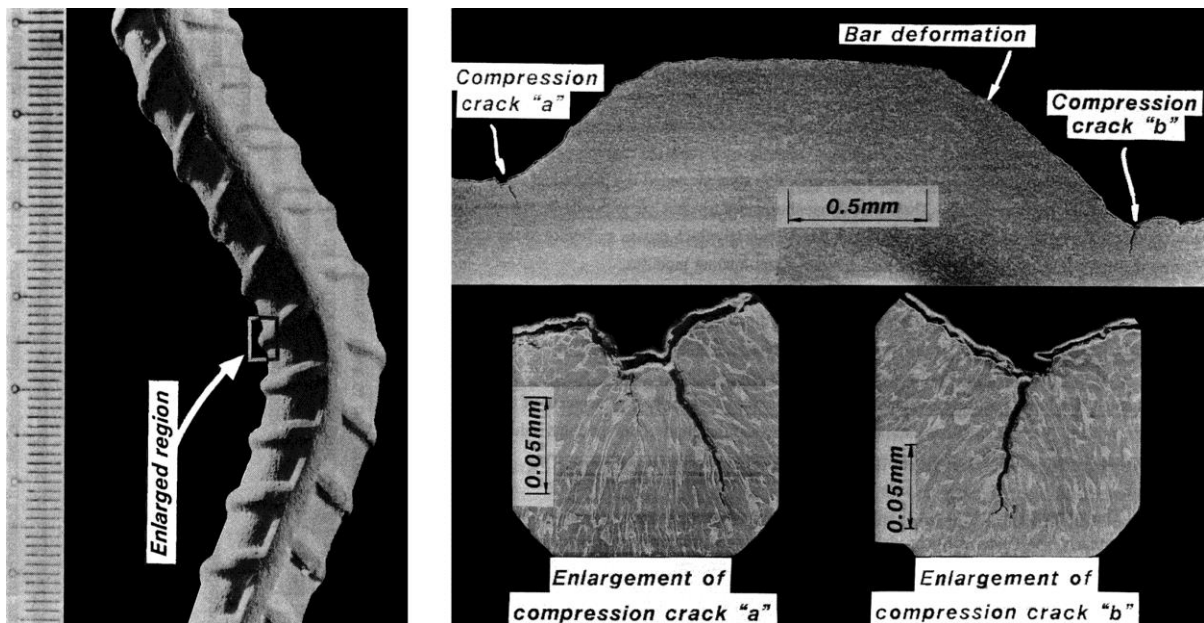
Figure 4.13 Micro-Cracks Present on a Buckled Reinforcing Bar, Photo Obtained from Restrepo-Posada et. al. (1994)
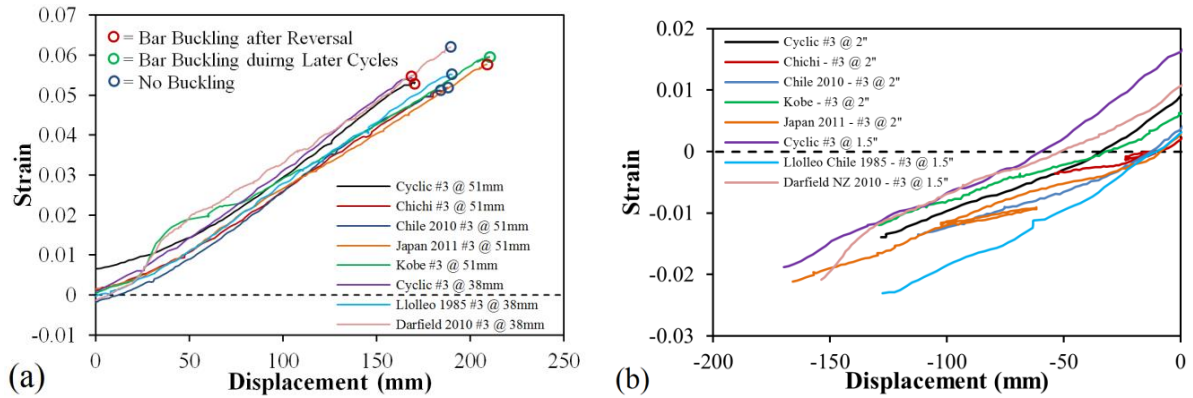
Figure 4.14 North Bar (Left) Peak Push Cycle Tensile Strain-Displacement and (Right) Peak Pull Cycle Compressive Strain-Displacement

Table 4.4 Bar Buckling Summary for the North Extreme Fiber Bar

Test	Disp. (mm) before Buckling North Bar	Disp. Ductility before Buckling North Bar	Peak Tensile Strain of North Bar	Peak Strain Compressive	Peak Spiral Strain
T9	171	8 (1st Cycle)	0.053	-0.018	0.0027
T8	No Buckling (184)	No Buckling, 8.7	No Buckling (0.051)	-0.013	0.0021
T8b	169	8 (1st Cycle)	0.043	-0.028	0.0255
T10	188	No Buckling, 8.9	No Buckling (0.052)	-0.003	0.0009
T10	169	No Buckling, 8	No Buckling (0.048)	-0.016	0.0115
T11	Initial 210, Buckled after Second Peak 197	Initial 9.9, Buckled after Second Peak 9.3	Initial 0.059, Buckled after Second Peak 0.053	-0.012	0.0017
T12	209	10	0.058	-0.021	Debonded after 0.008
T16	169	8 (3rd Cycle)	0.056	-0.019	0.0096
T17	No Buckling (190)	No Buckling, 9	No Buckling (0.055)	-0.023	0.0091
T17b	127	6 (2nd Cycle)	0.035	-0.039	Debonded after 0.011
T18	No Buckling (190)	No Buckling, 9	No Buckling (0.062)	-0.021	0.0031
T18b	No Buckling (127)	No Buckling, 6 (2nd Cycle)	No Buckling (0.036)	-0.023	0.0039
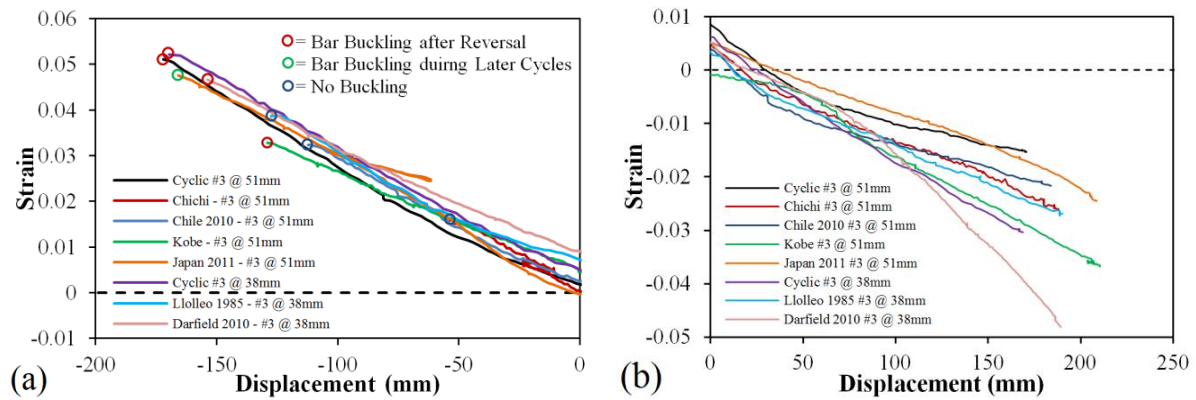
Figure 4.15 South Bar (Left) Peak Pull Cycle Tensile Strain-Displacement and (Right) Peak Push Cycle Compressive Strain-Displacement

Table 4.5 Bar Buckling Summary for the South Extreme Fiber Bar

Test	Disp. (mm) before Buckling South Bar	Disp. Ductility before Buckling South Bar	Peak Tensile Strain of South Bar	Peak Strain Compressive	Peak Spiral Strain
LH1	-170	-8 (1st Cycle)	0.051	-0.015	0.0034
LH2	No Buckling (-112)	No Buckling, -5.3	No Buckling (0.032)	-0.022	0.0055
LH2b	-169	-8 (1st Cycle)	0.048	-0.032	Off Scale >0.036
LH3	No Buckling (-54)	No Buckling, -2.5	No Buckling (0.016)	-0.032	0.0131
LH3b	-127	-6 (1st Cycle)	0.038	-0.045	Off Scale >0.036
LH4	-129	-6.1	0.033	-0.037	0.0159
LH5	Initial -166, Buckled after Peak to 107	Initial -7.9, Buckled after Peak to -5.1	Initial 0.044, Buckled after Peak to 0.028	-0.032	0.0120
LH6	-170	-8 (1st Cycle)	0.052	-0.030	0.0095
LH7	No Buckling (-128)	No Buckling (-6)	No Buckling (0.039)	-0.039	0.0077
LH7b	-127	-6 (Second)	0.036	-0.043	Debonded after 0.019
LH8	-154	-7.3	0.047	-0.048	Off Scale >0.016

4.3   Spread of Plasticity

4.3.1   Test 16 – Deformation Components Three Cycle Set Load History with #3 Spiral at 1.5" (38mm)

The Optotrak position monitoring system allows for a closer examination of column flexure and strain penetration deformation components.   To describe the process and capabilities of the instrumentation technique, sample test results related to the spread of plasticity in a symmetric three-cycle-set load history (T16) are presented. The displacement history along with data points which mark cycles where cover crushing, spiral yield, visible bar buckling, and bar fracture occurred in appear in Figure 4.16. The measured compressive and tensile strains for South and North extreme fiber bars during push cycles appear in Figure 4.16. This figure shows strain profiles for extreme fiber bars on each side of the specimen to illustrate the effects of tension shift. Figure 4.17 shows that cracks near the footing remain effectively horizontal, but above this section the flexural shear crack distribution is inclined. The cracks form a naturally inclined cut in a free body diagram representation of the bridge column. Hines et. al. (2004) developed a procedure for evaluating the effects of tension shift on the spread of plasticity by quantifying stress components acting along an inclined flexural shear crack. Due to the effects of tension shift, compressive strains are concentrated near the footing-column interface and tensile strains are fanned out to a greater height following the crack distribution. This mechanism is observable in Figure 4.16.

The instrumentation technique allows for monitoring of individual strain hysteresis, such as Figure 4.17 which depicts the outward buckled region of the North extreme fiber bar. Stable hysteretic loops were observed until the second pull cycle of displacement ductility eight where measurable deformation occurred at the location consistent with outward visible buckling during the following pull cycle. This measurable deformation was not discernible by eye, and therefore poses an issue for to post-earthquake inspection.

Since the deformations at performance limit states are required for design, a closer look at the relationship between strain and displacement is warranted. Monotonic moment-curvature analysis is typically utilized in design because it provides an accurate prediction for the envelope curve of the lateral force versus deformation response for flexure-dominated columns with constant axial load, as shown in Figure 4.21. Experimental tests by Esmaeily and Xiao (2005) show that alterations to the cyclic response prediction must be made to account for variable axial loads. The monotonic moment-curvature analysis was conducted in a script called CUMBIA (Montejo and Kowalsky 2007). The program utilizes the following material models for the confined and unconfined concrete and reinforcing steel: (Mander et al. 1988) and (King et al. 1986). Top column displacements are obtained using the plastic hinge method and shear displacement models presented in Priestley et. al. (2007).

A comparison of the measured and predicted relationships between strain and displacement during push cycles appears in Figure 4.18. The solid lines represent individual push cycles which begin with the column at zero displacement and end at the peak of the respective displacement ductility level. The dashed lines represent the subsequent reversal of loading. Moment-curvature analysis over predicts the measured tensile strains and under predicts compressive strains at an increasing rate at higher ductility levels. Due to the effects of tension shift, the tensile strains are fanned out to a greater height above the footing-column interface, which may decrease the peak tensile strain at the base of the column (near the footing). Compression strains are concentrated at the base of the column as the hinge region rotates about inclined flexural shear cracks. These compressive strains are further localized at the location of inelastic layers of transverse steel. Syntzirma et. al. (2010) proposed that the lumped rotation at the support caused by strain penetration of longitudinal steel into the footing may lead to a local increase in the axial strain in the compressive zone.

The measured compression strains in the South reinforcing bar (Figure 4.16) are larger at the location where several layers of transverse steel entered the inelastic range, as shown in Figure 4.19. The spiral layer closest to the footing-column interface remained elastic due to the additional confinement provided by the footing. Two layers of transverse steel entered

the inelastic range during displacement ductility six, but bar buckling did not occur until reversal from tensile strains sustained during the first pull cycle of ductility eight. The outward buckled region of the South extreme fiber bar occurred over the previously inelastic transverse steel layers as shown in Figure 4.19.

The measured strains of six reinforcing bars are plotted along the cross section to obtain curvatures in Figure 4.20. The curvature was taken as the slope of the least squared error line. Curvature profiles obtained from thirty-two horizontal cross sections at different heights above the footing appear in Figure 4.20. Procedures developed by Hines et al. (2004) were followed to extract numerical information related to the shape of the linear plastic curvature profiles. The dashed lines for each curvature distribution represent a least squared error linear fit to the plastic portion of the measured curvatures. Following recommendations from Hines et. al. (2004), the extent of plastic curvatures above the footing is calculated by determining where the linear plastic curvature distribution intersects the elastic curvature profile, shown as a grey dashed line. The elastic curvature profile forms a triangular shape along the length of the column with a value of zero at the top and the yield curvature at the base. The total base section curvature is determined by the intersection of the plastic least squared error line and the x-axis at the footing-column interface.

The target marker on each bar placed closest to the footing-column interface can be used to measure the effects of strain penetration. Development of fully anchored column longitudinal bars into the footing leads to bond slips along the partially anchored region of the bars near the footing-column interface, as described by Zhao and Sritharan (2007). They additionally note that this bond slip is not a pull-out of the entire bar embedment length resulting from poor bond between the concrete and reinforcing bar. If the measured bond slips of the target markers are plotted along the cross section, the fixed-end rotation attributable to strain penetration may be calculated as the slope of a least squared error line, Figure 4.21.

The hysteretic response in Figure 4.21 was obtained from a string potentiometer which measured deflections at the center of the applied lateral load. This total deformation is the

sum of the column flexure, column shear, and strain penetration components. The flexural displacement may be determined by integrating the measured curvature distribution and adding the strain penetration deformation component.   The curvatures above the instrumented region are assumed to follow the triangular yield curvature profile.   The integrated displacements from the Optotrak system are compared to the measured displacements in Figure 4.21.   The good agreement suggests that the shear deformation component is small relative to the total deformation.
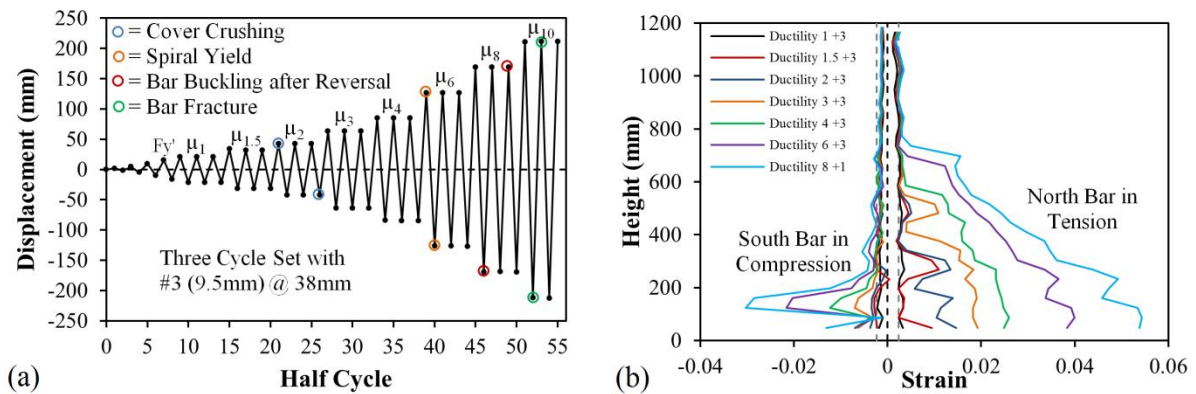
Figure 4.16 (a) T16 Load History and (b) Vertical Strain Profiles
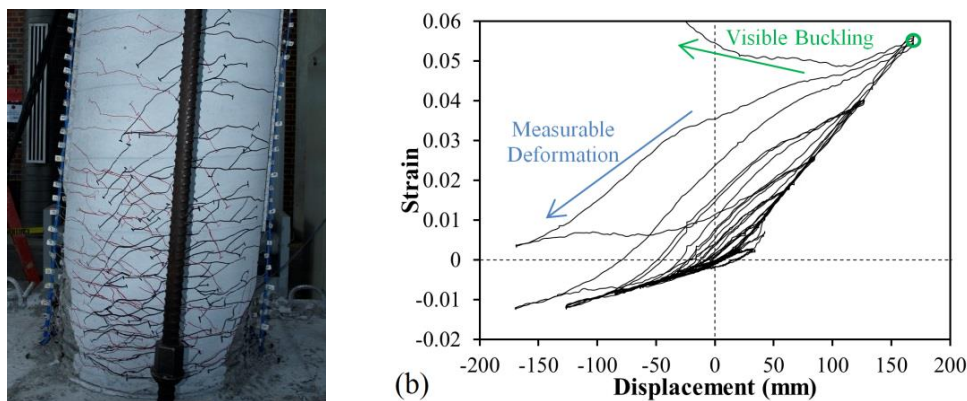
Figure 4.17 (a) Inclined Flexural Shear Cracks and (b) North Strain Hysteresis
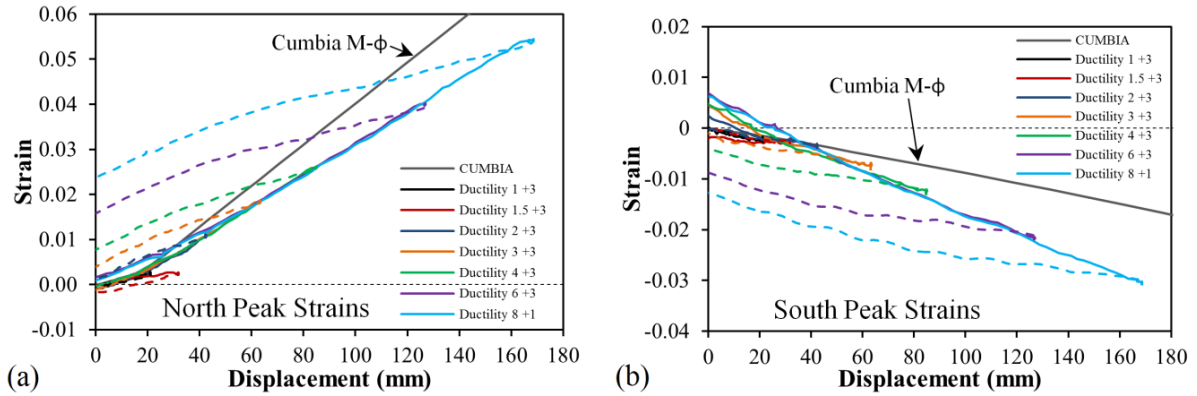
Figure 4.18 (a) North Tensile and (b) South Bar Compressive Strain-Displacement
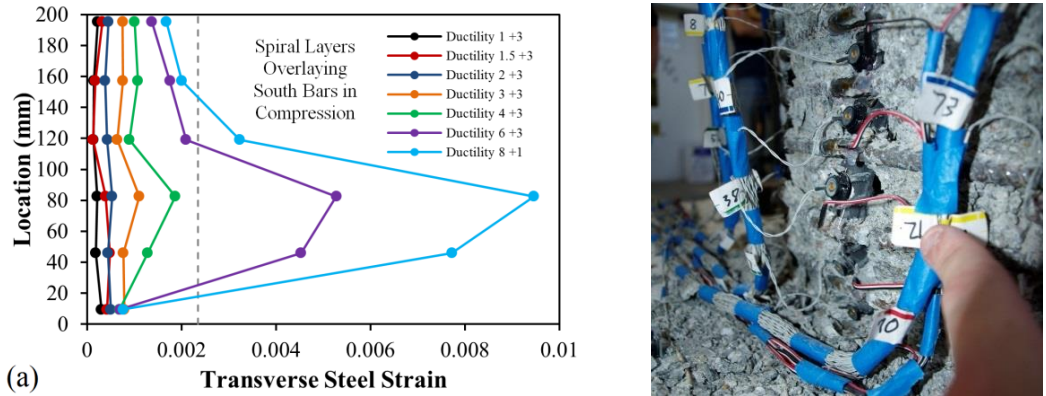
Figure 4.19 (a) South Spiral Strains and (b) South Buckled Bar
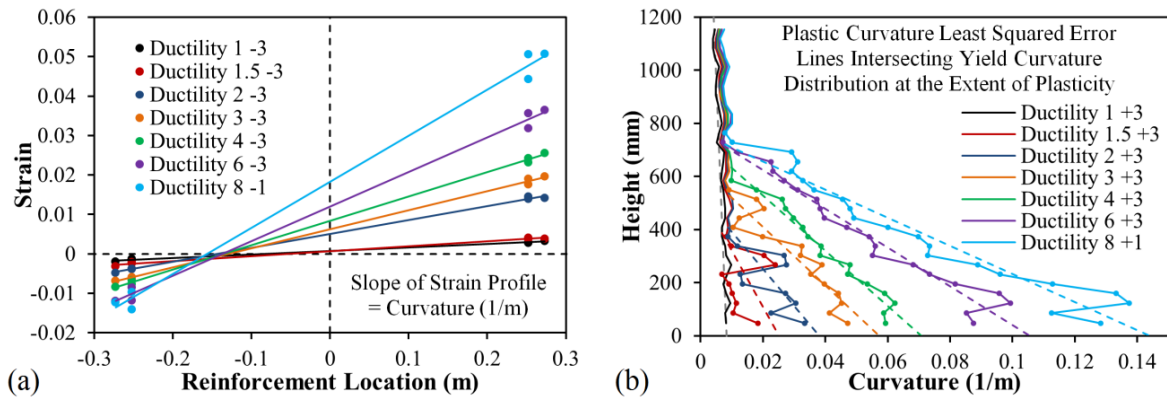
Figure 4.20 (a) Cross Section Strain Profiles and (b) Vertical Curvature Profiles
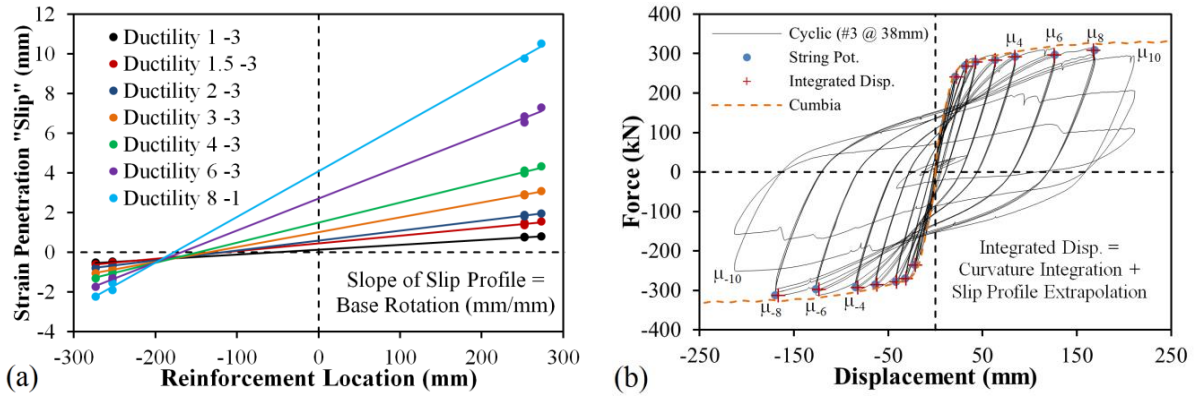
Figure 4.21 (a) Strain Penetration Rotation and (b) Optotrak Integrated Displacements
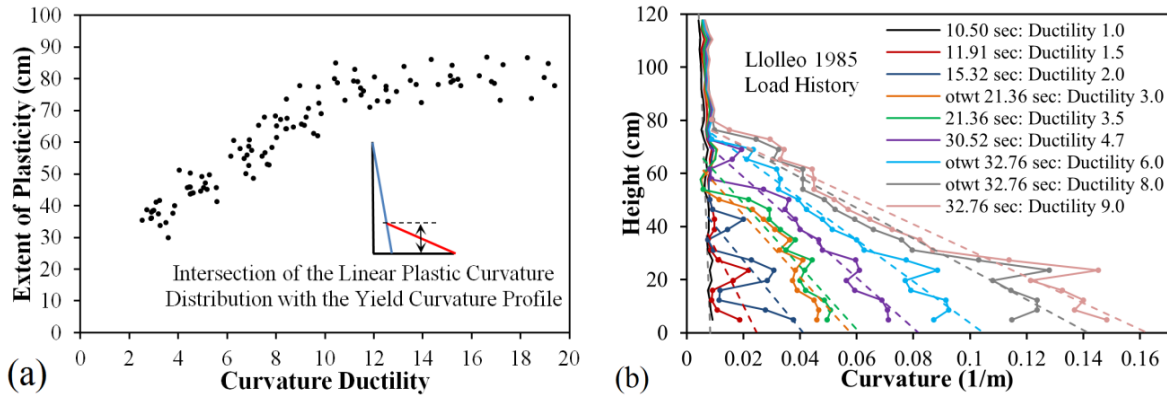
Figure 4.22 (a) Measured Spread of Plasticity and (b) Curvature Profiles for T17
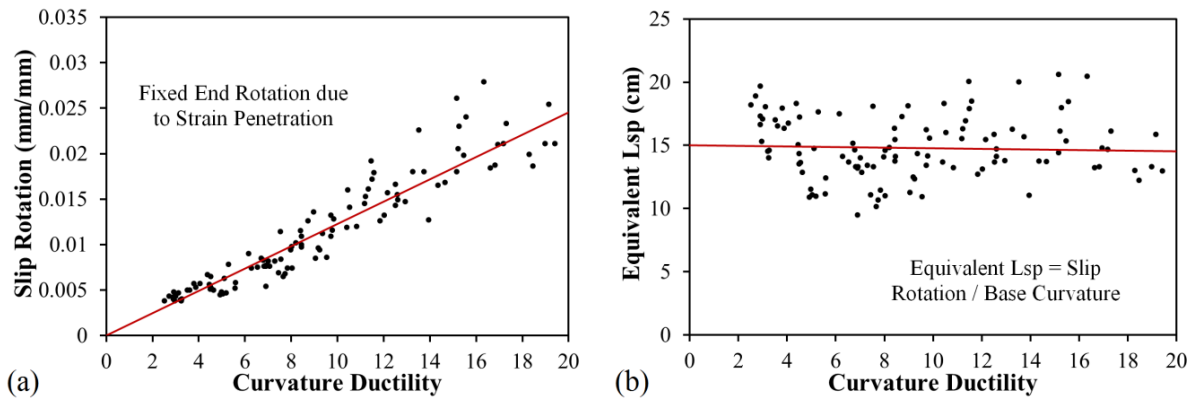
Figure 4.23 (a) Measured Rotations and (b) Equivalent Strain Penetration Lengths

4.3.2   Measured Spread of Plasticity

Plastic curvature profiles have a linear distribution which intersects the yield curvature profile at a height above the footing termed the extent of plasticity. This process is shown visually in the curvature profiles for the specimen subjected to the Llolleo Chile 1985 (T17) displacement history in Figure 4.22. For this test, the data points come from the first occurrence of the displacement ductility level along the envelope curve of cyclic response. The measured extent of plasticity vs. base curvature ductility is shown in Figure 4.22. The spread of plasticity for column tests with varying geometry and predictive equations for the extent of plasticity appear in Hines et. al. (2004).

In design, limit state curvatures are converted to target displacements using an equivalent curvature distribution. While there are many versions of the plastic hinge method, they all operate by integrating a simplified curvature distribution with the moment area method. The moment-curvature analysis presented in this section utilizes the plastic hinge method presented in Priestley et. al. (2007). In this method, the elastic and plastic curvature distributions are separated into simplified shapes to facilitate design. The elastic flexural displacement is determined using a triangular curvature distribution. The plastic flexural displacement is obtained using a uniform curvature distribution with a constant height called the plastic hinge length. The width of the rectangle is equal to the plastic curvature at the base section. To account for the effects of strain penetration, the curvature distribution extends into the footing by a depth termed the strain penetration length.

The use of a constant plastic hinge length does not account for the spread of plasticity observed in the physical tests. The constant plastic hinge length is not physical parameter; it is a numerical convenience to obtain the top column displacement. Improvements to the plastic hinge method for member deformation are necessary to produce accurate limit state target displacements at levels of response other than the ultimate condition. A further complication is noticed upon inspection of the tensile and compressive strain predictions in Figure 4.18. Accurate tensile strain predictions would require a plastic hinge length which

expands at higher ductility levels. The larger deformations at a given curvature would increase the accuracy of the prediction. The opposite is true for compression, where a shrinking plastic hinge length is needed to match measured compressive strain and displacement relationship. This is because moment-curvature analysis cannot capture the localization of compressive strains at the base of the column observed in test results with inelastic confinement steel.

The measured base rotation attributable to strain penetration is plotted against the base curvature ductility in Figure 4.21. Equivalent strain penetration lengths are determined by dividing the fixed-end rotations by the base curvatures in Figure 4.23. The top column displacement due to strain penetration is equal to the base curvature multiplied by the equivalent strain penetration length multiplied by the column clear height. A constant equivalent strain penetration length appears suitable for the range of curvature ductility presented in Figure 4.23. The effect of other variables on the spread of plasticity is studied in later sections of this report.

4.4 Conclusions

In this paper, the influence of unidirectional lateral displacement history on performance limit states, the relationship between strain and displacement, and the spread of plasticity in reinforced concrete bridge columns was explored. Results have shown that reinforcement bar buckling was influenced by load history, but the relationship between strain and displacement along the envelope curve of cyclic response was not. The symmetric three-cycle-set load history was found to be more severe than the displacement history produced by real earthquakes, when evaluated to the same peak displacement, due to the high number of inelastic reversals of loading of increasing magnitude.

Load histories with compressive demand sufficient to produce inelastic transverse steel may require lower values of peak tensile strain to initiate bar buckling after reversal of load. Every buckled longitudinal bar, with the exception for one, occurred over previously inelastic layers of transverse steel restraint. Additional research is required in order to relate

compressive demands to anticipated strains in the confinement steel of flexural tests. When bar buckling occurs over multiple spiral layers, the anticipated level of restraint provided by the transverse steel should include the effects of confinement.

In two experiments, fracture of previously buckled reinforcement occurred at levels of displacement equal to or lower than those required to initially produce bar buckling. The authors believe that a dependable level of displacement at which fracture of a previously buckled bar would occur cannot be reliably developed because it is dependent on the severity of the buckled deformation.

A technique of applying a commercially available position monitoring system (Optotrak Certus HD produced by Northern Digital Inc.) was developed which allows for monitoring longitudinal steel strains until bar buckling and subsequent fracture. The use of a constant plastic hinge length to calculate the displacements at varying levels of response does not account for the measured spread of plasticity in reinforced concrete bridge columns.

Chapter 5: Impact of Steel Content, Aspect Ratio, and Axial Load Ratio on Column Performance

This section discusses a research program supported by the Alaska Department of Transportation and Alaska University Transportation Center aimed at defining accurate limit state displacements which relate to specific levels of damage in reinforced concrete bridge columns subjected to seismic hazards. The experimental portion of the study aims to assess the performance of thirty large scale circular bridge columns. A key feature of the experiments is the high fidelity strain data obtained through the use of an optical 3D position measurement system. In this section, this data is utilized to explore the impact of design variables on key performance limit states. These design variables include: (1) lateral displacement history, (2) axial load, (3) longitudinal steel content, (4) aspect ratio, and (5) transverse steel detailing. The impact of lateral displacement history was the focus of Chapter 4, so this section instead focuses only on specimens subjected to symmetric three-cycle-set load histories.

The following sequence of damage was observed in all of the cyclically loaded tests: (1) concrete cracking, (2) longitudinal steel yield, (3) cover concrete crushing, (4) confinement steel yielding, (5) longitudinal bar buckling, and (6) fracture of previously buckled reinforcement. The deformation capacity of all of the specimens was limited by bar buckling and subsequent fracture. Spiral fracture was never observed, since longitudinal steel rupture occurred first, resulting in large levels of strength loss. The instrumentation system allowed for monitoring of longitudinal steel and transverse steel strains in the plastic hinge region. In this section, the impact of design variables on measured strains prior to the following limit states are explored: (1) cover concrete crushing, (3) confinement steel yielding and (3) longitudinal bar buckling. In Chapter 8, strain limit design expressions are developed based on the information provided in this section. In Chapter 7, an equivalent curvature

distribution which is consistent with strain-based displacement predictions is presented. In performance based design, an understanding of the damping-ductility relationship is needed to assess the correct value of damping at the design limit state. For columns subjected to cyclic loading, the equivalent viscous damping is calculated and compared to current design expressions which are based on specific hysteretic rules. In general, the equivalent viscous damping is equal to the viscous plus the hysteretic damping, both corrected and combined in a manner which is consistent with a design procedure based on secant stiffness to the design limit state.

5.1   Test Setup and Instrumentation

The goal of the experimental program is to investigate the impact of load history and other design variables on the relationship between strain and displacement, performance strain limits, and the spread of plasticity. The main variables for the thirty tests include: (1) lateral displacement history, (2) axial load, (3) longitudinal steel content, (4) aspect ratio, and (5) transverse steel detailing. The specimen was designed to represent a single degree of freedom bridge column subjected to lateral and axial load, Figure 5.1. The test specimen consists of a footing, column, and loading cap. The footing is a capacity protected member which secures the specimen to the lab strong floor using post tensioned bars. A 200kip hydraulic actuator, with a 40in stroke capacity, applies lateral load to the loading cap of the specimen. A spreader beam, two hydraulic jacks, and a load cell are placed above the loading cap to apply a constant axial compressive load. The top column displacement was obtained through a string potentiometer placed at the center of the lateral load.

The experimental program utilized multiple Optotrak Certus HD 3D position sensors developed by Northern Digital Inc. to monitor material strains. The position sensors track the locations of the target markers in 3D space, returning X-Y-Z spatial coordinates with an accuracy of 0.1mm with a resolution of 0.01mm. Two different cross sections were utilized in the study, an 18" and a 24" diameter configuration shown in Figure 5.2. The 24" configuration had 16 A706 longitudinal bars of either #6 (0.75 in) or #7 (0.875 in) diameter

and a #3 (0.375 in) or #4 (0.5 in) A706 spiral at variable spacing. For both specimens the cover depth to the outside of the spiral was ½", which led to an outside spiral diameter of either 23" or 17".

Two different instrumentation techniques were utilized for the 24" specimens. The first method, shown in the middle and left photos of Figure 5.1, utilized vertical cover concrete blockout strips over extreme fiber reinforcement which were installed during construction. This technique had two Optotrak position monitors, one facing each extreme fiber region. The blockout reached the outside surface of the longitudinal steel, where target markers were directly applied to the reinforcement. Care was taken during construction to insure that the spiral reinforcement was always in direct contact with the longitudinal reinforcement, therefore the blockout did not interfere with core concrete confinement or longitudinal bar restraint. The second instrumentation method, shown in Figure 5.3, had a full cover concrete blockout in the plastic hinge region.   This technique utilized three Optotrak position monitors, two facing the extreme fiber regions, and one facing a shear face. This allowed for instrumentation of additional longitudinal bars and transverse steel within the cross section. The Optotrak spatial coordinate output from this technique is shown in Figure 5.3.

The 18" column configuration utilized 10 A706 longitudinal bars of either #6 (0.75 in) or #8 (1 in) diameter and a #3 (0.375 in) A706 spiral at 2" on center. All of the 18" diameter specimens utilized the complete cover blockout instrumentation method, shown in the right photo of Figure 5.1. While all of the 24" specimens had an 8ft cantilever length (L/D = 4), the following aspect ratios were evaluated for 18" specimens: 8ft, 11ft, and 13ft for (L/D = 5.33, 7.33, and 8.67). The specimens were constructed in groups of six specimens, where each test series evaluated the impact of specific design variables. The impacts of these variables are discussed in individual sections of this chapter.   An overview of the longitudinal and transverse reinforcement properties for each test series is shown in Table 5.1. Note that Specimens 1-6 and Test 7 have been excluded, since they utilized a separate instrumentation technique whose measured strains ultimately should not be compared to the improved techniques previously mentioned.

5.2 Symmetric Three-Cycle-Set Loading Protocol

The symmetric three-cycle-set load history is commonly used to evaluate the seismic performance of structural components. An example of this load history utilized in column test twenty-five (T25) is shown in Figure 5.4. The load history begins with elastic cycles to the following increments of the analytically predicted first yield force: ¼ F_y', ½ F_y', ¾ F_y', and F_y'. The experimental first yield displacement is then determined by taking the average of the recorded displacements during the first yield push and pulls cycles. The equivalent yield displacement, used to determine the displacement ductility levels ($\mu_{\Delta 1} = 1 * \Delta_y$), is then calculated as $\Delta_y = \Delta_y'(M_n/M_y')$.

The symmetric three cycle set load history resumes with three balanced cycles at each of the following displacement ductility levels: 1, 1.5, 2, 3, 4. The traditional technique utilizes an increase of two displacement ductility levels for each series of three cycles past displacement ductility four. This load history was used for column T9, and T13 through T16. It became apparent that the increase from displacement ductility 4-6-8 was too large when the influence of individual variables was desired. For columns T19 through T30, a single displacement ductility increase was used for each set of cycles beyond displacement ductility four.
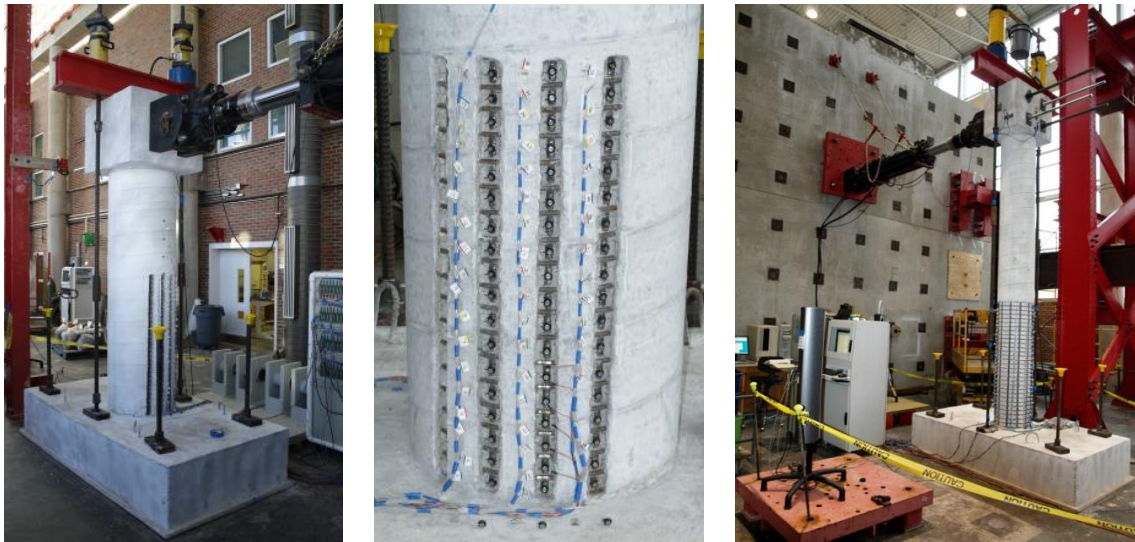
Figure 5.1 (Left and Middle) 24" Diameter Columns with 8ft Cantilever Lengths, (Right) 18" Diameter Columns Either 8ft, 11ft, or 13ft Cantilever Lengths
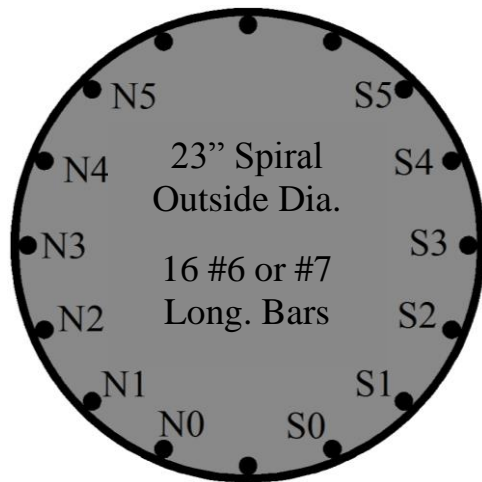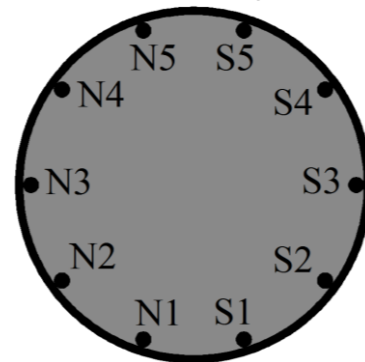
Figure 5.2 Tests 25-30 Cross Sections and Bar Designation for Both Diameters
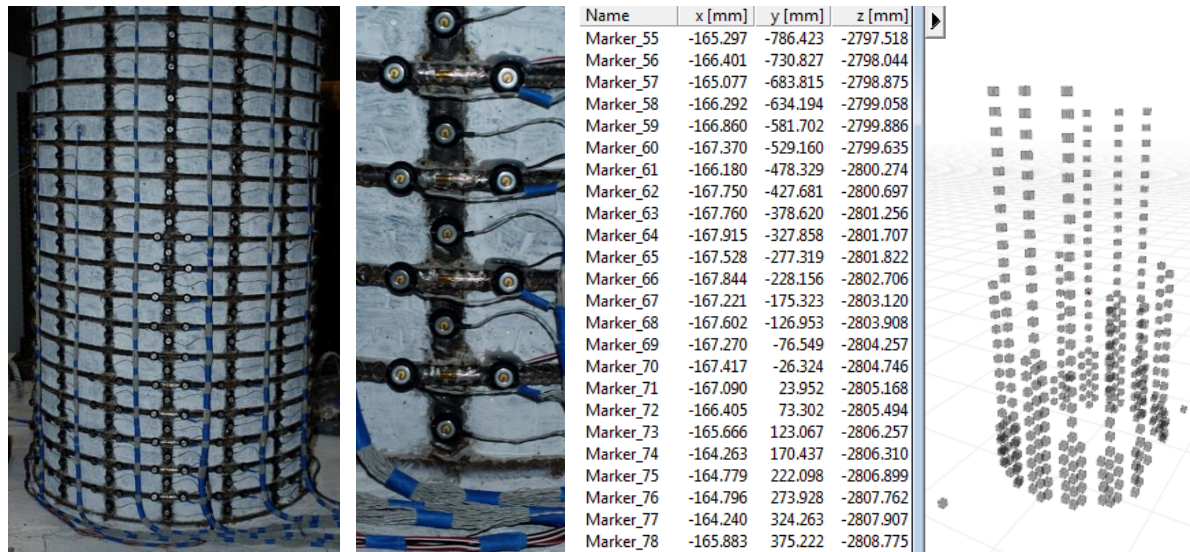
Figure 5.3 Target Marker Application and Optotrak Spatial Output

Table 5.1 Longitudinal and Transverse Reinforcement Properties

Longitudinal Reinforcement	Bar Size, Bar Diameter (in)	ε_y	f_y (ksi)	ε_h (hardening)	f_h (ksi)	ε_u (max stress)	f_u (ksi)
T8 – T12	#6, (0.75 in)	0.00235	68.1	0.0131	68.2	0.1189	92.8
T13 – T18	#6, (0.75 in)	0.00235	68.1	0.0146	68.2	0.1331	94.8
T19 – T24	#6, (0.75 in)	0.00250	68.1	0.0153	68.1	0.1208	92.4
T25 – T26	#7, (0.875 in)	0.00240	69.7	0.0126	69.7	0.1144	95.5
T27 – T29	#6, (0.75 in)	0.00237	68.7	0.0136	68.8	0.1178	93.7
T30	#8, (1 in)	0.00243	70.5	0.0110	70.5	0.1093	97.7

Transverse Reinforcement	Bar Size, Bar Diameter (in)	fy (ksi)
T8 – T12	#3, (0.375 in)	74.1
T13	#4, (0.5 in)	69.9
T14 – T18	#3, (0.375 in)	64.6
T19 – T24	#3, (0.375 in)	65.6
T25 – T30	#3, (0.375 in)	63.9

Test Series	Optotrak Target Marker Instrumentation Technique
T8 – T12	Vertical Blockout Strips
T13 – T18	Vertical Blockout Strips
T19 – T24	Complete Cover Blockout
T25 – T30	Complete Cover Blockout
T1 – T6, T7	Post Extensions, Tests Excluded

5.3 Gradual Bar Buckling Mechanism with Inelastic Transverse Steel Restraint

The deformation capacity of all of the cyclically loaded specimens was limited by longitudinal bar buckling and subsequent rupture of reinforcement during later cycles of loading. For many of these tests, measurable deformation could be observed in the recorded longitudinal and spiral strain hysteresis prior to the visible bar buckling observation. This deformation occurred once the transverse steel restraining the longitudinal bar went inelastic under prior compressive demands. This process is best demonstrated through analysis of strains collected from for Test 25. The 24" diameter column contains 16 #7 (A706) bars for longitudinal reinforcement ($A_{st}/A_g = 2.1\%$) and a #3 A706 spiral at 2" on center ($4A_{sp}/(D's) = 1\%$). The specimen had an 8ft cantilever length ($L/D = 4$), concrete strength ($f'_c = 6.29\ ksi$), and ($P/(f'_c A_g) = 5\%$) axial load. The imposed symmetric three-cycle-set displacement history and resulting hysteretic response appear in Figure 5.4 and Figure 5.5.
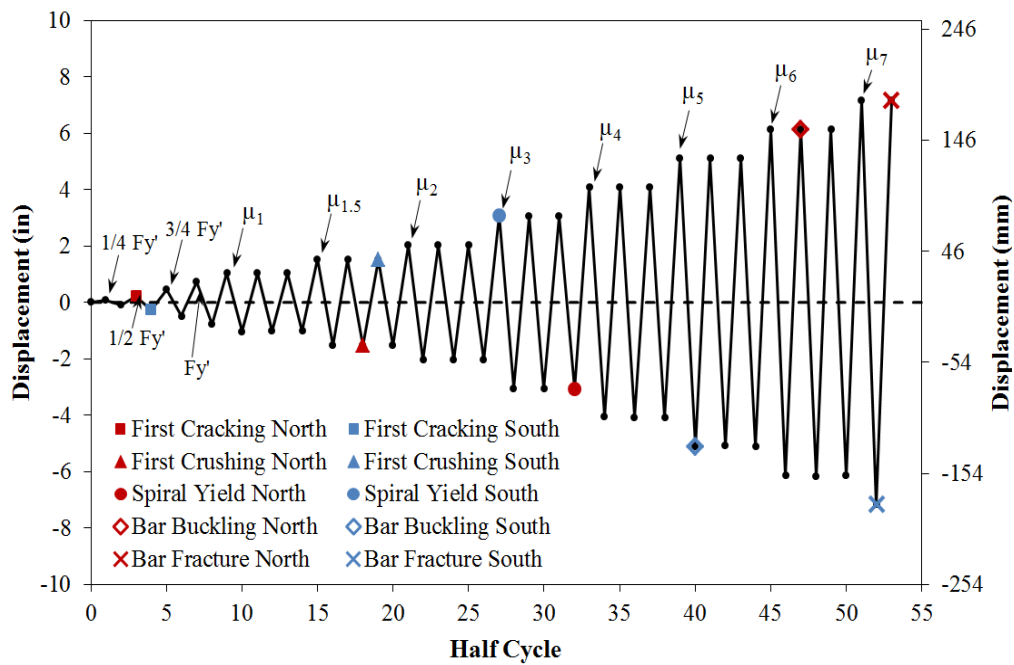
Figure 5.4 Test 25 – Symmetric Three-Cycle-Set Load History
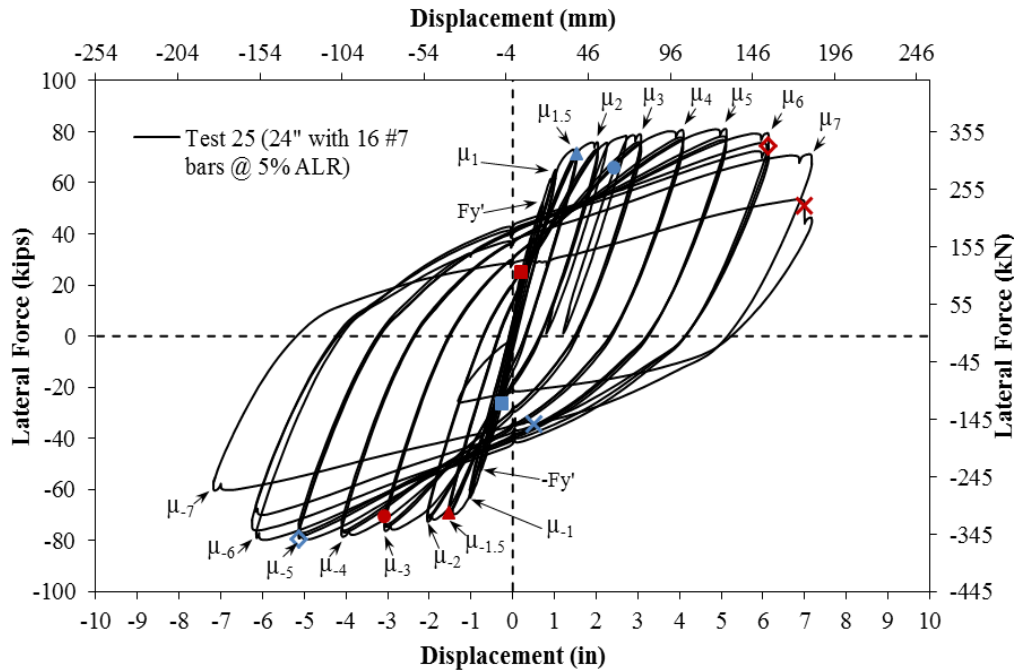
Figure 5.5 Test 25 – Lateral Force vs. Top Column Displacement Response

5.3.1   North Reinforcement

The north reinforcement is exposed to tension during push cycles and compression during pull cycles (negative displacements). Measured spiral strains in five layers which overlaid the north extreme fiber bar appear in Figure 5.11 for pull cycles which placed the north side in compression. A compressive strain of -0.0091 was measured 1.63" above the footing on bar N3 during $(\mu_3^{-3} = -3.06")$, when the second spiral layer above the footing yielded. In the cycle naming system, μ_3^{-3} represents the third pull cycle of dispalcmecement ductility three. Successive cycles during displacement ductility four and five produced larger inelastic demands on the spiral reinforcement. For the second spiral layer above the footing, inelastic strains decreased the lateral restraint stiffness, which led to measurable outward deformation of the north extreme fiber bar before visible buckling.   The measureable deformation formed a convex outward deformed region on the outside surface of the longitudinal bar, and an inward concave region just above the outward deformation. The locations for this deformation are easier to inspect on the later buckled shape of bar N3

shown in the left photo of Figure 5.6. Optotrak gage lengths in the convex outward deformed region would show increased tensile strains during compression cycles which should have resulted in larger levels of compression, left half of Figure 5.8. Similarly, gage lengths on the concave region would show some degree of increased compression due to the deformed geometry, right half of Figure 5.8.

As a comparison, the gage length just above the convex and concave regions remained straight and produced stable hysteretic response, left half of Figure 5.10. It is important to note that all three gage lengths on Bar N3 showed rapid increase in the apparent deformation when visible buckling was observed during $(\mu_6^{-2} = -6.17")$. Although the measured compression strains in bar N3 may have been influenced by bar deformation, a compression strain of -0.0161 was measured 5.45" above the footing during $(\mu_5^{-3} = -5.11")$. The peak compression strain of -0.0269, measured during $(\mu_6^{-1} = -6.14")$, was likely influenced by bar deformation. A peak tensile strain of 0.0422 was measured 7.44" above the footing on bar N3 during $(\mu_6^{+2} = 6.14")$, before the bar visibly buckled during the subsequent reversal of load. A strong argument can be made that the bar actually buckled during $(\mu_6^{-1} = -6.14")$, which is why the measured compression strain during this cycle is disregarded.

Tensile strain in the second spiral layer above the footing, which overlaid the outward deformed region of bar N3, spiked during visible bar buckling, left half of Figure 5.7. The figure contains spiral data obtained from a strain gage and an Optotrak gage length, Figure 5.6. The Optotrak strains were calculated from arc-lengths which utilized the measured 3D distance chord lengths between two adjacent LEDs and the known outside diameter of the spiral reinforcement. It is important to note that arc-length calculations become inaccurate once severe yielding in the spiral leads to the reinforcement straightening out to the left and right of the localized yielding directly over the longitudinal bar. The arc-strains are still presented because the strain gage debonded, preventing further measurement prior to visible bar buckling.

The distribution of arc-strains measured around the circumference of the second spiral layer above the footing appears in Figure 5.12. The north region is under compression during pull cycles in the right half of Figure 5.12. The middle of the section corresponds to zero along the circumference, and negative values wrap around the north side of the specimen. Specifically, measured-arc strains which overlay the three north extreme fiber bars N2, N3, and N4 are shown with vertical dashed lines. The spiral yielding is more evenly distributed along the north circumference, when compared to localized spiral yielding observed on the south side of the specimen. Also, yielding along multiple spiral layers above the footing on the north side of the specimen is more evenly distributed than localized yielding on the south side observed in Figure 5.11. These two observations support the fact that bar buckling occurred one displacement ductility level later on the north side in comparison to the south. Furthermore, when the north side did buckle, three bars buckled simultaneously due to the distributed spiral yielding.

5.3.2   South Reinforcement

A peak tension strain of 0.0353 was measured 7.36" above the footing on bar S3 during $(\mu_5^{-1} = -5.12")$, before visible bar buckling occurred during the subsequent reversal of load. The tension strains measured in lower gage lengths on bar S3 were smaller, although adjacent bars S2 and S4 had large tensile strains near the footing-column interface. A compressive strain of -0.0125 was measured 1.58" above the footing on bar S3 during $(\mu_3^{+1} = 3.08")$, when the first spiral in the confinement region yielded. Measured spiral strains in five layers which overlaid the south extreme fiber bar appear in Figure 5.11 for compressive push cycles. Successive cycles during displacement ductility four produced large inelastic demands on the second layer of spiral reinforcement. The measured strains obtained from the Optotrak system and a strain gage for second spiral overlaying bar S3 appear in Figure 5.7. The spiral strains spiked when the bar visibly buckled during $(\mu_5^{+2} = 5.10")$.

Since Optotrak LEDs are placed on the outside surface of the bar, measurable deformation can be monitored in the concave and convex regions of the deformed shape, Figure 5.6. Note again that that Figure 5.6 is taken after visible buckling. The outward deformed region (convex) developed in the gage length 3.47" above the footing on bar S3, Figure 5.9. Above the convex region, a concave region developed which increased the measured compression strains 5.44" above the footing, Figure 5.9. The region 7.36" above the footing on bar S3 appears to be unaffected by the measurable deformation which occurred below, Figure 5.10. The concave and convex deformed regions of bar S3 show a sharp deviation when visible bar buckling was observed during ($\mu_5^{+2} = 5.10"$). Spiral strains measured around the circumference of the second spiral layer above the footing depict large localized inelasticity at the location of the extreme fiber bars S3 and S4 during push cycles, Figure 5.12. The magnitude and localized nature of the spiral strains, both around the circumference (Figure 5.12) and vertically above the footing (Figure 5.11), contributed to bar buckling one displacement ductility level earlier than the north side of the specimen.
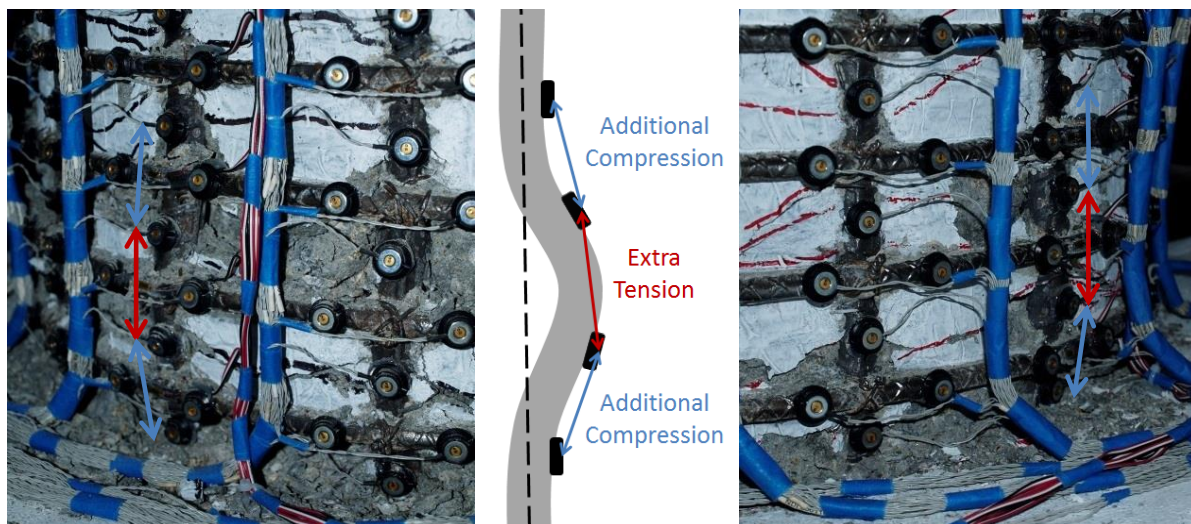
Figure 5.6 (Left) Three Buckled North Bars and (Right) Single Buckled South Bar
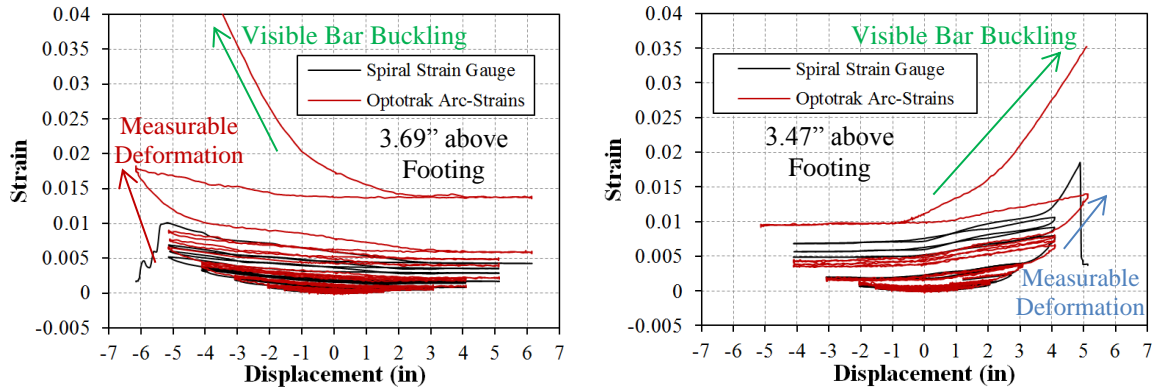
Figure 5.7 Spiral Strain Hysteresis for (Left) North and (Right) South Buckled Region
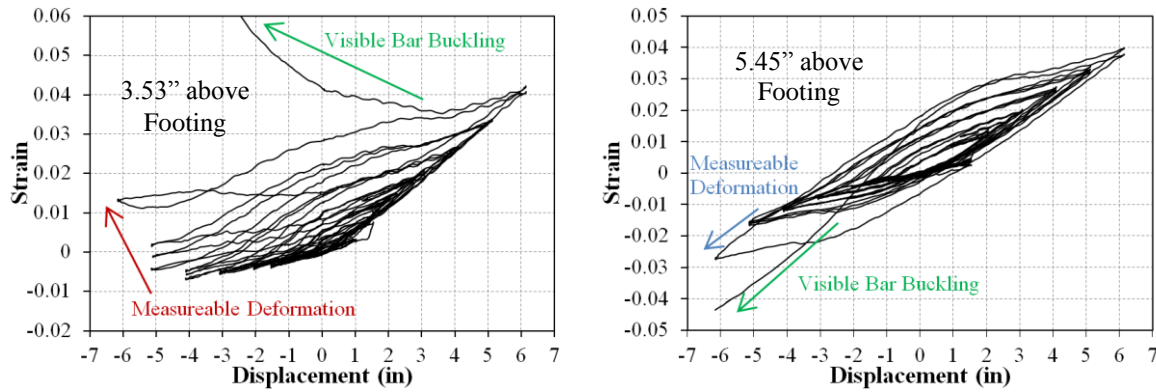
Figure 5.8 North Bar Strains for (Left) Outward Deformed Region and (Right) Inward
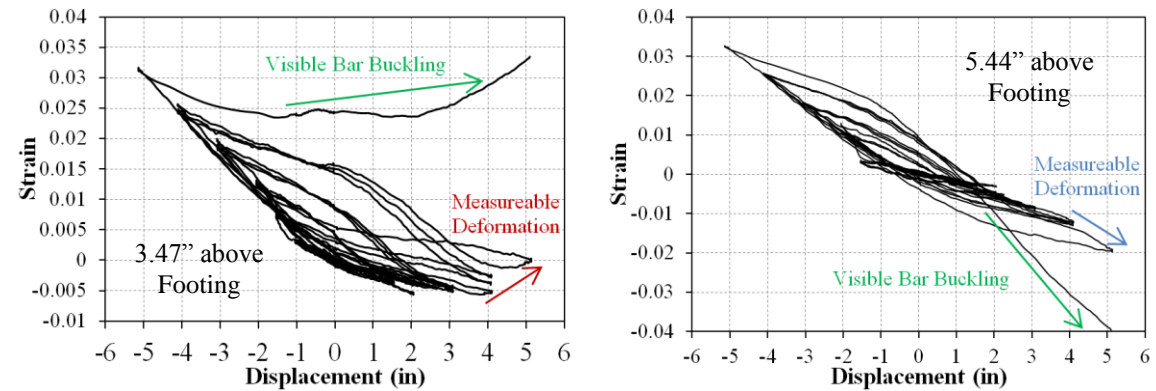
Figure 5.9 South Bar Strains for (Left) Outward Deformed Region and (Right) Inward
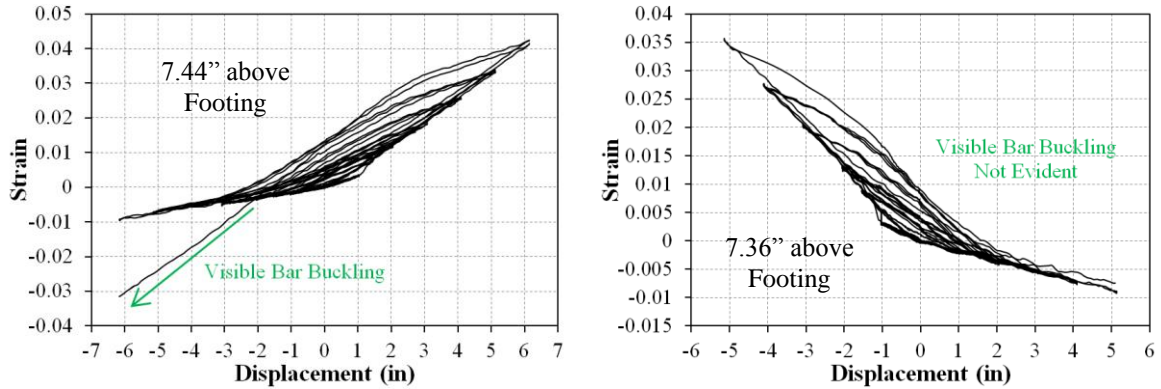
Figure 5.10 Strain Hysteresis above Deformation, (Left) North and (Right) South Bar
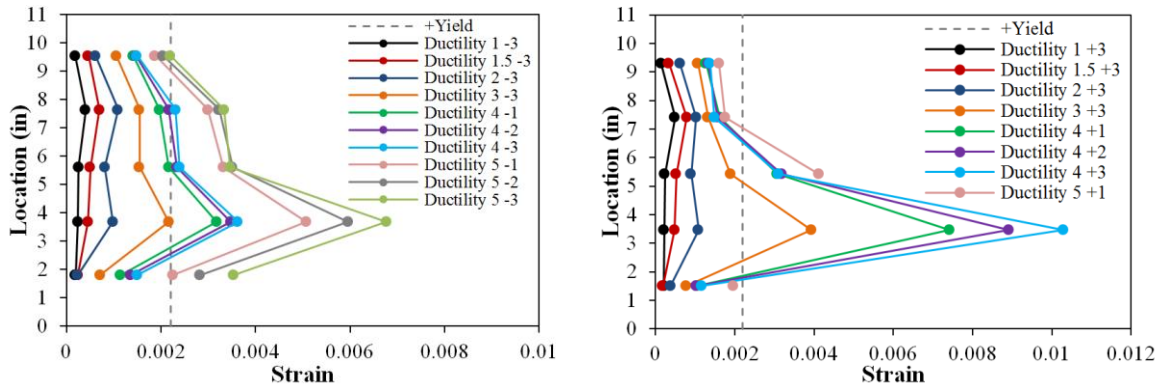
Figure 5.11 Spiral Strains Over Extreme Fiber Bars, (Left) North and (Right) South
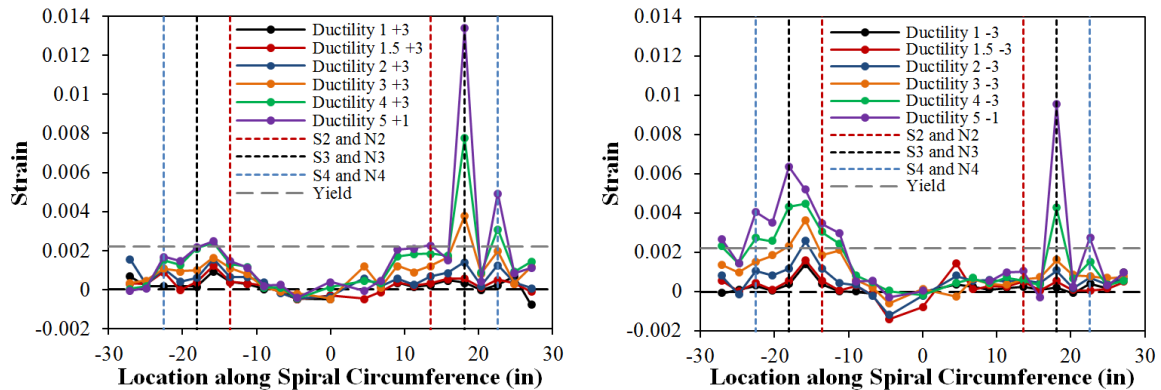
Figure 5.12 Strains around Spiral Circumference, (Left) Push and (Right) Pull Cycles

5.4   Transverse Steel Detailing Variable Experiments

The effect of transverse steel detailing on restraint of longitudinal bars was the main variable for the experiments in Table 5.2.   The 24" (610mm) diameter bridge columns contained 16 #6 (19mm) A706 bars for longitudinal reinforcement ($A_{st}/A_g = 1.6\%$) and either a #3 (9.5mm) or #4 (12.7mm) A706 spiral at variable spacing. The material properties for T9 differ from T13-T16 since the specimen came from a different test series, Table 5.1. The shear span for the cantilever columns was 8ft (244cm), and they had a moment to shear ratio of ($M/VD = 4$).   The specimens were subjected to a constant axial load of 170kips (756kN), ($P/(f_c'A_g) \approx 5\%$) depending on the concrete compressive strength.   The following transverse volumetric steel ratios were investigated: $(4A_{sp}/(D's)) = 0.5\%$ (6d$_{bl}$ spacing), 0.7%, 1%, and two separate detailing arrangements for 1.3%. Both the volumetric ratio and spacing of the transverse steel are important when describing confinement and bar buckling restraint. Two columns were tested with 1.3% transverse steel, one with a #3 spiral at 1.5" spacing and another with a #4 spiral at 2.75" spacing. For comparison, a specimen was tested with a #3 spiral at 2.75" spacing.

An engineer has the most control over the size and spacing of transverse steel to improve buckling resistance.   A summary of key displacement and strain values at damage observations in the tests appears in Table 5.3 and Table 5.4. The displacement and measured compression strain at the end of the cycle where cover concrete crushing was first observed appear in the second column. Similarly, the displacement and measured compression strain at the end of the cycle when spiral yielding was experimentally measured appear in the third column.   It is important to note that the displacement at the end of the cycle was used because there are two contributing factors to spiral yielding, demands due to dilation of the core concrete under compression and demands related to the restraint of longitudinal reinforcement.   The spiral yielding observation came from strain gages applied to spiral layers directly over the extreme fiber reinforcement.   In some instances, spiral yielding is attributed more to the longitudinal bar restraint, since it occurred at low levels of

displacement during the reversal from the peak tensile strain. The peak displacement appears in the table since the restraint demand is linked to the prior tensile displacement, which has the same magnitude as the compressive cycle where spiral yielding was observed. That being said, most spiral yielding observations were accompanied by large levels of compression strain near the compressive peak of a given cycle. The third column shows the peak displacement and tensile strain which occurred just prior to bar buckling during the subsequent reversal of load. The previous peak compressive strain and displacement which occurred before the tensile cycle which induced bar buckling is shown in the fourth column. Compressive demand is linked to the degree of inelasticity and thus stiffness of the spiral layers restraining the longitudinal bar.

Influence of transverse steel detailing on the peak tensile strain and drift prior to bar buckling after reversal of load is shown graphically in Figure 5.13. The transverse steel variable tests from Table 5.2 are shown with red data points while all experiments T8 – T30 are shown with blue data points. The influence of other variables is decreased when inspecting relationships for just the experiments in Table 5.2. Specimens T14 ($4A_{sp}/(D's)) = 0.5\%$) and T15 (0.7%) had bar buckling during displacement ductility six. In comparison, T9 (1%), T13 (1.3%), and T16 (1.3%) all had bar buckling occur during repeated cycles at displacement ductility eight. The peak tension strains measured prior to bar buckling are largely a function of the displacement amplitude at which bar buckling was observed. It became apparent that the increase from displacement ductility 4-6-8 was too large when the influence of individual variables was desired. For columns T19 through T30, a single displacement ductility increase was used for each set of cycles beyond displacement ductility four.

The degree of inelasticity in the spiral reinforcement overlaying the extreme fiber bar is direction related to its ability to restrain that bar from buckling. The measured peak spiral strains and measured longitudinal bar compressive strains for the peak compressive cycle prior to bar buckling appear in the right half of Figure 5.14. These measured peak compressive strains are quite large, and may be influenced by (1) localization of compression

over inelastic spiral layers and (2) the effects of measurable deformation prior to visible buckling which locally increase the perceived strain. The relationship between measured peak spiral strain and peak longitudinal steel tensile strains prior to bar buckling is shown in the left half of Figure 5.14. Larger inelastic spiral strains diminished its ability to restrain the reinforcement, which resulted in smaller peak tensile strains measured prior to bar buckling after reversal of load. There is still considerable scatter, since the distribution of spiral strains around the circumference of the column and over multiple layers influences bar buckling as discussed in the previous section for T25.

The impact of transverse steel content on measured compressive strains at the peak of the cycle when cover concrete crushing occurred appears in the left half of Figure 5.15. Among all of the variables investigated, volumetric steel ratio was the most impactful variable when considering cover concrete crushing. Larger amounts of confinement steel resulted in higher compressive strains at cover concrete crushing. This relationship did not carry over when considering the impact of volumetric steel ratio on the measured compressive strain at the peak of the cycle where spiral yielding was observed, right half of Figure 5.15. Higher amounts of confinement steel did not result in larger compressive strains measured at initial spiral yield. The majority of the columns had either 1% or 1.3% volumetric steel ratio, with only two specimens having 0.5% and 0.7%.

Table 5.2 Transverse Steel Detailing Variable Experiments

Test	Load History	D (in)	L/D	Long. Steel (ρ_l)	Spiral Detailing (ρ_s)	f'c (ksi)	P/f'c*Ag
T9	3-Cycle-Set	24	4	16 #6 bars (1.6%)	#3 at 2" (1%)	6.81	5.5%
T13	3-Cycle-Set	24	4	16 #6 bars (1.6%)	#4 at 2.75" (1.3%)	6.10	6.2%
T14	3-Cycle-Set	24	4	16 #6 bars (1.6%)	#3 at 4" (0.5%)	6.64	5.7%
T15	3-Cycle-Set	24	4	16 #6 bars (1.6%)	#3 at 2.75" (0.7%)	7.23	5.2%
T16	3-Cycle-Set	24	4	16 #6 bars (1.6%)	#3 at 1.5" (1.3%)	6.71	5.6%

Table 5.3 Transverse Steel Variable Experiments, Limit State Displacements

Test	Δ (μ_Δ) at Cover Crushing		Δ (μ_Δ) at Spiral Yielding		Δ (μ_Δ) at Peak Tension Prior to Bar Buckling		Δ (μ_Δ) at Peak Comp. Prior to Bar Buckling	
Side	North	South	North	South	North	South	North	South
T9	1.67" (2)	1.69" (2)	5.05" (6)	6.71" (8)	6.72" (8)	6.70" (8)	5.04" (6)	6.72" (8)
T13	1.61" (2)	1.60" (2)	4.85" (6)	6.46" (8)	6.46" (8)	6.50" (8)	4.85" (6)	6.46" (8)
T14	1.19" (1.5)	1.20" (1.5)	N/A	4.80" (6)	4.80" (6)	4.80" (6)	3.21" (4)	4.80" (6)
T15	1.25" (1.5)	1.68" (2)	5.00" (6)	3.33" (4)	5.00" (6)	5.00" (6)	5.00" (6)	5.01" (6)
T16	1.65" (2)	1.66" (2)	4.98" (6)	4.98" (6)	6.65" (8)	6.68" (8)	6.64" (8)	6.68" (8)

Table 5.4 Transverse Steel Variable Experiments, Limit State Strains

Test	εs at Cover Crushing		εs at Spiral Yielding		εs at Peak Tension Prior to Buckling		εs at Peak Comp. Prior to Buckling	
Side	North	South	North	South	North	South	North	South
T9	-0.0041	-0.0032	-0.0139	-0.0163	0.053	0.051	-0.018	-0.015
T13	-0.0046	-0.0036	-0.0166	-0.0162	0.047	0.047	-0.017	-0.017
T14	-0.0029	-0.0030	N/A	-0.0152	0.035	0.035	-0.011	-0.015
T15	-0.0027	-0.0041	-0.0199	-0.0125	0.037	0.038	-0.020	-0.023
T16	-0.0048	-0.0038	-0.0120	-0.0152	0.056	0.052	-0.019	-0.030
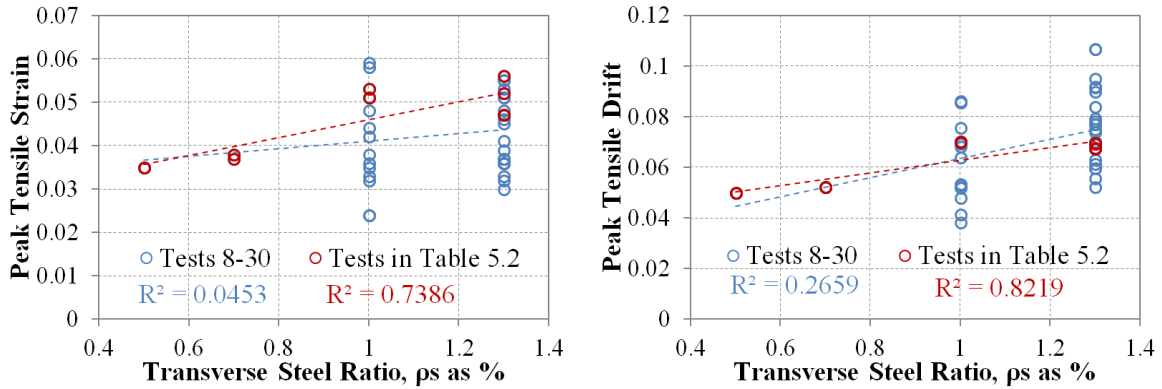
Figure 5.13 Trans. Steel and Peak Tension Strain or Disp. Prior to Bar Buckling
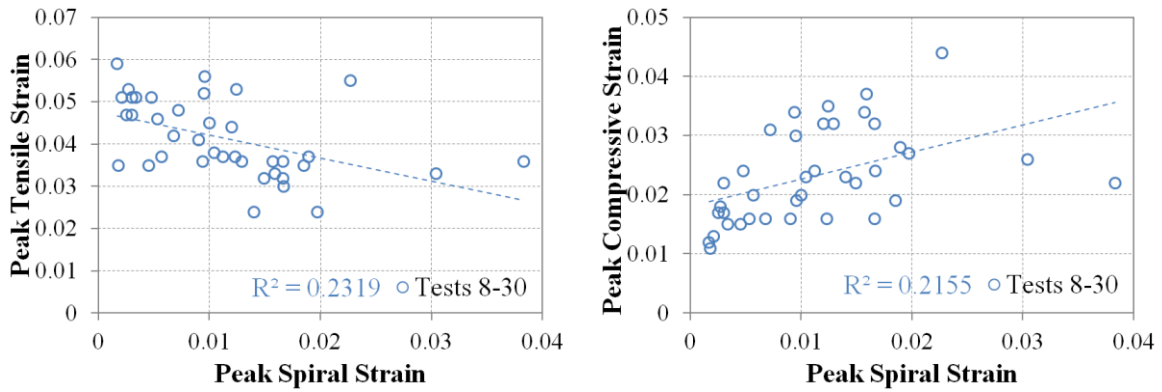
Figure 5.14 Peak Spiral Strains and Prior Tensile/Comp. Strain before Bar Buckling
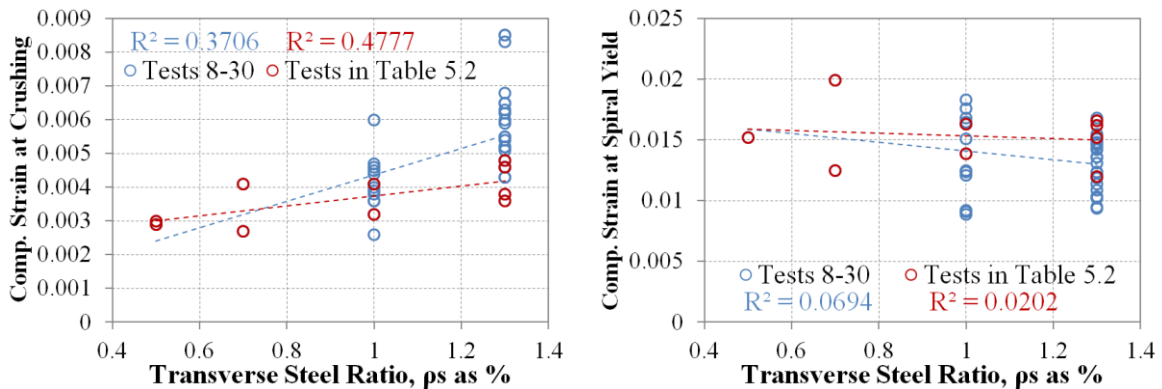
Figure 5.15 Trans. Steel and Comp. Strain at Cover Crushing and Spiral Yielding

5.5   Aspect Ratio Variable Experiments

The effects of aspect ratio and axial load ratio on column performance were the main variables for Tests 19-24 in Table 5.5. The 18" (457mm) diameter bridge columns contained 10 #6 (19mm) A706 bars for longitudinal reinforcement ($A_{st}/A_g = 1.7\%$) and a #3 (9.5mm) A706 spiral at 2" spacing ($4A_{sp}/D's = 1.3\%$). The shear span for the cantilever columns was either 8ft (244cm), 11ft (335cm), or 13ft (396cm) and they had a moment to shear ratio of ($M/VD = 5.33, 7.33, or\ 8.67$). For each aspect ratio, one specimen was subjected to ($P/(f_c'A_g) = 5\%$) and the other was subjected to 10% axial load. A photo of the test setup for the column with the largest aspect ratio appears in Figure 5.1. The test series had a full cover concrete blockout with target markers applied to both longitudinal and transverse steel.

In design, strain-based limit state displacements are evaluated using an equivalent curvature distribution such as the Plastic Hinge Method from Priestley, Calvi, and Kowalsky (2007). The moment gradient component of the plastic hinge length is dependent on the column length. Aspect ratio also influences shear in the column, which impacts the additional spread in plasticity due to tension shift. Aspect ratio is not expected to influence bar buckling behavior, but the tests are included to evaluate its effect on the spread of plasticity. The measured spread of plasticity is discussed in greater detail in Chapters 6 and 7.

The recorded displacements and strains at key damage observations appear in Table 5.6 and Table 5.7 for the aspect ratio variable experiments. The influence of aspect ratio on the recorded peak tensile strain and it associated lateral drift prior to bar buckling upon reversal of load is shown graphically in Figure 5.16. The trends imply that the peak tensile strain measured prior to bar buckling was not influenced by column aspect ratio. The lateral drift measured prior to bar buckling in the following load reversal is however strongly influenced by column aspect ratio.

Table 5.5 Aspect Ratio Variable Experiments

Test	Load History	D (in)	L/D	Long. Steel (ρ_l)	Spiral Detailing (ρ_s)	f'c (ksi)	P/f'c*Ag
T20	3-Cycle-Set	18	5.33	10 #6 bars (1.7%)	#3 at 2" (1.3%)	6.47	5%
T19	3-Cycle-Set	18	5.33	10 #6 bars (1.7%)	#3 at 2" (1.3%)	6.33	10%
T21	3-Cycle-Set	18	7.33	10 #6 bars (1.7%)	#3 at 2" (1.3%)	6.39	5%
T22	3-Cycle-Set	18	7.33	10 #6 bars (1.7%)	#3 at 2" (1.3%)	6.53	10%
T23	3-Cycle-Set	18	8.67	10 #6 bars (1.7%)	#3 at 2" (1.3%)	6.61	5%
T24	3-Cycle-Set	18	8.67	10 #6 bars (1.7%)	#3 at 2" (1.3%)	6.47	10%

Table 5.6 Aspect Ratio Variable Experiments, Limit State Displacements

Test	Δ (μ_Δ) at Cover Crushing		Δ (μ_Δ) at Spiral Yielding		Δ (μ_Δ) at Peak Tension Prior to Bar Buckling		Δ (μ_Δ) at Peak Comp. Prior to Bar Buckling	
Side	North	South	North	South	North	South	North	South
T20	2.36" (2)	2.36" (2)	4.72" (4)	3.35" (3)	7.10" (6)	5.89" (5)	7.12" (6)	5.92" (5)
T19	2.29" (2)	2.29" (2)	3.42" (3)	3.43" (3)	5.72" (5)	5.72" (5)	5.71" (5)	5.72" (5)
T21	3.95" (2)	3.97" (2)	7.91" (4)	5.94" (3)	11.9" (6)	9.88" (5)	9.89" (5)	9.88" (5)
T22	4.17" (2)	4.17" (2)	6.27" (3)	6.26" (3)	10.5" (5)	12.5" (6)	8.37" (4)	12.5" (6)
T23	5.56" (2)	5.54" (2)	11.1" (4)	11.1" (4)	16.7" (6)	16.7" (6)	13.9" (5)	16.7" (6)
T24	5.72" (2)	5.73" (2)	8.58" (3)	8.58" (3)	14.3" (5)	14.3" (5)	11.4" (4)	14.3" (5)

Table 5.7 Aspect Ratio Variable Experiments, Limit State Strains

Test	ε_s at Cover Crushing		ε_s at Spiral Yielding		ε_s at Peak Tension Prior to Bar Buckling		ε_s at Peak Comp. Prior to Bar Buckling	
Side	North	South	North	South	North	South	North	South
T20	-0.0065*	-0.0046*	-0.0114	-0.0109	0.046	0.037	-0.016	-0.016
T19	-0.0060*	-0.0065*	-0.0103	-0.0119	0.037	0.032	-0.024	-0.022
T21	-0.0046*	-0.0048	-0.0146	-0.0102	0.051	0.036	-0.024	-0.034
T22	-0.0063*	-0.0085*	-0.0103	-0.0124	0.041	0.053	-0.016	-0.035
T23	-0.0052*	-0.0062*	-0.0136	-0.0151	0.051	0.048	-0.022	-0.031
T24	-0.0085	-0.0083*	-0.0155	-0.0131	0.037	0.045	-0.028	-0.020

Figure 5.16 Aspect Ratio and Peak Tension Strain or Disp. Prior to Bar Buckling

5.6 Longitudinal Steel Content Variable Experiments

The effects of longitudinal steel content and higher levels of axial load on column performance were the main variables for Tests 25-30. The test matrix for the six columns and T9, which serves as basis of comparison for 24" diameter specimens, is shown in Table 5.8 and the material properties of the reinforcement appear in Table 5.1. Columns with similar 18" and 24" column configurations were used so that the results could be compared to previous experiments with either different axial load or longitudinal steel content. The shear span for the longitudinal steel content variable columns was 8ft (244cm). Tests 25-30 had the full cover concrete blockout, while Test 9 had vertical blockout strips over extreme fiber reinforcement, Figure 5.1.

The 18" (457mm) diameter bridge columns, Figure 5.2, contained either 10 #6 ($A_{st}/A_g = 1.7\%$) or 10 #8 ($A_{st}/A_g = 3.1\%$) A706 bars for longitudinal reinforcement and a #3 (9.5mm) A706 spiral at 2" spacing ($4A_{sp}/D's = 1.3\%$). Both 18" diameter columns, T28 and T30, were subjected to ($P/(f'_c A_g) = 15\%$) axial load. The 24" (610mm) diameter bridge columns contained either 16 #6 ($A_{st}/A_g = 1.6\%$) or 16 #7 ($A_{st}/A_g = 2.1\%$) A706 bars for longitudinal reinforcement and a #3 (9.5mm) A706 spiral at 2" spacing

$(4A_{sp}/D's = 1\%)$.   A pair of 24" diameter columns with each reinforcing ratio were subjected to similar levels of axial load, T9 and T25 with $(P/(f'_c A_g) \approx 5\%)$ and T26 and T27 with 10%. It is important to note that T9 came from a prior test series with different material properties.   The recorded displacements and strains at key limit states for the longitudinal steel content variable tests are shown in Table 5.9 and Table 5.10. As shown in Figure 5.17 and Figure 5.18, longitudinal steel content was found to not significantly impact bar buckling behavior, but higher levels of steel content did result in confinement steel yielding at lower compressive strain levels.

Table 5.8 Longitudinal Steel Content Variable Experiments

Test	Load History	D (in)	L/D	Long. Steel (ρ_l)	Spiral Detailing (ρ_s)	f'c (ksi)	P/f'c*Ag
T9	3-Cycle-Set	24	4	16 #6 bars (1.6%)	#3 at 2" (1%)	6.81	5.5%
T25	3-Cycle-Set	24	4	16 #7 bars (2.1%)	#3 at 2" (1%)	6.29	5%
T27	3-Cycle-Set	24	4	16 #6 bars (1.6%)	#3 at 2" (1%)	6.15	10%
T26	3-Cycle-Set	24	4	16 #7 bars (2.1%)	#3 at 2" (1%)	5.89	10%
T28	3-Cycle-Set	18	5.33	10 #6 bars (1.7%)	#3 at 2" (1.3%)	6.24	15%
T30	3-Cycle-Set	18	5.33	10 #8 bars (3.1%)	#3 at 2" (1.3%)	6.05	15%

Table 5.9 Longitudinal Steel Variable Experiments, Limit State Displacements

Test	Δ (μ_Δ) at Cover Crushing		Δ (μ_Δ) at Spiral Yielding		Δ (μ_Δ) at Peak Tension Prior to Bar Buckling		Δ (μ_Δ) at Peak Comp. Prior to Bar Buckling	
Side	North	South	North	South	North	South	North	South
T9	1.67" (2)	1.69" (2)	5.05" (6)	6.71" (8)	6.72" (8)	6.70" (8)	5.04" (6)	6.72" (8)
T25	1.52" (1.5)	1.53" (1.5)	3.06" (3)	3.08" (3)	6.14 (6)	5.12" (5)	5.11" (5)	5.11" (5)
T27	1.38" (1.5)	1.38" (1.5)	2.76" (3)	2.76" (3)	4.60" (5)	3.67" (4)	3.67" (4)	3.66" (4)
T26	1.49" (1.5)	1.50" (1.5)	2.99" (3)	2.97" (3)	4.98" (5)	3.98" (4)	4.98" (5)	3.98" (4)
T28	2.00" (1.5)	2.00" (1.5)	4.00" (3)	4.00" (3)	6.68" (5)	5.34" (4)	6.68" (5)	5.34" (4)
T30	2.21" (1.5)	2.21" (1.5)	2.95" (2)	2.95" (2)	7.39" (5)	7.39" (5)	5.91" (4)	7.39" (5)

Table 5.10 Longitudinal Steel Variable Experiments, Limit State Strains

Test	εs at Cover Crushing		εs at Spiral Yielding		εs at Peak Tension Prior to Bar Buckling		εs at Peak Comp. Prior to Bar Buckling	
Side	North	South	North	South	North	South	North	South
T9	-0.0041	-0.0032	-0.0139	-0.0163	0.053	0.051	-0.018	-0.015
T25	-0.0036	-0.0040	-0.0091	-0.0125	0.042	0.035	-0.016	-0.019
T27	-0.0036	-0.0038	-0.0168	-0.0124	0.036	0.024	-0.032	-0.023
T26	-0.0045	-0.0046	-0.0089	-0.0121	0.032	0.024	-0.016	-0.027
T28	-0.0051	-0.0055	-0.0123	-0.0143	0.036	0.030	-0.034	-0.024
T30	-0.0052	-0.0059	-0.0095	-0.0094	0.036	0.033	-0.022	-0.026
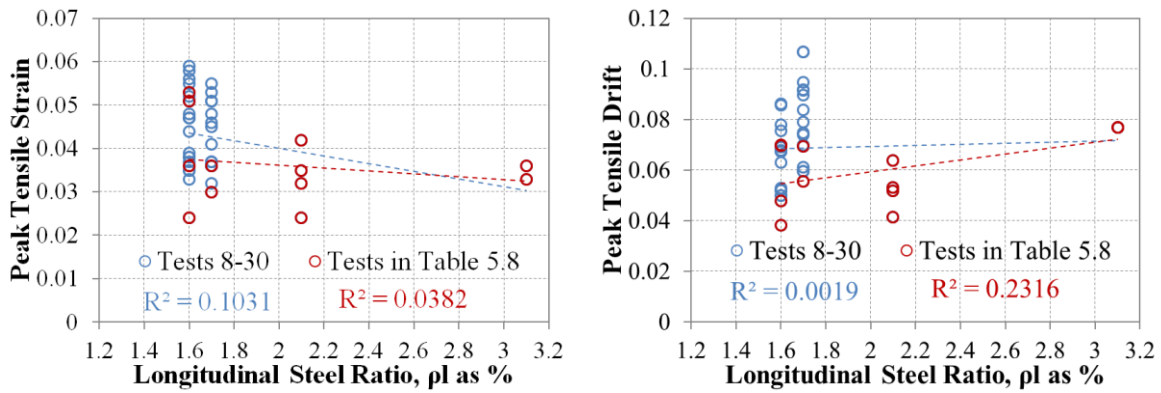
Figure 5.17 Long. Steel Ratio and Peak Tension Strain or Disp. Prior to Bar Buckling
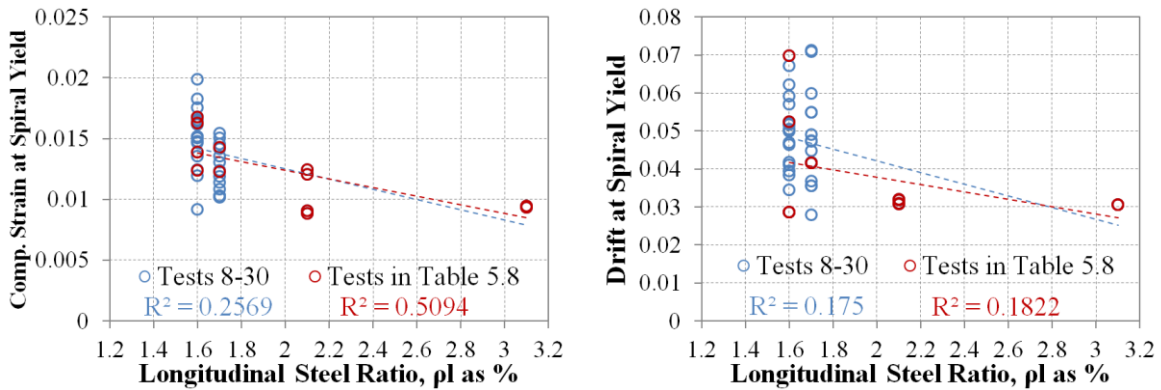
Figure 5.18 Long. Steel Ratio and Peak Comp. Strain or Drift Prior to Spiral Yielding

5.7 Axial Load Ratio Variable Experiments

Axial load influences the distribution of forces within the cross section. Columns with higher levels of axial load are expected to have a reduced deformation capacity but higher lateral forces. Axial load was maintained as a variable over multiple test series, so care should be taken when comparing tests results from Table 5.11. The 18" (457mm) diameter bridge columns contained 10 #6 ($A_{st}/A_g = 1.7\%$) A706 bars for longitudinal reinforcement and a #3 (9.5mm) A706 spiral at 2" spacing ($4A_{sp}/D's = 1.3\%$). Four of these columns with the same aspect ratio, ($M/VD = 5.33$), were subjected to ($P/(f_c'A_g) = 5, 10, 15,$ $and\ 20\%$) axial load. In these tests, the increase in axial load did not have a significant impact on the displacement ductility or peak tensile strain measured prior to bar buckling. However, as axial load increased, the measured compressive strains proceeding bar buckling also increased. Aspect ratio variable Tests 21-24, evaluated 18" diameter specimens subjected to 5 and 10% axial load with aspect ratios 7.33 and 8.67. For the two columns with an aspect ratio of 7.33, the increase in axial load did not lead to a reduction in the displacement measured prior to bar buckling. In the two columns with an aspect ratio of 8.67, bar buckling occurred one displacement ductility level earlier for the specimen subjected to 10% axial load.

Two 24" (610mm) diameter bridge columns containing 16 #7 ($A_{st}/A_g = 2.1\%$) A706 bars for longitudinal reinforcement and a #3 (9.5mm) A706 spiral at 2" spacing ($4A_{sp}/D's = 1\%$) were tested, one with 5% and the other with 10% axial load. The specimen subjected to the higher axial load level suffered bar buckling at lower levels of displacement ductility and with smaller previous peak tensile strains. Two 24" (610mm) diameter bridge columns containing 16 #6 ($A_{st}/A_g = 1.6\%$) A706 bars for longitudinal reinforcement and a #3 (9.5mm) A706 spiral at 2" spacing ($4A_{sp}/D's = 1\%$) were tested, one with 5.5% and the other with 10% axial load. Comparison between these tests requires consideration that they came from different test series, with different material properties for the longitudinal and transverse steel. Test 9, with 5.5% axial load, had transverse steel with a

yield stress of 74.1 ksi. Test 27, with 10% axial load, had transverse steel with a yield stress of 63.9ksi. Test 9 had bar buckling on each side of the specimen during displacement ductility eight. In Test 27, bar buckling occurring during the first push and pull cycles of displacement ductility five, with significantly larger values of previous peak compressive strains measured in the longitudinal steel when compared to Test 9. Since axial load did not have his large of an impact when considering columns within the same test series, this difference in performance is largely attributed to the increased strength in the transverse steel utilized in T9. This is further evident when comparing the displacement ductility levels at which initial spiral yielding in the confinement region was observed in the two tests.

A graphical summary of the influence of axial load ratio on bar bucking and initial spiral yielding behavior is shown in Figure 5.19 and Figure 5.20 respectively. For both limit states, axial load does not have as impactful of a change on the behavior as expected. It is important to note that comparatively fewer columns were test with higher levels of axial load though.

Table 5.11 Axial Load Ratio Variable Experiments

Test	Load History	D (in)	L/D	Long. Steel (ρ_l)	Spiral Detailing (ρ_s)	f'c (ksi)	P/f'c*Ag
T9	3-Cycle-Set	24	4	16 #6 bars (1.6%)	#3 at 2" (1%)	6.81	5.5%
T27	3-Cycle-Set	24	4	16 #6 bars (1.6%)	#3 at 2" (1%)	6.15	10%
T25	3-Cycle-Set	24	4	16 #7 bars (2.1%)	#3 at 2" (1%)	6.29	5%
T26	3-Cycle-Set	24	4	16 #7 bars (2.1%)	#3 at 2" (1%)	5.89	10%
T20	3-Cycle-Set	18	5.33	10 #6 bars (1.7%)	#3 at 2" (1.3%)	6.47	5%
T19	3-Cycle-Set	18	5.33	10 #6 bars (1.7%)	#3 at 2" (1.3%)	6.33	10%
T28	3-Cycle-Set	18	5.33	10 #6 bars (1.7%)	#3 at 2" (1.3%)	6.24	15%
T29	3-Cycle-Set	18	5.33	10 #6 bars (1.7%)	#3 at 2" (1.3%)	5.91	20%
T21	3-Cycle-Set	18	7.33	10 #6 bars (1.7%)	#3 at 2" (1.3%)	6.39	5%
T22	3-Cycle-Set	18	7.33	10 #6 bars (1.7%)	#3 at 2" (1.3%)	6.53	10%
T23	3-Cycle-Set	18	8.67	10 #6 bars (1.7%)	#3 at 2" (1.3%)	6.61	5%
T24	3-Cycle-Set	18	8.67	10 #6 bars (1.7%)	#3 at 2" (1.3%)	6.47	10%

Table 5.12 Axial Load Variable Experiments, Limit State Displacements

Test	Δ (μ_Δ) at Cover Crushing		Δ (μ_Δ) at Spiral Yielding		Δ (μ_Δ) at Peak Tension Prior to Bar Buckling		Δ (μ_Δ) at Peak Comp. Prior to Bar Buckling	
Side	North	South	North	South	North	South	North	South
T9	1.67" (2)	1.69" (2)	5.05" (6)	6.71" (8)	6.72" (8)	6.70" (8)	5.04" (6)	6.72" (8)
T27	1.38" (1.5)	1.38" (1.5)	2.76" (3)	2.76" (3)	4.60" (5)	3.67" (4)	3.67" (4)	3.66" (4)
T25	1.52" (1.5)	1.53" (1.5)	3.06" (3)	3.08" (3)	6.14 (6)	5.12 (5)	5.11" (5)	5.11" (5)
T26	1.49" (1.5)	1.50" (1.5)	2.99" (3)	2.97" (3)	4.98" (5)	3.98" (4)	4.98" (5)	3.98" (4)
T20	2.36" (2)	2.36" (2)	4.72" (4)	3.35" (3)	7.10" (6)	5.89" (5)	7.12" (6)	5.92" (5)
T19	2.29" (2)	2.29" (2)	3.42" (3)	3.43" (3)	5.72" (5)	5.72" (5)	5.71" (5)	5.72" (5)
T28	2.00" (1.5)	2.00" (1.5)	4.00" (3)	4.00" (3)	6.68" (5)	5.34" (4)	6.68" (5)	5.34" (4)
T29	2.02" (1.5)	2.01" (1.5)	4.03" (3)	2.69" (2)	8.06" (6)	6.72" (5)	6.72" (5)	6.72" (5)
T21	3.95" (2)	3.97" (2)	7.91" (4)	5.94" (3)	11.9" (6)	9.88" (5)	9.89" (5)	9.88" (5)
T22	4.17" (2)	4.17" (2)	6.27" (3)	6.26" (3)	10.5" (5)	12.5" (6)	8.37" (4)	12.5" (6)
T23	5.56" (2)	5.54" (2)	11.1" (4)	11.1" (4)	16.7" (6)	16.7" (6)	13.9" (5)	16.7" (6)
T24	5.72" (2)	5.73" (2)	8.58" (3)	8.58" (3)	14.3" (5)	14.3" (5)	11.4" (4)	14.3" (5)

Table 5.13 Axial Load Variable Experiments, Limit State Strains

Test	εs at Cover Crushing		εs at Spiral Yielding		εs at Peak Tension Prior to Bar Buckling		εs at Peak Comp. Prior to Bar Buckling	
Side	North	South	North	South	North	South	North	South
T9	-0.0041	-0.0032	-0.0139	-0.0163	0.053	0.051	-0.018	-0.015
T27	-0.0036	-0.0038	-0.0168	-0.0124	0.036	0.024	-0.032	-0.023
T25	-0.0036	-0.0040	-0.0091	-0.0125	0.042	0.035	-0.016	-0.019
T26	-0.0045	-0.0046	-0.0089	-0.0121	0.032	0.024	-0.016	-0.027
T20	-0.0065*	-0.0046*	-0.0114	-0.0109	0.046	0.037	-0.016	-0.016
T19	-0.0060*	-0.0065*	-0.0103	-0.0119	0.037	0.032	-0.024	-0.022
T28	-0.0051	-0.0055	-0.0123	-0.0143	0.036	0.030	-0.034	-0.024
T29	-0.0055	-0.0054	-0.0142	-0.0103	0.055	0.036	-0.044	-0.032
T21	-0.0046*	-0.0048	-0.0146	-0.0102	0.051	0.036	-0.024	-0.034
T22	-0.0063*	-0.0085*	-0.0103	-0.0124	0.041	0.053	-0.016	-0.035
T23	-0.0052*	-0.0062*	-0.0136	-0.0151	0.051	0.048	-0.022	-0.031
T24	-0.0085	-0.0083*	-0.0155	-0.0131	0.037	0.045	-0.028	-0.020

Figure 5.19 Axial Load Ratio and Peak Tension Strain or Drift Prior to Bar Buckling
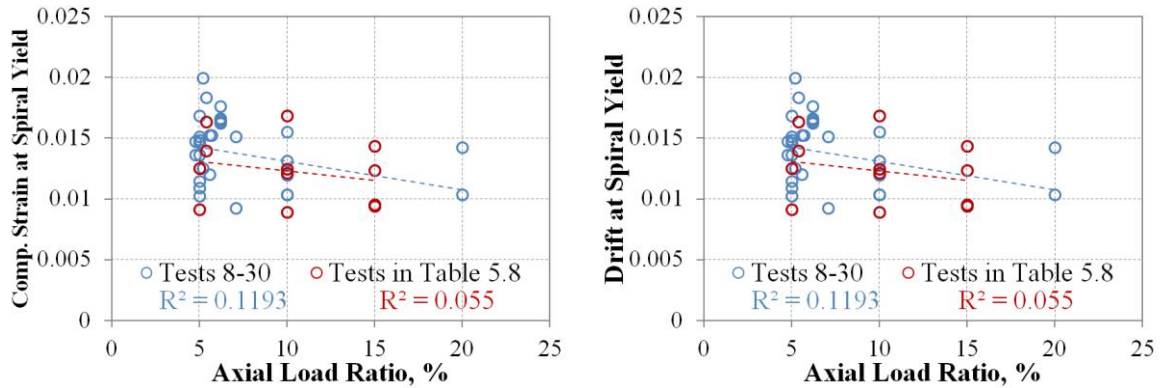
Figure 5.20 Axial Load Ratio and Peak Comp. Strain or Drift Prior to Spiral Yielding

5.8 Equivalent Viscous Damping

In direct displacement based design, the concept of equivalent viscous damping is used to reduce the elastic response spectra to a level consistent with the inelastic response at the design limit state. The equivalent viscous damping is the combination of viscous and hysteretic damping components. The hysteretic damping for a complete cycle at a given level of inelastic response is calculated using the Jacobsen's (1960) area-based approach,

Eqn 5.1. In Eqn 5.1, A_h is the area enclosed by a complete cycle of force-displacement response at given displacement amplitude, and A_{box} is the area of rectangular bounding box for the same hysteretic cycle. This process is shown graphically in Figure 5.21 for the third cycle of displacement ductility one and six for column Test 9. Jacobsen's (1960) approach is related to the secant stiffness to maximum response, which is consistent with the direct-displacement based design procedure which characterizes a structure based on secant stiffness and damping at the peak response.

Dwairi and Kowalsky (2007) studied the accuracy of the area-based hysteretic damping component using non-linear time history analysis and typical hysteretic loop shapes. This was accomplished by varying the damping value until the displacement for the equivalent substitute structure matched the response obtained from time-history analysis with a non-linear hysteretic rule. Dwairi and Kowalsky (2007) produced displacement ductility dependent correction factors for the hysteretic damping of many common loop shapes, and an expression was developed based on these results to correct the damping of other loop shapes, Eqn 5.2. The uncorrected and corrected Jacobsen's (1960) hysteretic damping applied to Tests 8-30 appears in Figure 5.22. The 18" and 24" diameter specimens were separated since it is apparent that the results are different between the two datasets.

The equivalent viscous damping is the combination of the viscous damping and the corrected hysteretic damping. The viscous damping is connected to either the initial or tangent stiffness while the hysteretic damping is related to the secant stiffness. Analytical predictions to shake table experiments using non-linear time history analysis have shown that tangent stiffness proportional damping offers a better prediction to the peak response displacement. Grant et al. (2005) offered separate correction factors to translate either initial or tangent stiffness viscous damping to secant stiffness proportional damping. These correction factors are specific to a given hysteretic loop shape. The Thin Takeda (TT) tangent stiffness proportional viscous damping correction factor presented in Eqn 5.3 is appropriate for bridge columns since it is based on the Thin Takeda Hysteretic rule and

tangent stiffness proportional viscous damping. The result of this correction factor applied to 5% viscous damping appears in Figure 5.23.

The final equivalent viscous damping ratio is the combination of the corrected viscous and corrected hysteretic damping, Eqn 5.4. These values were computed at the peak of each cycle for Tests 8-30 which utilized a symmetric three-cycle-set load history.   Design expressions from Priestley, Calvi, and Kowalsky (2007) for the equivalent viscous damping with 5% elastic tangent stiffness damping appear in Eqn 5.5 and Eqn 5.6 for two typical hysteretic rules used for reinforced concrete structures. The Thin Takeda (TT) hysteretic rule is commonly used for columns with axial load while the Fat Takeda (TF) is used for beams. The computed equivalent viscous damping for Tests 8-30, lies between the two design expressions, and is apparently more linear in shape. Application of the area-based hysteretic damping approach includes additional damping at displacement ductility one, Figure 5.21.

$$\xi_{JAC}^{hyst} = \frac{A_h}{2\pi A_{box}}$$ Jacobsen's (1960) Hysteretic Damping   Eqn 5.1

$$EVD_{\mu_\Delta}^{Ratio} = (0.53\mu_\Delta + 0.8)\left(\xi_{JAC}^{hyst}\right)^{-\left(\frac{\mu_\Delta}{40}+0.4\right)}$$ Correction Factor for Area-Based Hysteretic Damping   Eqn 5.2

$$\kappa = \mu_\Delta^{\lambda} \quad \text{*where, } \lambda = -0.378$$ *Thin Takeda (TT) Tangent Stiffness, Viscous Damping Correction Factor   Eqn 5.3

$$\xi_{EVD} = \kappa(\xi_{el}) + EVD_{\mu_\Delta}^{Ratio}\left(\xi_{JAC}^{hyst}\right)$$ Equivalent Viscous Damping   Eqn 5.4

$$\xi_{EVD} = 0.05 + 0.444\left(\frac{\mu_\Delta - 1}{\mu_\Delta \pi}\right)$$ Equivalent Viscous Damping Expression for Thin Takeda Hysteretic Rule (Columns)   Eqn 5.5

$$\xi_{EVD} = 0.05 + 0.565\left(\frac{\mu_\Delta - 1}{\mu_\Delta \pi}\right)$$ Equivalent Viscous Damping Expression for Fat Takeda Hysteretic Rule (Beams)   Eqn 5.6
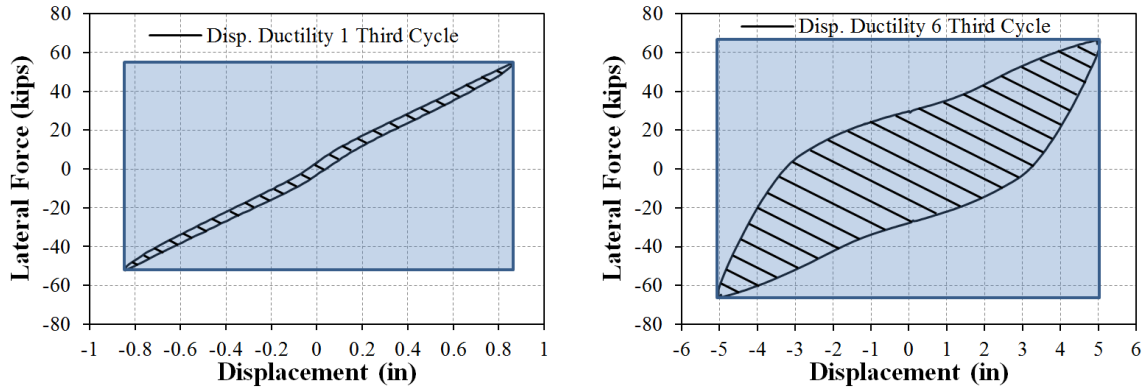
Figure 5.21 Jacobsen's Area-Based Hysteretic Damping for Ductility 1 and 6 of Test 9
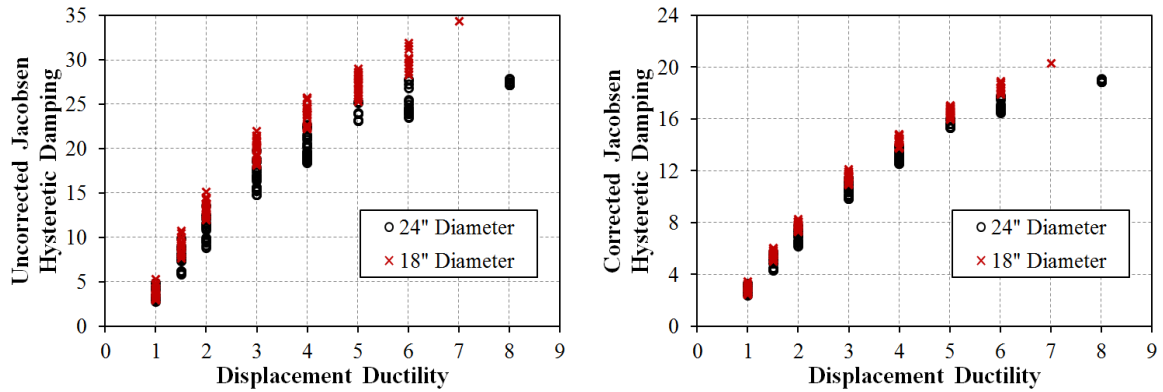
Figure 5.22 (Left) Uncorrected and (Right) Corrected Jacobsen Hysteretic Damping
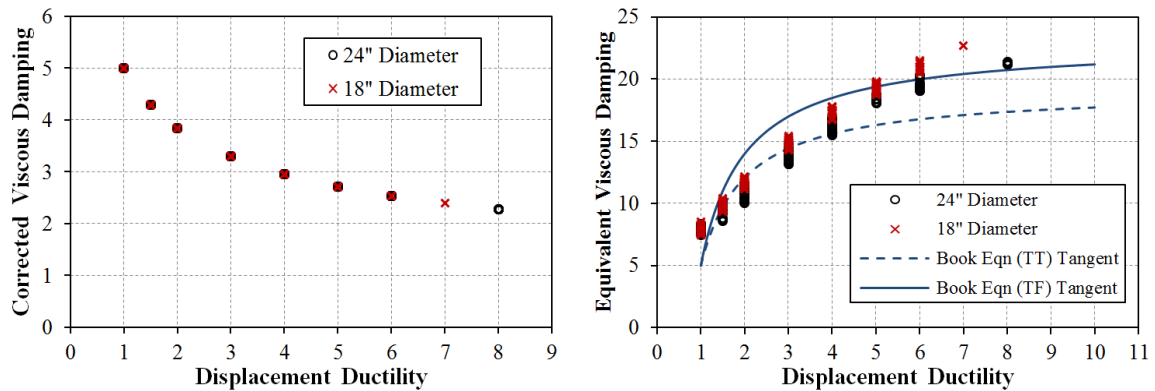
Figure 5.23 (Left) Corrected Viscous Damping, (Right) Equivalent Viscous Damping

5.9 Conclusions

An experimental study was conducted to assess the impact of design variables on the seismic performance of circular well-confined bridge columns. A key feature of the experiments is the high fidelity strain data obtained through the use of an optical 3D position measurement system. The instrumentation system allowed for monitoring of longitudinal steel and transverse steel strains in the plastic hinge region. For many of these tests, measurable deformation could be observed in the recorded longitudinal and spiral strain hysteresis prior to the visible bar buckling observation. This deformation occurred once the transverse steel restraining the longitudinal bar went inelastic under prior compressive demands. The distribution of spiral strains measured both around the circumference of the column and over multiple layers was found to impact the observed bar buckling behavior. Localized spiral demands led to increased levels of measured compressive strain and early buckling of longitudinal reinforcement.

In this section, the impact of design variables on measured strains prior to the following limit states was explored: (1) cover concrete crushing, (3) confinement steel yielding and (3) longitudinal bar buckling. Inspection of the compressive strains measured at the peak of the cycle where cover crushing was observed suggests that the behavior is dependent on the amount of confinement steel in the bridge columns. Specimens with larger transverse volumetric steel ratios had higher measured compressive strains at cover concrete crushing. Initial yielding of confinement steel under compressive demands was found to be influenced most significantly by longitudinal steel content. Higher longitudinal reinforcing content increases both confinement and restraint demands in the transverse reinforcement. For specimens with similar levels of volumetric steel ratio, the spiral yield strength was found to significantly influence compressive behavior.

The deformation capacity of all of the cyclically loaded specimens was limited by bar bucking and subsequent fracture during later cycles of loading. Specimens with higher amounts of confinement steel had larger peak tensile strains measured in the longitudinal

reinforcement and higher drifts recorded prior to bar buckling after reversal of load. In general, specimens with higher axial load ratio had reduced peak tensile strains and drifts measured prior to bar buckling. The magnitude of the peak tensile strain measured prior to bar buckling was significantly influenced by the previous compressive demand and measured peak spiral strain in the layers restraining the bar from buckling. Column aspect ratio was not found to influence the strains measured prior to bar buckling, but it did have a significant influence on the lateral drift. Columns with higher aspect ratios had larger drifts measured prior to bar buckling.

The goal of the research program is to define accurate limit state displacements which relate to specific levels of damage in reinforced concrete bridge columns. In Chapter 8, strain limit design expressions are developed based on the information provided in this section. In Chapter 7, an equivalent curvature distribution which is consistent with strain-based displacement predictions is presented. In performance based design, an understanding of the damping-ductility relationship is needed to assess the correct value of damping at the design limit state. For the cyclically loaded experiments of this study, the equivalent viscous damping was calculated and compared to current design expressions which are based on specific hysteretic rules. In general, the equivalent viscous damping is equal to the viscous plus the hysteretic damping, both corrected and combined in a manner which is consistent with a design procedure based on secant stiffness to the design limit state.

Chapter 6: Bridge Column Response Prediction Techniques

6.1 Background and Motivation

This section discusses a research program supported by the Alaska Department of Transportation and Alaska University Transportation Center aimed at defining accurate limit state displacements which relate to specific levels of damage in reinforced concrete bridge columns subjected to seismic hazards. The experimental portion of the study aims to assess the performance of thirty large scale circular bridge columns. A key feature of the experiments is the high fidelity strain data obtained through the use of an optical 3D position measurement system. In this section, this data is utilized to explore column deformation components, the relationship between material strain and displacement, and the accuracy of two common response prediction techniques utilized in design: (1) monotonic moment-curvature analysis paired with an equivalent curvature distribution and (2) cyclic fiber analysis paired with an element representation of the beam or column.

6.1.1 Experimental Program

The goal of the experimental program is to investigate the impact of load history and other design variables on the relationship between strain and displacement, performance strain limits, and the spread of plasticity. The main variables for the thirty tests include: (1) lateral displacement history, (2) axial load, (3) longitudinal steel content, (4) aspect ratio, and (5) transverse steel detailing. The specimen was designed to represent a single degree of freedom bridge column subjected to lateral and axial load, Figure 6.2. The test specimen consists of a footing, column, and loading cap. The footing is a capacity protected member which secures the specimen to the lab strong floor using post tensioned bars. A 200kip hydraulic actuator, with a 40in stroke capacity, applies lateral load to the loading cap of the specimen. A spreader beam, two hydraulic jacks, and a load cell are placed above the

loading cap to apply a constant axial compressive load. The top column displacement was obtained through a string potentiometer placed at the center of the lateral load.

Instrumentation

While the progression of damage in flexural bridge columns has been thoroughly investigated in the past, to the authors' knowledge, none of the previous studies measured strains at the level of the reinforcement throughout the entire range of response. Traditional instrumentation methods utilized linear potentiometers placed on the ends of threaded rods embedded in the core concrete to calculate changes in displacement outside of the cover concrete. A diagram of this instrumentation system from Hose et al. (1997) appeared in Hines et al. (2003), Figure 6.1. This method does not measure material strains at the locations of interests, and its measurements are influenced small rotations of the rods themselves which result due to the curvature gradient over the gage length. The experimental program discussed in this paper utilized multiple Optotrak Certus HD 3D position sensors developed by Northern Digital Inc. to monitor material strains. The position sensors track the locations of the target markers in 3D space, returning X-Y-Z spatial coordinates with an accuracy of 0.1mm with a resolution of 0.01mm.

A technique of applying target markers to longitudinal and transverse reinforcement, Figure 6.2, was utilized in the plastic hinge region. Strains were computed by dividing the change in three dimensional distance between two adjacent target markers by the original unloaded gage length. An illustration of the accuracy of the Optotrak system compared to traditional measurement techniques appears in Figure 6.2. The tensile test on a reinforcing bar contained the following instrumentation: (1) 2" Optotrak gage length, (2) 2" MTS Extensometer, and (3) centrally located electrical resistance strain gage.
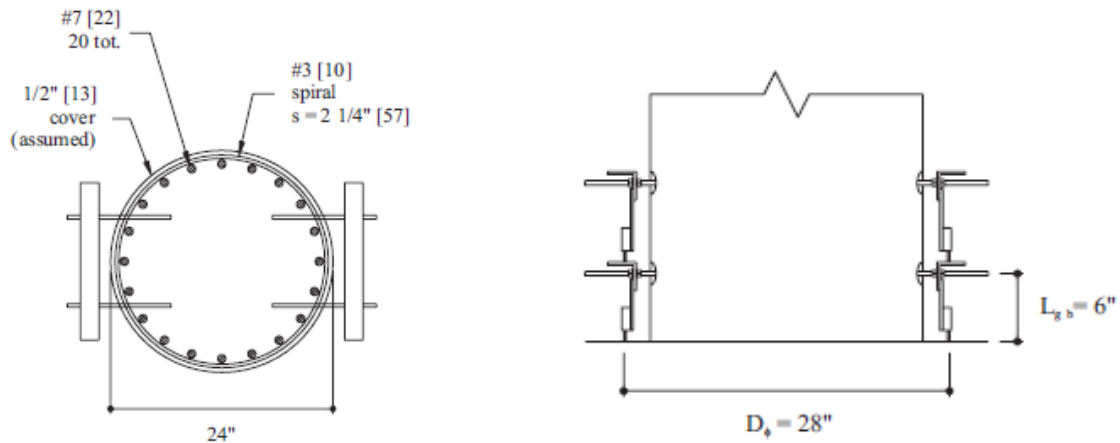
Figure 6.1 Curvature Rod and Linear Potentiometer Instrumentation from Tests by (Hose et al. 1997), Figure appears in (Hines et al. 2003)
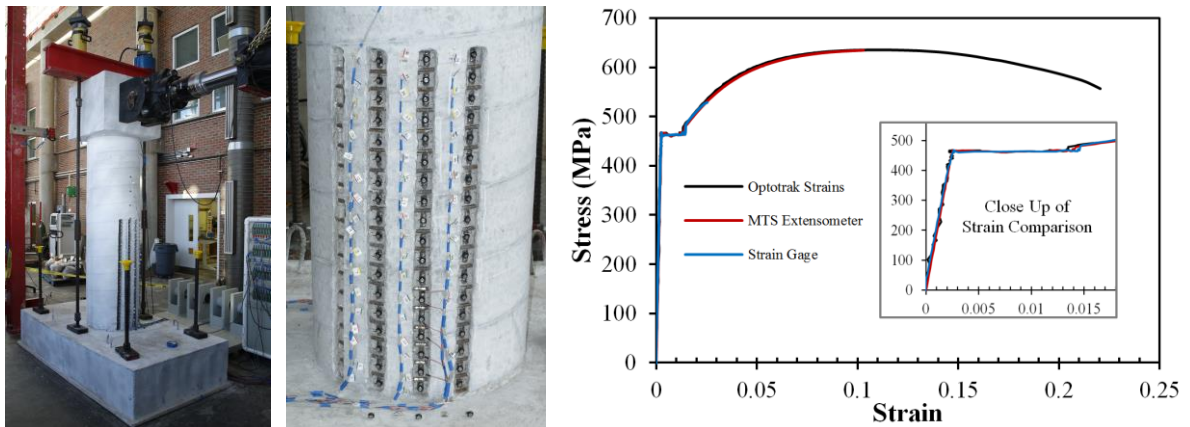
Figure 6.2 (Left) Test Setup, (Middle) Optotrak Target Marker Application Method, (Right) Optotrak Strain Comparison to Traditional Techniques

Loading Protocol

The specimens were subjected to various unidirectional top-column displacement histories including standardized laboratory reversed cyclic loading and recreations of the displacement responses obtained from non-linear time history analysis of multiple earthquakes with distinct characteristics.   The experiments utilized a quasi-static

displacement controlled loading procedure. The symmetric three-cycle-set load history is commonly used to evaluate the seismic performance of structural components. The load history begins with elastic cycles to the following increments of the analytically predicted first yield force: ¼ F_y', ½ F_y', ¾ F_y', and F_y'. The experimental first yield displacement is then determined by taking the average of the recorded displacements during the first yield push and pulls cycles. The equivalent yield displacement, used to determine the displacement ductility levels ($\mu_{\Delta 1} = 1 * \Delta_y$), is then calculated as $\Delta_y = \Delta_y'(M_n/M_y')$. The symmetric three-cycle-set load history resumes with three balanced cycles at each of the following displacement ductility levels: 1, 1.5, 2, 3, 4, 5, etc.

6.2 Measured Deformation Components

An understanding of the components of deformation and the spread of plasticity in reinforced concrete bridge columns is necessary to determine the relationship between material strain limits and lateral displacements, which are required for design. In the following section, the non-linear behavior of RC bridge columns is explored through presentation of sample results for Test #9. The 24" diameter bridge column contained 16 #6 A706 bars for longitudinal reinforcement ($A_{st}/A_g = 1.6\%$) and a #3 A706 spiral at 2" pitch ($4A_{sp}/(D's) = 1\%$). The column was subjected to symmetric three-cycle-set load history, Figure 6.3, and a constant compressive axial load of 170 kips ($P/(f_c'A_g) = 5.5\%$). The cantilever specimen had an aspect ratio ($L/D = 4$). The following sequence of damage was observed in all of the cyclically loaded columns: (1) concrete cracking, (2) cover concrete crushing, (3) spiral yielding in confinement regions, (4) longitudinal bar buckling, and (5) fracture of previously buckled longitudinal reinforcement. The lateral force versus deformation response for Test 9 appears in Figure 6.3. Longitudinal bar buckling occurred on each side of the specimen during cycles at displacement ductility eight, while bar fracture occurred during the first push cycle to displacement ductility ten. Reinforcement strains obtained by Optotrak target markers are no longer reliable once the buckled deformation develops over multiple spiral layers, Figure 6.4.
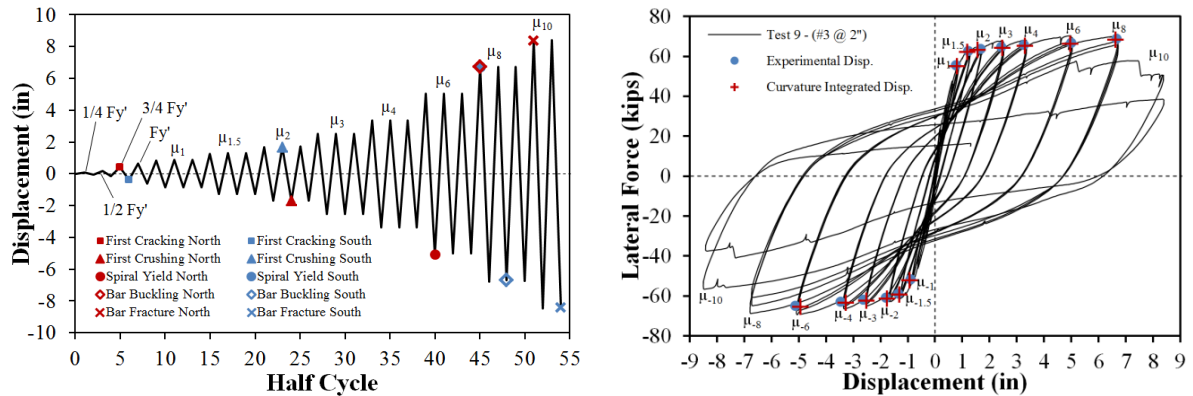
Figure 6.3 (Left) Symmetric Three-Cycle-Set Top Column Displacement History from Test #9, (Right) Lateral Force vs. Top Column Displacement Response

Extreme fiber vertical strain profiles, Figure 6.4, depict strains measured in North and South reinforcing bars in the plastic hinge region, which forms just above the footing-column interface in the region of maximum moment. Compressive strains are concentrated near the footing, while tension strains are fanned out to a greater height following the inclined flexural shear crack distribution. This phenomenon is known as tension shift, and it leads to tension strains above the base section which are larger than those which would develop based on the plane sections hypothesis and the moment at that height alone, Hines et al. (2004). It is important to note that the crack distribution in Figure 6.4 is from a separate experiment (Test #16), but this photo is selected for its clarity. The tension shift effect leads to a fanned compression strut pattern which emanates from the compressive toe region of the column. In this region, yielding of the transverse steel can lead to a localization of compressive demand. This occurred over the second gage length above the footing for the North extreme fiber bar in Figure 6.4. The relationship between compressive strain and displacement for this gage length and the measured strain in six spiral layers overlaying the North bar are shown in Figure 6.5. Spiral yielding occurred during the first pull cycle of displacement ductility six, and each successive cycle at ductility six produced larger compressive strains in the North bar and larger tensile strains in the second spiral layer above the footing.
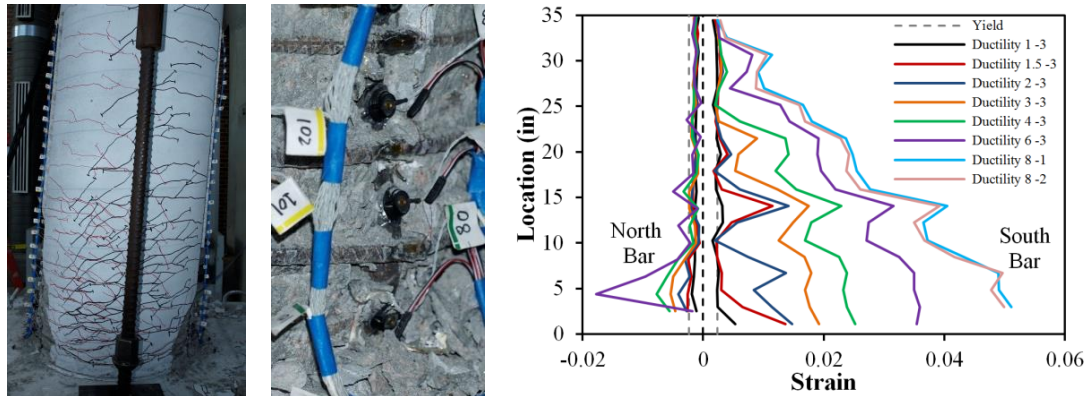
Figure 6.4 (Left) Inclined Crack Pattern for Test 16, (Middle) Buckling of North Extreme Fiber Bar in Test 9, and (Right) Extreme Fiber Bar Strain Profiles
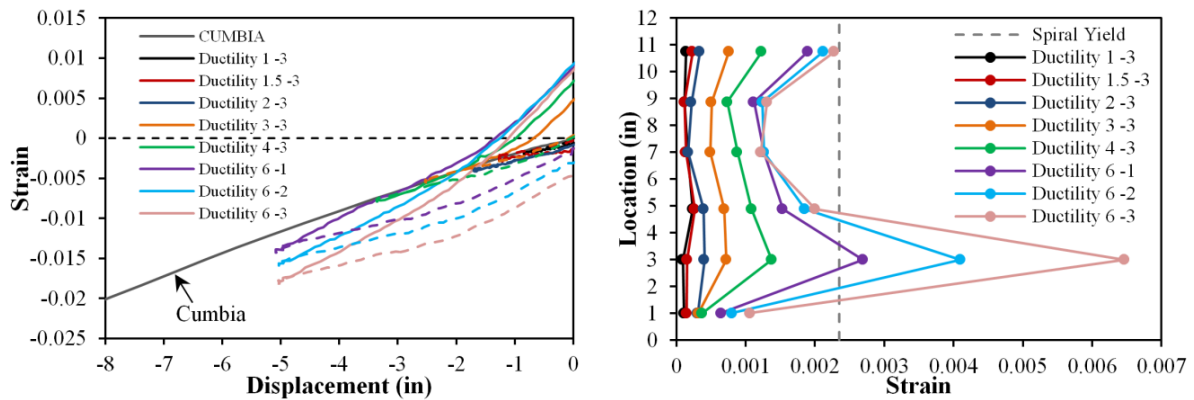
Figure 6.5 (Left) Relationship between Compressive Strain and Displacement for North Bar, (Right) Strains in Six Spiral Layers over the North Extreme Fiber Bar

Cross section strain profiles for the first horizontal cross section above the footing appear in Figure 6.6. The cross section curvature is calculated by the slope of the least squared line connecting strains measured in six reinforcing bars in extreme fiber regions of the column. If the curvatures for many horizontal cross sections are analyzed, curvature profiles for the plastic hinge region can be constructed, Figure 6.7. Measured curvatures during displacement ductility one closely match the elastic curvature profile, which linearly decreases from yield curvature at the footing-column interface to zero at the center of the

applied lateral load. Plastic curvatures were found to follow a linear distribution, which agrees with observations made by Hines et. al. (2004). Procedures developed by Hines et. al. (2004) were followed to extract important information about the curvature profiles. Linear least squared error lines were fit to the plastic portion of the curvature profiles to highlight their linearity. The base curvature is calculated as the intersection of the linear plastic curvature profile with the footing-column interface. The initial plastic curvature profiles are heavily influenced by individual crack locations, so the linear representation does not fit as well. As the base curvature increases, the height at which the linear plastic curvature profile intersects the elastic curvature profile also increases. This spread of plasticity can be attributed to two sources: (1) increases in moment which influence the moment gradient and (2) the effects of tension shift which spread tension strains higher above the footing.

Curvature profiles in Figure 6.7 describe the elastic and plastic flexural displacements of the column, but do not address fixed-end rotations which result from strain penetration of longitudinal reinforcement into the footing. Development of fully anchored column longitudinal bars into the footing leads to bond slip along the partially anchored region of the bars near the footing-column interface, as described by Zhao and Sritharan (2007). The vertical displacement of target markers placed closest to the footing-column interface can be used to monitor the pull out and push in of the reinforcing bar over the partially bonded region. If the measured bond slips of six reinforcing bars are plotted along the cross section, the fixed-end rotation attributable to strain penetration may be calculated as the slope of a least squared error line, Figure 6.6. The strain penetration displacement is obtained by multiplying this rotation by the cantilever height of the column. If an elastic curvature profile assumption is made for curvatures higher than those measured in Figure 6.7, then the entire curvature profile may be integrated to obtain the total column flexural displacement. This column flexural displacement was added to the strain penetration displacement, and compared to the experimentally measured displacements in the right half of Figure 6.3. The Optotrak integrated displacement matches well with those obtained from a string potentiometer placed at the center of the lateral load, which indicates that the shear deformation component is small.
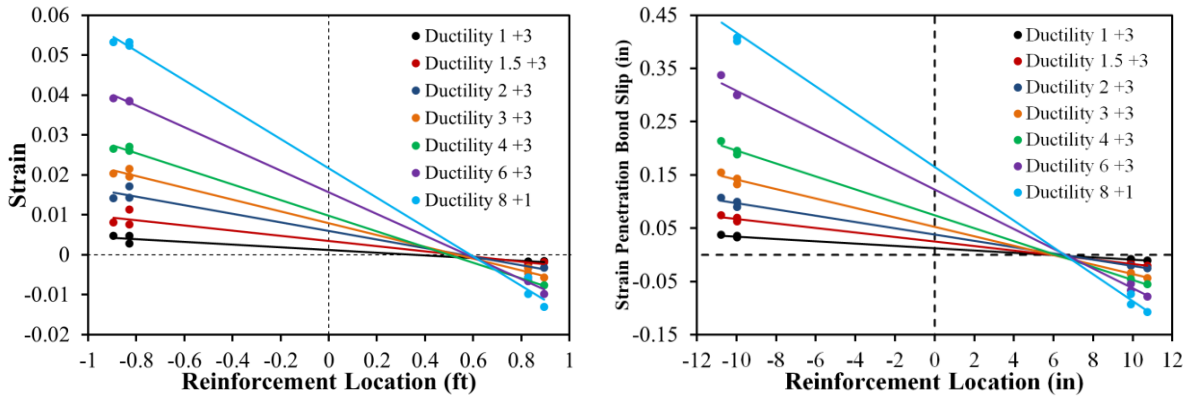
Figure 6.6 (Left) Strain Profile for the 1st Horizontal Section above the Footing, (Right) Measured Fixed-End Rotations due to Strain Penetration of Reinforcement
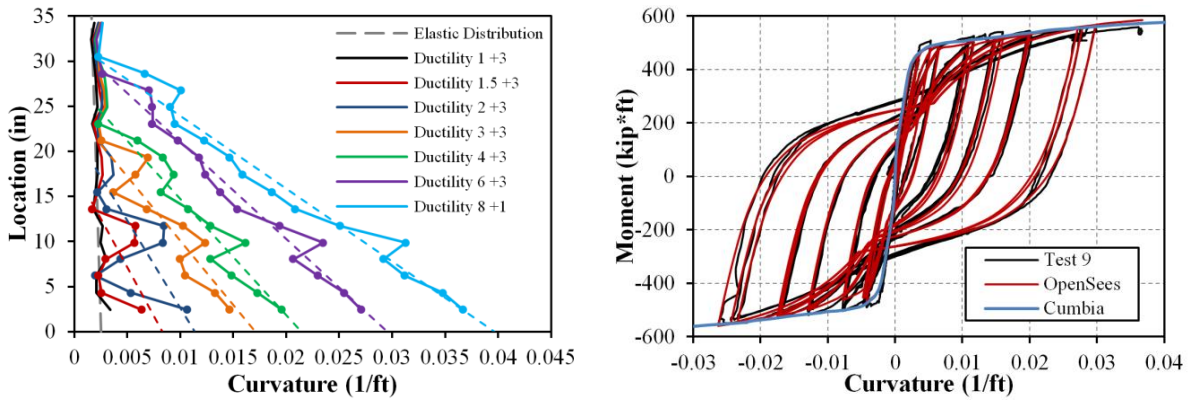
Figure 6.7 (Left) Curvature Profiles with Linear Plastic Curvature Least Squared Error Lines, (Right) Comparison of Measured and Predicted Sectional Response

6.3 Response Prediction Methods

In order to successfully design for a particular performance strain limit, methods of relating strain to lateral displacement must accurately describe the components of deformation and the spread of plasticity in reinforced concrete bridge columns. There are two main techniques which are currently utilized in design to accomplish this task: (1) monotonic moment-curvature analysis paired with an equivalent curvature distribution and

(2) cyclic fiber analysis paired with an element representation of the beam or column. In the following section, the predictive capabilities of these two techniques are examined.

6.3.1   Sectional Response Prediction

The first, and most basic, functionality of these two methods is relating strains to curvatures and moments through monotonic moment-curvature analysis or cyclic section analysis with fiber discretization. A script developed by Montejo and Kowalsky (2007) called Cumbia was selected to perform monotonic M-φ. In the program, the cover concrete is assumed to follow the Mander (1988) unconfined concrete model, while the core concrete follows the Mander (1988) confined concrete model. The fiber-based cyclic M-φ analysis was conducted in OpenSees − Open System for Earthquake Engineering Simulation, Version 2.4.2. The confined and unconfined concrete fiber parameters for the Concrete02 model were selected to emulate the associated Mander (1988) confined an unconfined stress-strain curves. The cyclic ReinforcingSteel model was selected for the longitudinal steel fibers. In both analysis techniques, the Mander model input was based on the geometry, transverse steel detailing, tested spiral yield strength, and tested concrete compressive cylinder strength. Uniaxial tensile tests on reinforcing bars were used to calibrate the monotonic and cyclic material models utilized in the respective techniques.

The cross section curvature history for the first horizontal section above the footing, calculated in the same manner as Figure 6.6, is plotted against the base moment in right half of Figure 6.7. The backbone curve of the measured cyclic M-φ response (black) is reasonably predicted by the monotonic section analysis in Cumbia (blue). Similarly, the measured cyclic M-φ response is adequately predicted by the cyclic fiber-based section analysis in OpenSees (red). Both analysis methods perform well in predicting the strain history for the South bar, Figure 6.8.
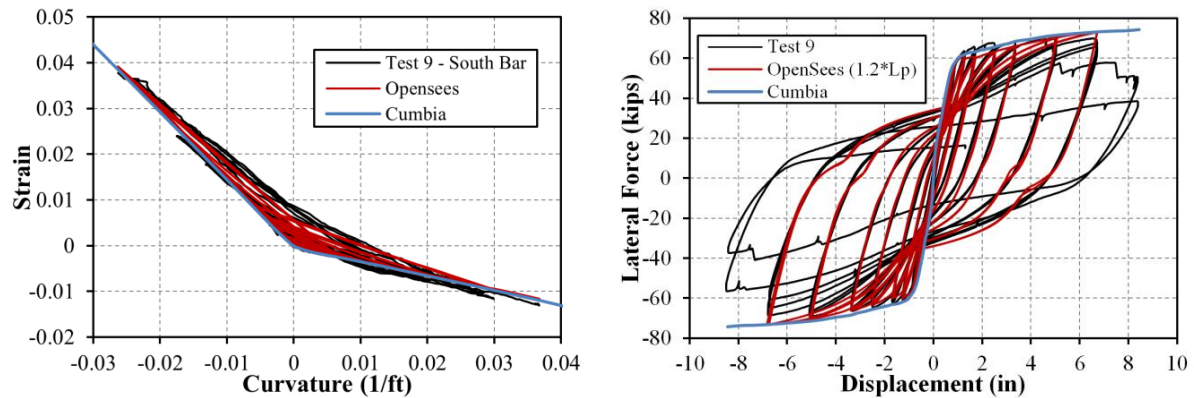
Figure 6.8 (Left) Comparison of Measured and Predicted Strain History, (Right) Comparison Measured and Predicted Lateral Force vs. Displacement

6.3.2   Member Response Prediction

Now that each analysis technique has shown adequate performance in predicting sectional response, the next level of analysis involves predicting member response. The monotonic M-φ analysis in Cumbia is translated into member response using the plastic hinge method presented in Priestley, Calvi, and Kowalsky (2007). In this method, Figure 6.9, the elastic and plastic curvature distributions are separated into equivalent simplified shapes to facilitate design. The elastic flexural displacement is determined using a triangular yield curvature distribution. The plastic flexural displacement is obtained using a uniform curvature distribution with a constant height termed the plastic hinge length. The width of the rectangle is equal to the plastic curvature at the base section. To account for the effects of strain penetration, the curvature distribution extends into the footing by a depth termed the strain penetration length.

$$\boxed{\Delta = \Delta'_y \frac{M}{M'_y} + \Delta_p + \Delta_{shear}}$$

$$L_{sp} = 0.022 f_y d_{bl} \quad (\text{MPa})$$

$$L_{eff} = L_c + L_{sp}$$

$$\Delta'_y = \frac{\phi'_y L_{eff}^2}{3}$$

$$L_p = k L_c + L_{sp} \geq 2 L_{sp}$$

$$k = 0.2 \left(\frac{f_u}{f_y} - 1 \right) \leq 0.08$$

$$\phi_p = \phi - \phi'_y \frac{M}{M'_y}$$

$$\Delta_p = \phi_p L_p (L_c + L_{sp} - 0.5 L_p)$$
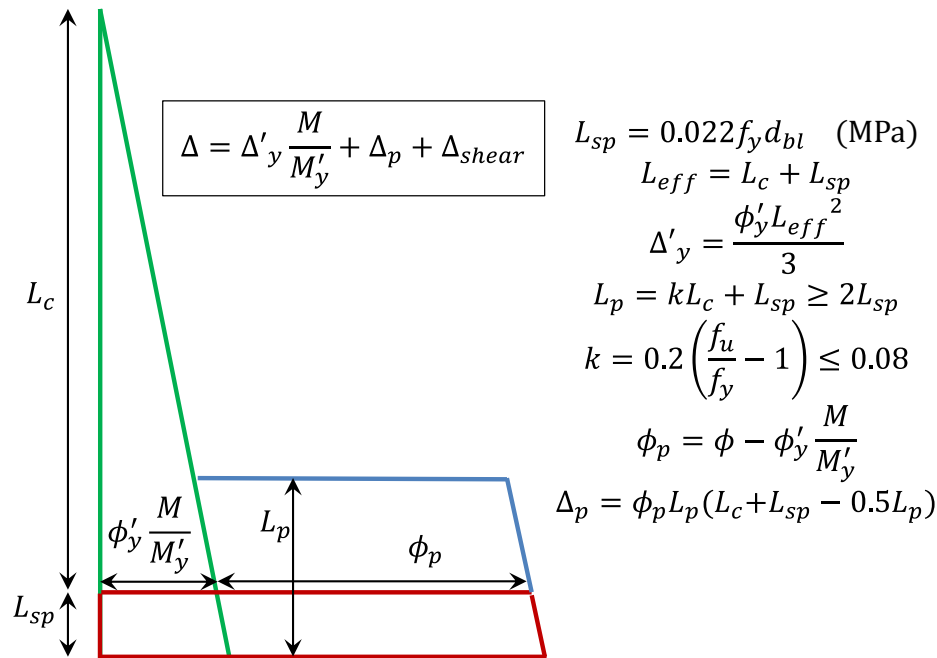
Figure 6.9 Plastic Hinge Method from Priestley, Calvi, and Kowalsky (2007)

The cyclic displacement history from the experiment was recreated using a combination of two elements in OpenSees: (1) a beam with hinges element to model the column flexural deformations and (2) a zero length strain penetration element to model the fixed end rotations due to strain penetration. The beam with hinges element, developed by Scott and Fenves (2006), is a force-based beam column element with a plastic hinge integration method based on modified Gauss–Radau quadrature. The zero length strain penetration element, developed by Zhao and Sritharan (2007), models the fixed-end rotations attributable to strain penetration of longitudinal reinforcement into the footing. The reinforcement fibers in the zero length element are replaced with Bond SP01 bar stress-slip uniaxial material which accounts for the bond slip of reinforcement at the footing-column interface. The recorded strains in the South reinforcing bar and measured bond slip at the footing-column interface were used to calibrate the Bond SP01 stress-slip model. The measured strain history, left of Figure 6.11, was converted into a stress-strain history using the calibrated ReinforcingSteel

material model in OpenSees. The model derived stresses are paired with the measured strain penetration bond slips in Figure 6.10. This stress-slip history for the South reinforcing bar was used to calibrate parameters in the Bond SP01 uniaxial material model in OpenSees.

The measured lateral force versus top column displacement response from Test 9 appears in the right half of Figure 6.8 with response predictions using the modeling techniques previously described.   The backbone curve of the hysteretic response is reasonably predicted by Cumbia, which utilized the plastic hinge method to translate curvatures to displacements. The measured compressive strains in Figure 6.11 match well with the Cumbia prediction, but the tensile strains are over predicted at higher displacement ductility levels. A plastic hinge length of 1.2*Lp, where Lp was calculated using the plastic hinge method presented in Priestley, Calvi, and Kowalsky (2007), was selected in the beam with hinges element in OpenSees to match the recorded strain data presented in Figure 6.11. A plastic hinge length equal to 1.0*Lp led to larger strains than those recorded, therefore a blind prediction would not have offered such good agreement.   Furthermore the peak compressive gage length, left half of Figure 6.5, had measured compressive strains which exceed both predictive methods in regions with inelastic confinement steel.
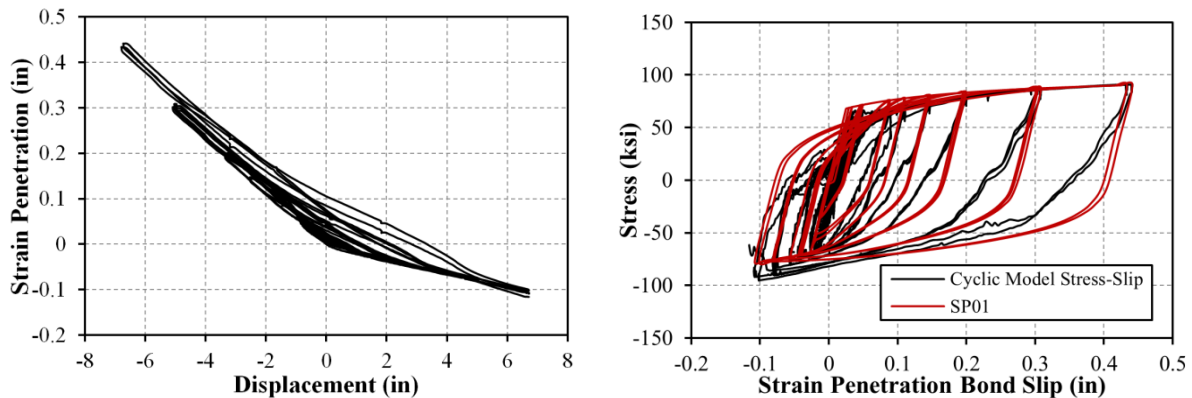
Figure 6.10 (Left) Measured Strain Penetration Bond Slip Hysteresis at Footing-Column Interface, (Right) Method of Calibrating the Stress-Slip Model
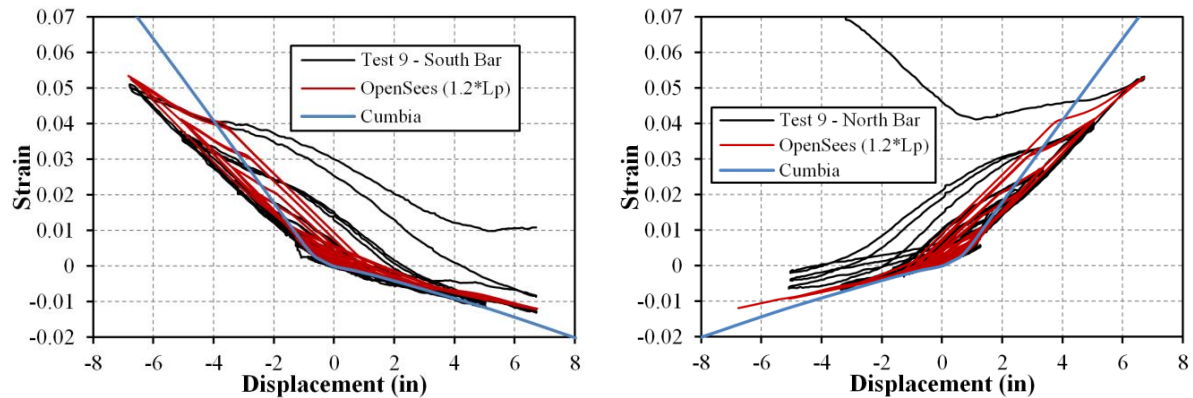
Figure 6.11 (Left) South and (Right) North Bar Measured vs. Predicted Strains

6.3.3 Motivation for a New Equivalent Curvature Distribution

The analysis techniques produced accurate sectional response predictions, but they both over predicted the relationship between tension strain and displacement with the plastic hinge length recommended in Priestley, Calvi, and Kowalsky (2007). It is clear that improvements can be made to each analysis technique if either the equivalent curvature distribution or the integration scheme for the respective methods better reflect the measured spread in plasticity. Plastic curvatures were found to follow a linear distribution which intersects the elastic curvature profile at a height termed the extent of plasticity, Figure 6.7. This measured extent of plasticity is plotted versus base section curvature ductility in Figure 6.12 for Tests 8-30 in the research program. Furthermore, the additional column deformation attributable to strain penetration of reinforcement into the footing is described by measured fixed-end rotations in Figure 6.13. A new equivalent curvature distribution is formulated in the next chapter to improve material strain-displacement predictions.
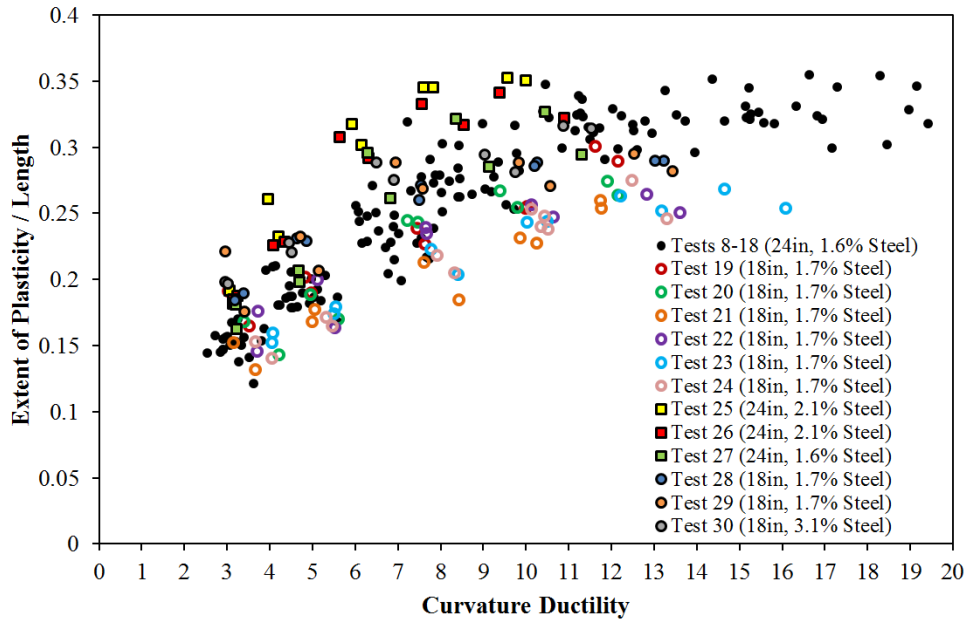
Figure 6.12 Measured Spread of Plasticity in Circular Bridge Column Tests 8-30
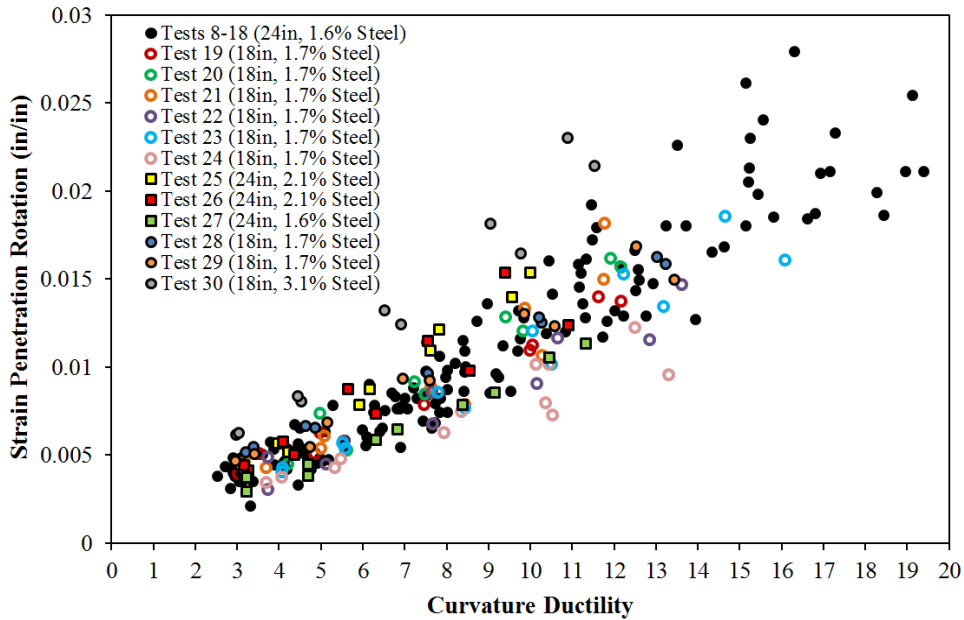
Figure 6.13 Measured Fixed-End Rotation Attributable to Strain Penetration

Chapter 7: Modified Plastic Hinge Method

7.1   Goals for the Modified Plastic Hinge Method

Accurate predictions of column deformation at key performance limit states are necessary to design bridge structures for specific levels of performance under defined levels of seismic hazard. In design, limit state curvatures are converted to target displacements using an equivalent curvature distribution. An experimental study was carried out to assess the performance of thirty circular, well-confined, bridge columns with varying lateral displacement history, transverse reinforcement detailing, axial load, aspect ratio, and longitudinal steel content. A key feature of the experiments is the high fidelity strain data obtained through the use of an optical 3D position measurement system. The process through which this instrumentation system was used to quantify components of column deformation was explained in Chapter 5. Specifically, column curvature distributions and fixed-end rotations attributable to strain penetration of reinforcement into the footing were quantified. In Chapter 5, the measured tensile and compressive strain-displacement relationships were compared to the current plastic hinge method recommended in Priestley, Calvi, and Kowalsky (2007), Figure 7.1. This method was found to over predict the tensile strain-displacement relationship and under-predict the compressive strains.

In the following section, the measured curvature and strain penetration data is used to formulate a new equivalent curvature distribution to improve the accuracy of strain-displacement predictions. There are several key aspects of the proposed Modified Plastic Hinge Model, Figure 7.2, which differentiate it from the current method: (1) strain penetration and column flexure are decoupled, (2) plastic curvatures are assumed to follow a linear distribution, and (3) separate plastic hinge lengths are recommended for tensile and compressive strain-displacement predictions.

$$\Delta = \Delta'_y \frac{M}{M'_y} + \Delta_p + \Delta_{shear}$$

$$L_{sp} = 0.022 f_y d_{bl} \quad \text{(MPa)}$$
$$L_{eff} = L_c + L_{sp}$$
$$\Delta'_y = \frac{\phi'_y L_{eff}^2}{3}$$
$$L_p = kL_c + L_{sp} \geq 2L_{sp}$$
$$k = 0.2 \left(\frac{f_u}{f_y} - 1 \right) \leq 0.08$$
$$\phi_p = \phi - \phi'_y \frac{M}{M'_y}$$
$$\Delta_p = \phi_p L_p (L_c + L_{sp} - 0.5 L_p)$$
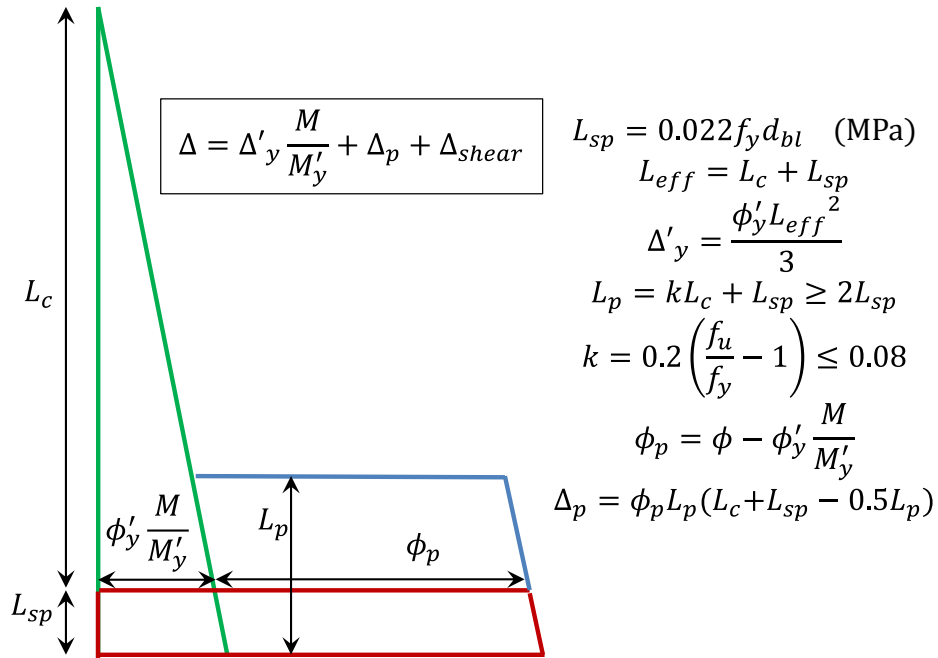
Figure 7.1 Plastic Hinge Method from Priestley, Calvi, and Kowalsky (2007)

$$\Delta = \Delta'_y \frac{M}{M'_y} + \Delta_p + \Delta_{sp} + \Delta_{shear}$$

$$L_{sp} = new\ expression$$
$$L_{pr} = new\ expression$$
$$\Delta'_y = \frac{\phi'_y L_c^2}{3}$$
$$\phi_p = \phi - \phi'_y \frac{M}{M'_y}$$
$$\Delta_p = \left(\frac{1}{2} \phi_p L_{pr} \right) \left(L_c - \frac{1}{3} L_{pr} \right)$$
$$\Delta_{sp} = \phi L_{sp} L_c$$

Extent of Plasticity, L_{pr}
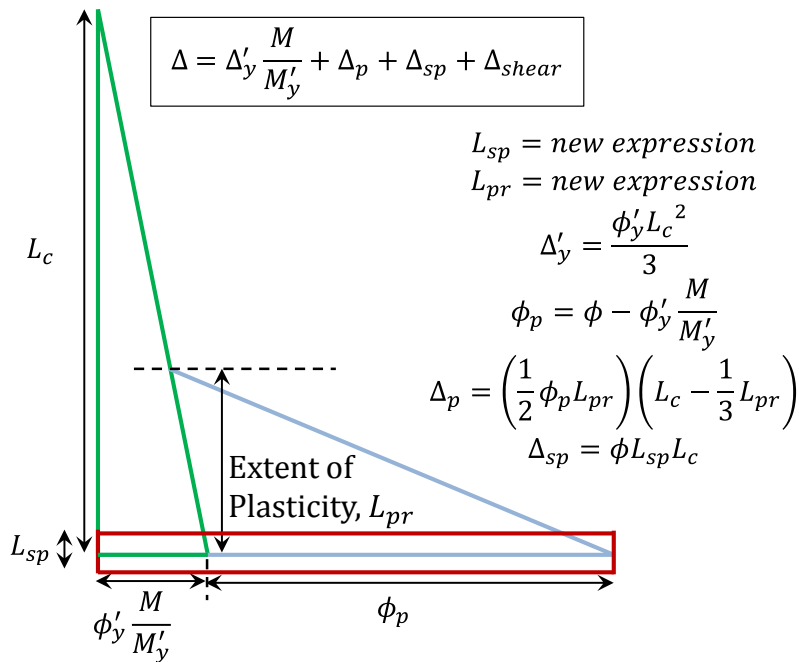
Figure 7.2 Goal for the Modified Plastic Hinge Method

7.2   Deformation due to Strain Penetration of Reinforcement into Adjoining Members

Development of fully anchored column longitudinal bars into the footing leads to bond slips along the partially anchored region of the bars near the footing-column interface, as described by Zhao and Sritharan (2007). They additionally note that this bond slip is not a pull-out of the entire bar embedment length resulting from poor bond between the concrete and reinforcing bar. The measured strain penetration bond slip hysteresis for an extreme fiber bar in Test 9 appears in Figure 7.3. Measured bond slips in multiple bars were used to quantify the fixed-end rotation due to strain penetration of reinforcement into the footing, Figure 7.3. In the proposed Modified Plastic Hinge Method, the displacement due to strain penetration is separated from column flexural displacements. An equivalent curvature block is placed at the footing-column or column-cap interface which describes the rotation due to strain penetration or reinforcement into the adjoining member, Figure 7.2. The area of this strain penetration block, $\theta_{sp} = L_{sp}\phi_{base}$ in Eqn 7.1, represents the fixed-end rotation. The top column displacement due to strain penetration is obtained my multiplying the fixed-end rotation by the column length, Eqn 7.2. Equivalent strain penetration lengths were calculated for each column test, Figure 7.6, by dividing the measured fixed-end rotation, Figure 7.5, by the base-section curvature, Eqn 7.3. These equivalent strain penetration lengths were found to remain constant over the range of ductility experienced in individual tests.

$\theta_{sp} = L_{sp}\phi_{base}$ Fixed-End Rotation due to Strain Penetration   Eqn 7.1

$\Delta_{sp} = \theta_{sp}L = L_{sp}\phi_{base}L$ Top Column Deformation due to Strain Penetration   Eqn 7.2

$L_{sp}^{meas} = \dfrac{\theta_{sp}^{meas}}{\phi_{base}^{meas}}$ Eqn 7.3
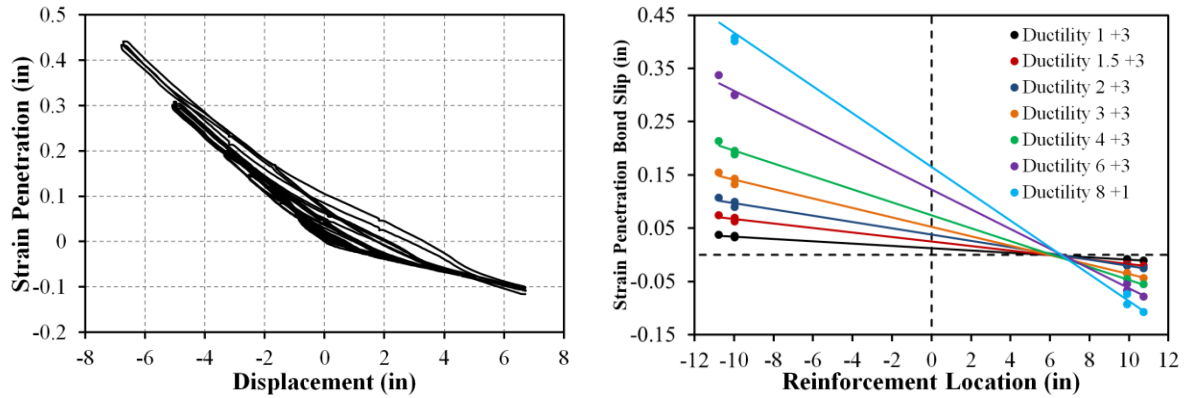
Figure 7.3 (Left) Bond Slip Hysteresis and (Right) Rotation due to Strain Penetration

The proposed form of the equivalent strain penetration length (L_{sp}) equation takes the form Eqn 7.4 with parameters X which account for the effect of individual variables. Parameters and coefficients were selected by minimizing the sum of the squared error between the equation result and the average measured equivalent strain penetration length from each test, since the measured values were found not to vary as a function of ductility.

$$L_{sp} = X \frac{f_{ye} d_{bl}}{\sqrt{f'_{cef}}}$$
<div align="right">Eqn 7.4</div>

After experimentation with a constant for X, it was found the accuracy of the equation could be improved by including the following parameters Eqn 7.5. The variable U changes depending on the units of stress input into the equation, with the final result taking the same units used for the longitudinal bar diameter.

$$L_{sp} = U \left(1 - \frac{P}{f'_{ce}A_g} - \frac{L_c}{16D} \right) \frac{f_{ye}d_{bl}}{\sqrt{f'_{ce_f}}}$$ Eqn 7.5

$U = 0.4$ for stress input as ksi, $U = 0.152$ for stress input as MPa

$\frac{P}{f'_{ce}A_g}$ column axial load ratio expressed as a decimal rather than a percent

$\frac{L_c}{D}$ cantilever aspect ratio, equivalent to $\frac{M}{VD}$

f_{ye} and d_{bl} are the yield stress and bar diameter of the longitudinal reinforcement

f'_{ce_f} expected concrete strength of the adjoining member

An overview of the accuracy of the proposed L_{sp} equation is shown in Figure 7.7. The sensitivity of the proposed equation to individual test variables appears in Figure 7.8. Variables without a significant trend indicate that their influence on strain penetration behavior is appropriately described by Eqn 7.5. Alternatively, the accuracy of the proposed equation can be compared to individual observations at various levels of ductility, rather than the average value from each test. The numerical results of this comparison appear below for both the equivalent strain penetration length, and the resulting column displacement attributable to strain penetration of reinforcement into the adjoining member.   This comparison is shown graphically in Figure 7.9 as a function of base section curvature ductility.

A cumulative probability distribution for the ratio of measured to predicted strain penetration displacement for each data observation appears in Figure 7.10. Each observation of measured to predicted strain penetration displacement is given a probability of 1/n, where n is the total number of observations. These individual observations are sorted in ascending order.   The first observation, with the lowest ratio of measured/equation value has a probability of 1/n, while the second has a probability of 2/n, until the final observation has a

probability of 1. A near vertical line at a measured/predicted ratio of one would denote an accurate prediction with low variability.

$$mean\left(\frac{L_{sp}^{meas}}{L_{sp}^{eqn}}\right) = 0.99, COV = 0.152 \quad \text{Statistics for Equivalent Strain Penetration Length}$$

$$mean\left(\frac{\Delta_{sp}^{meas} = \theta_{sp}^{meas} L_c}{\Delta_{sp}^{eqn} = L_{sp}^{eqn} \phi_{base}^{meas} L_c}\right) = 0.99, COV = 0.146 \quad \begin{array}{l}\text{Statistics for Deformation}\\\text{Attributable to Strain Penetration}\end{array}$$

• Tests 8-18 [L/D=4] (ALR=5%) [24" Dia] (1.6% Long. Steel)
○ Test 19 [L/D=5.33] (ALR=10%) [18" Dia] (1.7% Long. Steel)
○ Test 20 [L/D=5.33] (ALR=5%) [18" Dia] (1.7% Long. Steel)
○ Test 21 [L/D=7.33] (ALR=5%) [18" Dia] (1.7% Long. Steel)
○ Test 22 [L/D=7.33] (ALR=10%) [18" Dia] (1.7% Long. Steel)
○ Test 23 [L/D=8.67] (ALR=5%) [18" Dia] (1.7% Long. Steel)
○ Test 24 [L/D=8.67] (ALR=10%) [18" Dia] (1.7% Long. Steel)
▫ Test 25 [L/D=4] (ALR=5%) [24" Dia] (2.1% Long. Steel)
▪ Test 26 [L/D=4] (ALR=10%) [24" Dia] (2.1% Long. Steel)
▫ Test 27 [L/D=4] (ALR=10%) [24" Dia] (1.6% Long. Steel)
○ Test 28 [L/D=5.33] (ALR=15%) [18" Dia] (1.7% Long. Steel)
○ Test 29 [L/D=5.33] (ALR=20%) [18" Dia] (1.7% Long. Steel)
○ Test 30 [L/D=5.33] (ALR=15%) [18" Dia] (3.1% Long. Steel)

Figure 7.4 Additional Information about Each Experiment
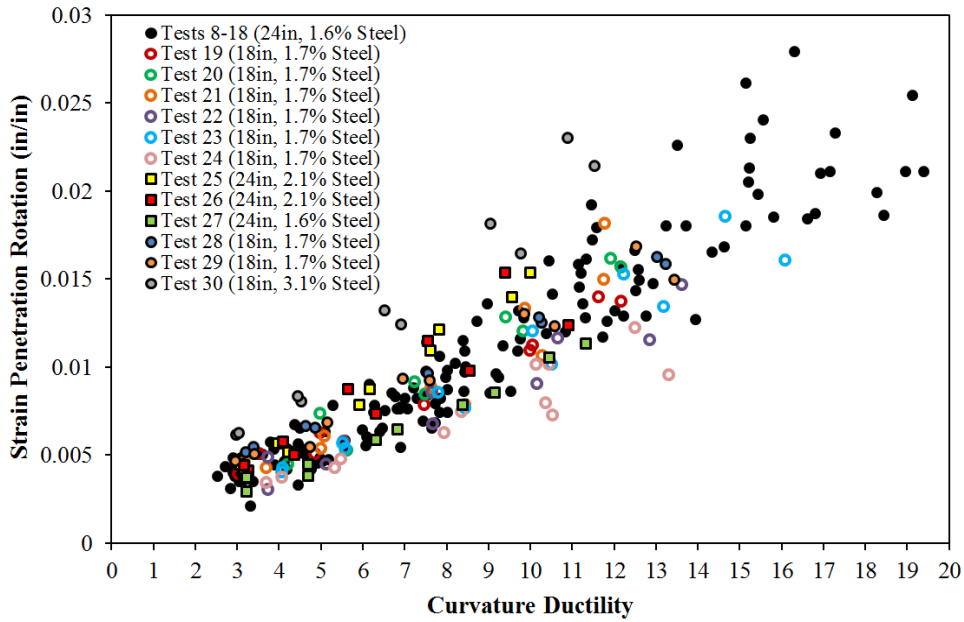
Figure 7.5 Strain Penetration Rotation Measured in Experiments
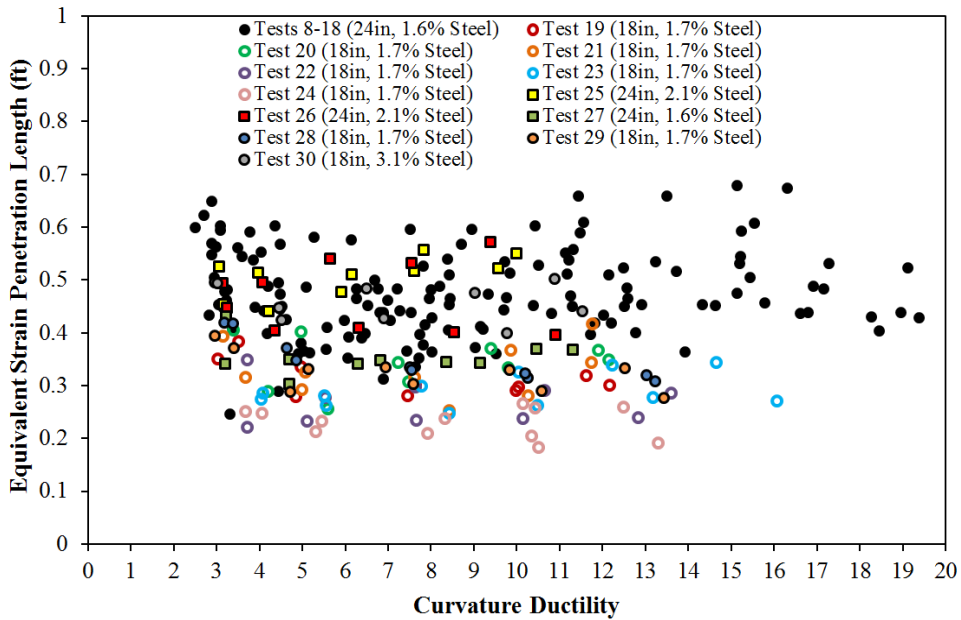
Figure 7.6 Equivalent Strain Penetration Lengths for Individual Experiments
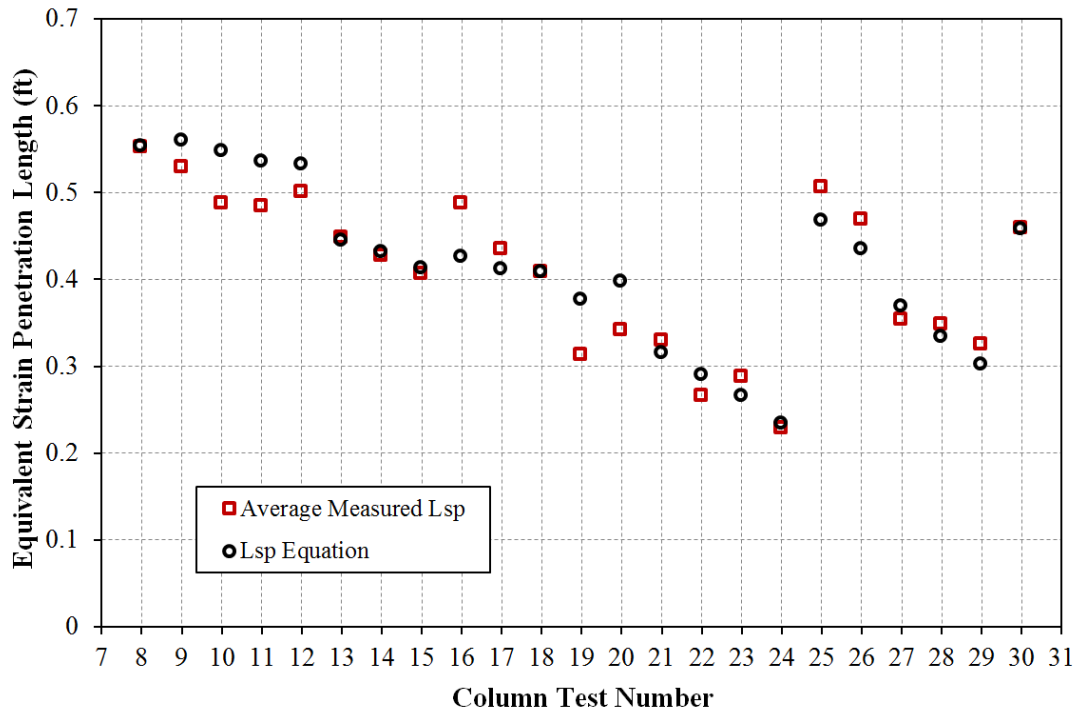
Figure 7.7 Average Measured Strain Penetration Lengths and Result of Eqn 7.5
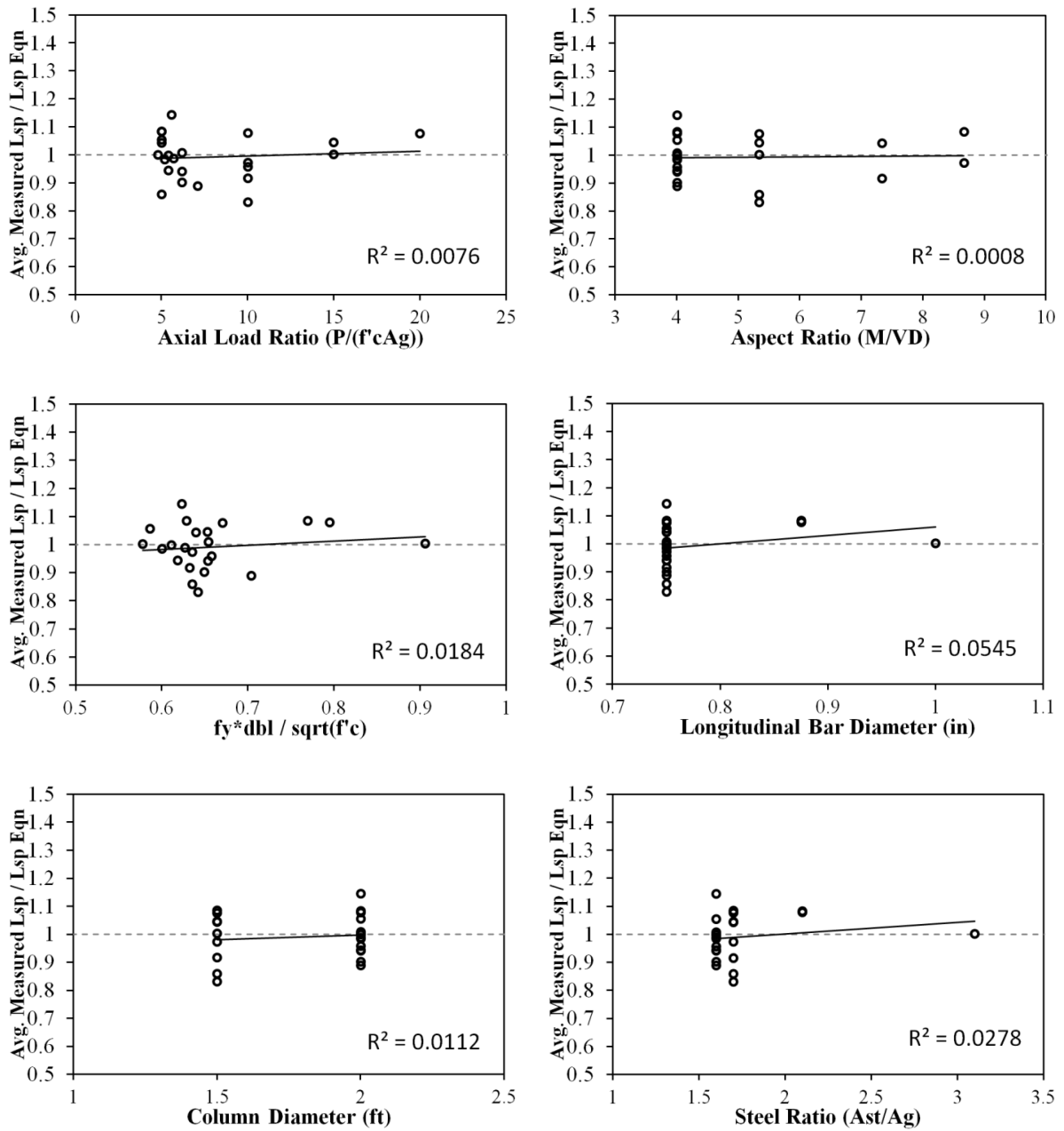
Figure 7.8 Sensitivity of Strain Penetration Length Equation to Individual Variables
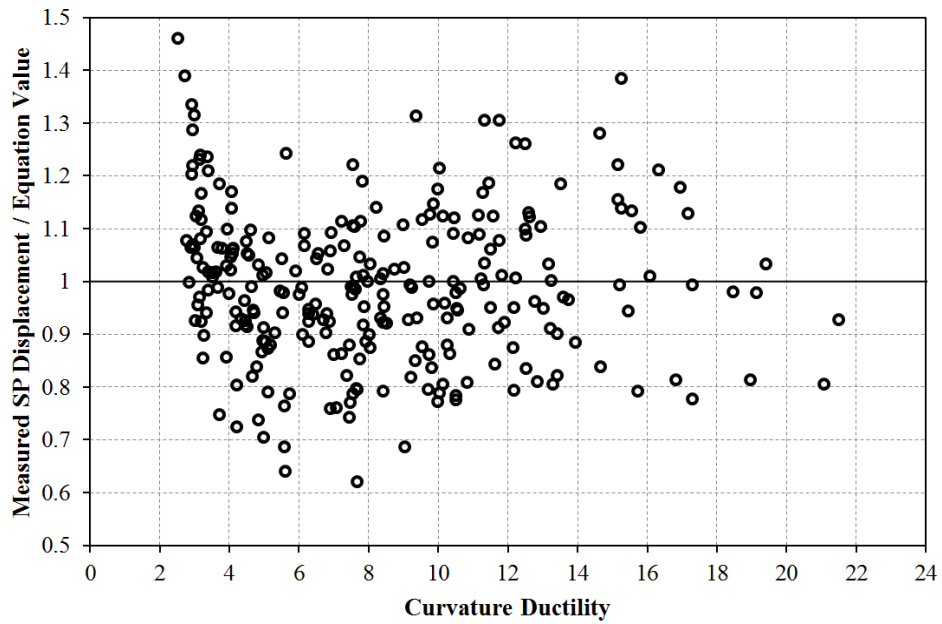
Figure 7.9 Strain Penetration Length from Each Observation Compared to Eqn 7.5
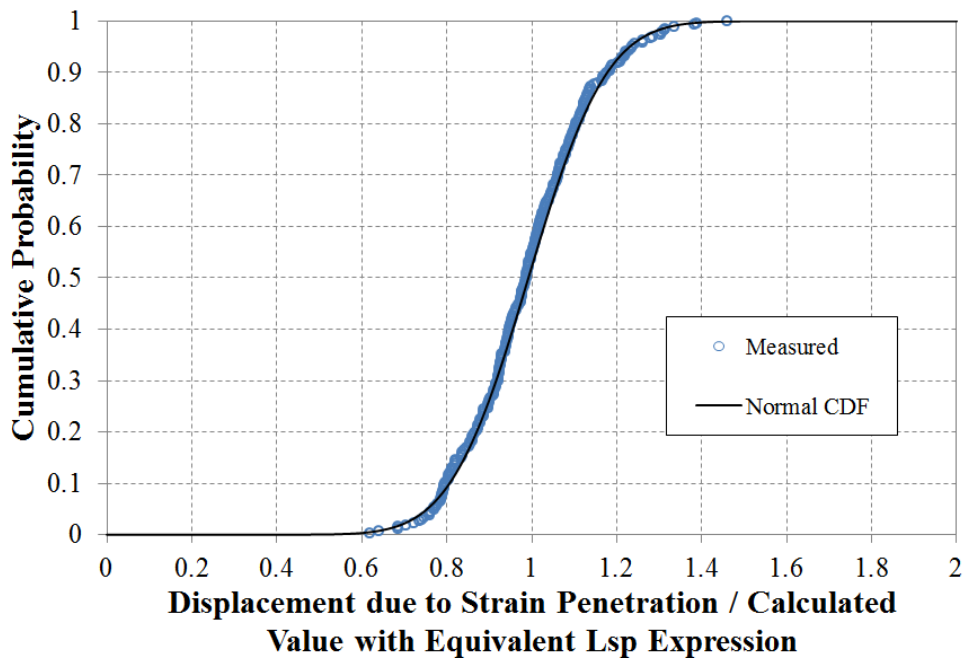
Figure 7.10 CDF for Strain Penetration Disp. / Value with Eqn 7.5 and Eqn 7.2

7.3   Tensile and Compressive Plastic Hinge Lengths

Plastic curvatures were found to follow a linear distribution as shown in the push cycle curvature profiles for Test 13, Figure 7.11.   This section aims to answer the following question, would a plastic hinge length expression based on the measured spread of plasticity offer a better prediction for the relationship between strain and displacement?   Measured curvatures at displacement ductility one closely match the assumed elastic curvature profile which has a value of $\phi_y'\left(M_n/M_y'\right) = \phi_y$ at the column base and zero at the center of the applied lateral load.   As curvature ductility increases, the height at which the linear plastic curvature distribution intersects the elastic curvature distribution also increases.   This spread in plasticity is due to the effects of moment gradient and tension shift.

Vertical strain profiles for Test 13, Figure 7.12, depict strains measured in the extreme fiber reinforcing bars during push cycles.   Compressive strains are concentrated near the footing, while tension strains are fanned out to a greater height following the inclined flexural shear crack distribution.   This is due in large part to the effects of tension shift, which leads to tension strains above the base section which exceed those that would develop based on the plane sections hypothesis and the moment at that height alone.   Tension shift leads to a fanned compression strut pattern which emanates from the compressive toe region of the column, where the local compressive demand is increased beyond that which would be predicted based on the plane sections hypothesis.   Since tension strain are spread further above the base section, the magnitude of the peak tensile strain near the footing may be reduced.   Observations of peak tensile and peak compressive strain-displacement relationships support this theory, as will be discussed in later sections of this report.
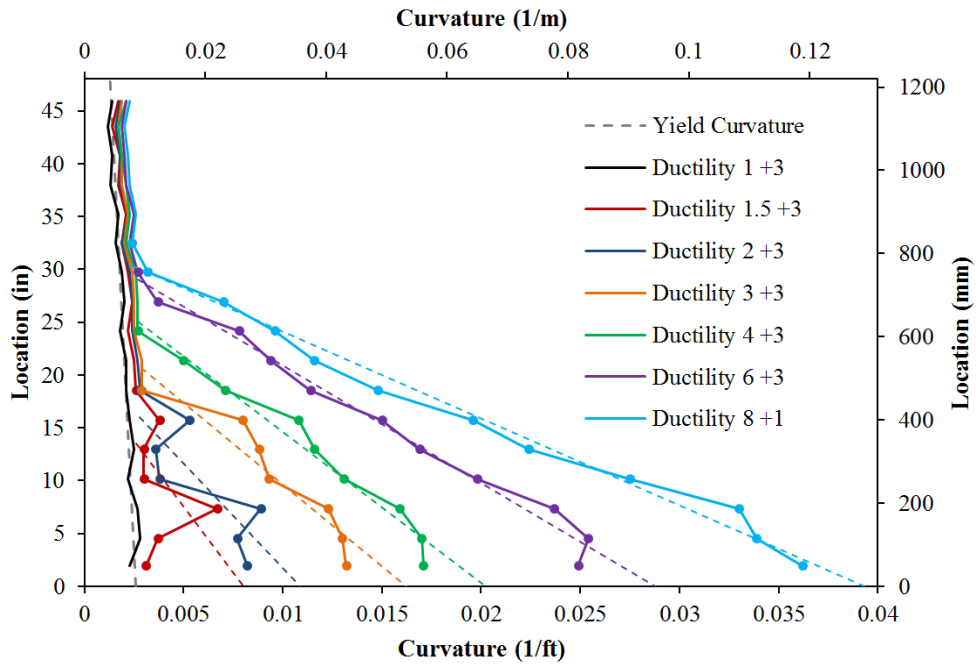
Figure 7.11 Curvature Profiles with Linear Plastic Curvature Regressions
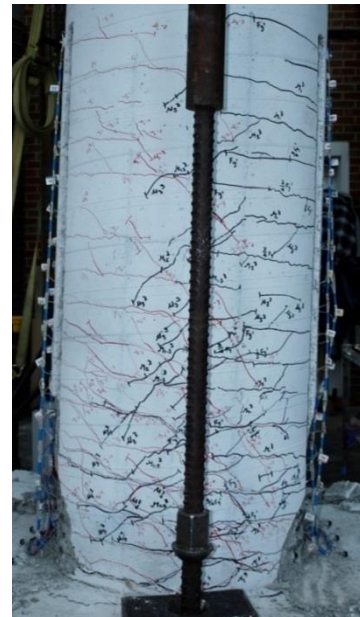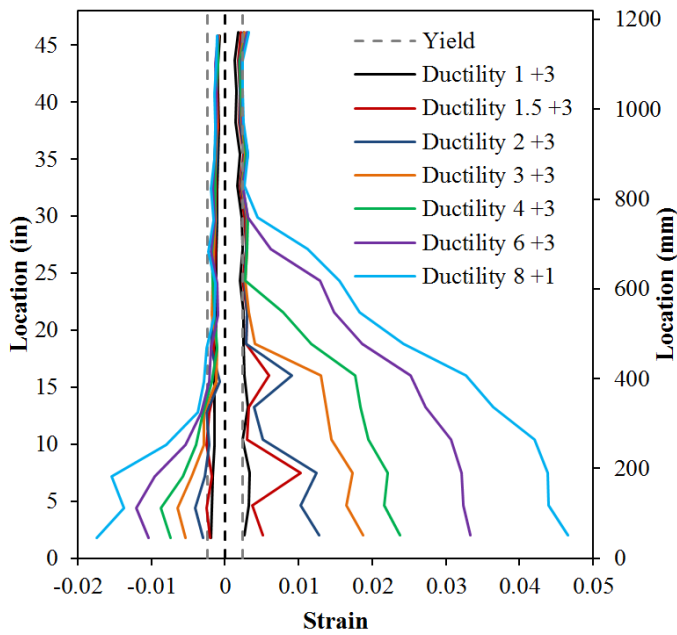
Figure 7.12 (Left) Extreme Fiber Bar Vertical Strain Profiles and (Right) Crack Profile

The influence of moment gradient on the spread of plasticity can be evaluated by superimposing the moment-curvature relation for the cross-section upon the moment profile of the column at specific levels of response, Figure 7.13 for Test 13. The deformation at the center of the applied lateral load can be evaluated using a layered integration technique and the Moment-Area method, Eqn 7.6. The plastic displacement from curvature integration, Eqn 7.9, is obtained by subtracting the elastic displacement from the total integrated displacement. The elastic post yield displacement takes the form of Eqn 7.7 for a column in single bending, and Eqn 7.8 for a column in double bending.

$$\Delta_{Ti} = \left[\int_{x=0}^{x=L} \phi(x) dx \right] \bar{x}$$
First moment of curvature diagram, where $\bar{x}$ is its centroid. Evaluated using layered approach and the Moment-Area method.
Eqn 7.6

$$\Delta_e = \phi_y' \left(M/M_y' \right) L^2 / 3$$
(Single Bending) Elastic Displacement after Frist Yield
Eqn 7.7

$$\Delta_e = \phi_y' \left(M/M_y' \right) L^2 / 6$$
(Double Bending) Elastic Displacement after Frist Yield
Eqn 7.8

$$\Delta_{pi} = \Delta_T - \Delta_e$$
Plastic Displacement from Curvature Integration
Eqn 7.9
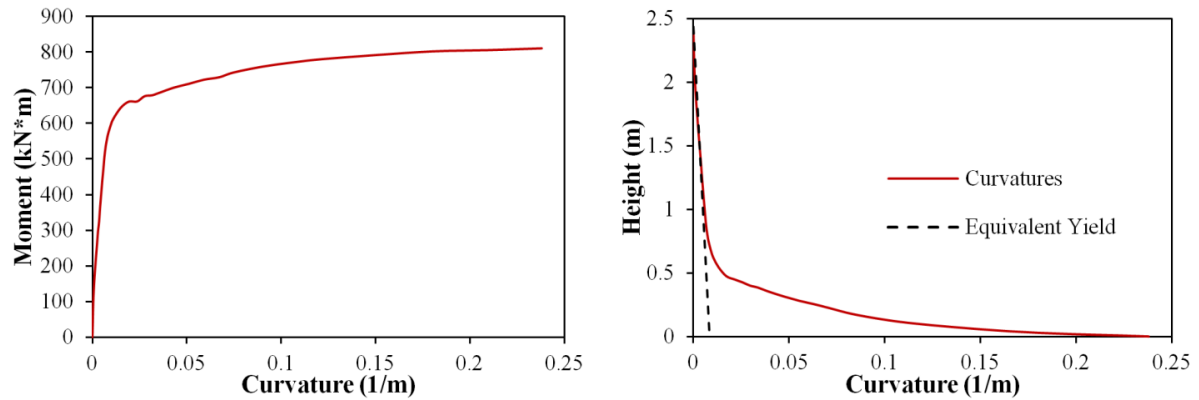
Figure 7.13 Moment-Curvature for Test 13 Superimposed over Moment Profile

Equivalent curvature distributions are utilized in design to translate a known moment-curvature relation into a member force-deformation response. The current iteration of the plastic hinge method from Priestley, Calvi, and Kowalsky (2007) appears in Figure 7.1. In this approach, abbreviated as PCK (2007) Lp, an equivalent rectangular distribution of constant curvature is used to compute the plastic flexural displacement of the column. A portion of this rectangular hinge length $\left(L_p = kL + Lsp\right)$ is attributed to moment gradient (kL), while the (Lsp) component describes the influence of strain penetration. Since a separate strain penetration model is recommended in this study, consider only on the moment gradient component (kL) in the following discussion. The value of k can be solved for by setting Δ_{pi} from Eqn 7.9 equal to the Δ_p evaluated using an assumed rectangular plastic curvature distribution Eqn 7.11. Alternatively, a parameter k^* can be solved for by setting Δ_{pi} from Eqn 7.9 equal to the Δ_p from a triangular plastic curvature distribution Eqn 7.13. For this discussion, the height of a rectangular plastic curvature distribution is termed Lp, while the height of a triangular plastic curvature distribution is termed Lpr, Figure 7.14.

Notation: $L_c = L/2$ for Double Bending and $L_c = L$ for Single Bending.

$$\phi_p = \phi_{base} - \phi_y'(M/M_y')$$ Plastic Curvature at the Base Section   Eqn 7.10

$$\Delta_p = \phi_p(kL)[L - kL/2]$$ (Single Bending) Plastic Displacement from a Rectangular Hinge Length (Lp)   Eqn 7.11

$$\Delta_p = \phi_p(kL_c)[L - kL_c]$$ (Double Bending) Plastic Displacement from a Rectangular Hinge Length (Lp)   Eqn 7.12

$$\Delta_p = \phi_p(k^*L/2)[L - k^*L/3]$$ (Single Bending) Plastic Displacement from a Triangular Hinge Length (Lpr)   Eqn 7.13

$$\Delta_p = \phi_p(k^*L_c/2)[L - 2k^*L_c/3]$$ (Double Bending) Plastic Displacement from a Triangular Hinge Length (Lpr)   Eqn 7.14

An equivalent triangular plastic curvature distribution is proposed since it reflects the shape of experimentally measured curvature profiles, Figure 7.11. Linear least squared error lines were fit to the plastic portion of the measured curvature profiles to quantify their shape following recommendations proposed by Hines, Restrepo, and Seible (2004). The base-section curvature is computed as the intersection of the linear plastic curvature distribution and the footing-column interface. The extent of plasticity is evaluated as the intersection of the linear plastic curvature distribution and the elastic curvature profile. This extent of plasticity is plotted as a function of base-section curvature ductility in Figure 7.19 for individual experiments.
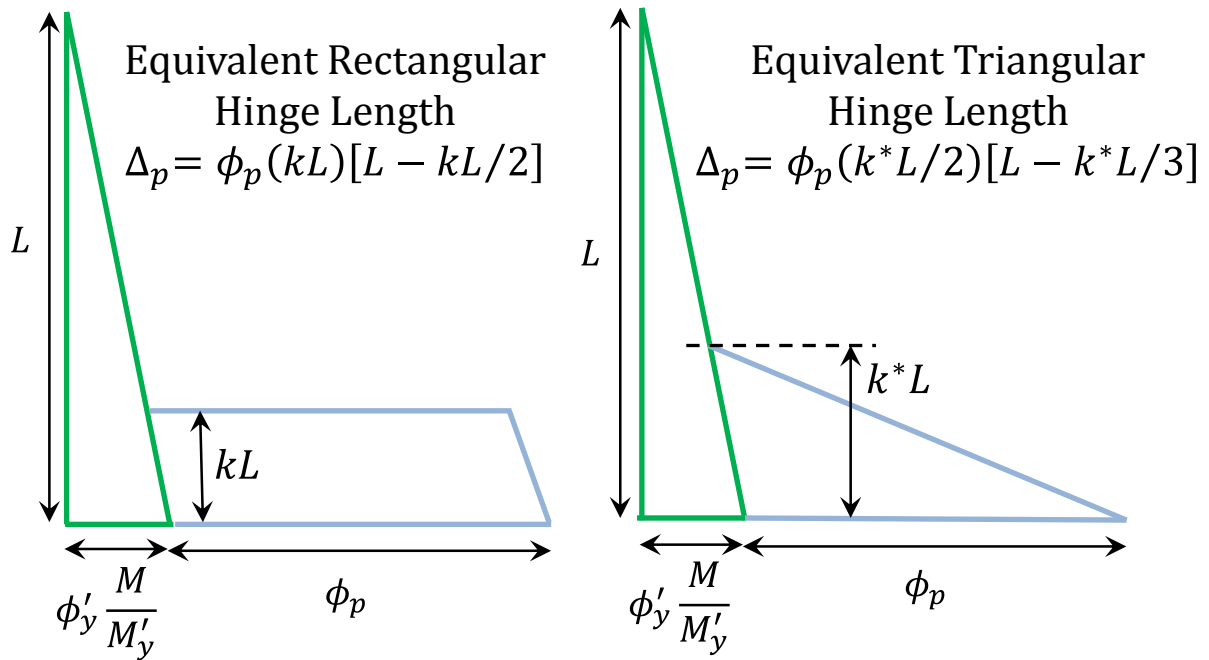
Figure 7.14 (Single Bending) Parameters k and k* Describe the Moment Gradient Component of the Plastic Hinge Length
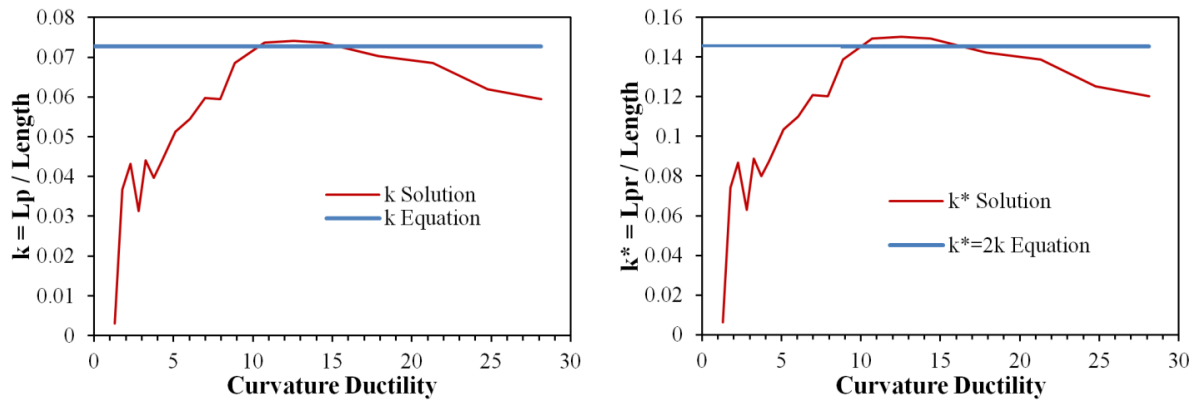
Figure 7.15 Parameter k and k* Solution for Test 13 Using Rectangular and Triangular Plastic Curvature Distributions

The result of the solution process for k and k^* appears in Figure 7.15 as a function of curvature ductility. The equation for k presented in Priestley, Calvi, and Kowalsky (2007), in Figure 7.1, compares well with the maximum value of k computed for Test 13. The shape of the k^* distribution in Figure 7.15 is similar to that of k, except the values are scaled by a factor of two. To further evaluate the relationship between k and k^*, Eqn 7.11 and Eqn 7.13 were set equal to each other and k^* was evaluated over a range of k, Figure 7.17. This process was performed for single bending, and separately for double bending using Eqn 7.12 and Eqn 7.14 described graphically in Figure 7.16. For both single and double bending, the analysis implies that $k^* \cong 2k$ with sufficient accuracy.

In Figure 7.18, the height of the equivalent triangular plastic curvature profile, $Lpr = k^*L$, is compared with measured extent of plasticity obtained from the intersection of the measured linear plastic curvature profile and the elastic curvature distribution at various levels of curvature ductility, Figure 7.11. The extent of plasticity obtained from integration of the analytical curvature distribution only accounts for the influence of moment gradient, which explains why it under predicts the measured values.

Equivalent Rectangular
Hinge Length
$$\Delta_p = \phi_p(kL_c)[L - kL_c]$$

Equivalent Triangular
Hinge Length
$$\Delta_p = \phi_p(k^*L_c/2)[L - 2k^*L_c/3]$$
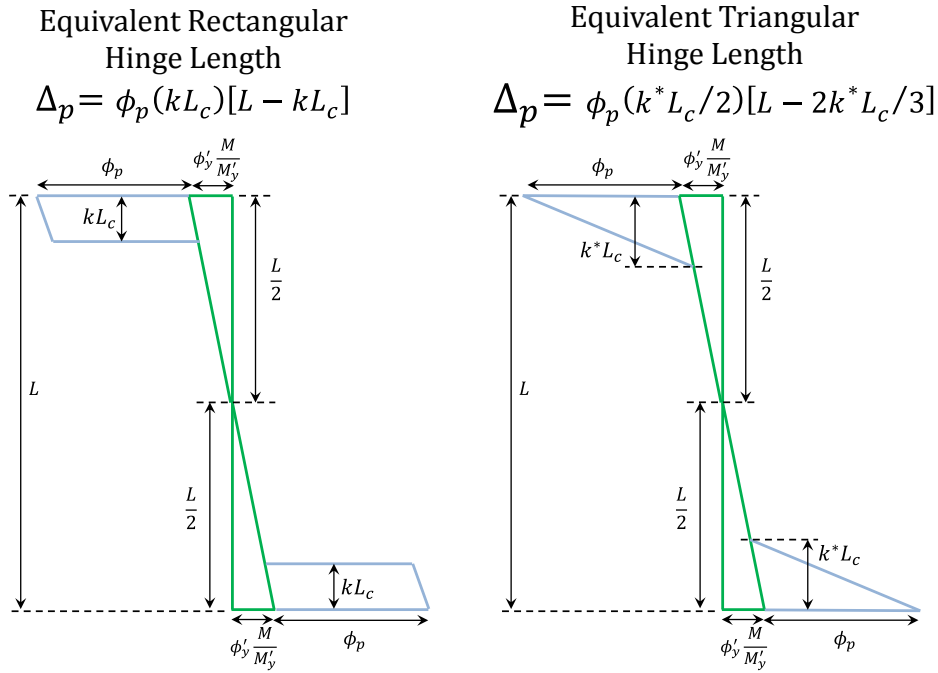
Figure 7.16 (Double Bending) Parameters k and k* for Moment Gradient Component
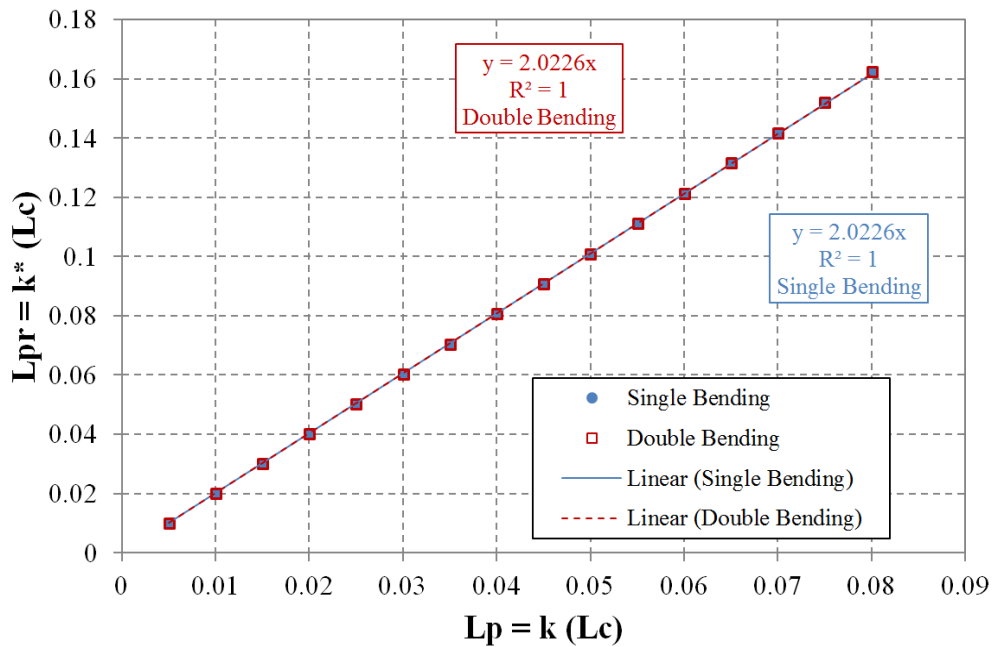
Figure 7.17 Relationship between k and k* for Plastic Hinge Distributions
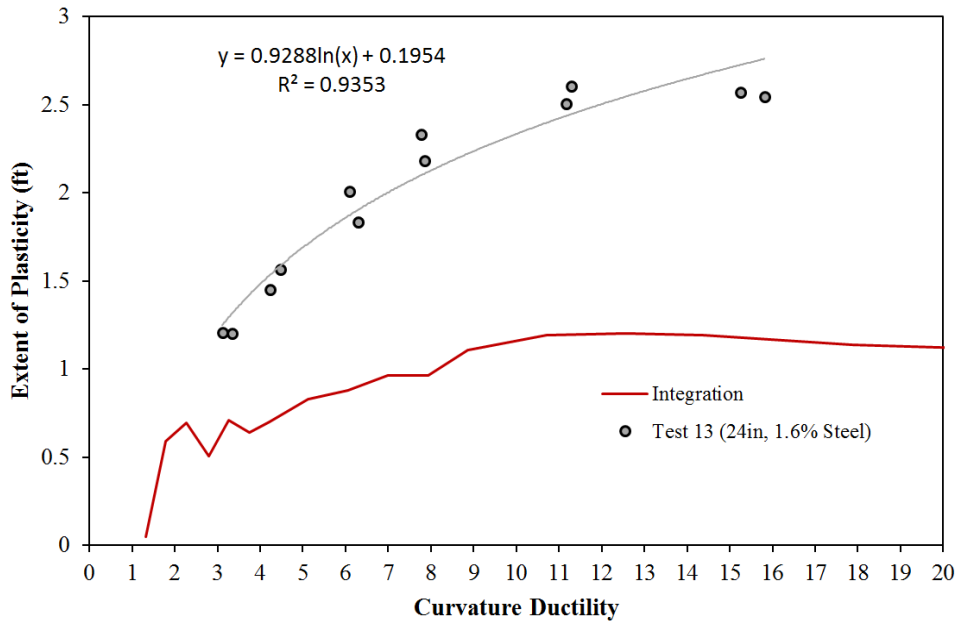
Figure 7.18 Comparison of Numerically Integrated Lpr with Measured Lpr for Test 13
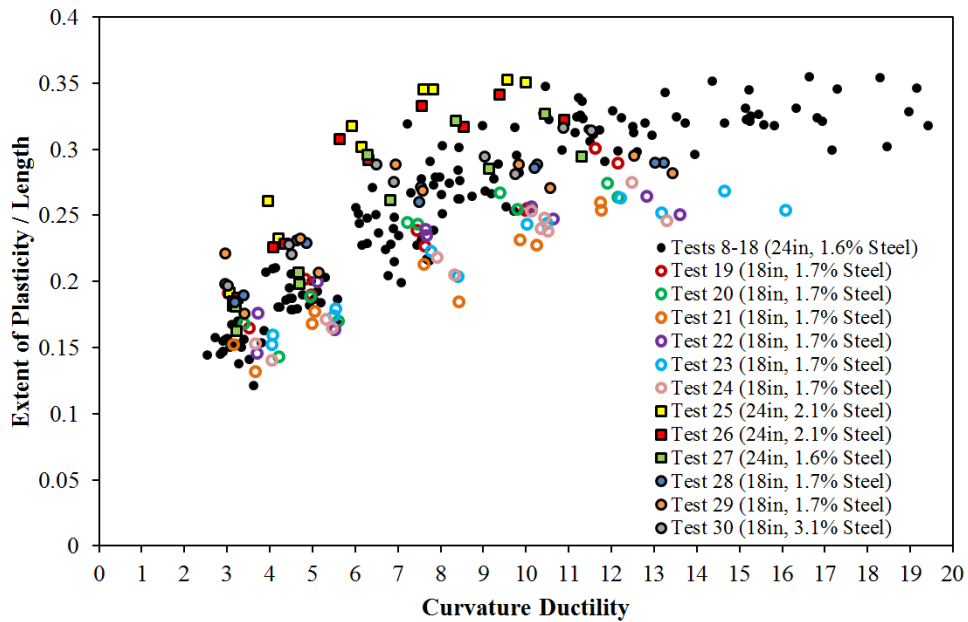
Figure 7.19 Extent of Plasticity Normalized to Column Length for Each Experiment

The difference between the measured and moment-curvature integrated extent of plasticity in Figure 7.18 is largely attributed to the influence of tension shift. The additional spread of plasticity due to tension shift is related to the distance between the tensile and compressive force resultants, jd, and the angle of the inclined flexural shear cracks. The logarithmic best fit to the measured extent of plasticity for Test 9, Figure 7.22, can be used to evaluate the accuracy of strain-displacement predictions with an equivalent curvature distribution which reflects measured spread in plasticity. The plastic hinge method presented in Priestley, Calvi, and Kowalsky (2007) is coded into the monotonic moment-curvature analysis script CUMBIA. The response predicted by the logarithmic best fit to the measured spread in plasticity for Test 9, Figure 7.22, is computed using Eqn 7.15 through Eqn 7.26 for the column in single bending. Equations for the plastic displacement of a column in double bending using either a rectangular or triangular plastic curvature distribution are derived in Figure 7.20 and Figure 7.21 respectively.   For the purpose of the strain-displacement comparison using the logarithmic best fit to the measured spread of plasticity in Test 9, Figure 7.22, the same shear displacement model built into CUMBIA was utilized for both methods. The logarithmic fit to the measured spread of plasticity provided a more accurate tensile strain-displacement prediction, but decreased the accuracy of the compressive strain-displacement prediction.

$$\Delta_e = \phi_{base}L^2/3 \quad \text{(Single) Elastic Flexural Displacement before First Yield} \qquad \text{Eqn 7.15}$$

$$\Delta_e = \phi_{base}L^2/6 \quad \text{(Double) Elastic Flexural Disp. before First Yield} \qquad \text{Eqn 7.16}$$

$$\Delta_e = \phi_y'(M/M_y')L^2/3 \quad \text{(Single) Elastic Flexural Disp. after First Yield} \qquad \text{Eqn 7.17}$$

$$\Delta_e = \phi_y'(M/M_y')L^2/6 \quad \text{(Double) Elastic Flexural Disp. after First Yield} \qquad \text{Eqn 7.18}$$

$$\phi_p = \phi_{base} - \phi_y'(M/M_y') \quad \text{Plastic Curvature at the Base Section} \qquad \text{Eqn 7.19}$$

$$\Delta_p = \phi_p(L_{pr}/2)[L - L_{pr}/3] \quad \text{(Single) Plastic Disp. for Triangular Plastic Curvature Distribution} \qquad \text{Eqn 7.20}$$

$$\Delta_p = \phi_p(L_{pr}/2)[L - 2\,L_{pr}/3] \quad \text{(Double) Plastic Disp. for Triangular Plastic Curvature Distribution} \qquad \text{Eqn 7.21}$$

$$\Delta_p = \phi_p L_p[L - L_p/2] \quad \text{(Single) Plastic Disp. for Rectangular Plastic Curvature Distribution} \qquad \text{Eqn 7.22}$$

$$\Delta_p = \phi_p L_p[L - L_p] \quad \text{(Double) Plastic Disp. for Rectangular Plastic Curvature Distribution} \qquad \text{Eqn 7.23}$$

$$L_{sp} = U\left(1 - \frac{P}{f_{ce}'A_g} - \frac{L_c}{16D}\right)\frac{f_{ye}d_{bl}}{\sqrt{f_{ce_f}'}} \quad U = 0.4 \text{ for ksi and } 0.152 \text{ for MPa units} \qquad \text{Eqn 7.24}$$

$$\Delta_{sp} = L_{sp}\phi_{base}L \quad \text{Displacement due to Strain Penetration} \qquad \text{Eqn 7.25}$$

$$\Delta_T = (\Delta_e + \Delta_{sp} + \Delta_p + \Delta_{shear}) \quad \text{Total Top Column Displacement} \qquad \text{Eqn 7.26}$$

Separate plastic hinge lengths for tension and compressive strain-displacement predictions are needed to evaluate accurate strain limit based target displacements. Tension strains are influenced by the total spread in plasticity, while compressive strains are more closely related to only the moment gradient component, Figure 7.23. The proposed tension hinge length, Lpr_t Eqn 7.28, was calibrated to match the upper bound of the measured spread of palsticity in each test. The proposed compressive hinge length, Lpr_c Eqn 7.29, only

contains a term related to the moment gradient effect.   Both expressions utilize the observation that $k^* \cong 2k$ from Figure 7.17. This geometric relationship between triangular and rectangular plastic curvature distributions can be used to translate the proposed triangular-based Lpr expressions to rectangular-based Lp equations (Eqn 7.30 and Eqn 7.31). Even though the form of the proposed compressive hinge length resembles Lp from Priestley, Calvi, and Kowalsky (2007), Figure 7.1, the predicted strain-displacement relationships differ due to the fact that strain penetration is now decoupled from column flexural displacements.

$$k = 0.2\left(\frac{f_u}{f_y} - 1\right) \le 0.08 \qquad \text{Same Definition of k as Priestley, Calvi, and Kowalsky (2007)} \qquad \text{Eqn 7.27}$$

$$Lpr_t = 2kL_c + 0.75D \qquad \text{Tension Hinge Length Based on Triangular Distribution} \qquad \text{Eqn 7.28}$$

$$Lpr_c = 2kL_c \qquad \text{Compression Hinge Length Based on Triangular Distribution} \qquad \text{Eqn 7.29}$$

$$Lp_t = Lpr_t/2 = kL_c + 0.375D \qquad \text{Tension Hinge Length Based on Rect. Dist.} \qquad \text{Eqn 7.30}$$

$$Lp_c = Lpr_c/2 = kL_c \qquad \text{Compression Hinge Length Based on Rectangular Dist.} \qquad \text{Eqn 7.31}$$
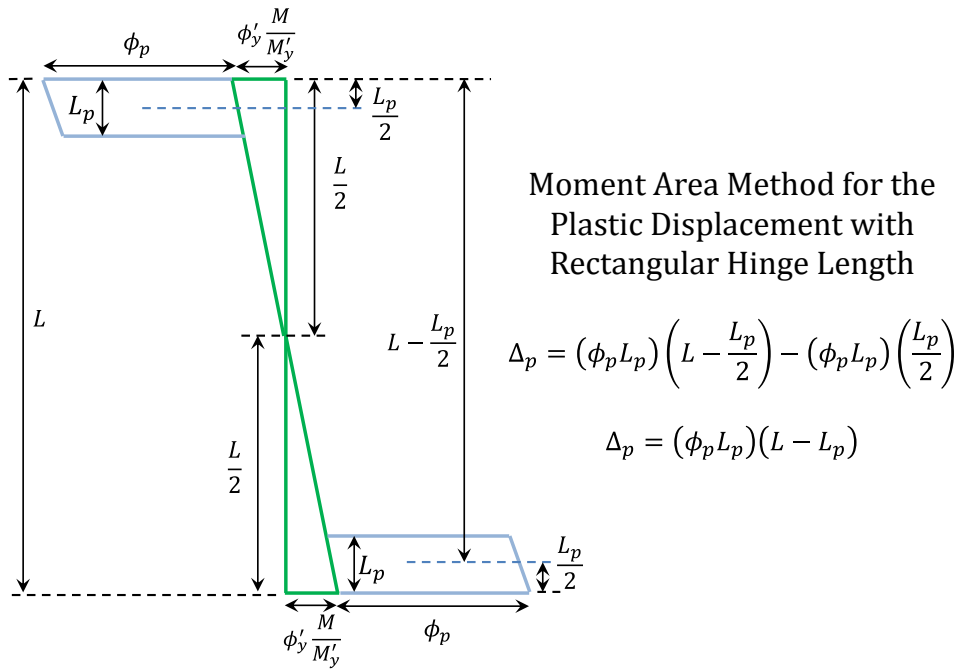
Figure 7.20 (Double Bending) Plastic Displacement with a Rectangular Hinge Length

Moment Area Method for the Plastic Displacement with Rectangular Hinge Length

$$\Delta_p = (\phi_p L_p)\left(L - \frac{L_p}{2}\right) - (\phi_p L_p)\left(\frac{L_p}{2}\right)$$

$$\Delta_p = (\phi_p L_p)(L - L_p)$$
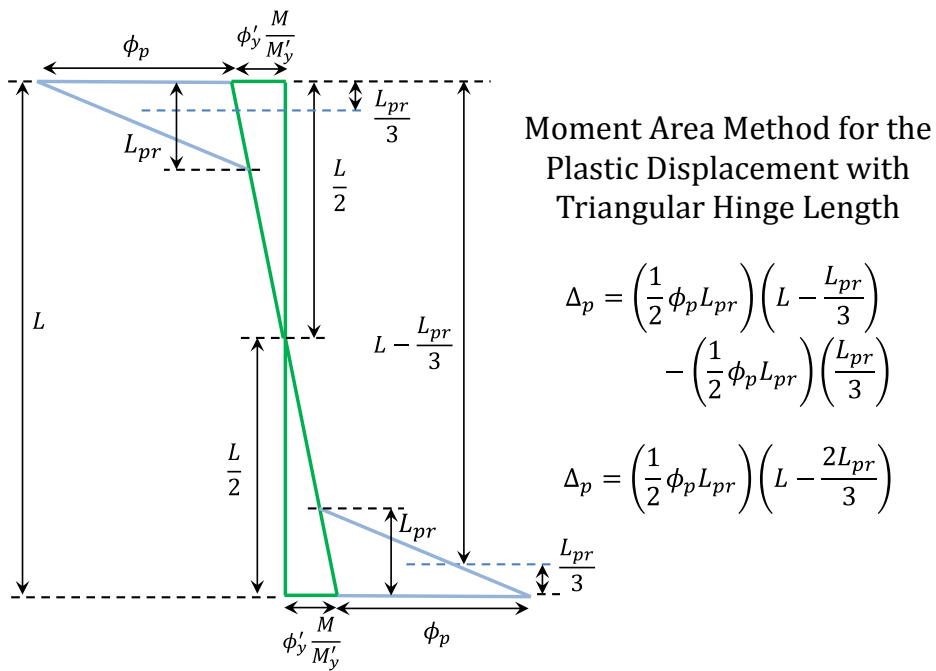
Figure 7.21 (Double Bending) Plastic Displacement with a Triangular Hinge Length

Moment Area Method for the Plastic Displacement with Triangular Hinge Length

$$\Delta_p = \left(\frac{1}{2}\phi_p L_{pr}\right)\left(L - \frac{L_{pr}}{3}\right)$$
$$- \left(\frac{1}{2}\phi_p L_{pr}\right)\left(\frac{L_{pr}}{3}\right)$$

$$\Delta_p = \left(\frac{1}{2}\phi_p L_{pr}\right)\left(L - \frac{2L_{pr}}{3}\right)$$
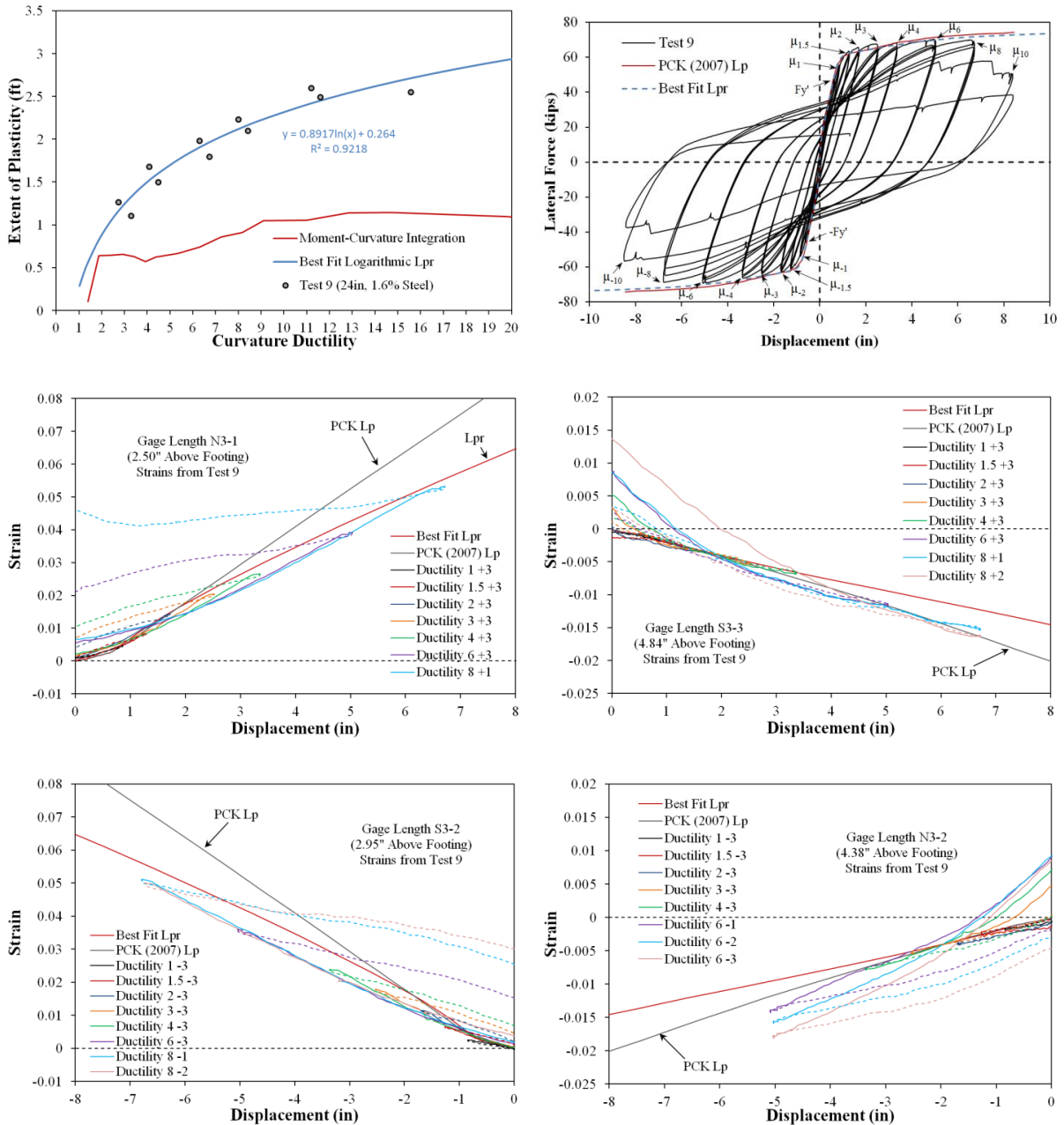
Figure 7.22 (Test 9) Response Comparison with Logarithmic Best Fit to Measured Spread of Plasticity (Best Fit Lpr)

$$k = 0.2(f_u/f_y - 1) \leq 0.08 \quad \text{from Priestley, Calvi, and Kowalsky (2007)}$$

Tensile Hinge Length Based
on Total Spread of Plasticity
Including Tension Shift
$$Lpr_t = 2kL + 0.75D$$

L

$Lpr_{tension}$

L_{sp}

$\phi'_y \dfrac{M}{M'_y}$

ϕ_p

Compressive Hinge Length
Based only on Moment
Gradient Component
$$Lpr_c = 2kL$$

L

$Lpr_{compression}$

L_{sp}

$\phi'_y \dfrac{M}{M'_y}$

ϕ_p
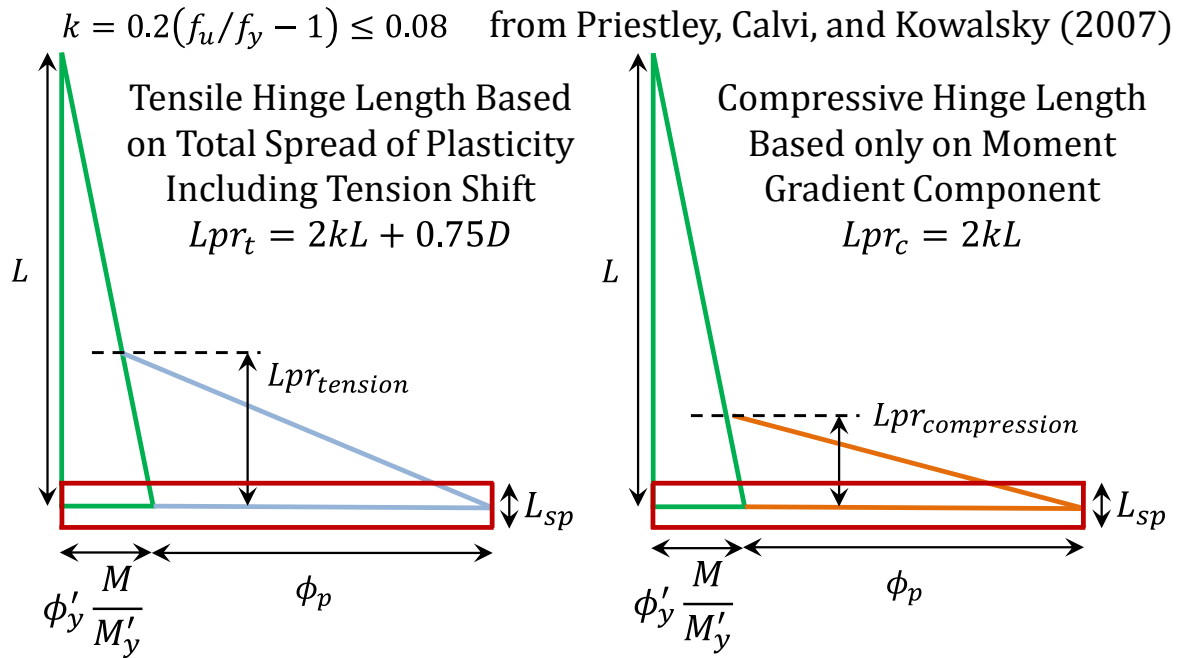
Figure 7.23 Tensile and Compressive Triangular Plastic Hinge Lengths

Since the Lpr_t equation was calibrated based on the uperbound extent of plasticity of each experiment, these regions need to be isolated in order to compare the accuracy of the proposed equation. For example, data points from the three highest curvature ductility values in Test 9, Figure 7.24, are included in the formulation. A comparison of the measured upperbound extent of plasticity and the result of the tensile plastic hinge length expression, Lpr_t Eqn 7.28, appears in Figure 7.25. A sensativity analysis of the proposed Lpr_t equation to individual test variables is shown in Figure 7.26. Of the variables investigated, the Lpr_t expression underpredicts the spread of plasticity for tests Tests 23 and 24 with the highest aspect ratio. However, this was not found to influence the accuracy of tensile strain-displacement predictions for these tests, Figure 7.54 and Figure 7.55.

$$mean\left(\frac{L_{pr}^{meas}}{L_{pr_t}^{eqn}}\right) = 0.98, COV = 0.069$$

Statistics for Tensile Triangular
Plastic Hinge Length

A strain-dispalcement comparison for Test 9 appears in Figure 7.29 for the Priestley, Calvi, and Kowalsky (2007) Lp method integrated into CUMBIA and the proposed Modified Lpr method.   Both the tensile and the compressive strain-displacement predictions are improved with proposed method.   The degree of improvement for the compressive strain-displacement relationship becomes more apparent when evaluating the dataset as a whole.   A test by test comparison of the strain-dispalcement relationship prediction appears in Figure 7.40 through Figure 7.61.   There are still many instances where the measured compressive strains significantly exceed the prediction in regions of the column with inelastic transverse steel.   The strain-displacement prediction for column Test 9 using the triangular distribution of curvature from Lpr_t is compared to the rectangular-based Lp_t in Figure 7.30 and Figure 7.31.   The slight difference in the two methods is attributed to the factor of two approximation used as a conversion between rectangular and triangular equivalent curvature distributions, Figure 7.17.

The purpose of an equivalent curvature distribution is to translate a known moment-curvature relationship into the backbone curve of a member force-deformation response.   The question remains, which hinge length, tension or compression, offers a better member response prediction.   For column Test 9, Figure 7.27 and Figure 7.28 plot the force-deformation response predicted with Lp from Priestley, Calvi, and Kowalsky (2007) integrated into CUMBIA, and the response from either Lpr_c or Lpr_t.   Of the two proposed methods, the compressive hinge length provides a more accurate force-displacement prediction since the analysis was terminated at 140% of the Mander ultimate concrete compression strain for the confined core, which can only be assessed with Lpr_c. The elastic range of response closely resembles that of the current method.
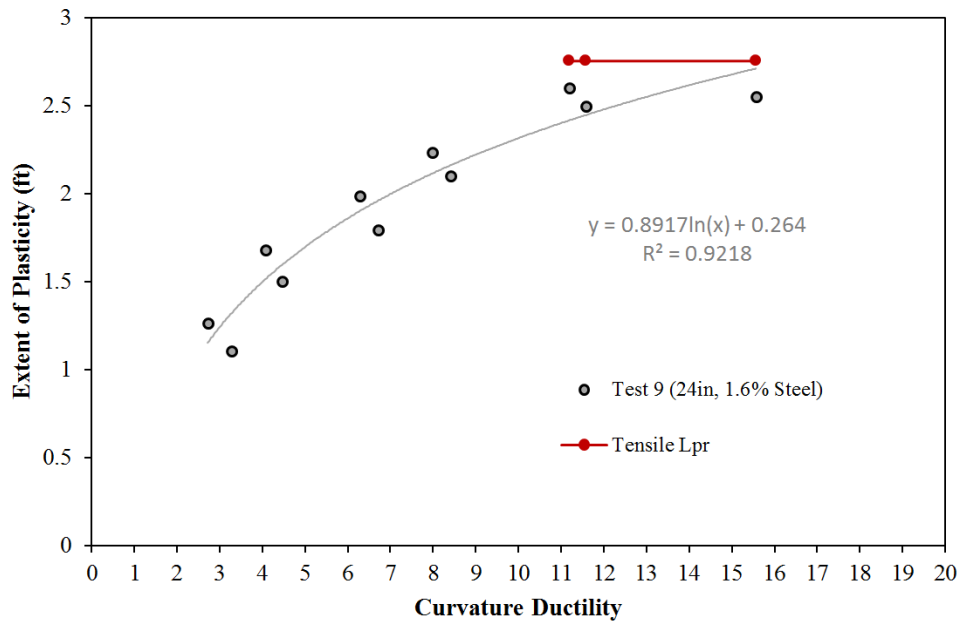
Figure 7.24 Isolated Upper Bound Lpr used in Sensitivity Analysis for Eqn 7.28
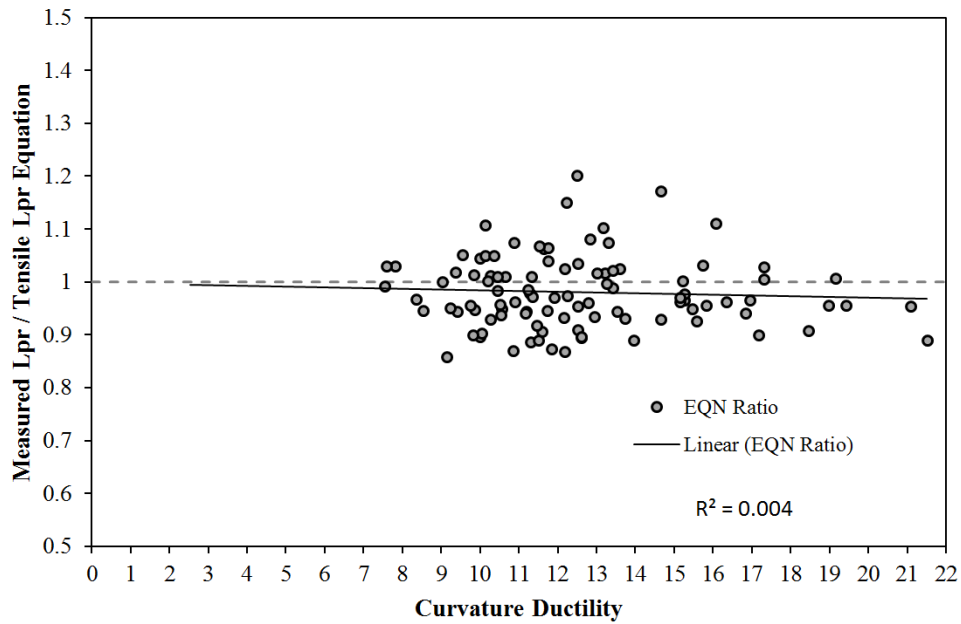
Figure 7.25 Comparison of Tensile Lpr Equation and Measured Extent of Plasticity
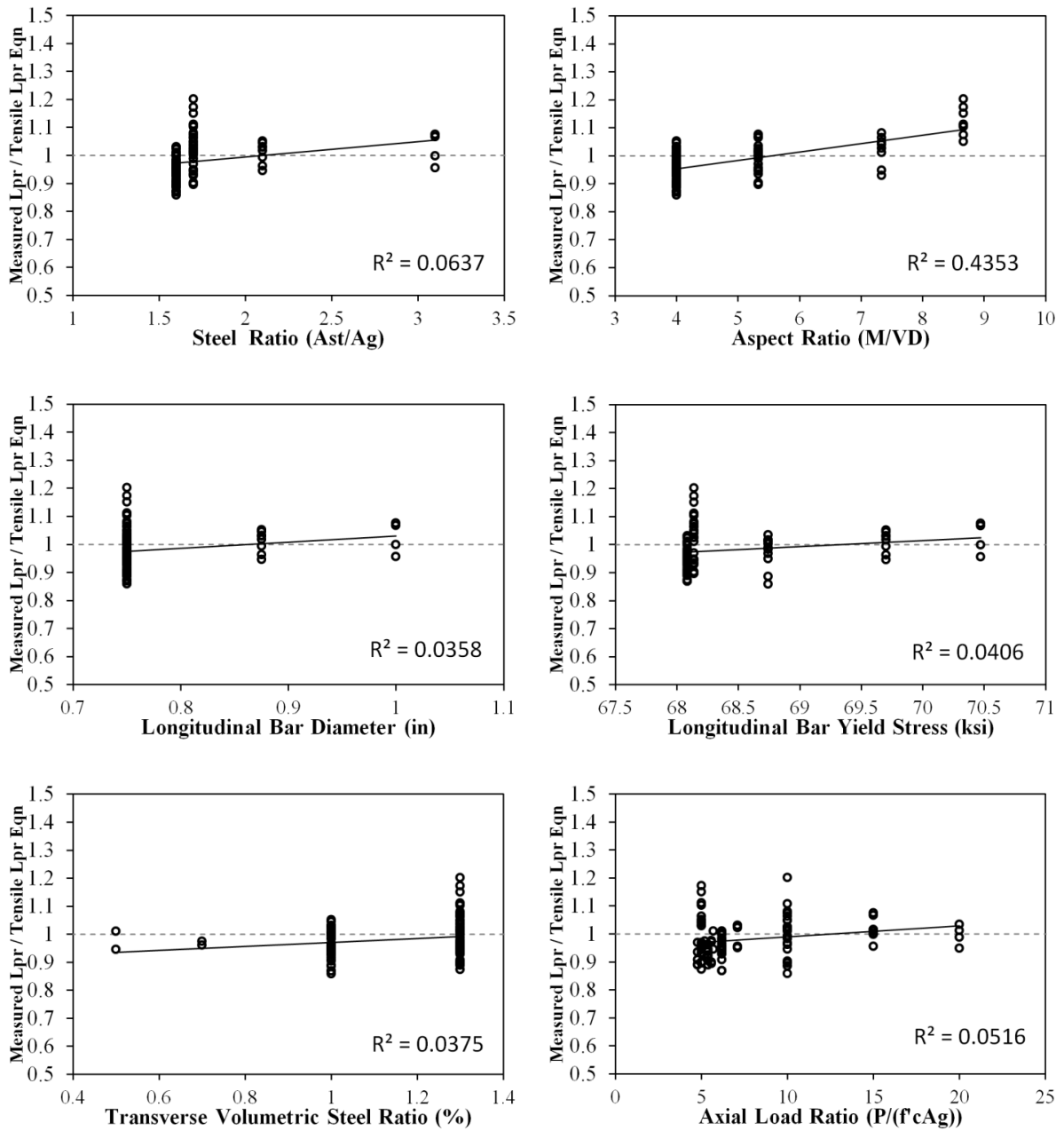
Figure 7.26 Sensitivity of Tensile Lpr Equation to Individual Variables
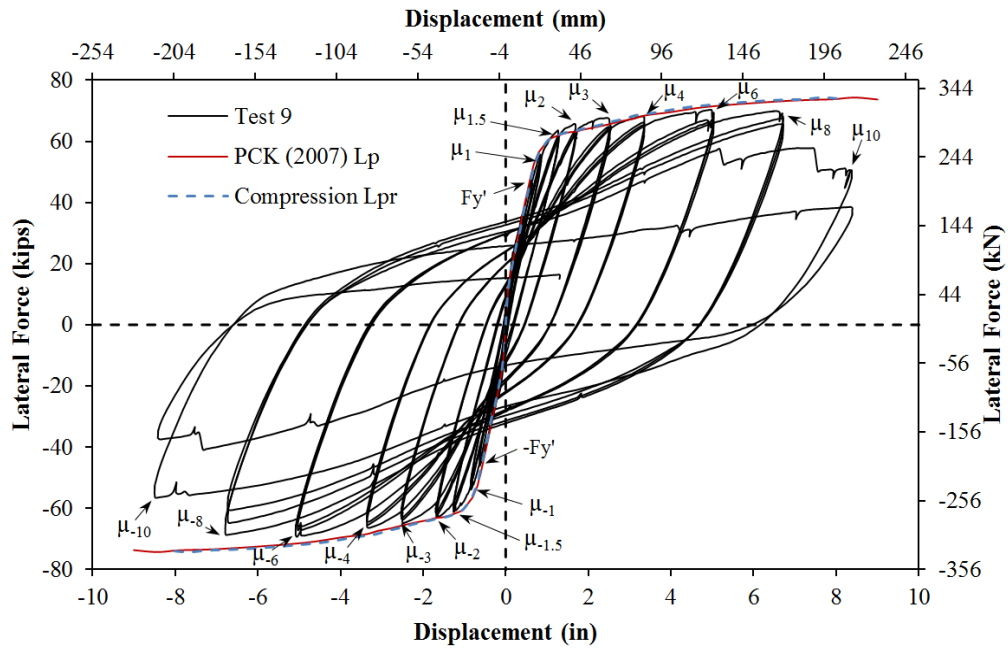
Figure 7.27 Hysteretic Response for Test 9 with Compressive Lpr and PCK (2007) Lp
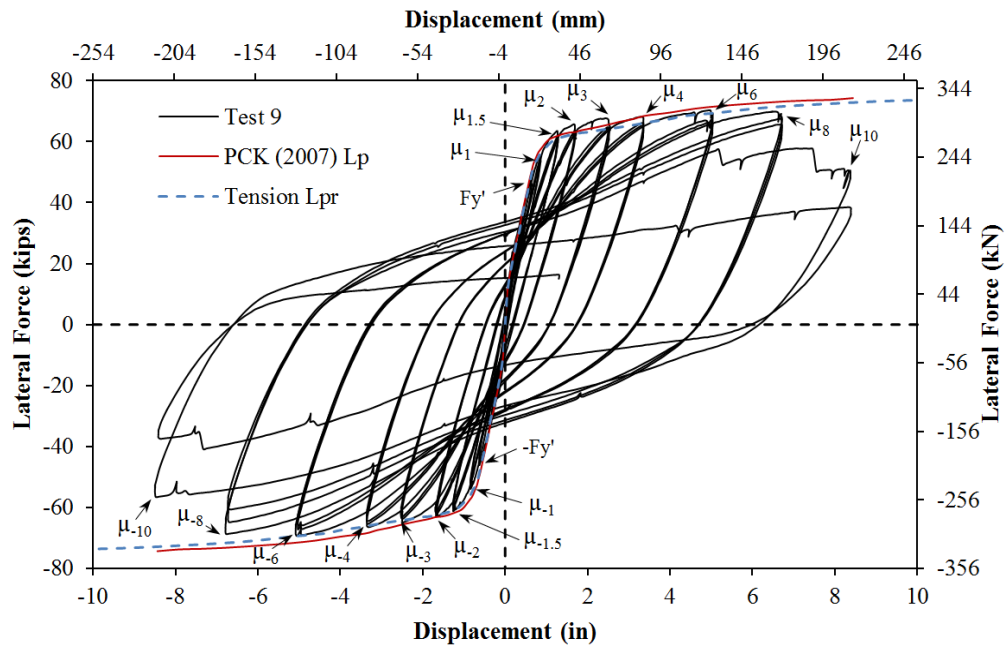
Figure 7.28 Hysteretic Response for Test 9 with Tensile Lpr and PCK (2007) Lp
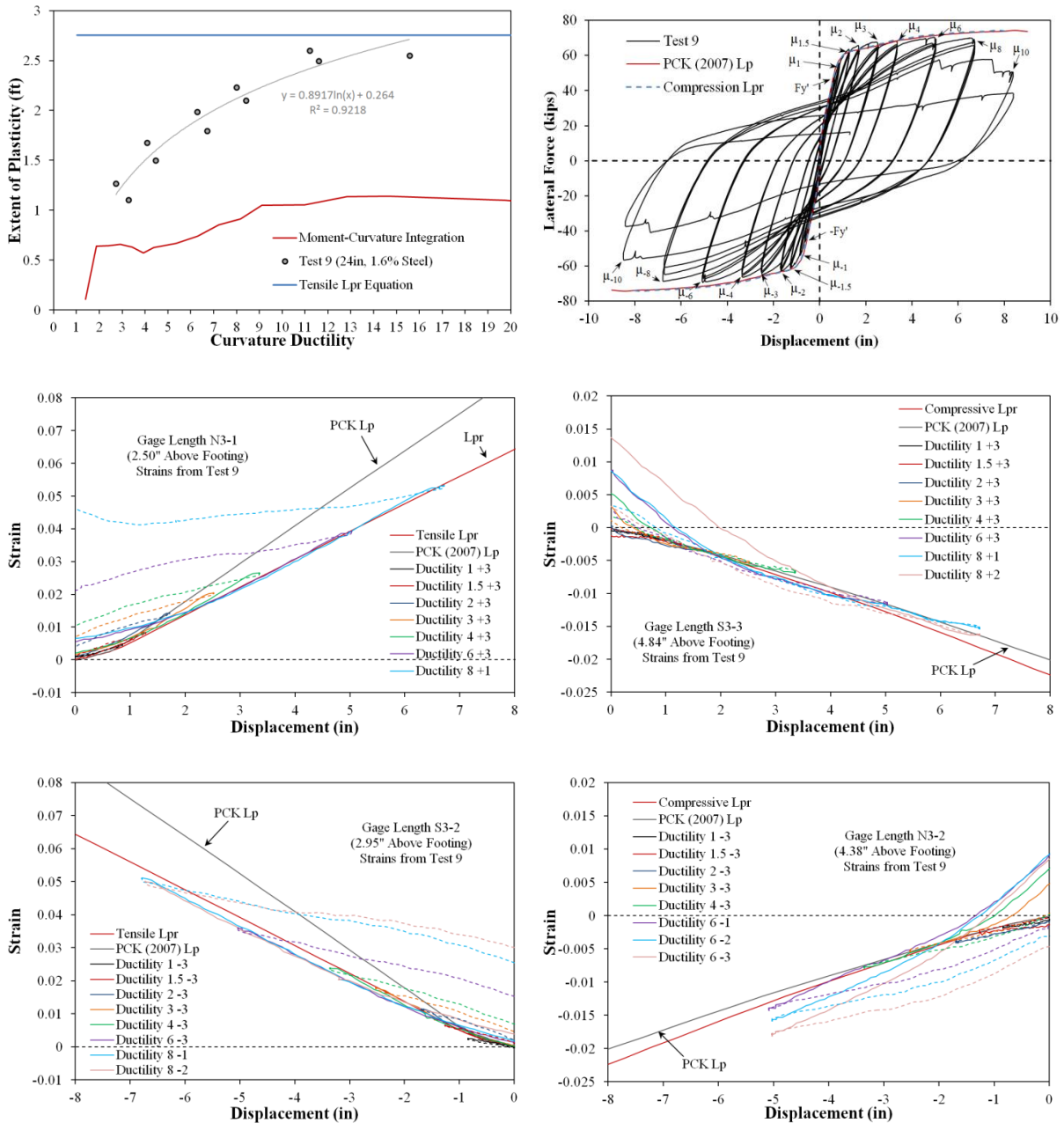
Figure 7.29 Spread of Plasticity and Strain-Displacement Relationship for Test 9 with Modified Lpr Hinge Method
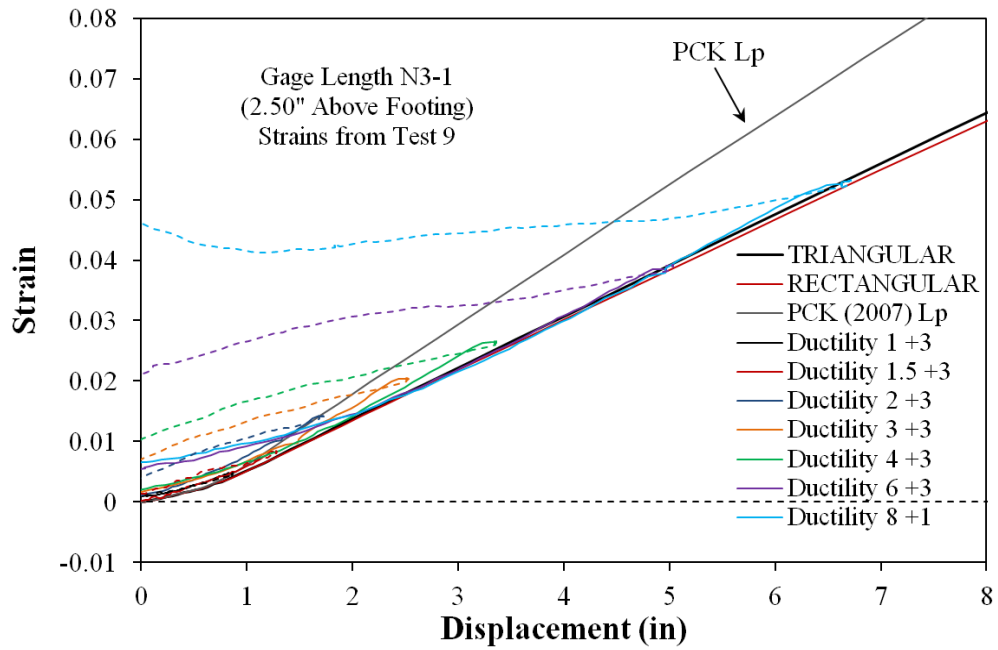
Figure 7.30 Prediction using Triangular and Rectangular Tensile Hinge Lengths
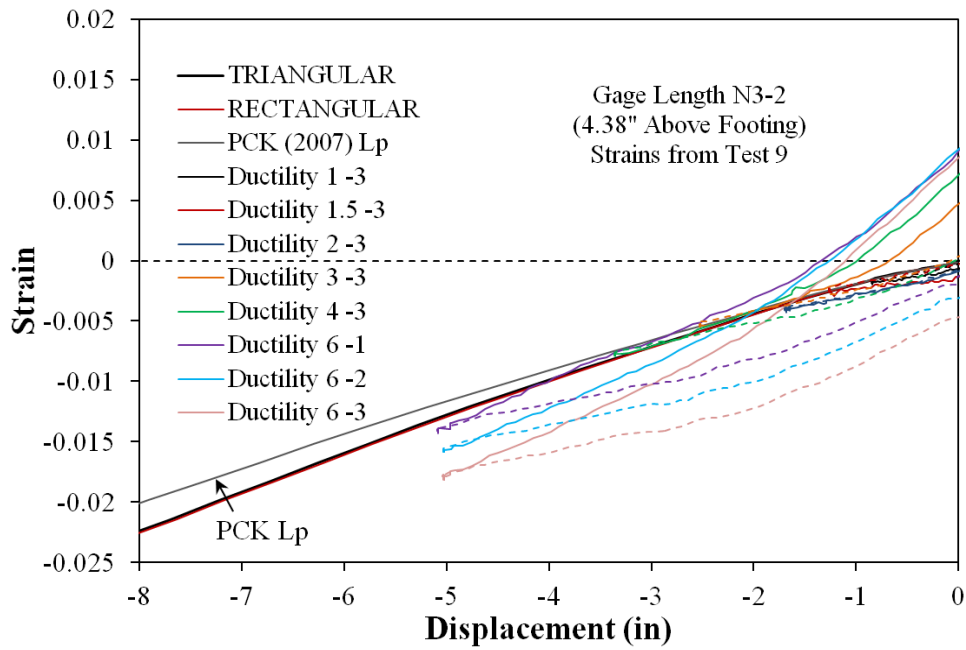
Figure 7.31 Prediction using Triangular and Rectangular Tensile Hinge Lengths

7.4   Tensile Strain-Displacement Predictions using the Modified Plastic Hinge Method

Tensile strain-displacement predictions using Modified Plastic Hinge Model are based on the upper bound measured extent of plasticity of bridge column tests. A comparison of the accuracy of the Modified vs. the current Plastic Hinge Method from Priestley, Calvi, and Kowalsky (2007), Figure 7.1, is made utilizing the measured peak tensile strains prior to bar buckling and their associated top-column displacements. As shown in the statistics below, both equivalent curvature distributions yield conservative predictions for the tensile strain-displacement relationship, however, the modified plastic hinge method shows significant improvement. The tensile triangular plastic hinge length, Eqn 7.28, was formulated using the upper bound measured spread of plasticity. Near the footing, tensile strains only gradually reduce with increases in height. The linear shape of the plastic curvature profile near the footing is attributed to larger compressive strains near the footing-column interface. The distribution of tensile strains is influenced by the tension shift effect, which may decrease the amplitude of tensile strains at the footing-column interface and instead increase tensile strain magnitudes above the base section following the inclined flexural-shear crack distribution.

* Mean, Coefficient of Variation, and Root Mean Squared Error

$$mean\left(\frac{\Delta^{bb}_{Meausred}\ at\ \varepsilon s^{bb}_{Meausred}}{\Delta_{Cumbia}\ at\ \varepsilon s^{bb}_{Meausred}\ with\ Lpr_t\ EQN}\right) = 1.12, COV = 0.061, RMSE = 0.121$$

$$mean\left(\frac{\Delta^{bb}_{Meausred}\ at\ \varepsilon s^{bb}_{Meausred}}{\Delta_{Cumbia}\ at\ \varepsilon s^{bb}_{Meausred}\ with\ Lp\ EQN\ (PCK\ 2007)}\right) = 1.27, COV = 0.116, RMSE = 0.222$$

Alternatively, this tensile predictive capacity of the hinge models can be compared using cumulative probability distributions, Figure 7.32. Each observation of measured/predicted bar buckling displacement is given a probability of 1/n, where n is the total number of observations. These individual observations are sorted in ascending order. The first observation, with the lowest ratio of measured/equation value has a probability of 1/n, while the second has a probability of 2/n, until the final observation has a probability of 1. A near vertical line at a measured/predicted ratio of one would denote an accurate prediction with low variability. Both hinge methods produce cumulative probability distributions to the right of one with conservative predictions for the bar buckling displacement which were lower than those experienced in the tests. The cumulative probability distributions and the comparison of the Root Mean Squared Error for the two equivalent curvature distributions show that the Modified Lpr hinge method is more accurate for tensile strain-displacement predictions. A sensitivity analysis for the Tensile Lpr bar buckling strain-displacement for individual test variables appears in Figure 7.33.
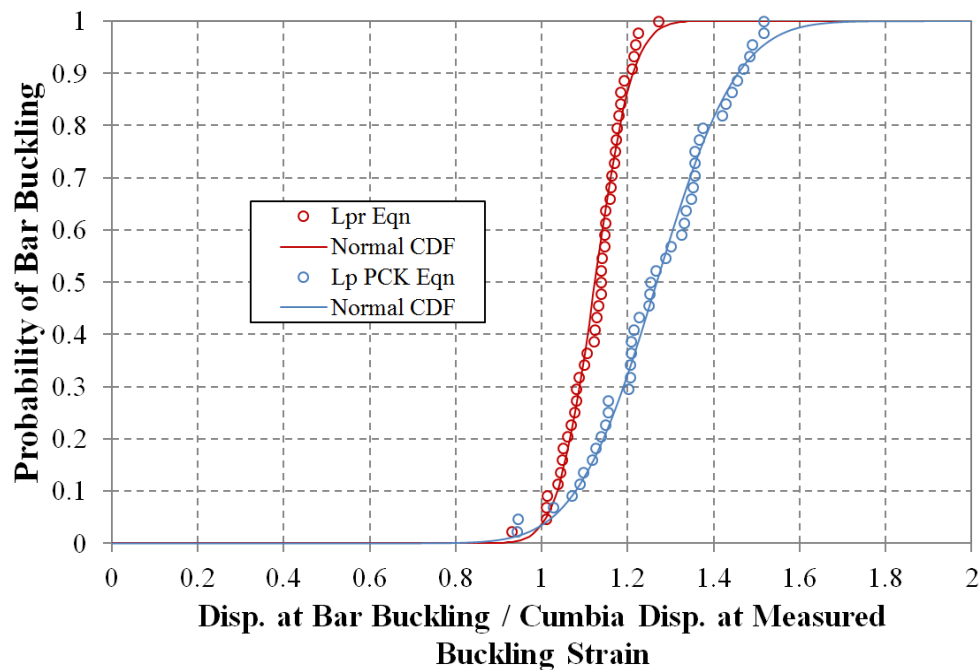
Figure 7.32 Comparison of Plastic Hinge Method Tensile Predictive Capabilities
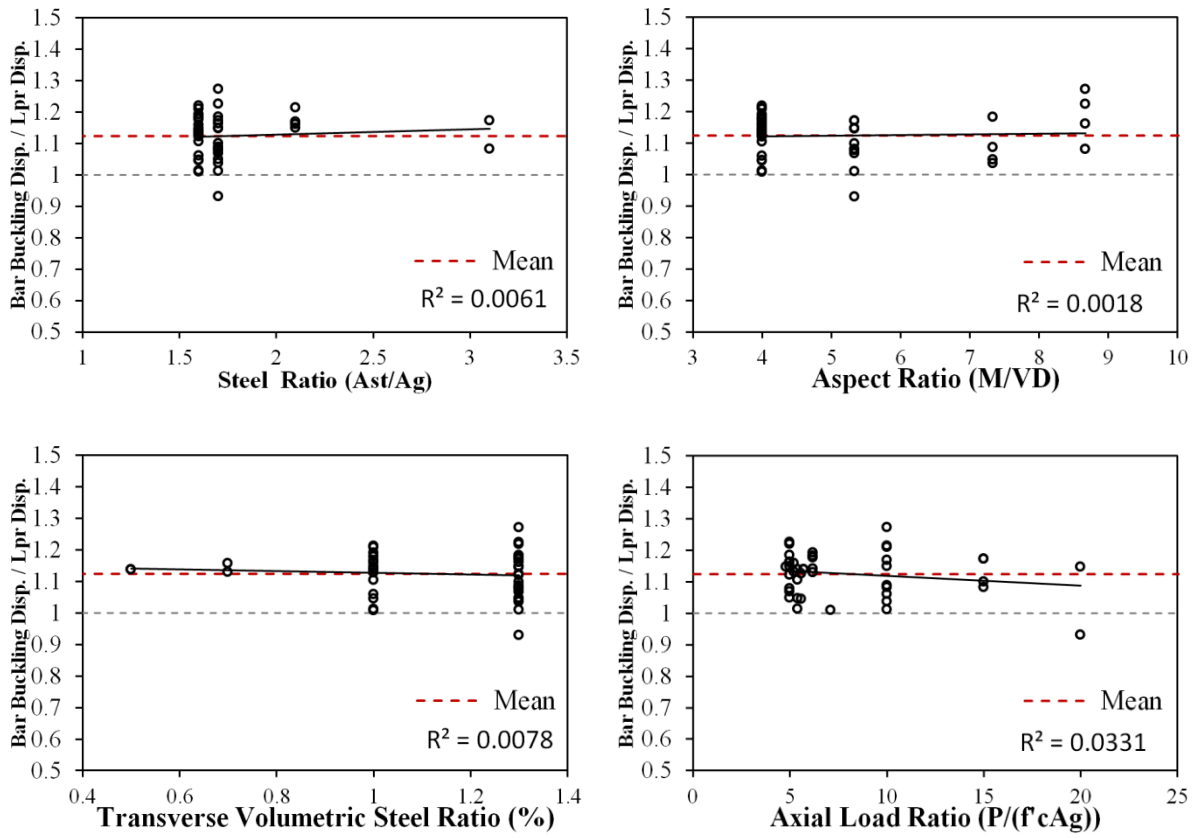
Figure 7.33 Sensitivity of Tensile Lpr Bar Buckling Strain-Displacement Predictions to Individual Variables

7.5   Compressive Strain-Displacement Predictions using the Modified Plastic Hinge Method

Compressive strain-displacement predictions using Modified Plastic Hinge Model are based on only the moment gradient component of the spread of plasticity ($Lpr_c = 2kL$). Comparisons of the accuracy of the Modified vs. the current Plastic Hinge Method from Priestley, Calvi, and Kowalsky (2007), Figure 7.1, were made utilizing the measured compressive strain and displacement at cover concrete crushing and confinement (spiral) steel yielding observations.   Note that these measured compression strains are from instruments applied to the extreme fiber longitudinal bar, which is an approximation to the cover and core concrete strain. Both equivalent curvature distributions yield unconservative predictions for the displacement at cover crushing and spiral yielding, but the Modified Plastic Hinge Method shows improvement.

The cumulative probability distribution describing the accuracy of both hinge models in predicting the column displacement at the measured cover crushing strain appears in Figure 7.34. A sensitivity analysis of the impact of individual variables on the accuracy of the cover crushing strain-displacement prediction is shown in Figure 7.35. The same comparison was repeated in Figure 7.36 and Figure 7.37 for the displacement prediction at the measured compression strain that coincided with the observation of spiral yielding. More accurate compressive strain-displacement predictions were made at the lower cover crushing strain when compared to that of spiral yielding, which may be influenced by more localized compressive behavior. After spiral yielding, significantly larger compressive strains were measured in many tests, as can be seen in the peak compressive strain-displacement relationships of individual tests results, Figure 7.40 through Figure 7.61. The Modified Plastic Hinge Method improved the accuracy of compressive strain-displacement predictions, but it can be argued that the effects of tension shift should reduce the compressive hinge length below that of just the moment gradient component, due to the localization of compressive demands at the pivot point for the fanned diagonal compressive strut pattern.

Mean, Coefficient of Variation, and Root Mean Squared Error

$$mean\left(\frac{\Delta_{Measured} \ at \ \varepsilon s_{Meausred}^{crushing}}{\Delta_{Cumbia} \ at \ \varepsilon s_{Meausred}^{crushing} \ with \ Lpr_c \ EQN}\right) = 0.93, COV = 0.105, RMSE = 0.145$$

$$mean\left(\frac{\Delta_{Measured} \ at \ \varepsilon s_{Meausred}^{crushing}}{\Delta_{Cumbia} \ at \ \varepsilon s_{Meausred}^{crushing} \ with \ Lp \ EQN \ (PCK \ 2007)}\right) = 0.80, COV = 0.152, RMSE = 0.340$$
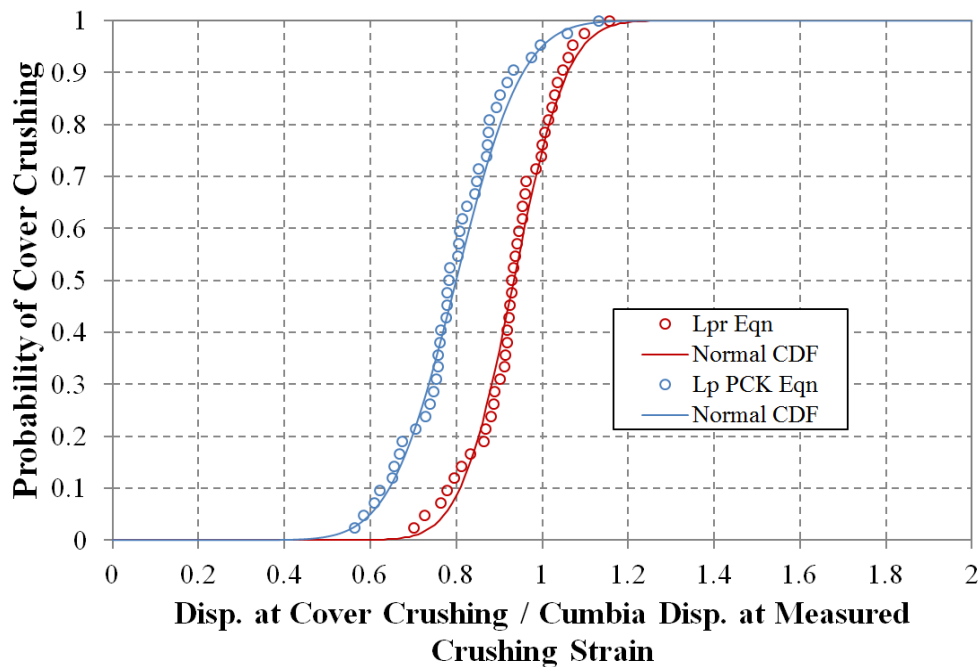
Figure 7.34 Comparison of Plastic Hinge Method Compressive Predictive Capabilities at Cover Crushing Observations
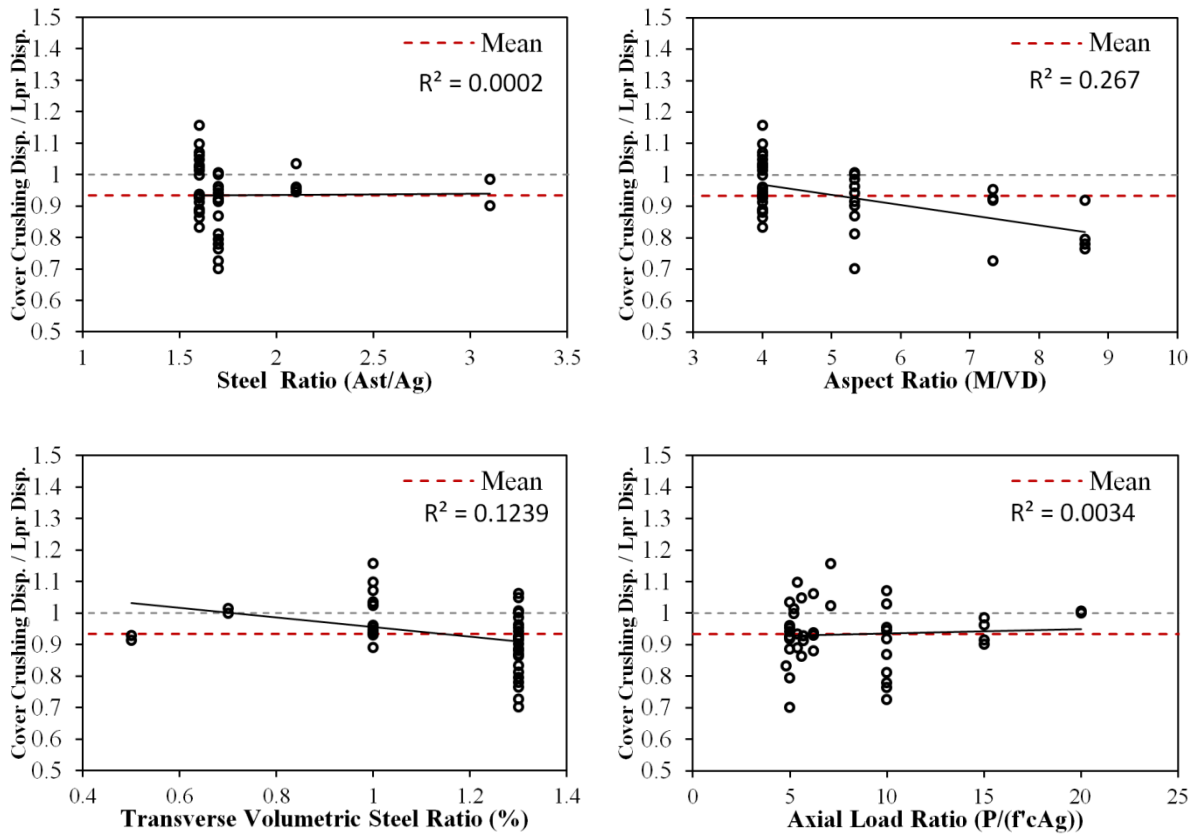
Figure 7.35 Sensitivity of Compressive Lpr Cover Crushing Strain-Displacement Predictions to Individual Variables

Mean, Coefficient of Variation, and Root Mean Squared Error

$$mean\left(\frac{\Delta_{Measured}\ at\ \varepsilon s_{Meausred}^{spiral\ yield}}{\Delta_{Cumbia}\ at\ \varepsilon s_{Meausred}^{spiral\ yield}\ with\ Lpr_c\ EQN}\right) = 0.88, COV = 0.192, RMSE = 0.266$$

$$mean\left(\frac{\Delta_{Measured}\ at\ \varepsilon s_{Meausred}^{spiral\ yield}}{\Delta_{Cumbia}\ at\ \varepsilon s_{Meausred}^{spiral\ yield}\ with\ Lp\ EQN\ (PCK\ 2007)}\right) = 0.71, COV = 0.221, RMSE = 0.529$$
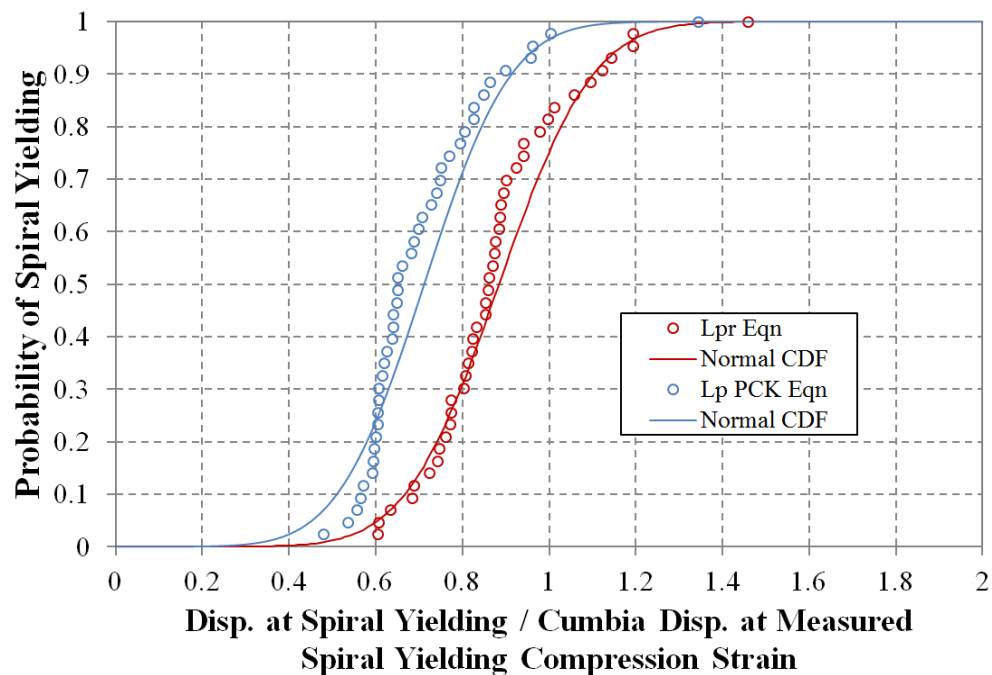
Figure 7.36 Comparison of Plastic Hinge Method Compressive Predictive Capabilities at Spiral Yielding Observations
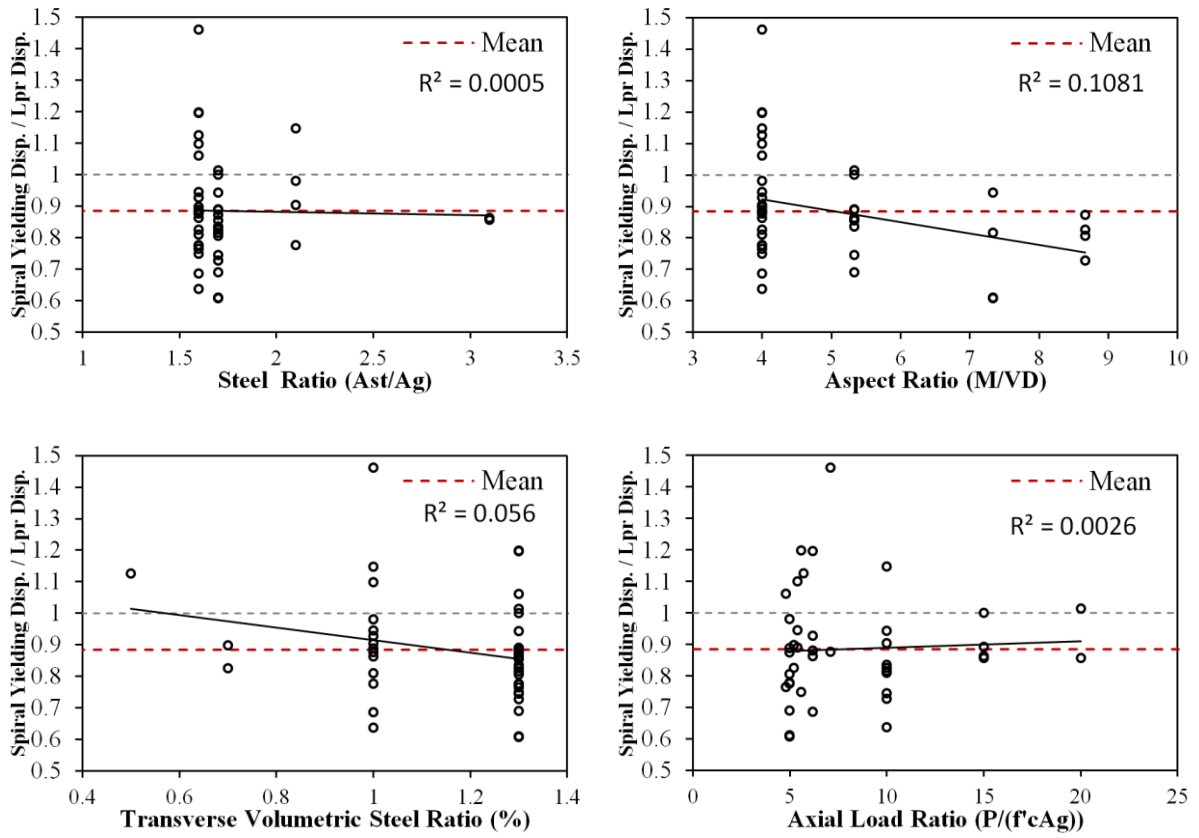
Figure 7.37 Sensitivity of Compressive Lpr Spiral Yielding Strain-Displacement Predictions to Individual Variables

7.6   Elastic Force-Deformation Predictions using the Modified Plastic Hinge Method

The equivalent curvature distributions prior to first yield of longitudinal reinforcement for the Priestley, Calvi, and Kowalsky (2007) and the Modified Plastic Hinge Methods closely resemble one another, Figure 7.1 and Figure 7.2. Separate equivalent curvature distributions are used for elastic column flexure and base rotations attributable to strain penetration in the Modified Plastic Hinge Method. These two deformation components are combined into a single equivalent curvature distribution in the PCK (2007) method through the use of an effective column length which extends into adjoining members by a depth equal to the strain penetration length.

A comparison of the accuracy of the Modified vs. the current Plastic Hinge Method from Priestley, Calvi, and Kowalsky (2007), Figure 7.1, is made utilizing the measured top column displacement at the analytically predicted first yield force for longitudinal reinforcement. Both methods yield conservative predictions for the column displacement at the analytical first yield force. The cumulative probability distributions for both equivalent curvature profiles appear in Figure 7.38, and a sensitivity analysis for results of the Modified Plastic Hinge Method is shown in Figure 7.39.

Mean, Coefficient of Variation, and Root Mean Squared Error

$$mean\left(\frac{\Delta_{Meausred}^{first\ yield}\ at\ F_y'}{\Delta_{Cumbia}\ at\ F_y'\ with\ Lpr_t\ EQN}\right) = 1.09, COV = 0.058, RMSE = 0.404$$

$$mean\left(\frac{\Delta_{Meausred}^{first\ yield}\ at\ F_y'}{\Delta_{Cumbia}\ at\ F_y'\ with\ Lp\ EQN\ (PCK\ 2007)}\right) = 1.07, COV = 0.059, RMSE = 0.332$$
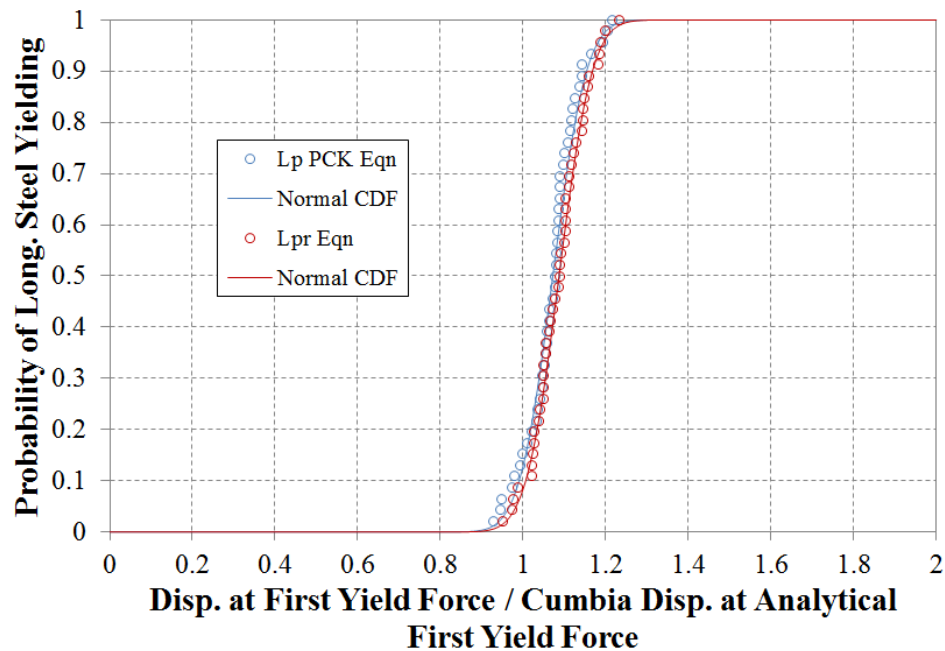
Figure 7.38 Comparison of Plastic Hinge Method Predictive Capabilities at Analytical First Yield Force
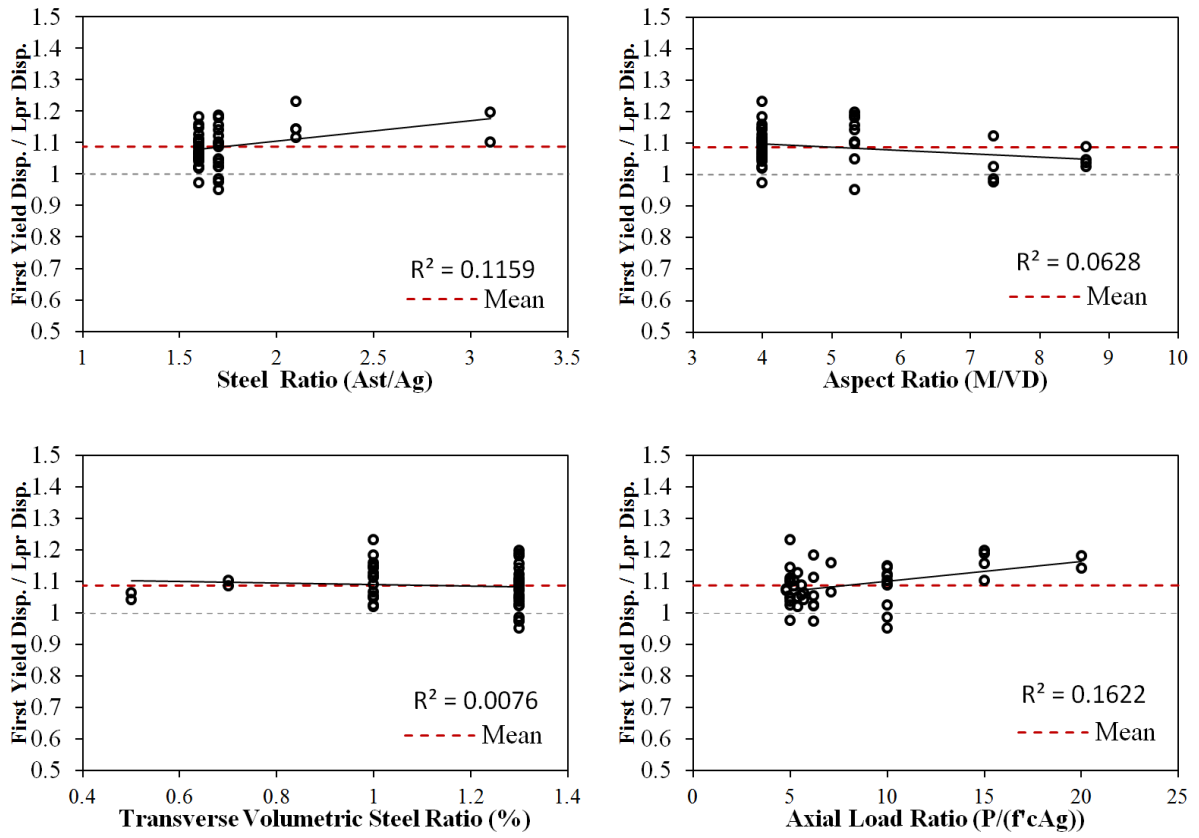
Figure 7.39 Sensitivity of Modified Hinge Method Displacement at Analytical First Yield Force Predictions to Individual Variables

7.7 Conclusion

In design, concrete compressive and steel tensile strain limits are related to column deformations through the use of an equivalent curvature distribution. An experimental study was carried out to assess the performance of thirty circular, well-confined, bridge columns with varying lateral displacement history, transverse reinforcement detailing, axial load, aspect ratio, and longitudinal steel content. Material strains, cross section curvatures, and fixed-end rotations due to strain penetration of reinforcement into the adjoining member were quantified through the use of a 3D position monitoring system. This data was used to formulate a new equivalent curvature distribution aimed at improving tensile and compressive strain-displacement predictions.

The key aspects of the proposed Modified Plastic Hinge Model which differentiate it from the current method recommended in Priestley, Calvi, and Kowalsky (2007) include: (1) a decoupling of column flexure and strain penetration deformation components, (2) a linear plastic curvature distribution which emulates the measured curvature profiles, and (3) separate plastic hinge lengths for tensile and compressive strain-displacement predictions. In the experiments, the measured extent of plasticity was found to increase due to the combined effects of moment gradient and tension shift. The proposed tension hinge length, Lpr_t Eqn 7.28, was calibrated to match the upper bound of the measured spread of palsticity in each test. The proposed compressive hinge length, Lpr_c Eqn 7.29, only contains a term related to the moment gradient effect. Expressions for the elastic and plastic column flexural displacement for both single and double bending were derived. Expressions which describe the additional column deformation due to strain penetration of reinforcement into the adjoining member were formulated based on the measured fixed-end rotations. When compared to the current plastic hinge method recommended in Priestley, Calvi, and Kowalsky (2007), the proposed Modified Plastic Hinge method improved the tensile and compressive-strain displacement predictions while maintaining similar levels of accuracy for elastic displacements.
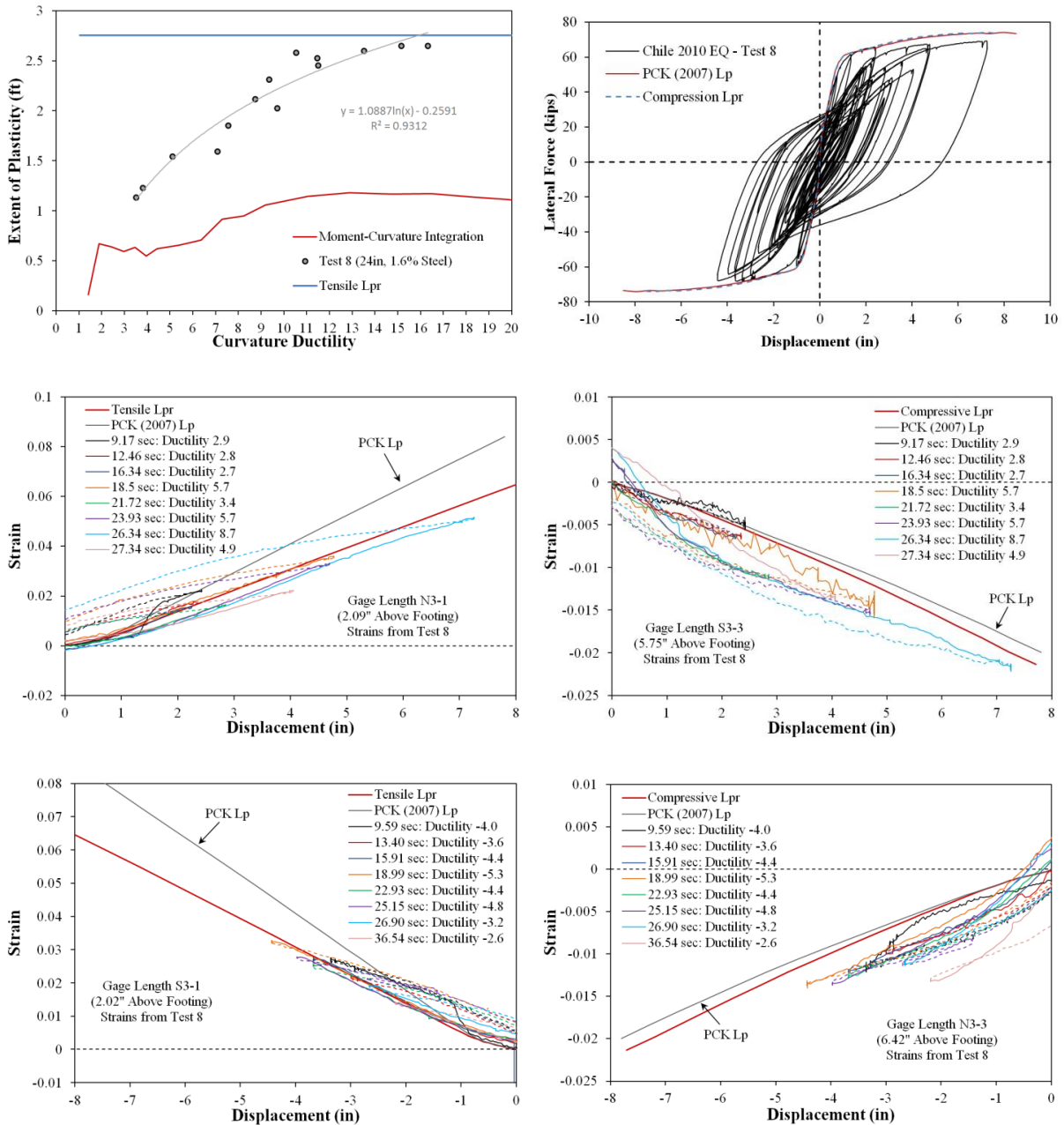
Figure 7.40 Spread of Plasticity and Strain-Displacement Relationship for Earthquake Load History Test 8
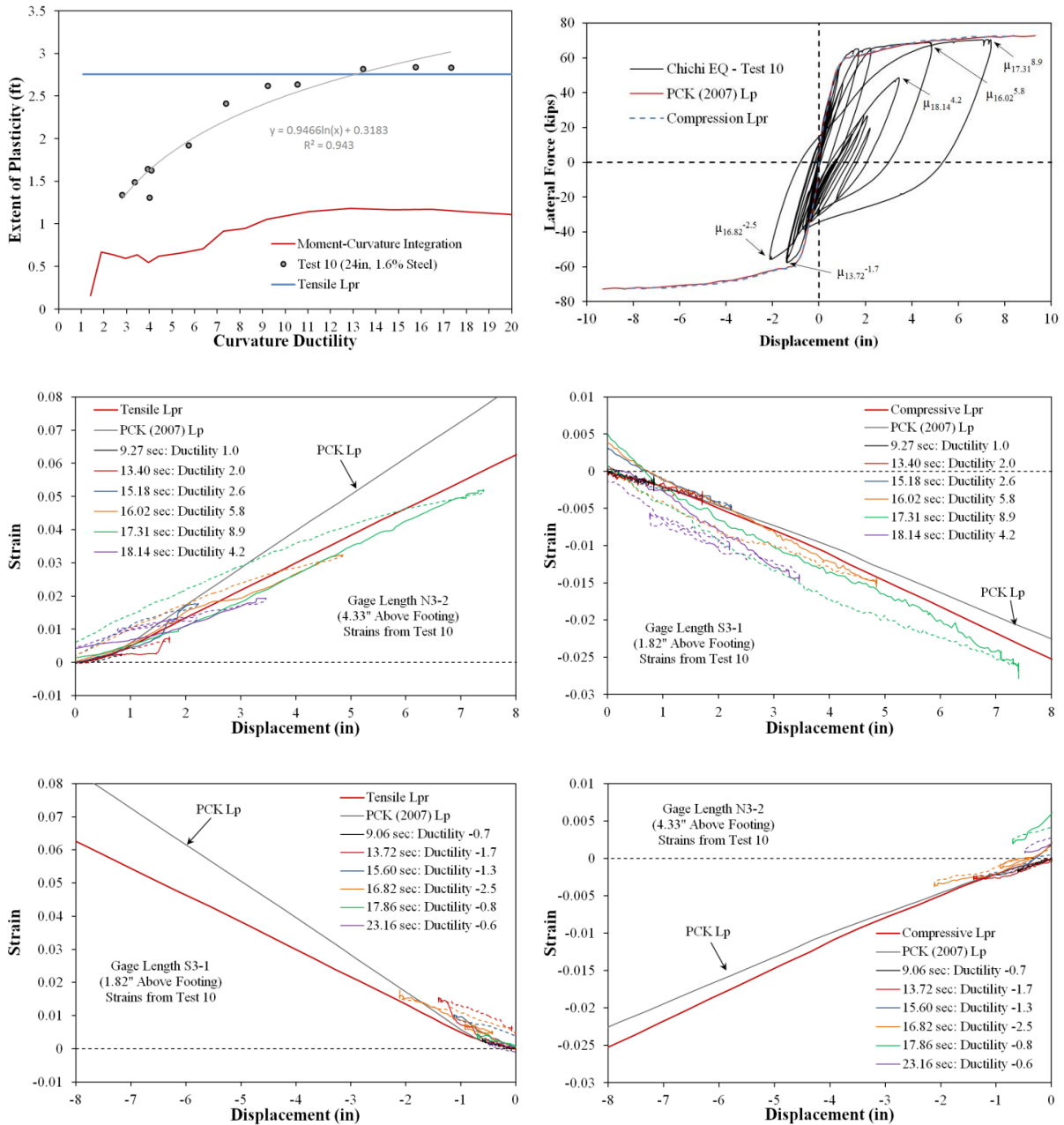
Figure 7.41 Spread of Plasticity and Strain-Displacement Relationship for Earthquake Load History Test 10
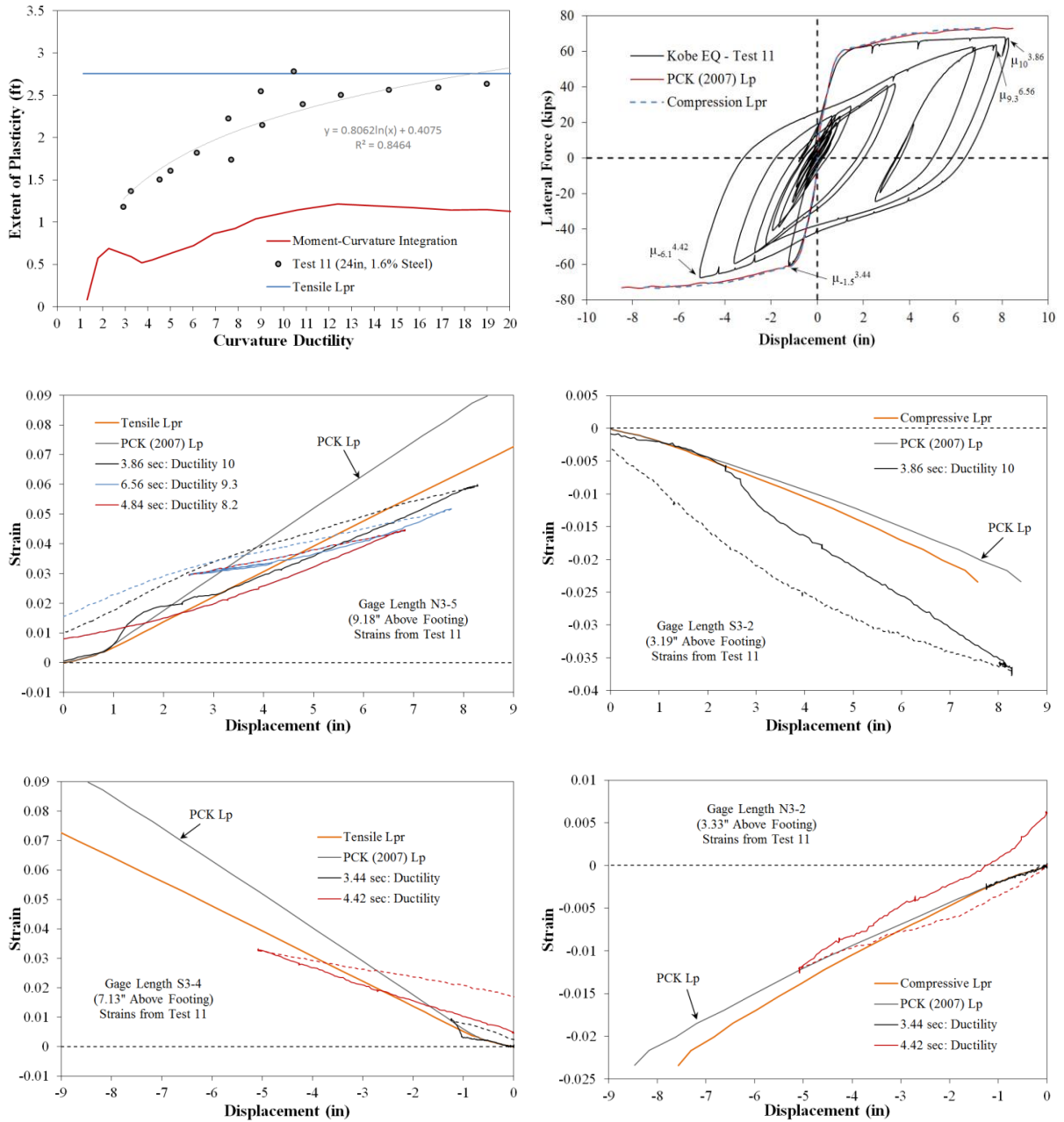
Figure 7.42 Spread of Plasticity and Strain-Displacement Relationship for Earthquake Load History Test 11
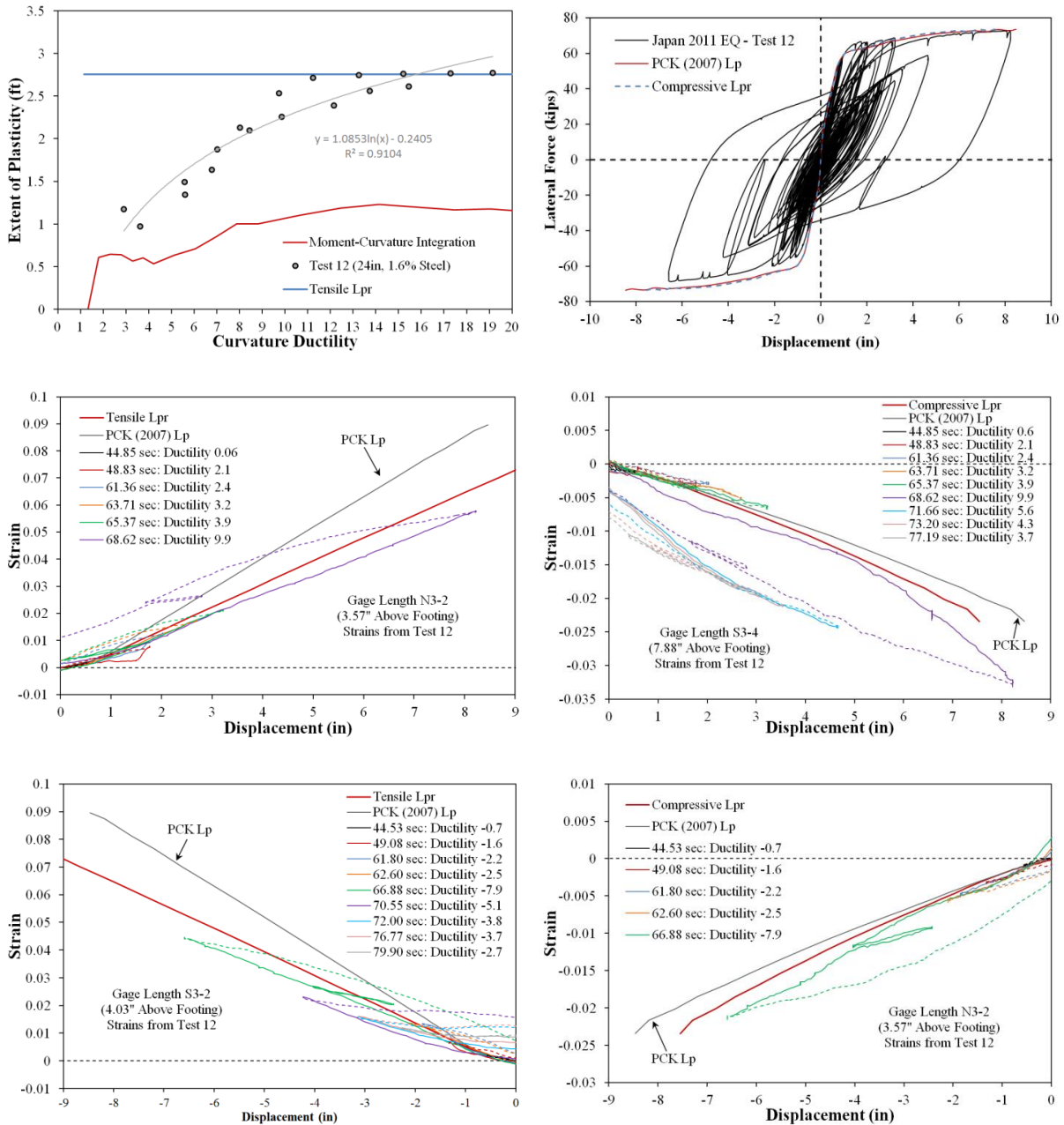
Figure 7.43 Spread of Plasticity and Strain-Displacement Relationship for Earthquake Load History Test 12
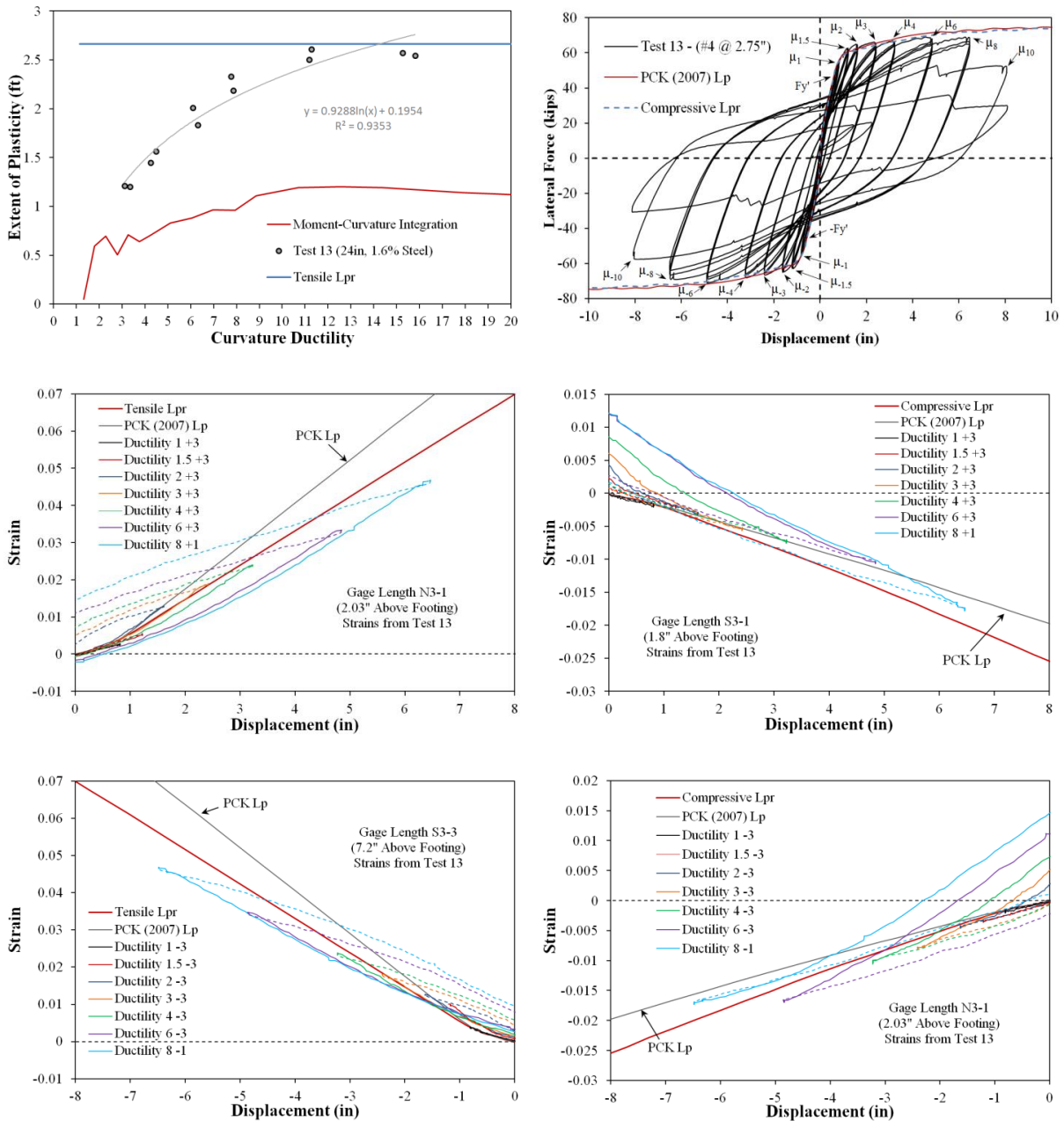
Figure 7.44 Spread of Plasticity and Strain-Displacement Relationship for Test 13
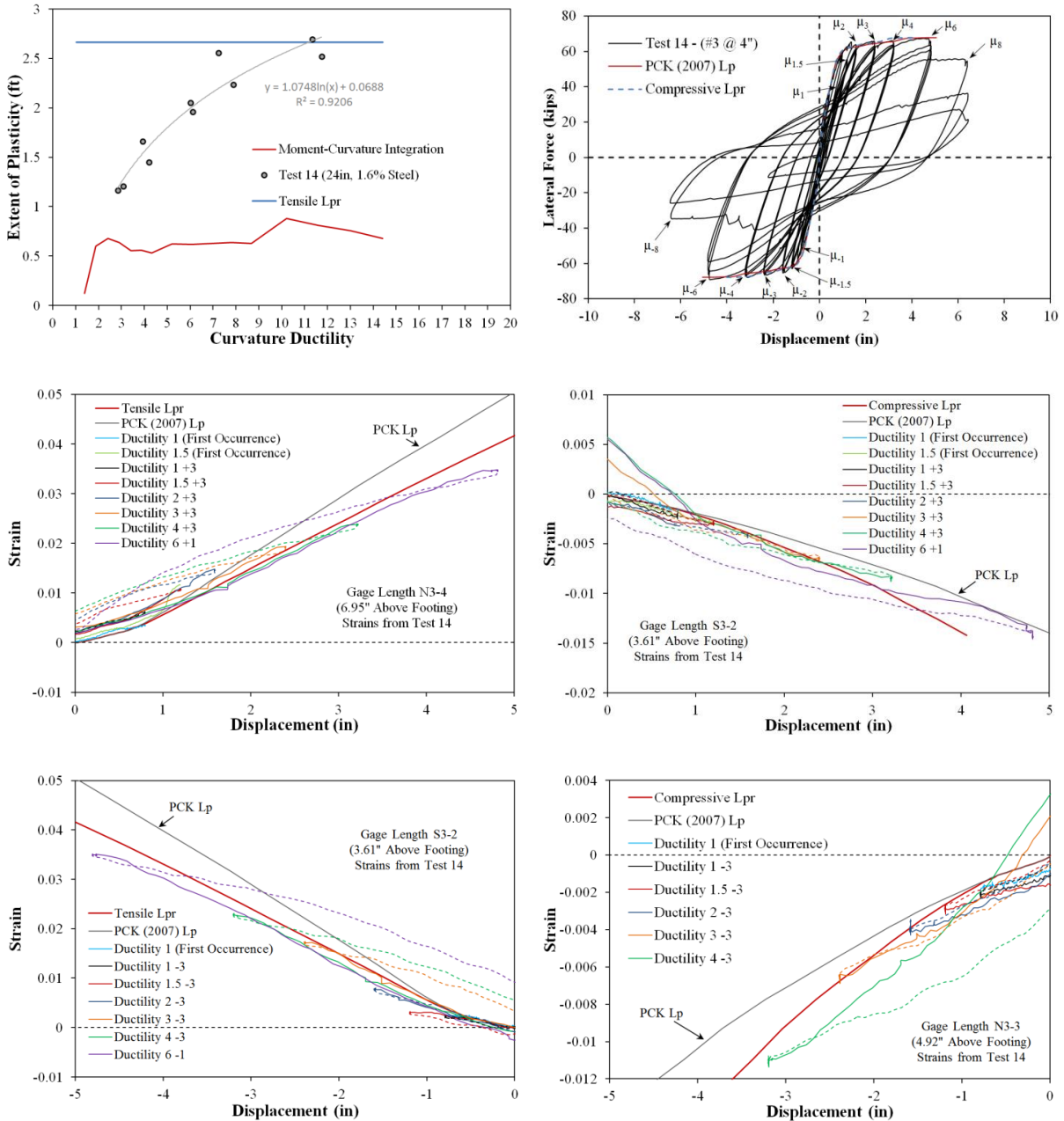
Figure 7.45 Spread of Plasticity and Strain-Displacement Relationship for Test 14
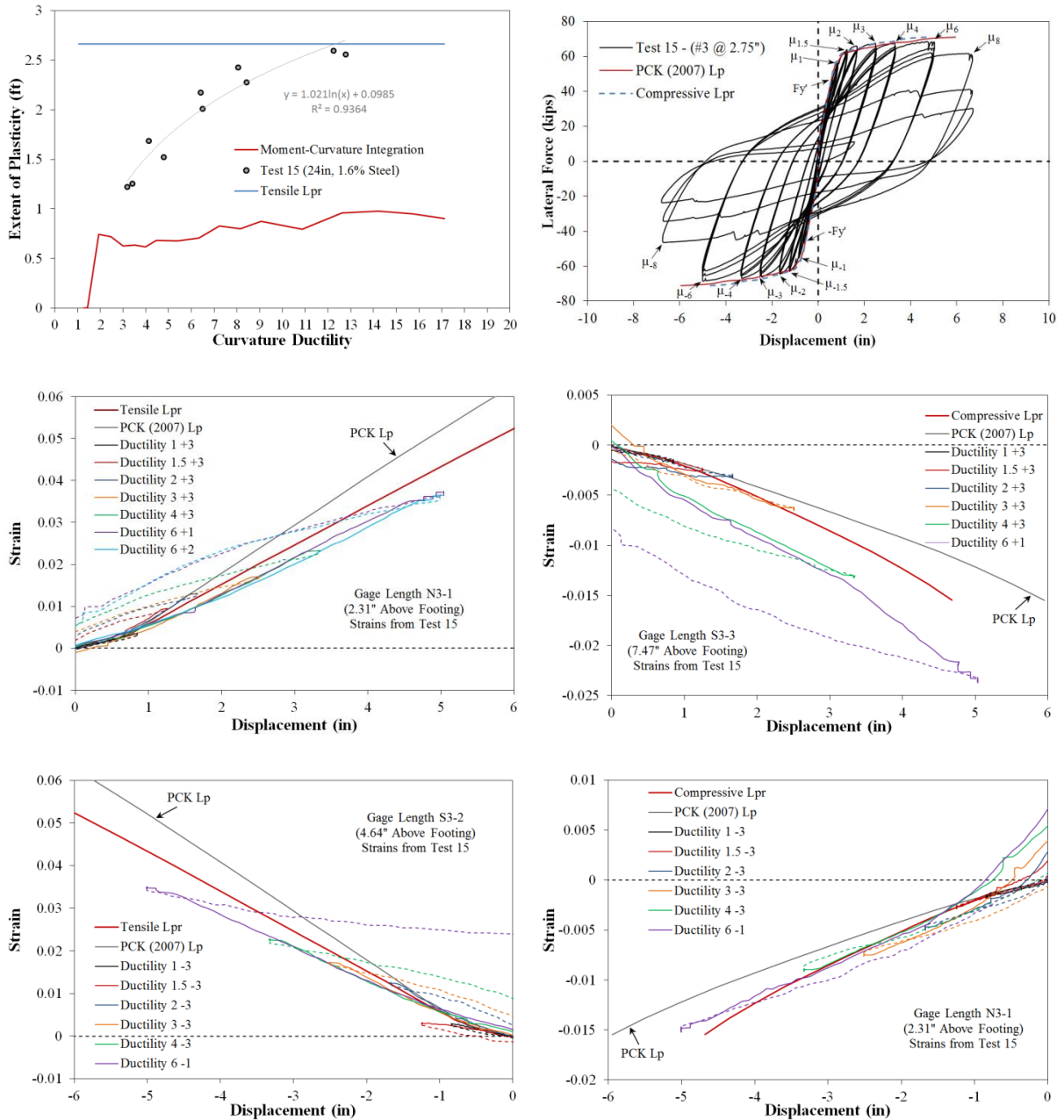
Figure 7.46 Spread of Plasticity and Strain-Displacement Relationship for Test 15
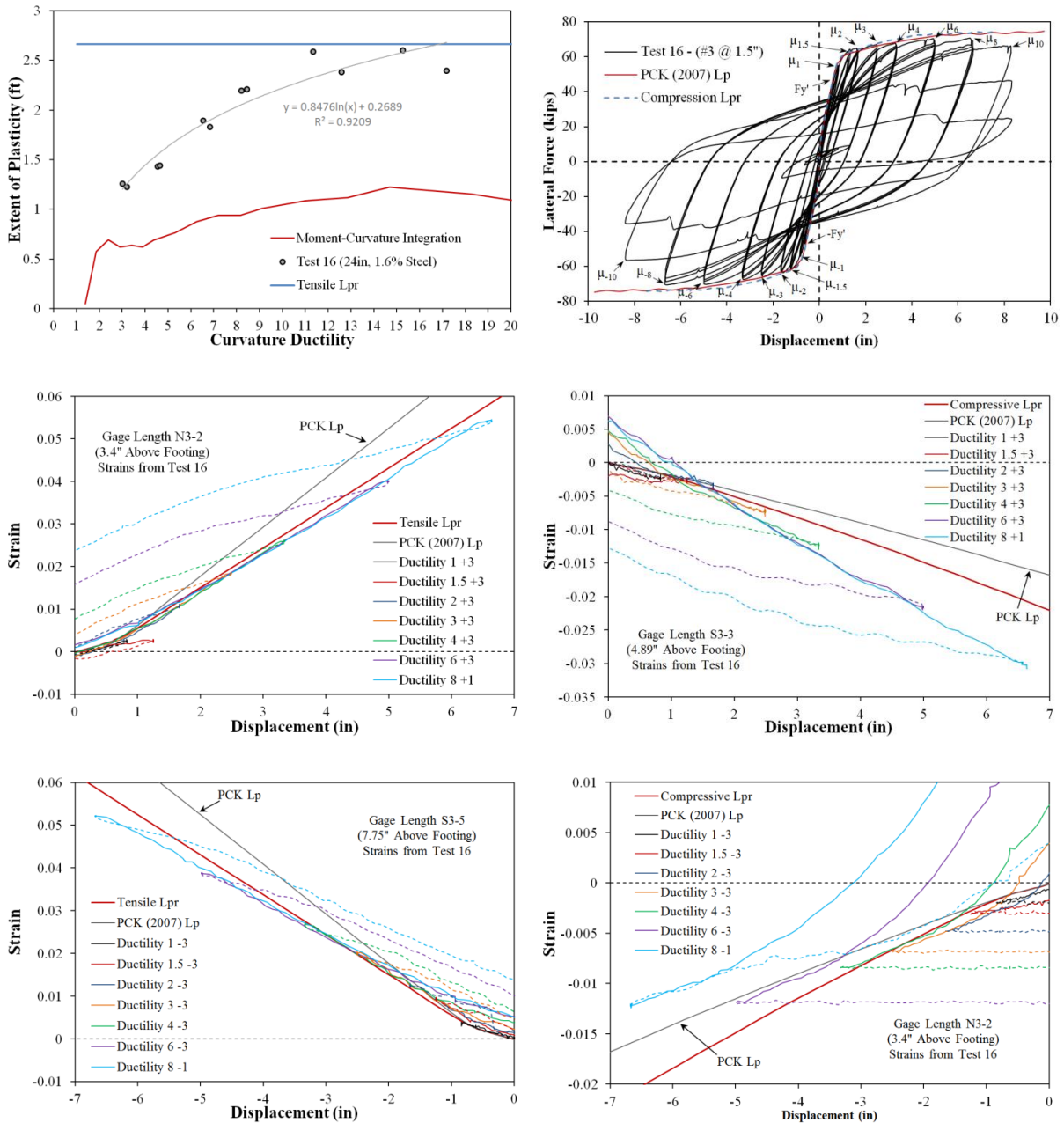
Figure 7.47 Spread of Plasticity and Strain-Displacement Relationship for Test 16
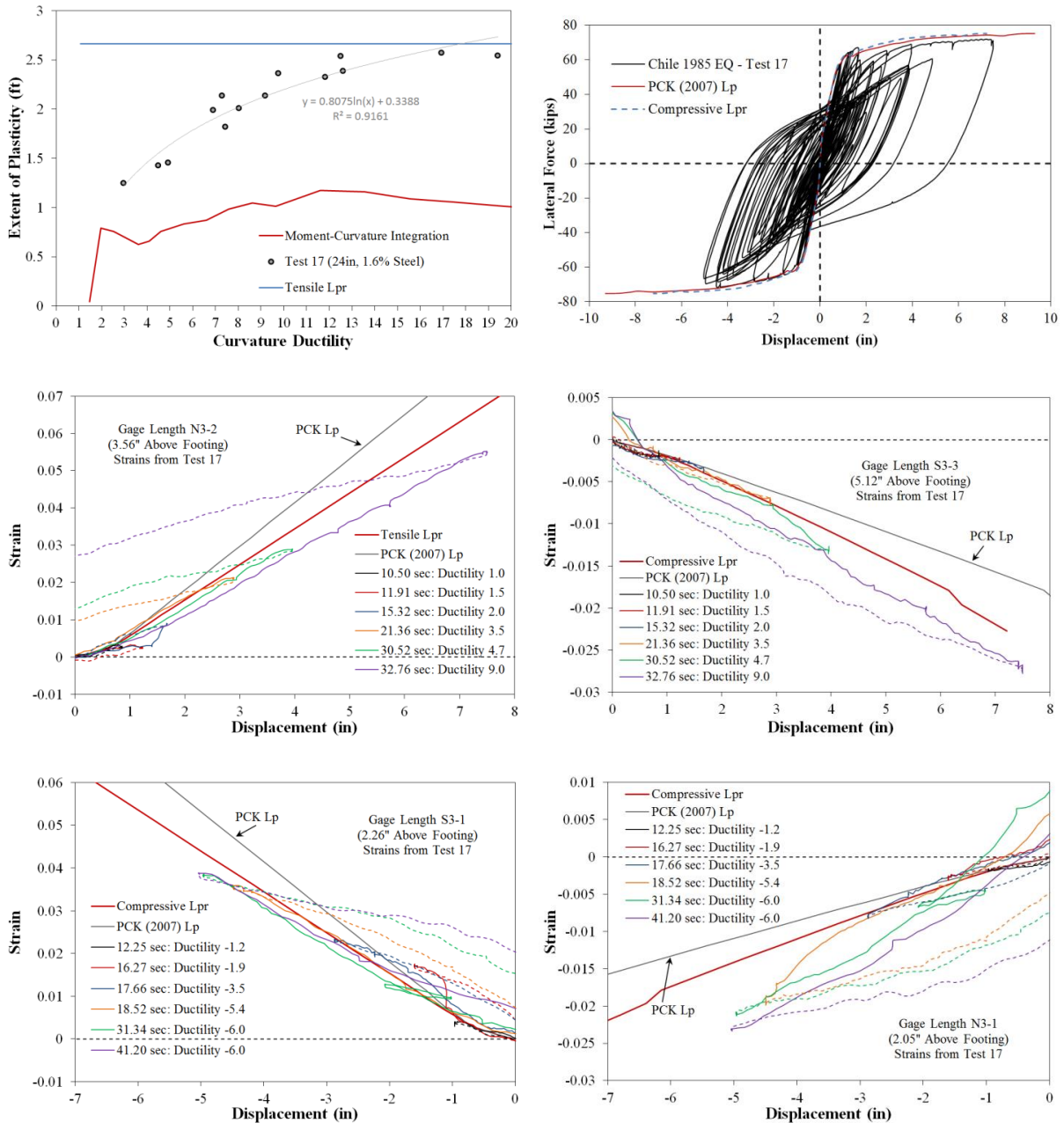
Figure 7.48 Spread of Plasticity and Strain-Displacement Relationship for Earthquake Load History Test 17
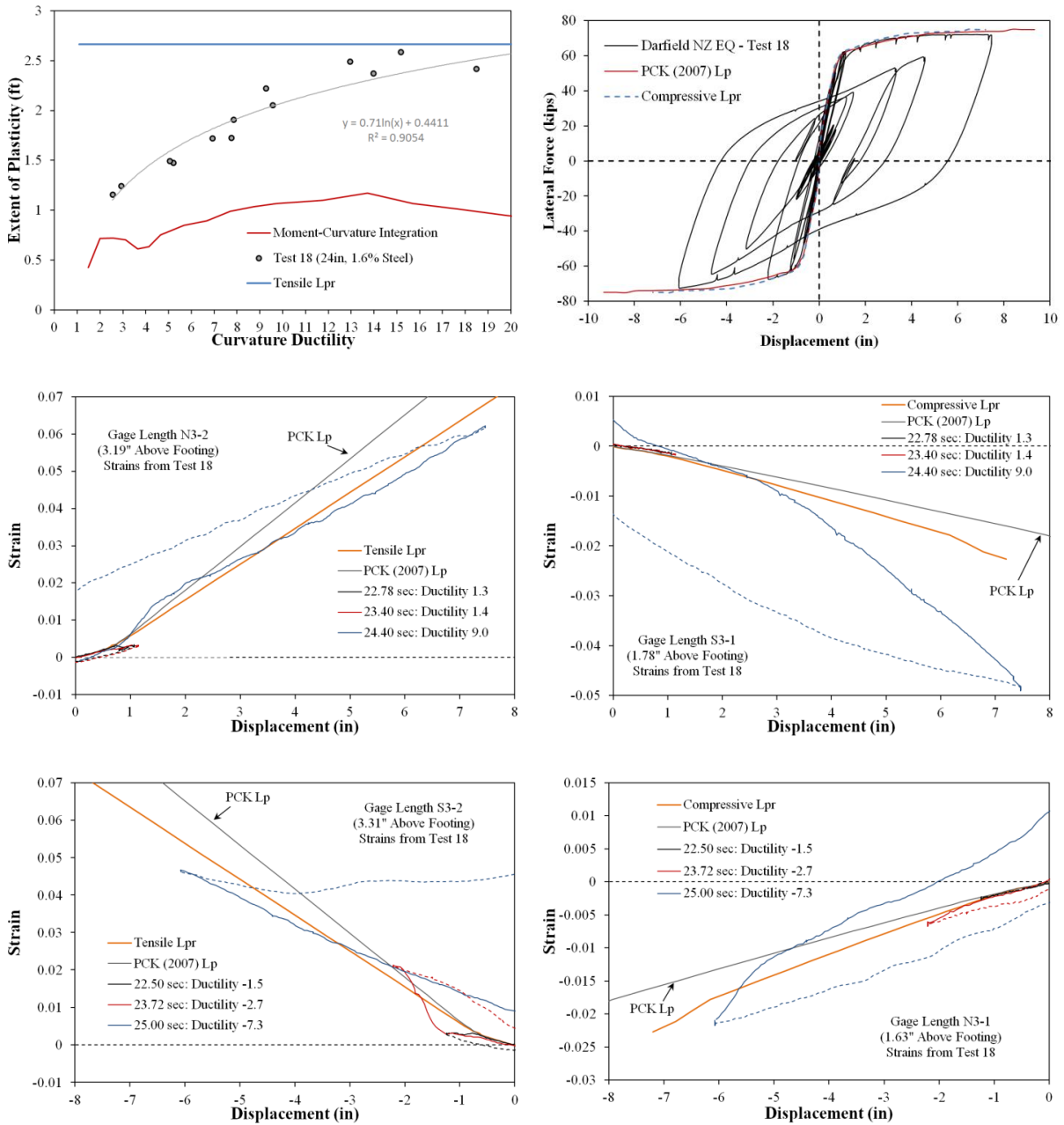
Figure 7.49 Spread of Plasticity and Strain-Displacement Relationship for Earthquake Load History Test 18
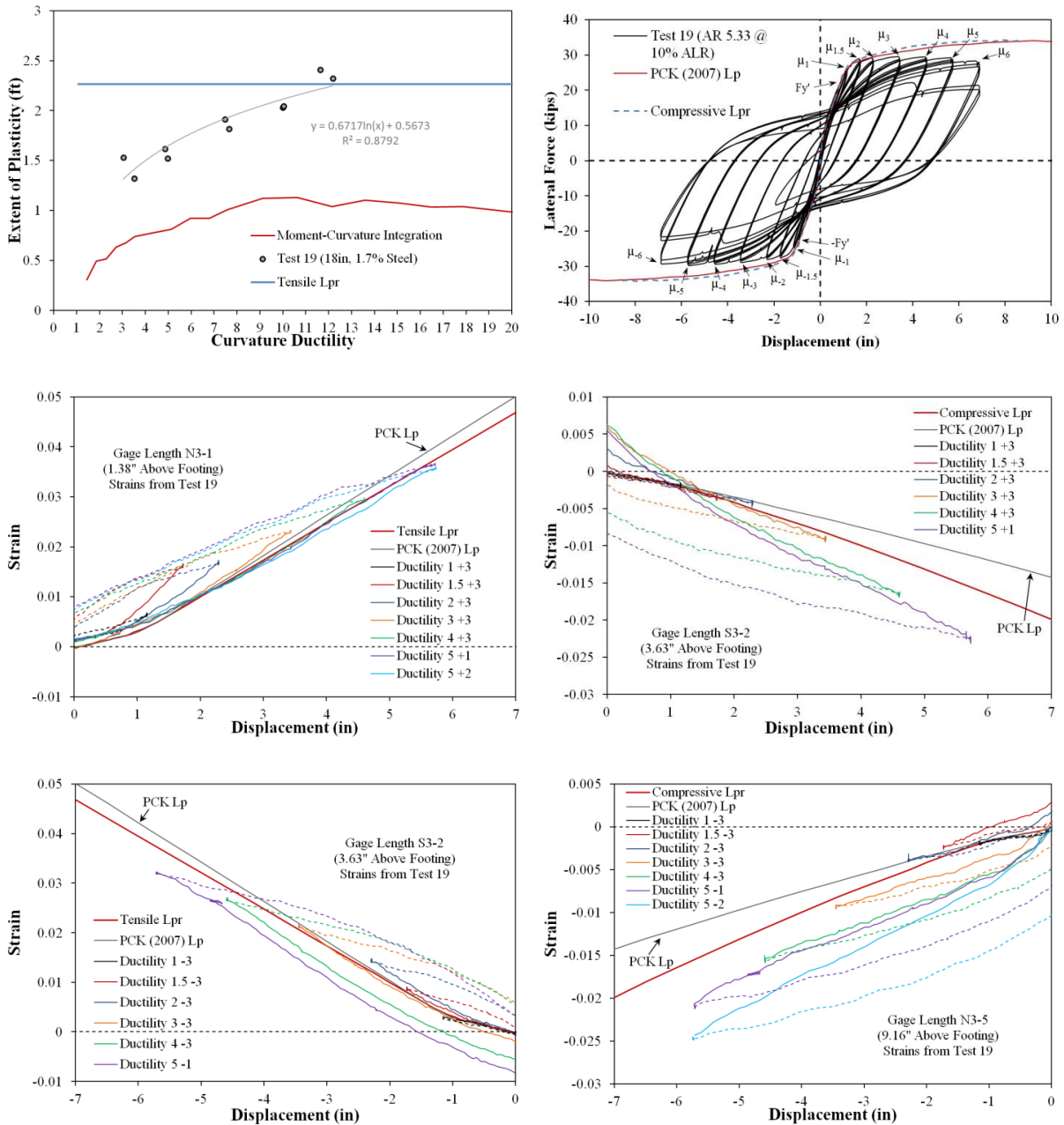
Figure 7.50 Spread of Plasticity and Strain-Displacement Relationship for Test 19
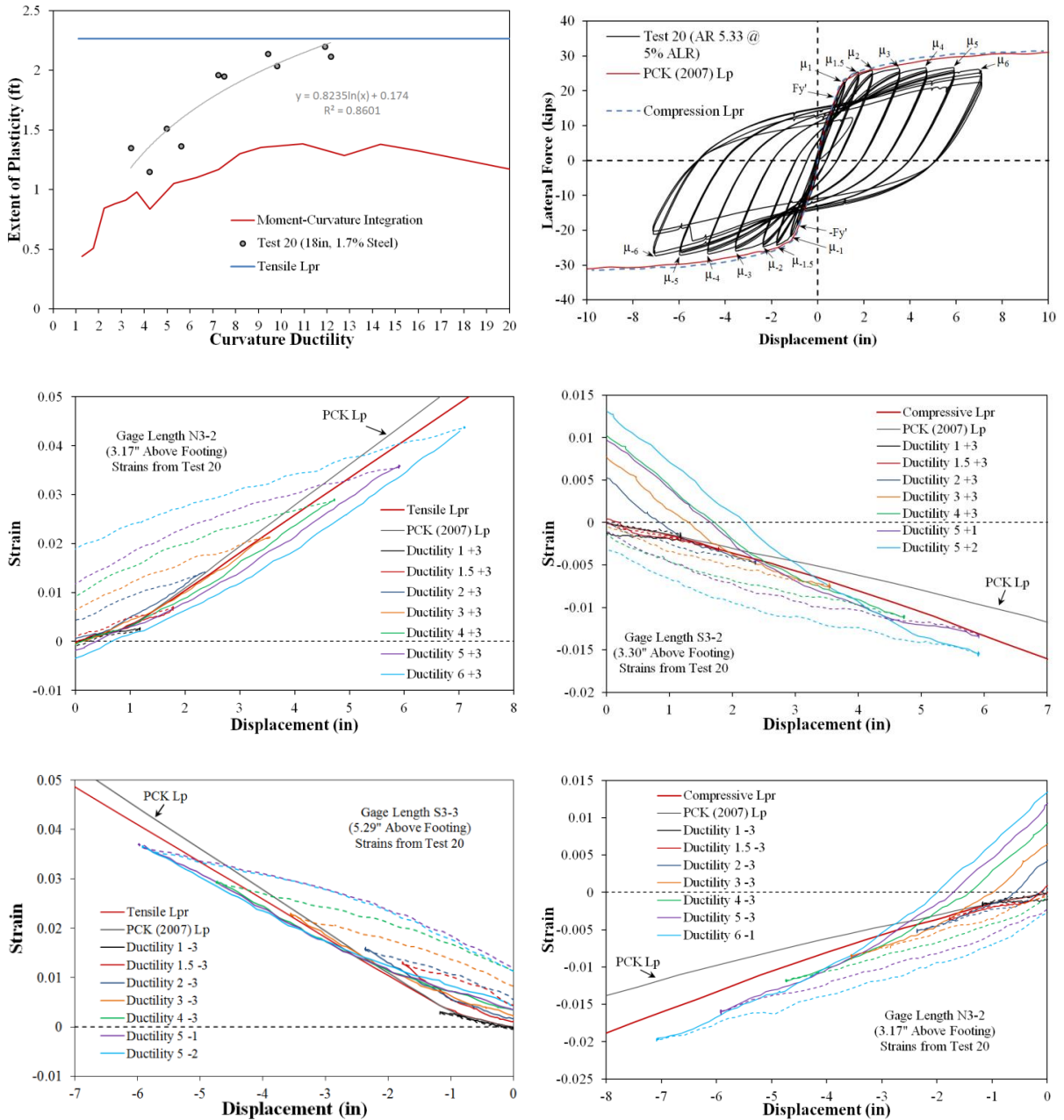
Figure 7.51 Spread of Plasticity and Strain-Displacement Relationship for Test 20
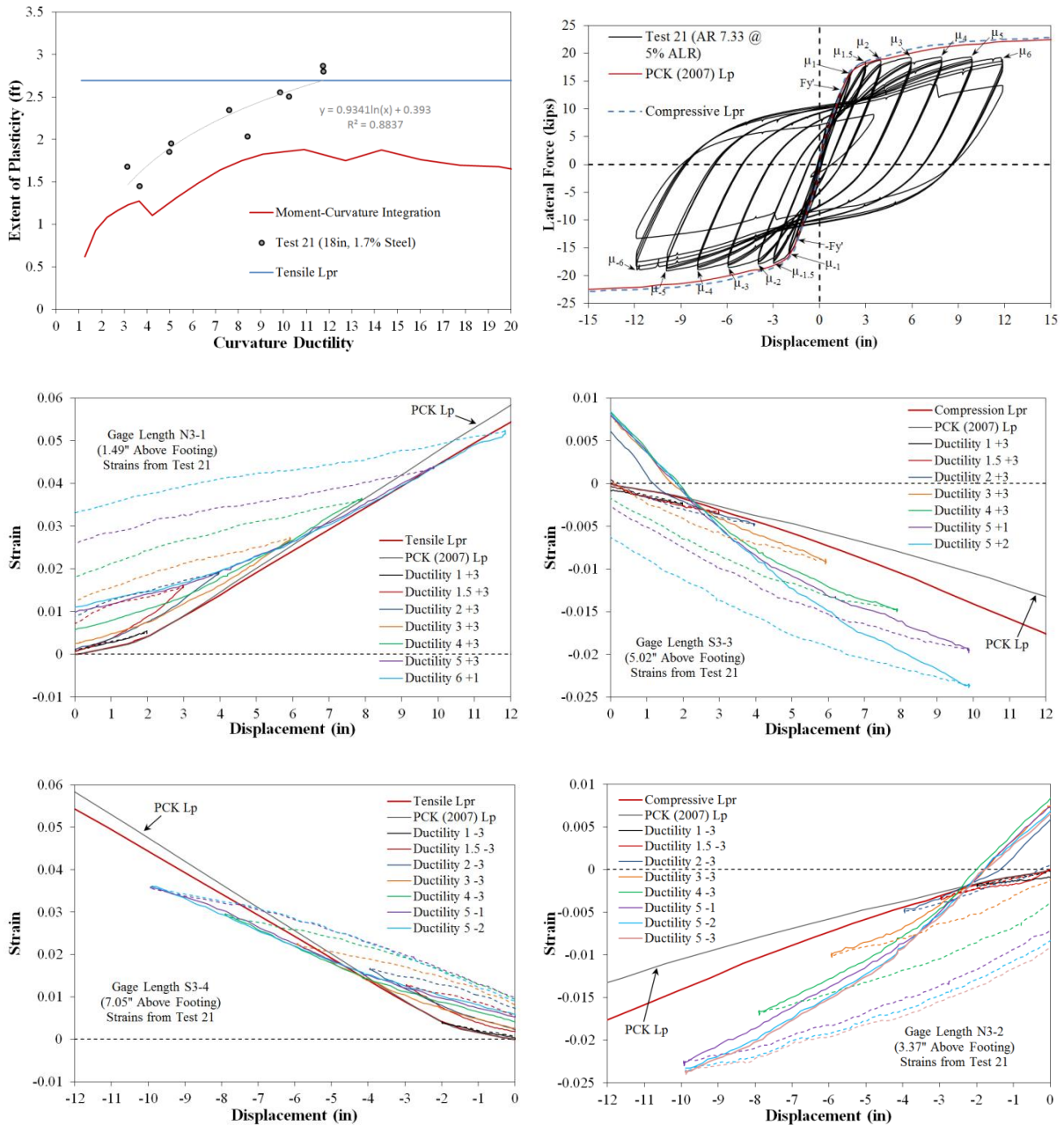
Figure 7.52 Spread of Plasticity and Strain-Displacement Relationship for Test 21
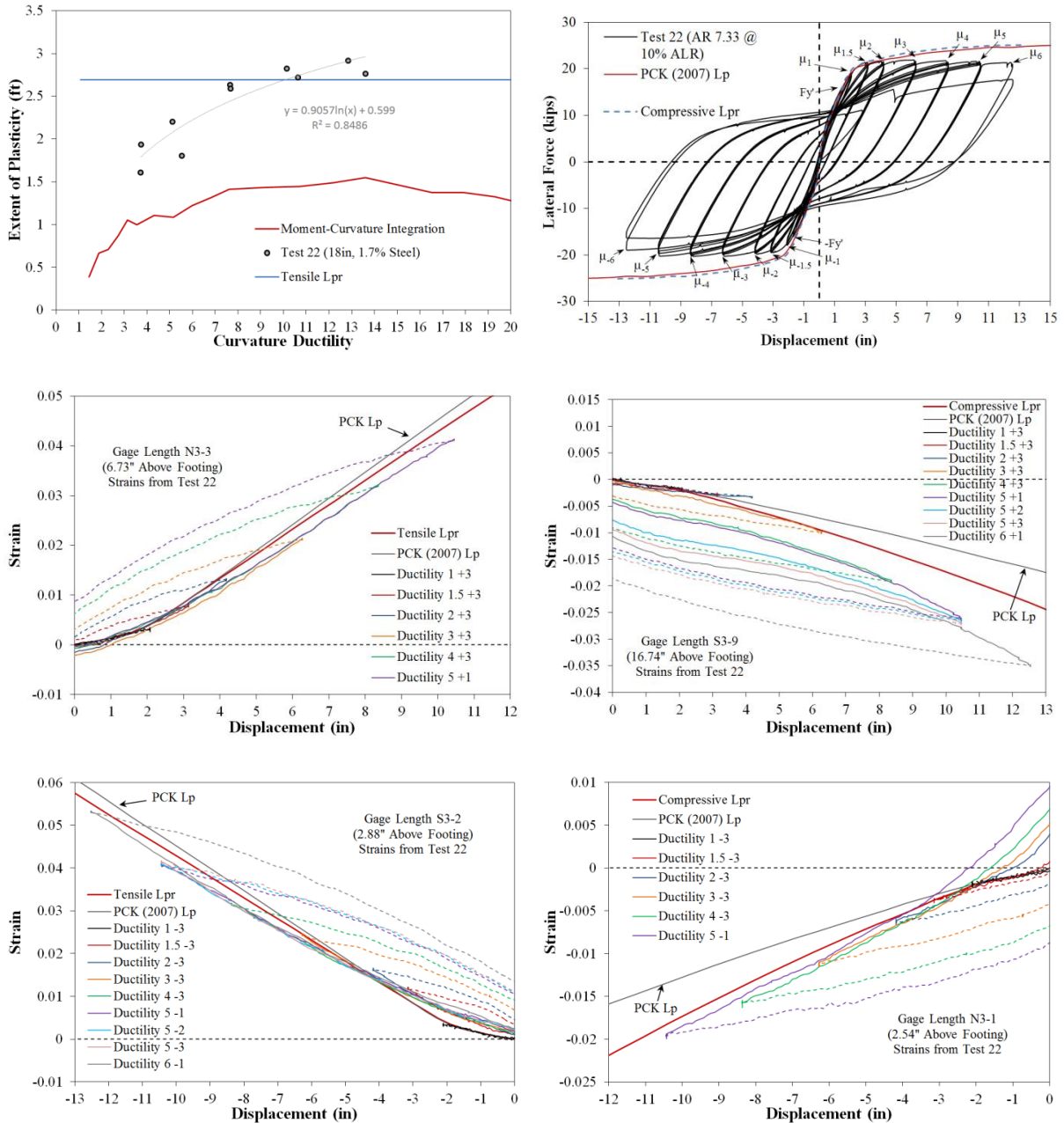
Figure 7.53 Spread of Plasticity and Strain-Displacement Relationship for Test 22
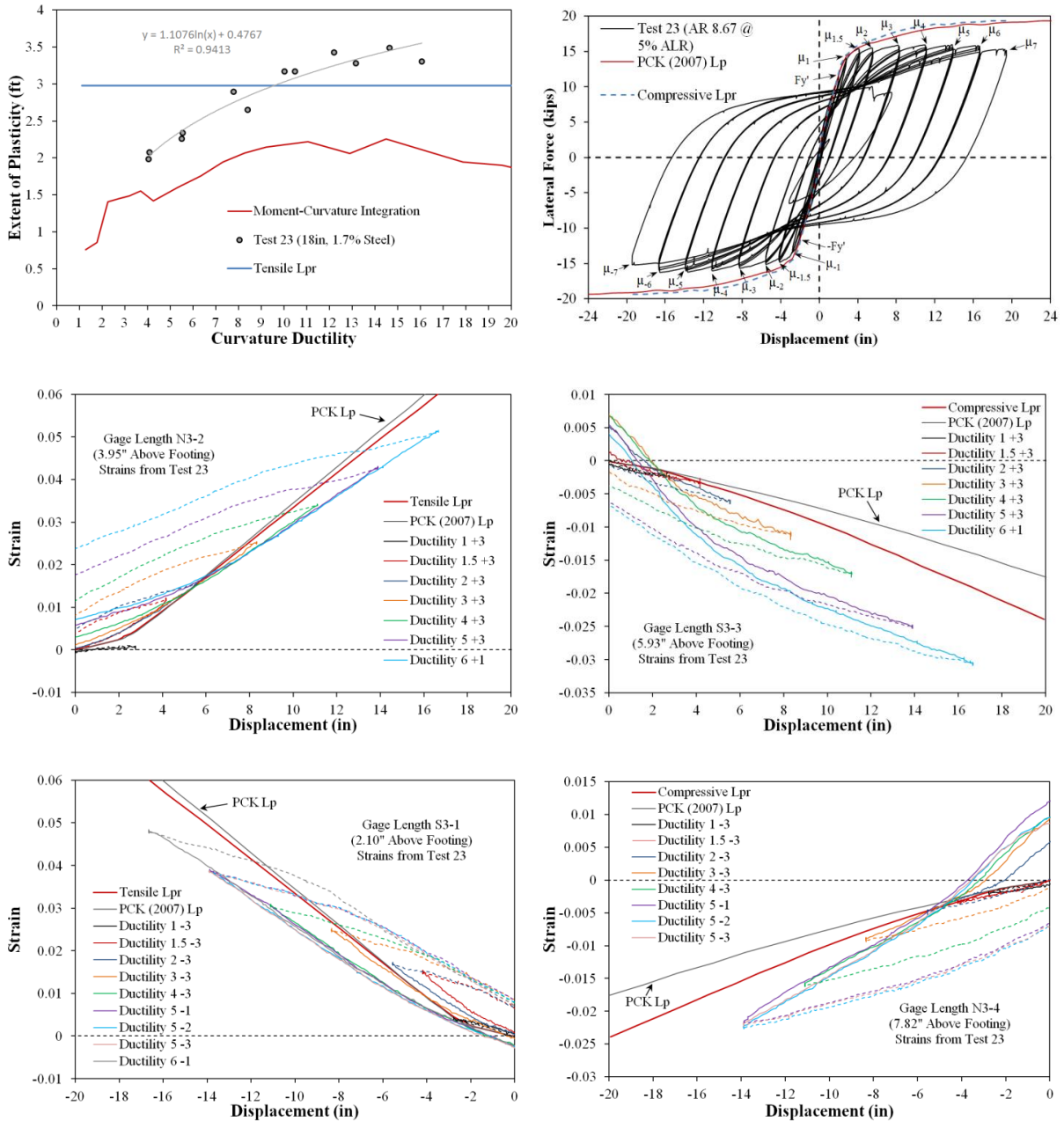
Figure 7.54 Spread of Plasticity and Strain-Displacement Relationship for Test 23
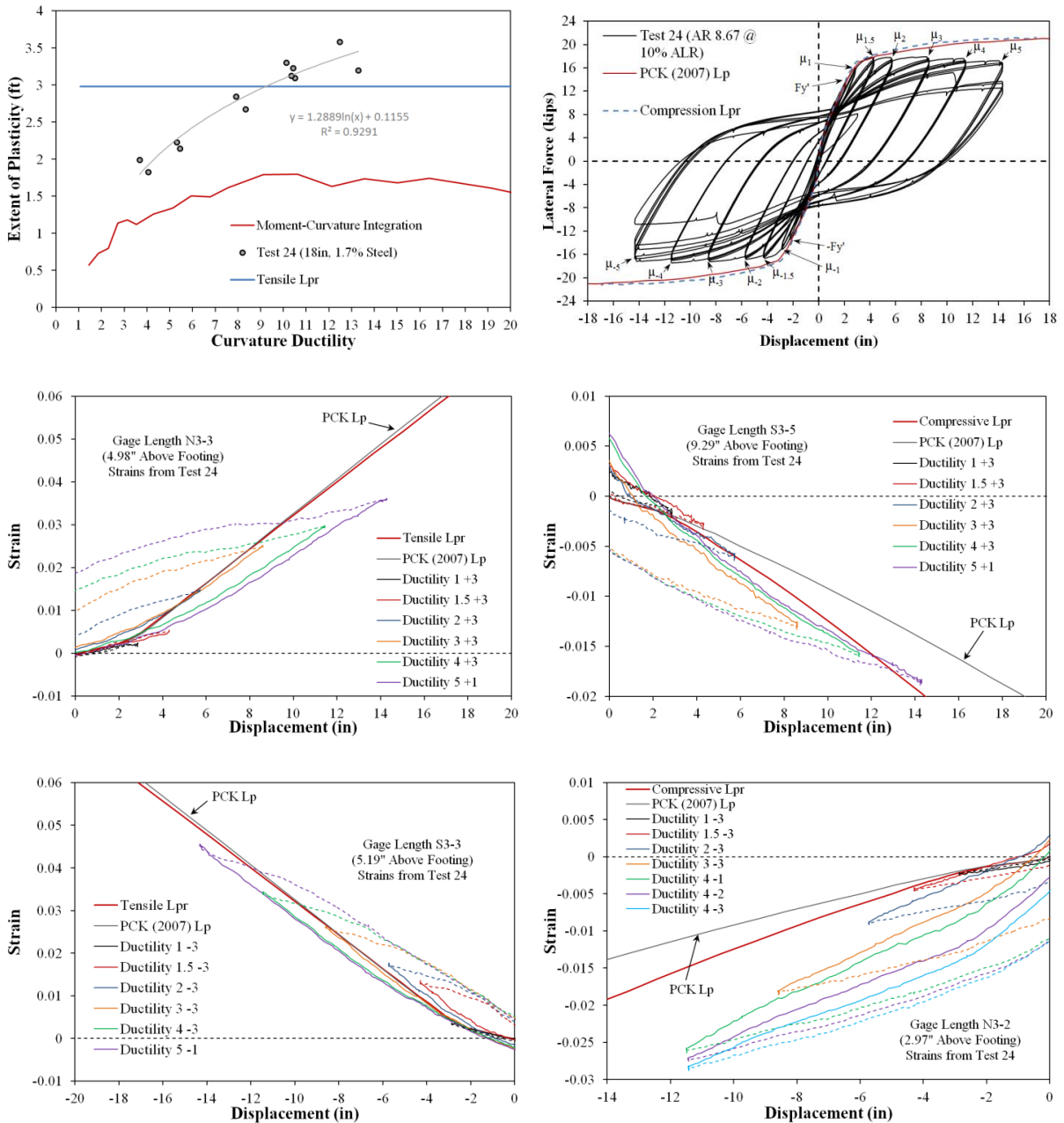
Figure 7.55 Spread of Plasticity and Strain-Displacement Relationship for Test 24
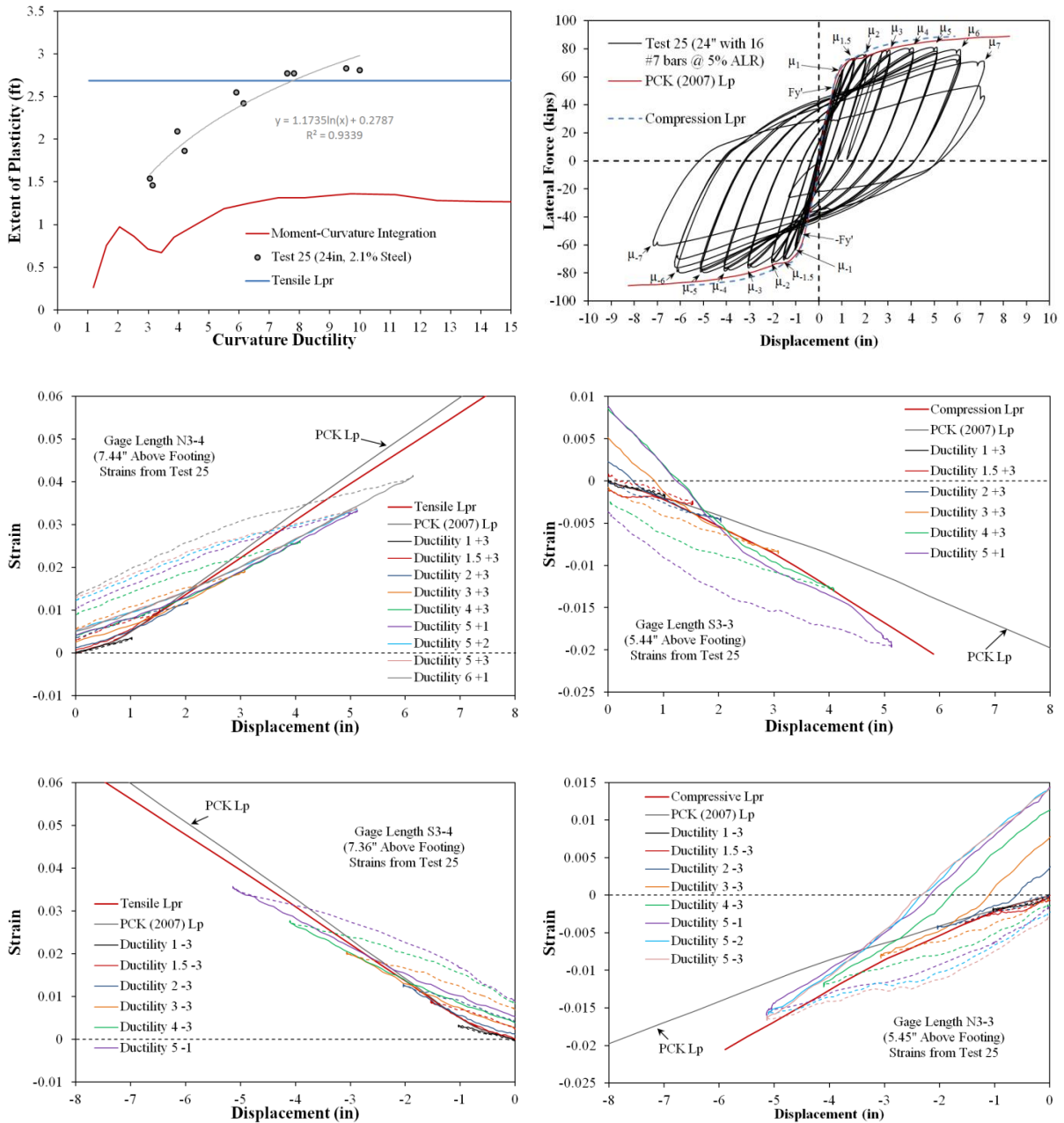
Figure 7.56 Spread of Plasticity and Strain-Displacement Relationship for Test 25
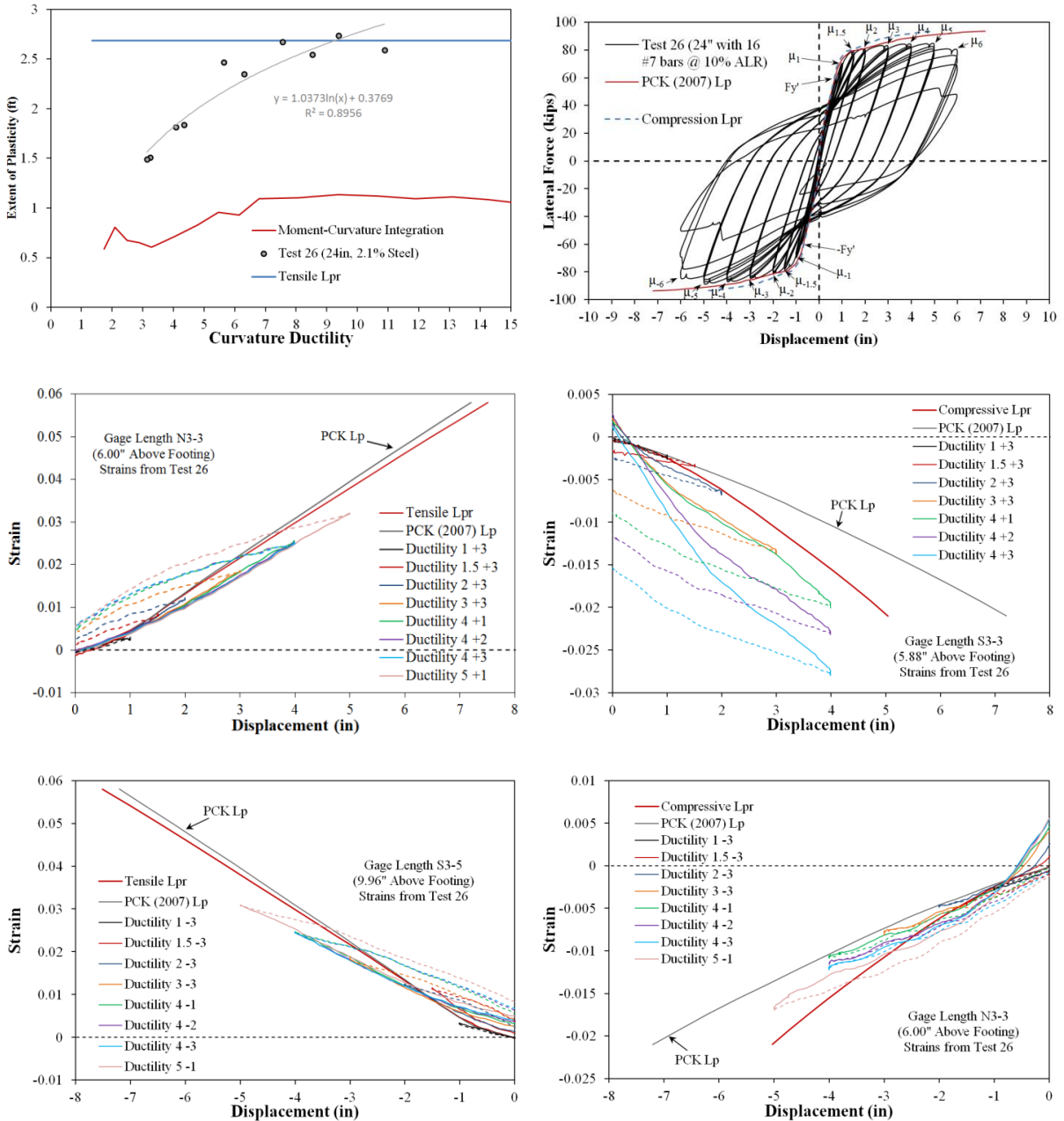
Figure 7.57 Spread of Plasticity and Strain-Displacement Relationship for Test 26
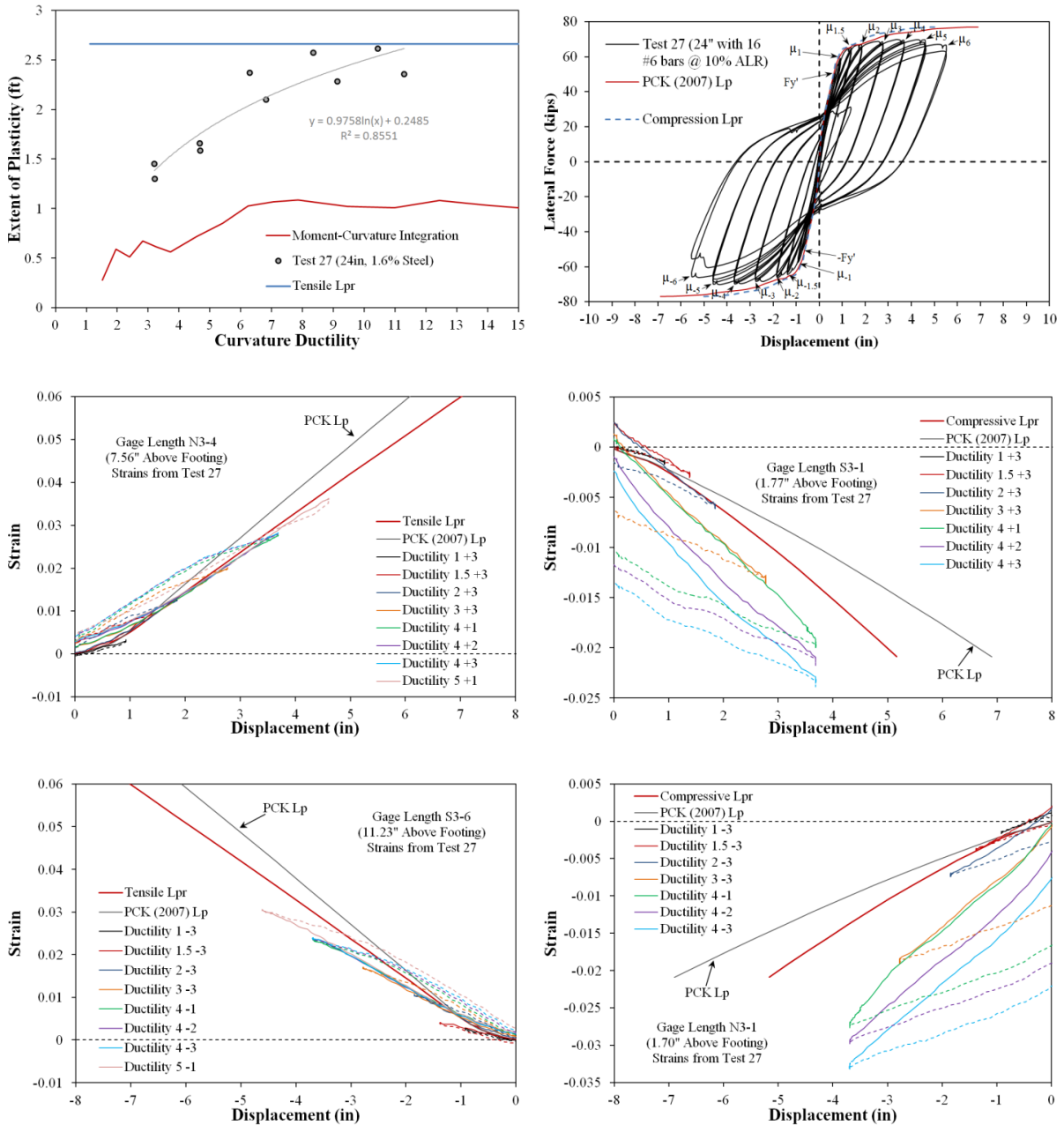
Figure 7.58 Spread of Plasticity and Strain-Displacement Relationship for Test 27
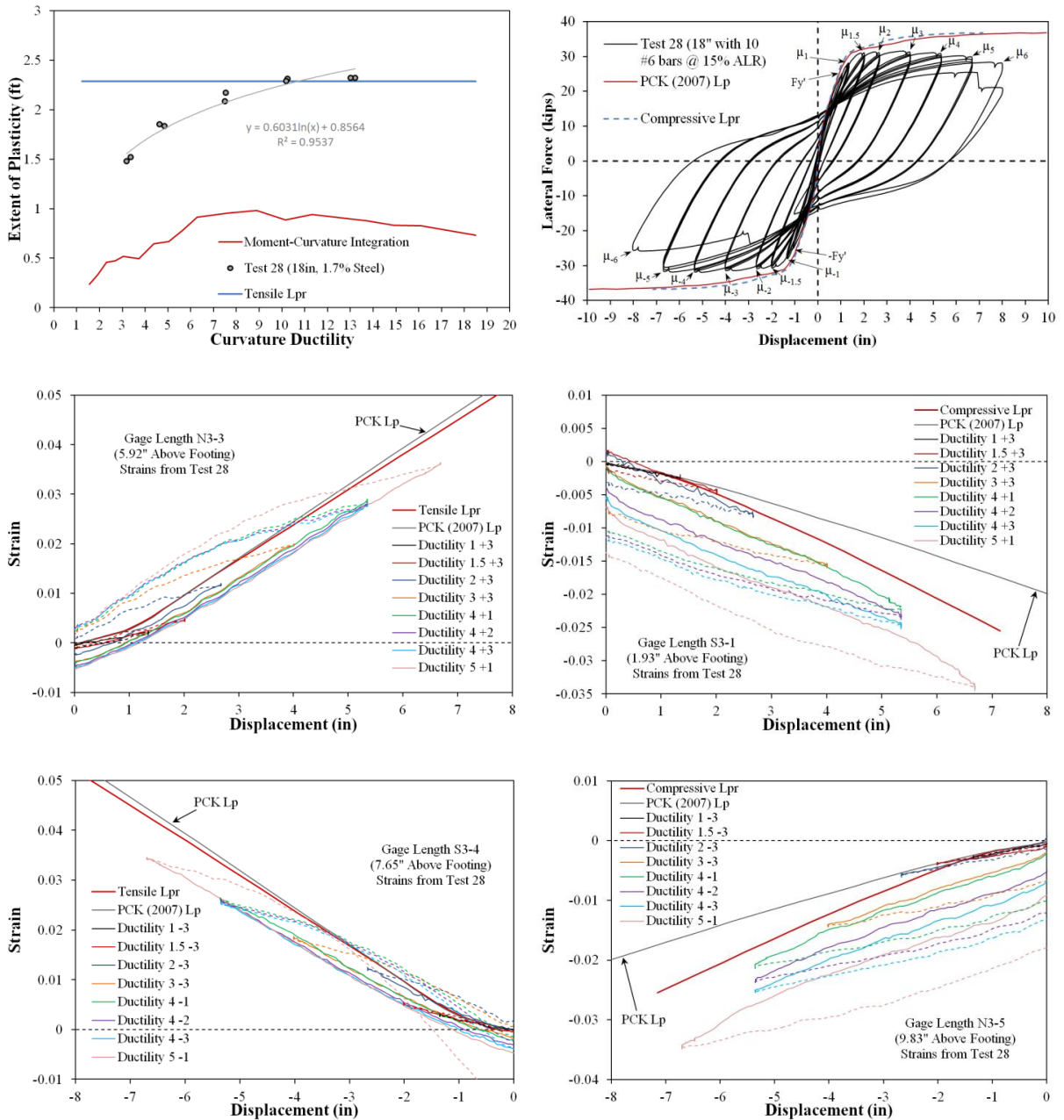
Figure 7.59 Spread of Plasticity and Strain-Displacement Relationship for Test 28
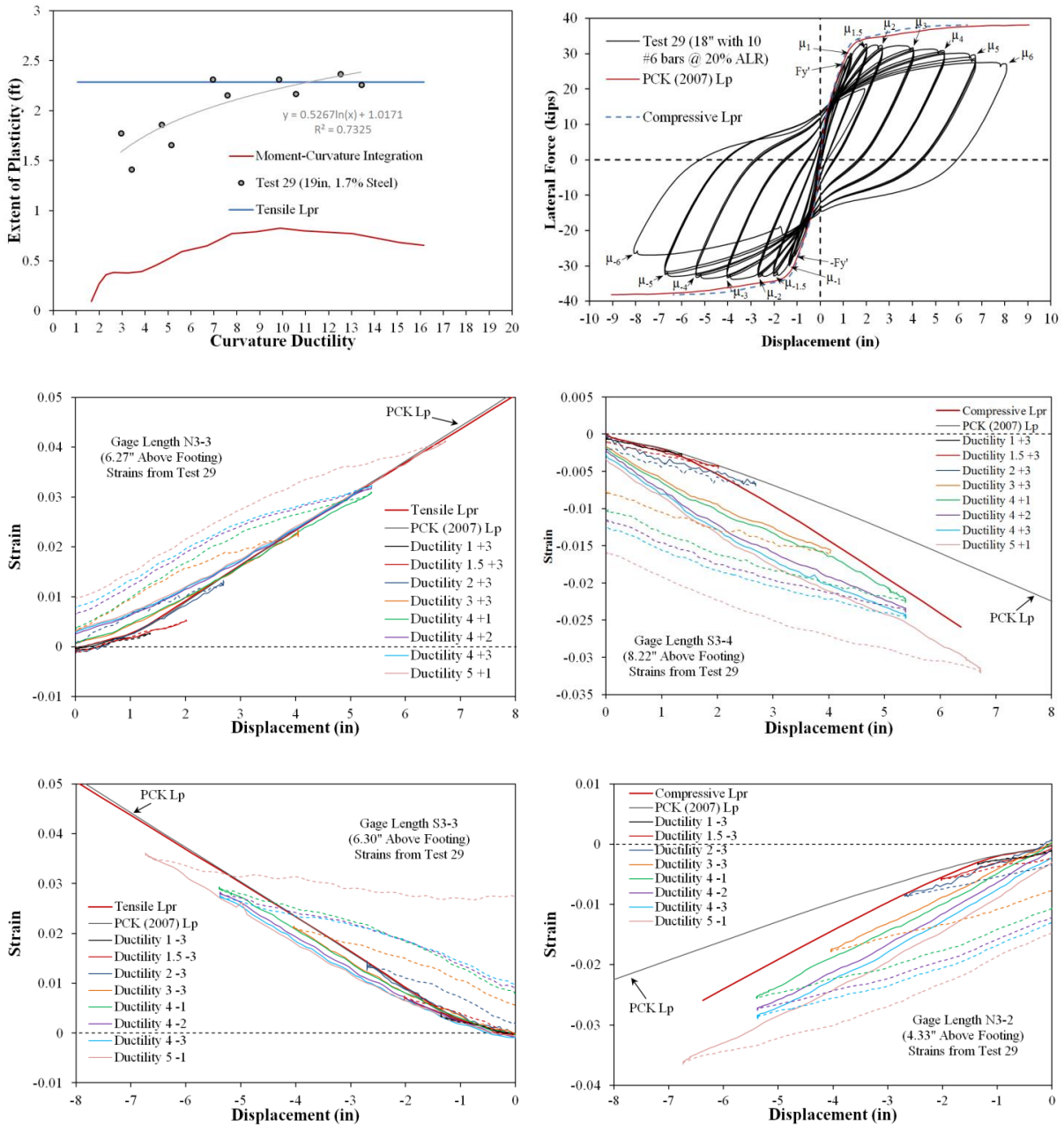
Figure 7.60 Spread of Plasticity and Strain-Displacement Relationship for Test 29
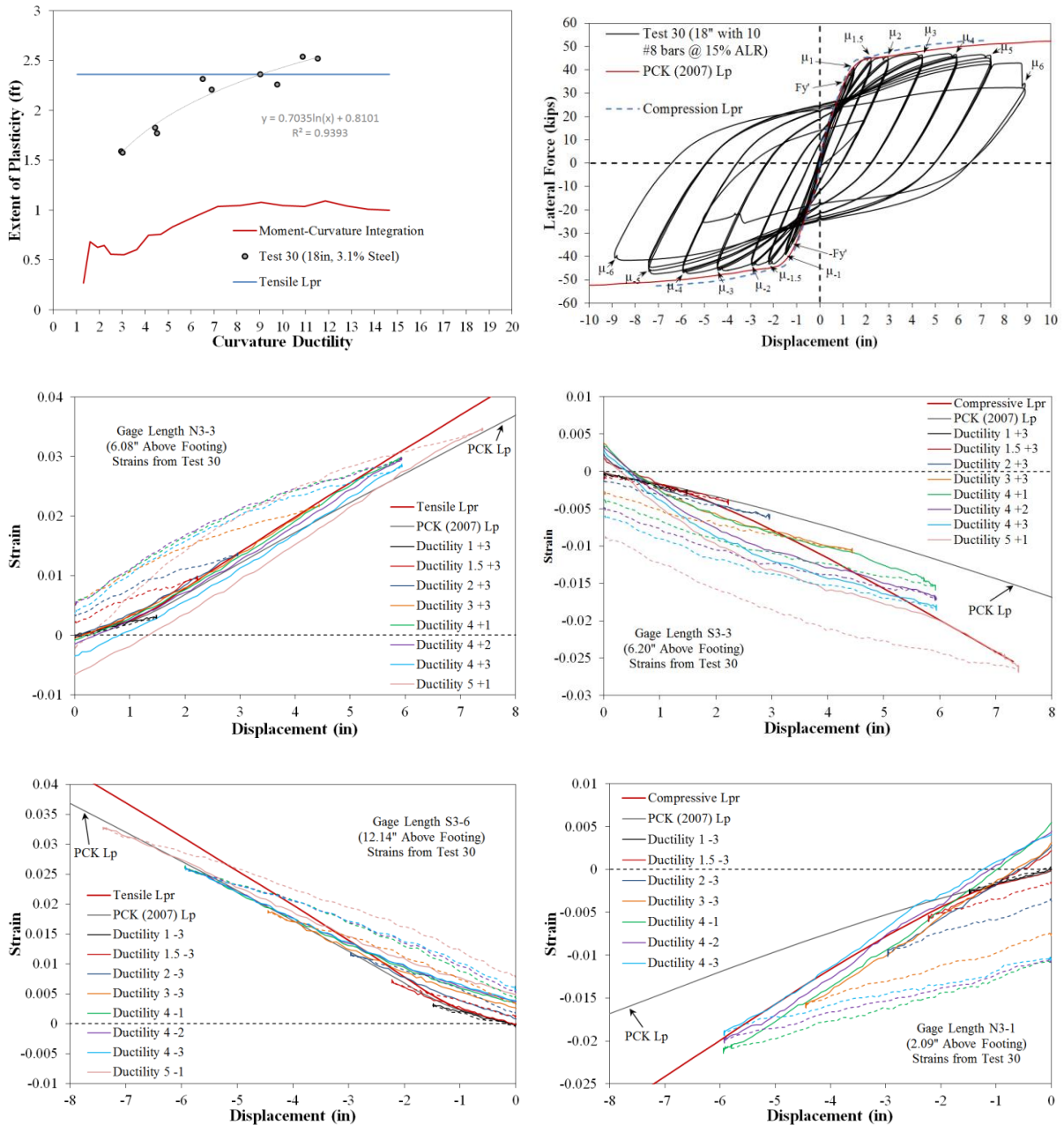
Figure 7.61 Spread of Plasticity and Strain-Displacement Relationship for Test 30

Chapter 8: Performance Strain Limits for Circular Bridge Columns

8.1 Background

This section discusses a research program supported by the Alaska Department of Transportation and Alaska University Transportation Center aimed at defining accurate limit state displacements which relate to specific levels of damage in reinforced concrete bridge columns subjected to seismic hazards. Bridge columns are designed as ductile elements which form plastic hinges to dissipate energy in a seismic event. To satisfy the aims of performance based design, levels of damage which interrupt the serviceability of the structure or require more invasive repair techniques must be related to engineering criteria. For reinforced concrete flexural members such as bridge columns, concrete compressive and steel tensile strain limits are very good indicators of damage.

Serviceability limit states such as concrete cover crushing or residual crack widths exceeding 1mm may occur during smaller, more frequent earthquakes, Priestley et al. (1996). While the serviceability limit states do not pose a safety concern, the hinge regions must be repaired to prevent corrosion of internal reinforcing steel. At higher ductility demands produced by larger less frequent earthquakes, reinforcing bar buckling may lead to permanent elongation in the transverse steel, which diminishes its effectiveness in confining the concrete core. Bar buckling and significant damage to the core concrete represent the damage control limit states, which when exceeded lead to significant repair costs, Priestley et al. (1996). Furthermore, rupture of previously buckled bars during subsequent cycles of loading leads to rapid strength loss. The life safety or collapse prevention limit state is characterized by fracture of previously buckled bars or confinement steel.

A summary of the current performance strain limit recommendations from (Kowalsky 2000) appear in Table 8.1. The first occurrence of these limit states in a cyclic column test

by Goodnight et al. is shown in Figure 8.1. The symmetric three-cycle-set load history and resulting force versus deformation response are shown with labels representing the first occurrence of cover crushing, bar buckling, and bar fracture limit states. Note that the damage control concrete compressive strain limit of 0.018 is shown as a typical value of the Mander et al (1988) ultimate concrete compressive strain for a volumetric steel ratio around 1%. If the exact detailing is known based on confinement or shear demands, then the appropriate ultimate concrete compressive strain value should be used instead.

While the progression of damage in flexural bridge columns has been thoroughly investigated in the past, to the authors' knowledge, none of the previous studies measured strains at the level of the reinforcement throughout the entire range of response. Traditional instrumentation methods utilized linear potentiometers placed on the ends of threaded rods embedded in the core concrete to calculate changes in displacement outside of the concrete cover. A diagram of this instrumentation system from tests by Hose et al. (1997) appeared in Hines et al. (2003), Figure 8.5. This method does not measure material strains at the locations of interests, and its measurements are influenced small rotations of the rods themselves which result due to the curvature gradient over the gage length.

Table 8.1 Performance Strain Limits from (Kowalsky 2000)

Limit State	Concrete Compressive Strain Limit	Steel Tensile Strain Limit
Serviceability	0.004 Cover Concrete Crushing	0.015 Residual Crack Widths Exceed 1mm
Damage Control	0.018 Mander et al. (1988), ε_{cu} Limit of Economical Concrete Repair	0.060 Tension Based Bar Buckling
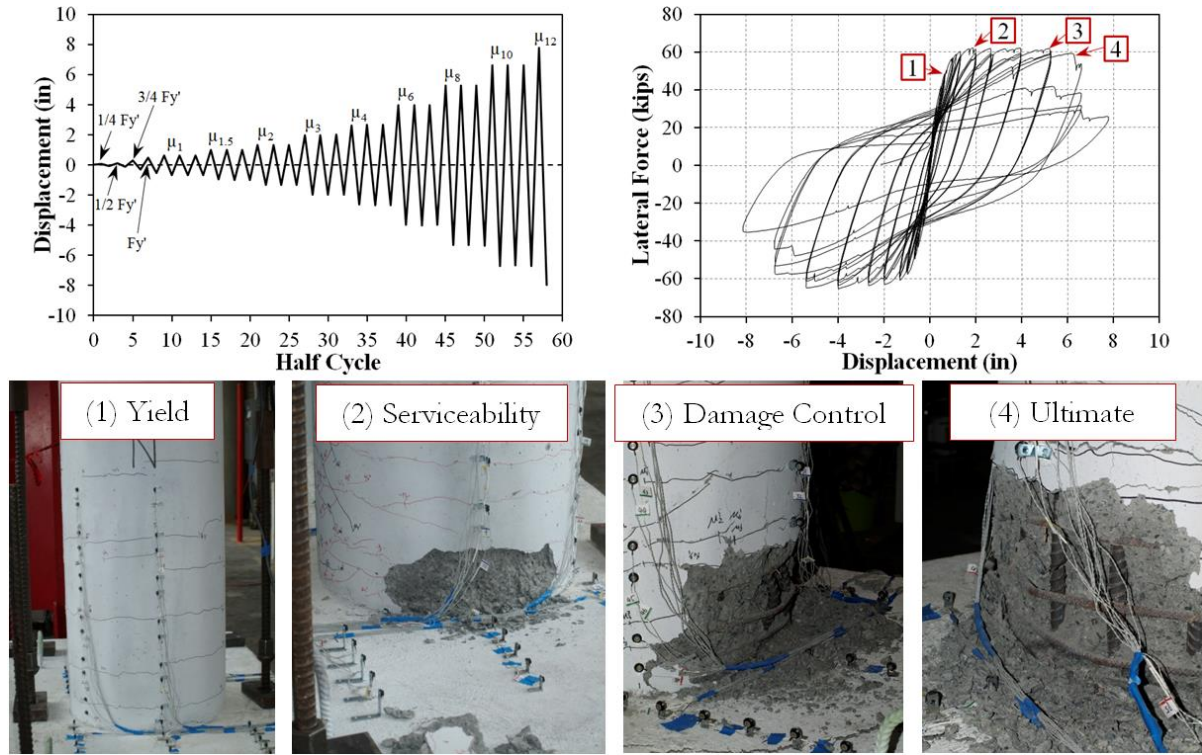
Figure 8.1 Displacement History, Hysteretic Response, and Performance Limit States
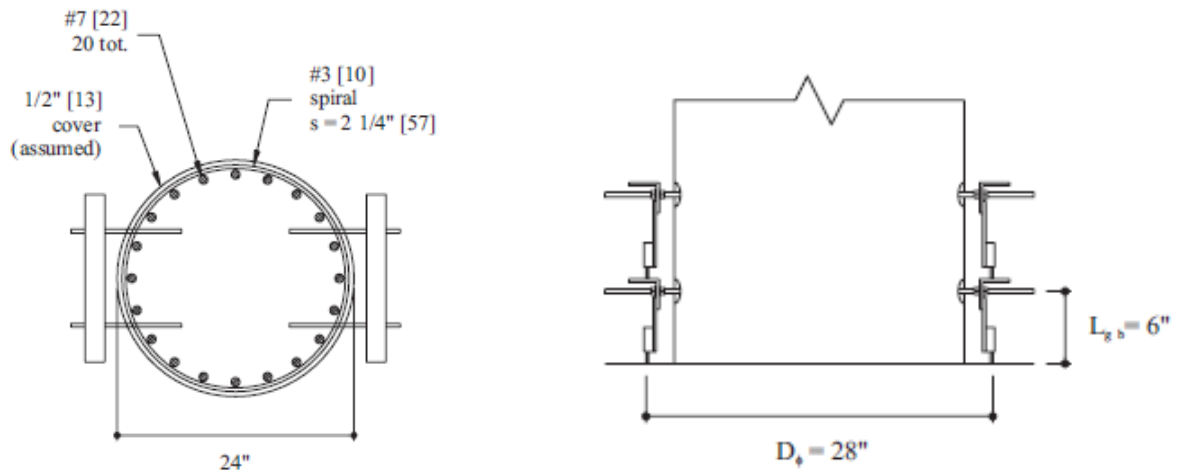
Figure 8.2 Curvature Rod and Linear Potentiometer Instrumentation from Tests by (Hose et al. 1997), Figure appears in (Hines et al. 2003)

8.2 Experimental Program

The goal of the experimental program is to investigate the impact of load history and other design variables on the relationship between strain and displacement, performance strain limits, and the spread of plasticity. In this section, the details of the experimental program are briefly described before presenting a series of predictive limit state expressions which were formulated based on the test results. The main variables for the thirty circular bridge column tests included: (1) lateral displacement history, (2) axial load, (3) longitudinal steel content, (4) aspect ratio, and (5) transverse steel detailing.

The specimen was designed to represent a single degree of freedom bridge column subjected to lateral and axial load, Figure 8.3. The test specimen consists of a footing, column, and loading cap. The footing is a capacity protected member which secures the specimen to the lab strong floor using post tensioned bars. A 200kip hydraulic actuator, with a 40in stroke capacity, applies lateral load to the loading cap of the specimen. A spreader beam, two hydraulic jacks, and a load cell are placed above the loading cap to apply a constant axial compressive load. The top column displacement was obtained through a string potentiometer placed at the center of the lateral load.

A key feature of the experiments was the high fidelity strain data obtained through the use of an optical 3D position measurement system. The experimental program utilized multiple Optotrak Certus HD 3D position sensors developed by Northern Digital Inc. to monitor material strains. The position sensors track the locations of the target markers in 3D space, returning X-Y-Z spatial coordinates with an accuracy of 0.1mm with a resolution of 0.01mm. A technique of applying target markers to longitudinal and transverse reinforcement, Figure 8.6, was utilized in the plastic hinge region. Strains are computed by dividing the change in three dimensional distance between two adjacent target markers by the original unloaded gage length.

An overview of geometry, reinforcement, material properties, and bar buckling observations for column Tests 8-30 appears in Table 8.2. An observational summary for

each test appears in Volume 2 of this report. The impact of lateral displacement history is the subject of Chapter 4, and the influence of other design variables is summarized in Chapter 5. Two different cross sections were utilized in the study, an 18" and a 24" diameter configuration as shown in Figure 8.4. The 24" configuration had 16 A706 longitudinal bars of either #6 (0.75 in) or #7 (0.875 in) diameter and a #3 (0.375 in) or #4 (0.5 in) A706 spiral at variable spacing. For both specimens the cover depth to the outside of the spiral was ½", which led to an outside spiral diameter of either 23" or 17". Two techniques of blocking out the cover concrete were employed to attach the Optotrak target markers to the outside surface of the reinforcing steel. Cover concrete was either blocked out in longitudinal strips over extreme fiber bars or around the entire circumference of the column plastic hinge region, Figure 8.3. The results of Tests 1-6 were excluded in the formulation of design recommendations because they utilized a steel post extension instrumentation technique which suffered from the same limitations as the curvature rod method.
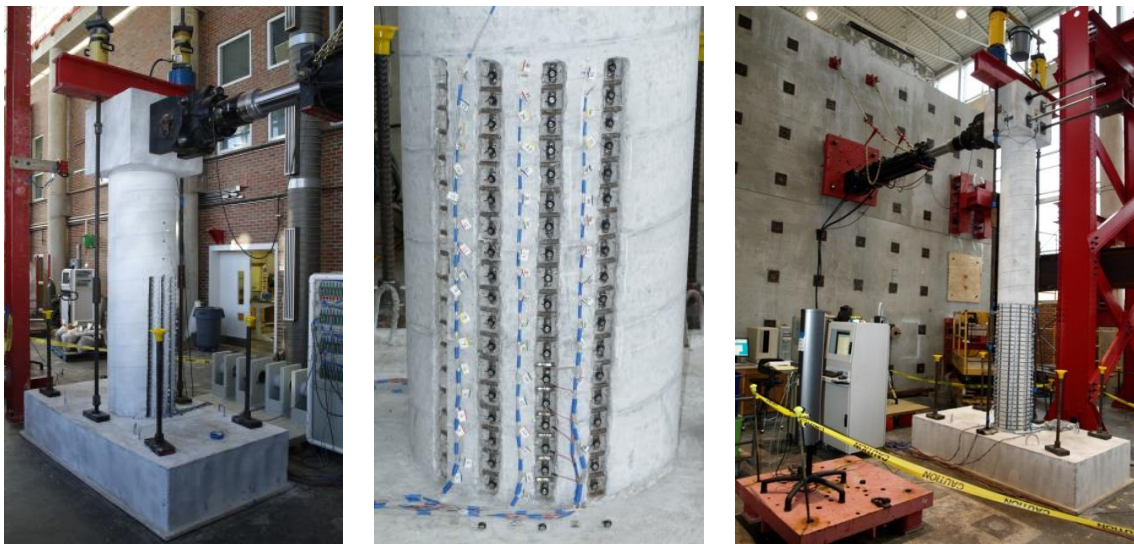
Figure 8.3 (Left) Test Setup, (Middle) Optotrak Target Marker Application Method, (Right) Optotrak Strain Comparison to Traditional Techniques
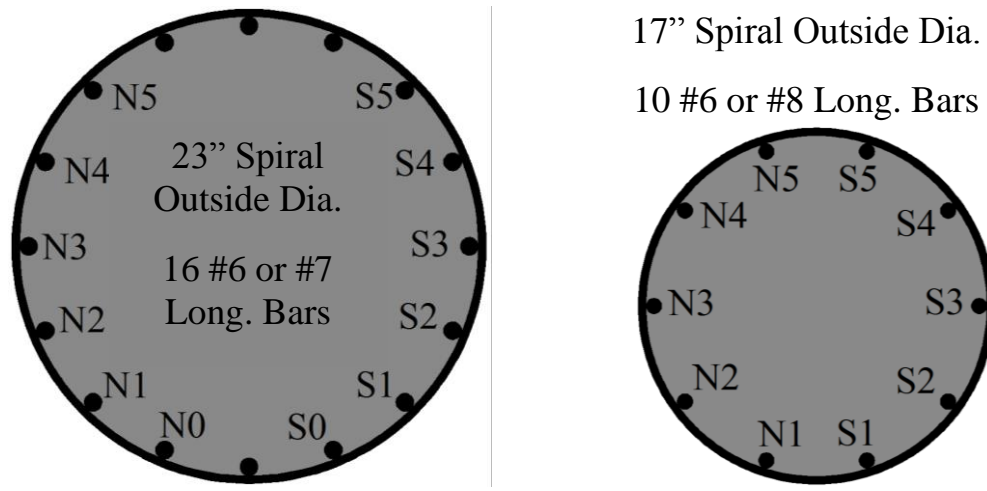
Figure 8.4 Tests 25-30 Cross Sections and Bar Designation for Both Diameters

8.2.1 Loading Protocol

The specimens were subjected to various unidirectional top-column displacement histories including standardized laboratory reversed cyclic loading and recreations of the displacement responses obtained from non-linear time history analysis of multiple earthquakes with distinct characteristics. The experiments utilized a quasi-static displacement controlled loading procedure. The symmetric three-cycle-set load history is commonly used to evaluate the seismic performance of structural components. The load history begins with elastic cycles to the following increments of the analytically predicted first yield force: ¼ F_y', ½ F_y', ¾ F_y', and F_y'. The experimental first yield displacement is then determined by taking the average of the recorded displacements during the first yield push and pulls cycles. The equivalent yield displacement, used to determine the displacement ductility levels ($\mu_{\Delta 1} = 1 * \Delta_y$), is then calculated as $\Delta_y = \Delta_y'(M_n/M_y')$. The symmetric three-cycle-set load history resumes with three balanced cycles at each of the following displacement ductility levels: 1, 1.5, 2, 3, 4, 5, etc.

8.3 Observed Damage Sequence

The following sequence of damage was observed in all of the cyclically loaded experiments: (1) concrete cracking, (2) longitudinal steel yielding, (3) cover concrete crushing, (4) confinement steel yielding, (5) longitudinal bar buckling, and (6) fracture of previously buckled reinforcement. The first significant loss in strength occurred when previously buckled reinforcement fractured. Fracture of confinement steel was never observed. The impact of individual variables on the displacement and material strains at key performance limit states was the main focus of Chapters 4 and 5.

In this section, the measured strain data is used to refine strain limit recommendations from Kowalsky (2000) in Figure 8.1. Particular attention is paid to the limit state of longitudinal bar buckling, since it limited the deformation capacity of all of the cyclically loaded specimens. Empirical expression are developed to predict the compressive strain at cover crushing, the compressive strain at spiral yielding, and the peak tensile strain prior to visible buckling after reversal of loading. Limit state displacements are evaluated using the Modified Lpr Plastic Hinge Method and compared to those observed experimentally. The formulation for this equivalent curvature distribution appears in Chapter 7.

Analytical studies by Berry (2006) utilized a database of experimentally tested bridge columns with defined material, geometric, and reinforcing properties, with reported bar buckling observations. The dataset, in Table 8.3, is a subset of the Column Structural Performance Database <www.ce.washington.edu/~peera1>. Berry (2006) created a predictive drift-based bar buckling expression for the dataset. As a means of comparison, the strain-based bar buckling expression and displacement formulated based on the Goodnight et al. dataset is compared to observed buckling displacements for columns in the Berry (2006) dataset. A second empirical drift-based expression was developed to predict bar buckling in the combined dataset.

Feng (2013) proposed a series of equations to describe bar buckling behavior observed in finite element analysis of reinforcing bars. The influence of the following behaviors were

included in the analysis: (1) dilation of core concrete under compression, (2) restraint provided by individual spiral layers which can go inelastic, and (3) development of the longitudinal bar into the adjoining member. The analysis resulted in a multi-linear regression model which forms a boundary for tensile versus compressive strain relationship which would initiate bar buckling after reversal of load.

The results for each of these bar buckling prediction methods are compared to the combined Berry (2006) and Goodnight et al. datasets, and limitations of each method are explored. At the end of this discussion, recommendations for each of the performance limit states are provided. In some cases the current values are either verified or shown to be conservative, while in others new expressions are recommended.

Table 8.2 Goodnight et al. Bridge Column Dataset

Reference	fyh (Mpa)	fy (Mpa)	fu (Mpa)	f'c (Mpa)	dbl (mm)	ρl	ρs	ρeff	P/(f'c*Ag)	Length (mm)	Dia (mm)	Δbb (mm)	(Δbb/L)
Goodnight et al, 9	511	469	654	47.0	19.05	0.016	0.01	0.109	0.054	2438.4	609.6	170.7	0.070
Goodnight et al, 9	511	469	654	47.0	19.05	0.016	0.01	0.109	0.054	2438.4	609.6	170.2	0.070
Goodnight et al, 13	482	469	640	42.0	19.05	0.016	0.013	0.149	0.062	2438.4	609.6	164.1	0.067
Goodnight et al, 13	482	469	640	42.0	19.05	0.016	0.013	0.149	0.062	2438.4	609.6	165.1	0.068
Goodnight et al, 14	445	469	640	45.8	19.05	0.016	0.005	0.049	0.057	2438.4	609.6	121.9	0.050
Goodnight et al, 14	445	469	640	45.8	19.05	0.016	0.005	0.049	0.057	2438.4	609.6	121.9	0.050
Goodnight et al, 15	445	469	640	49.9	19.05	0.016	0.007	0.062	0.052	2438.4	609.6	127.0	0.052
Goodnight et al, 15	445	469	640	49.9	19.05	0.016	0.007	0.062	0.052	2438.4	609.6	127.0	0.052
Goodnight et al, 16	445	469	640	46.3	19.05	0.016	0.013	0.125	0.056	2438.4	609.6	168.9	0.069
Goodnight et al, 16	445	469	640	46.3	19.05	0.016	0.013	0.125	0.056	2438.4	609.6	169.7	0.070
Goodnight et al, 25	440	481	659	43.3	22.225	0.021	0.01	0.102	0.05	2438.4	609.6	156.0	0.064
Goodnight et al, 25	440	481	659	43.3	22.225	0.021	0.01	0.102	0.05	2438.4	609.6	130.0	0.053
Goodnight et al, 26	440	481	659	40.6	22.225	0.021	0.01	0.108	0.1	2438.4	609.6	126.5	0.052
Goodnight et al, 26	440	481	659	40.6	22.225	0.021	0.01	0.108	0.1	2438.4	609.6	101.1	0.041
Goodnight et al, 27	440	474	646	42.4	19.05	0.016	0.01	0.104	0.1	2438.4	609.6	116.8	0.048
Goodnight et al, 27	440	474	646	42.4	19.05	0.016	0.01	0.104	0.1	2438.4	609.6	93.2	0.038
Goodnight et al, 19	452	470	637	43.7	19.05	0.017	0.013	0.135	0.1	2438.4	457.2	145.3	0.060
Goodnight et al, 19	452	470	637	43.7	19.05	0.017	0.013	0.135	0.1	2438.4	457.2	145.3	0.060
Goodnight et al, 20	452	470	637	44.6	19.05	0.017	0.013	0.132	0.05	2438.4	457.2	180.3	0.074
Goodnight et al, 20	452	470	637	44.6	19.05	0.017	0.013	0.132	0.05	2438.4	457.2	149.6	0.061
Goodnight et al, 21	452	470	637	44.1	19.05	0.017	0.013	0.133	0.05	3352.8	457.2	301.2	0.090
Goodnight et al, 21	452	470	637	44.1	19.05	0.017	0.013	0.133	0.05	3352.8	457.2	251.0	0.075
Goodnight et al, 22	452	470	637	45.0	19.05	0.017	0.013	0.130	0.1	3352.8	457.2	265.4	0.079
Goodnight et al, 22	452	470	637	45.0	19.05	0.017	0.013	0.130	0.1	3352.8	457.2	318.3	0.095
Goodnight et al, 23	452	470	637	45.5	19.05	0.017	0.013	0.129	0.05	3962.4	457.2	422.9	0.107
Goodnight et al, 23	452	470	637	45.5	19.05	0.017	0.013	0.129	0.05	3962.4	457.2	422.9	0.107
Goodnight et al, 24	452	470	637	44.6	19.05	0.017	0.013	0.132	0.1	3962.4	457.2	363.0	0.092
Goodnight et al, 24	452	470	637	44.6	19.05	0.017	0.013	0.132	0.1	3962.4	457.2	363.7	0.092
Goodnight et al, 28	440	474	646	43.0	19.05	0.017	0.013	0.133	0.15	2438.4	457.2	169.7	0.070
Goodnight et al, 28	440	474	646	43.0	19.05	0.017	0.013	0.133	0.15	2438.4	457.2	135.6	0.056
Goodnight et al, 29	440	474	646	40.8	19.05	0.017	0.013	0.140	0.2	2438.4	457.2	204.7	0.084
Goodnight et al, 29	440	474	646	40.8	19.05	0.017	0.013	0.140	0.2	2438.4	457.2	170.7	0.070
Goodnight et al, 30	440	486	674	41.7	25.4	0.031	0.013	0.137	0.15	2438.4	457.2	187.7	0.077
Goodnight et al, 30	440	486	674	41.7	25.4	0.031	0.013	0.137	0.15	2438.4	457.2	187.7	0.077
Goodnight et al, 8	511	469	654	48.2	19.05	0.016	0.01	0.106	0.054	2438.4	609.6	184.2	0.076
Goodnight et al, 8	511	469	654	48.2	19.05	0.016	0.01	0.106	0.054	2438.4	609.6	168.9	0.069
Goodnight et al, 10	511	469	654	36.3	19.05	0.016	0.01	0.141	0.071	2438.4	609.6	127.3	0.052
Goodnight et al, 11	511	469	654	42.6	19.05	0.016	0.01	0.120	0.062	2438.4	609.6	210.3	0.086
Goodnight et al, 11	511	469	654	42.6	19.05	0.016	0.01	0.120	0.062	2438.4	609.6	129.0	0.053
Goodnight et al, 12	511	469	654	42.1	19.05	0.016	0.01	0.121	0.062	2438.4	609.6	208.8	0.086
Goodnight et al, 12	511	469	654	42.1	19.05	0.016	0.01	0.121	0.062	2438.4	609.6	165.9	0.068
Goodnight et al, 17	445	469	640	52.3	19.05	0.016	0.013	0.111	0.05	2438.4	609.6	190.2	0.078
Goodnight et al, 17	445	469	640	52.3	19.05	0.016	0.013	0.111	0.05	2438.4	609.6	127.5	0.052
Goodnight et al, 18	445	469	640	53.8	19.05	0.016	0.013	0.108	0.048	2438.4	609.6	153.7	0.063
MIN	440	469	637	36.3	19.05	0.016	0.005	0.049	0.048	2438.4	457.2	93.2	0.038
MAX	511	485.87	674	53.8	25.40	0.031	0.013	0.149	0.200	3962.4	609.6	422.9	0.107
AVG	461	471.91	646	44.6	19.63	0.018	0.011	0.118	0.080	2660.1	547.3	188.2	0.069

Table 8.3 Berry et al. (2006) Dataset

Reference	fyh (Mpa)	fy (Mpa)	fu (Mpa)	f'c (Mpa)	dbl (mm)	ρl	ρs	ρeff	P/(f'c*Ag)	Length (mm)	Dia (mm)	Δbb (mm)	(Δbb/L)
Wong et al. 1990, No. 1	300	423	577	38.0	16	0.032	0.015	0.118	0.19	800	400	40	0.050
NIST, Full Scale Flexure	493	475	665	35.8	43	0.02	0.006	0.083	0.069	9140	1520	538	0.059
NIST, Full Scale Shear	435	475	665	34.3	43	0.02	0.015	0.190	0.071	4570	1520	285	0.062
NIST, Model N1	441	446	624	24.1	7	0.02	0.015	0.274	0.101	750	250	77.2	0.103
NIST, Model N2	441	446	624	23.1	7	0.02	0.015	0.286	0.211	750	250	44.7	0.060
NIST, Model N3	441	476	666	25.4	7	0.02	0.007	0.122	0.096	1500	250	102.4	0.068
NIST, Model N4	441	446	624	24.4	7	0.02	0.015	0.271	0.1	750	250	53.3	0.071
NIST, Model N5	441	446	624	24.3	7	0.02	0.015	0.272	0.2	750	250	48.3	0.064
NIST, Model N6	476	446	624	23.3	7	0.02	0.007	0.143	0.105	1500	250	67.2	0.045
Kunnath et al. 1997, A2	434	448	690	29	9.5	0.02	0.01	0.150	0.094	1372	305	68.3	0.050
Kunnath et al. 1997, A4	434	448	690	35.5	9.5	0.02	0.01	0.122	0.086	1372	305	57	0.042
Kunnath et al. 1997, A5	434	448	690	35.5	9.5	0.02	0.01	0.122	0.086	1372	305	75	0.055
Kunnath et al. 1997, A6	434	448	690	35.5	9.5	0.02	0.01	0.122	0.086	1372	305	75	0.055
Kunnath et al. 1997, A7	434	448	690	32.8	9.5	0.02	0.01	0.132	0.093	1372	305	80	0.058
Kunnath et al. 1997, A8	434	448	690	32.8	9.5	0.02	0.01	0.132	0.093	1372	305	80	0.058
Kunnath et al. 1997, A9	434	448	690	32.5	9.5	0.02	0.01	0.134	0.093	1372	305	63	0.046
Kunnath et al. 1997, A10	434	448	690	27	9.5	0.02	0.01	0.161	0.101	1372	305	82	0.060
Kunnath et al. 1997, A12	434	448	690	27	9.5	0.02	0.01	0.161	0.101	1372	305	81	0.059
Hose et al., 1997, SRPH1	414	455	746	41.1	22.2	0.026	0.009	0.091	0.148	3660	610	320	0.087
Kowalsky et al. 1996, FL3	445	477	620	38.6	15.9	0.036	0.009	0.104	0.281	3656	457	340	0.093
Lehman et al. 1998, 415	606.8	462	630	31	15.9	0.015	0.007	0.137	0.072	2438.4	609.6	127	0.052
Lehman et al. 1998, 815	606.8	462	630	31	15.9	0.015	0.007	0.137	0.072	4876.8	609.6	445	0.091
Lehman et al. 1998, 1015	606.8	462	630	31	15.9	0.015	0.007	0.137	0.072	6096	609.6	635	0.104
Lehman et al. 1998, 407	606.8	462	630	31	15.9	0.007	0.007	0.137	0.072	2438.4	609.6	127	0.052
Lehman et al. 1998, 430	606.8	462	630	31	15.9	0.03	0.007	0.137	0.072	2438.4	609.6	178	0.073
Calderone et al. 2000, 328	606.8	441	602	34.5	19	0.027	0.009	0.158	0.091	1828.8	609.6	125	0.068
Calderone et al. 2000, 828	606.8	441	602	34.5	19	0.027	0.009	0.158	0.091	4876.8	609.6	465	0.095
Calderone et al. 2000, 1028	606.8	441	602	34.5	19	0.027	0.009	0.158	0.091	6096	609.6	889	0.146
Henry 1998, 415p	606.8	462	647	37.2	15.9	0.015	0.007	0.114	0.12	2438.4	609.6	127	0.052
Henry 1998, 415s	606.8	462	647	37.2	15.9	0.015	0.004	0.065	0.06	2438.4	209.6	127	0.052
Ang et al. 1981, No. 1	308	308	465	26	16	0.026	0.008	0.095	0.208	1600	400	60	0.038
Vu et al. 1998, NH3	430.2	428	599	39.4	15.9	0.024	0.012	0.131	0.15	910	457	50	0.055
Moyer and Kowalsky, C1	434.37	565	696	32.7	19.1	0.021	0.009	0.120	0.043	2438.4	457.2	149.9	0.061
Moyer and Kowalsky, C2	434.37	565	696	34.2	19.1	0.021	0.009	0.114	0.043	2438.4	457.2	261.6	0.107
Moyer and Kowalsky, C3	434.37	565	696	31.7	19.1	0.021	0.009	0.123	0.043	2438.4	457.2	261.9	0.107
Moyer and Kowalsky, C4	434.37	565	696	33.9	19.1	0.021	0.009	0.115	0.043	2438.4	457.2	335.3	0.138
			*Assumed (fu/fy = 1.4)										
MIN	300	308	465	23.1	7	0.007	0.004	0.065	0.043	750.0	209.6	40.0	0.038
MAX	607	565	746	41.1	43	0.036	0.015	0.286	0.281	9140.0	1520.0	889.0	0.146
AVG	478	461	649	32.0	15	0.021	0.010	0.145	0.104	2455.7	475.9	192.8	0.070

* Additional information for each test can be found in the Column Structural Performance Database <www.ce.washington.edu/~peera1>.

8.4   Equation to Predict Peak Tension Strain Prior to Bar Buckling Upon Reversal of Load

Based on the Goodnight et al. dataset, Table 1.1, which contained measured strain data for reinforcing bars, an empirical equation was devised to predict the peak tensile strain prior to bar buckling upon reversal of load, Eqn 8.1. Due to the empirical nature of the equation, limits on its applicability to columns outside the dataset must be employed. These limits will be addressed when comparing the accuracy of bar buckling predictions for the Berry et al. dataset, Table 8.3. A comparison of the accuracy of Eqn 8.1 evaluated against the measured peak tensile strains prior to bar buckling from the Goodnight et al. dataset appears in Figure 8.5.   The accuracy of the equations can alternatively be visualized in the format of a cumulative probably distribution, Figure 8.6.   The x-axis of Figure 8.6, (Strain at Bar Buckling / Equation Strain), can be interpreted as a ratio of demand to capacity.   Each observation of bar buckling is given a probability of 1/n where n is to the total number of observations.   These individual observations are sorted in ascending order of measured/equation strain. The first observation, with the lowest ratio of measured/equation value has a probability of 1/n, while the second has a probability of 2/n, until the final observation has a probability of 1. The normal cumulative distribution function is evaluated with the mean and standard deviation of the (Strain at Bar Buckling / Equation Strain) dataset. If the normal distribution is selected, and the Goodnight et al. dataset is chosen to be representative of bridge columns in general, Figure 8.6 would imply that there is a 40% probability of bar buckling if the demand equals the predicted capacity. Comments on applicability of Eqn 8.1 to columns outside the dataset will be reserved for later sections of this report when predictions are made for the Berry et al. (2006) dataset in Table 8.3.

$$\varepsilon s_{bb} = 0.03 + 700\rho_s \frac{f_{yhe}}{E_s} - 0.1 \frac{P}{f'_{ce}A_g}$$

Peak Tension Strain Prior to Bar Buckling during Load Reversal

Eqn 8.1

$$\rho_s = \frac{4A_{sp}}{D's}$$ Transverse Volumetric Steel Ratio, influences confinement and bar restraint.

$$\frac{f_{yhe}}{E_s}$$ Inelastic Transverse steel is less effective at restraining longitudinal bars.

$$\frac{P}{f'_{ce}A_g}$$ Axial Load Ratio expressed as a decimal with expected material properties.

$$mean\left(\frac{\varepsilon s_{Meausred}^{bb}}{\varepsilon s_{Eqn\ 8.1}^{bb}}\right) = 1.05 \ and \ COV = 0.199$$
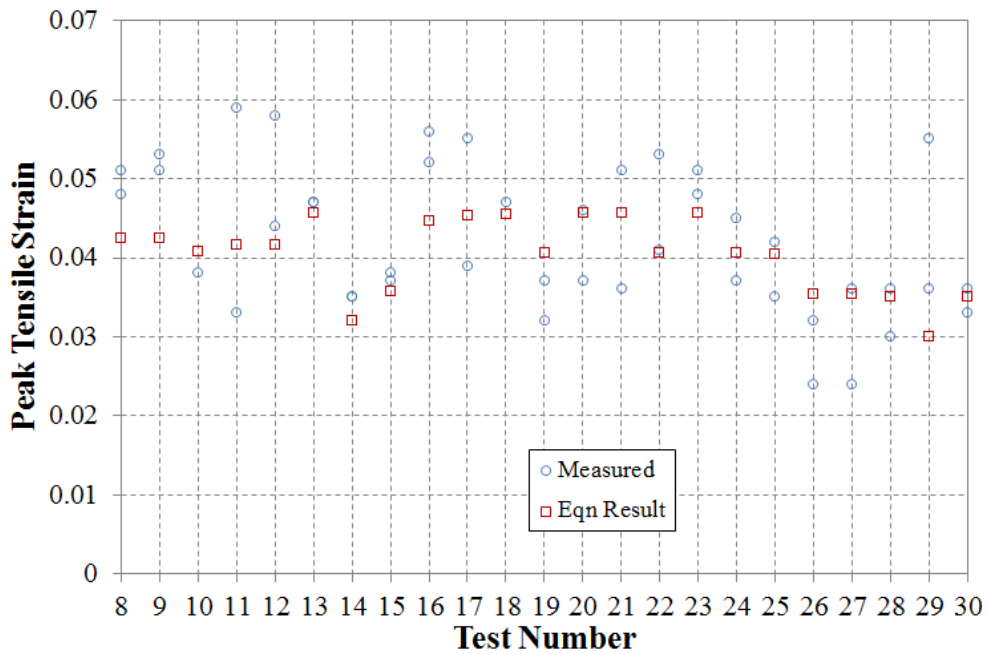
Figure 8.5 Graph of Measured Peak Tensile Strains and Result of Eqn 8.1
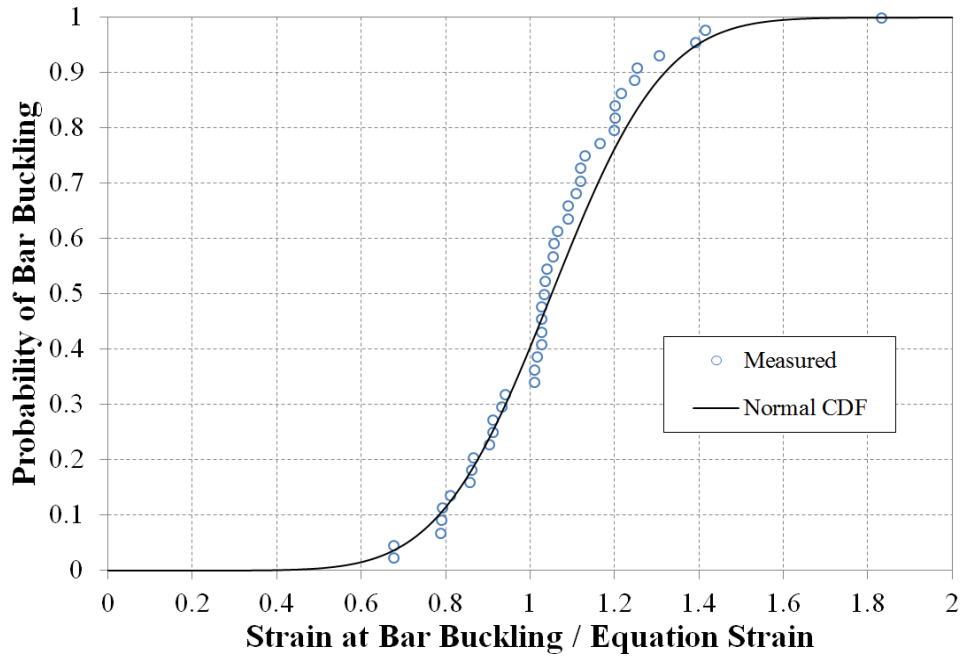
Figure 8.6 Cumulative Probability Distribution for Peak Tensile Strain Prior to Bar Buckling Eqn 8.1 (x-axis represents demand / calculation)
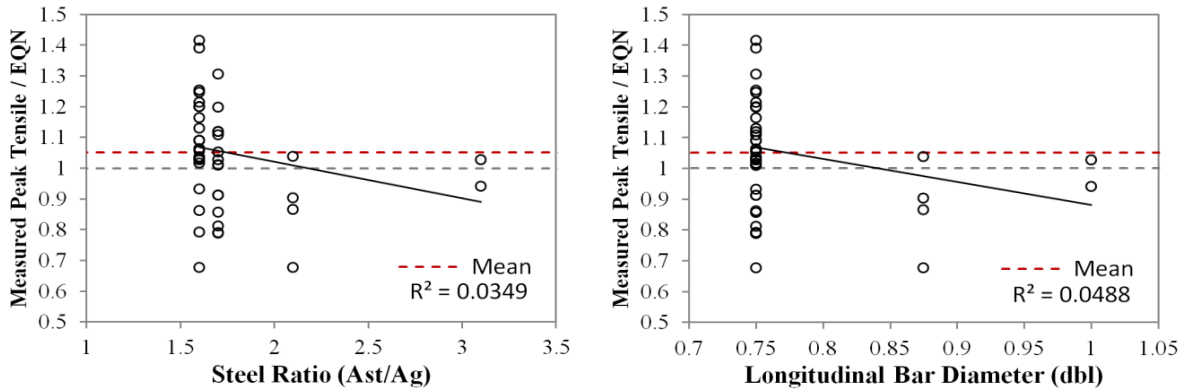
Figure 8.7 Sensitivity of Eqn 8.1 to Individual Variables in the Goodnight et al. Dataset
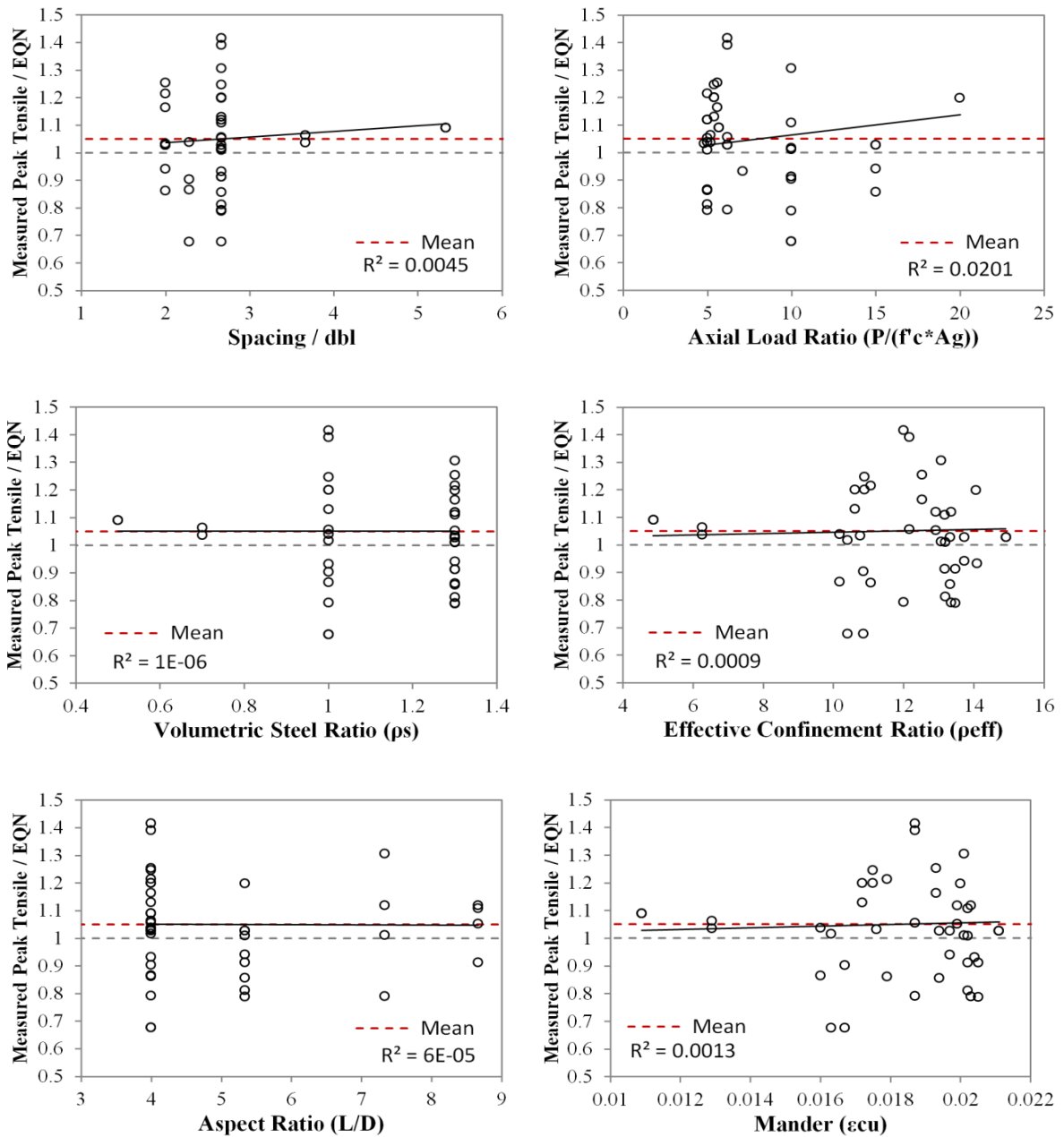
Figure 8.8 Sensitivity of Eqn 8.1 to Individual Variables in the Goodnight et al. Dataset

8.5   Column Deformation at Peak Tensile Strain Prior to Bar Buckling

Predictions for the lateral column deformation at the peak tension strain prior to bar buckling can be made by employing monotonic section analysis and an equivalent curvature distribution. A modified plastic hinge method based on the measured spread of plasticity in the Goodnight et al. dataset is briefly described below for a cantilever column in single bending, Eqn 8.2 through Eqn 8.11 and Figure 8.9.

$\Delta_T = \left(\Delta_e + \Delta_{sp} + \Delta_p + \Delta_{shear}\right)$ Total Top Column Displacement   Eqn 8.2

$\Delta_e = \phi_{base}L^2/3$ (Single) Elastic Flexural Displacement before First Yield   Eqn 8.3

$\Delta_e = \phi_y'\left(M/M_y'\right)L^2/3$ (Single) Elastic Flexural Displacement after First Yield   Eqn 8.4

$L_{sp} = U\left(1 - \dfrac{P}{f_{ce}'A_g} - \dfrac{L_c}{16D}\right)\dfrac{f_{ye}d_{bl}}{\sqrt{f_{ce_f}'}}$ $U = 0.4$ for ksi and 0.152 for MPa units   Eqn 8.5

$\Delta_{sp} = \left(\phi_{base}L_{sp}\right)L$ Strain Penetration Displacement   Eqn 8.6

$\phi_p = \phi_{base} - \phi_y'\left(M/M_y'\right)$ Plastic Curvature at the Base Section   Eqn 8.7

$\Delta_p = \phi_p\left(L_{pr}/2\right)\left[L - L_{pr}/3\right]$ (Single) Plastic Displacement for Triangular Plastic Curvature Distribution   Eqn 8.8

$k = 0.2\left(\dfrac{f_u}{f_y} - 1\right) \leq 0.08$ Same Definition of k as Priestley, Calvi, and Kowalsky (2007)   Eqn 8.9

$$Lpr_t = 2kL_c + 0.75D$$

(Single Bending, $L_c = L$) Tension Hinge Length

Based on Triangular Distribution

Eqn 8.10

$$Lpr_c = 2kL_c$$

(Single Bending, $L_c = L$) Compression Hinge Length

Based on Triangular Distribution

Eqn 8.11
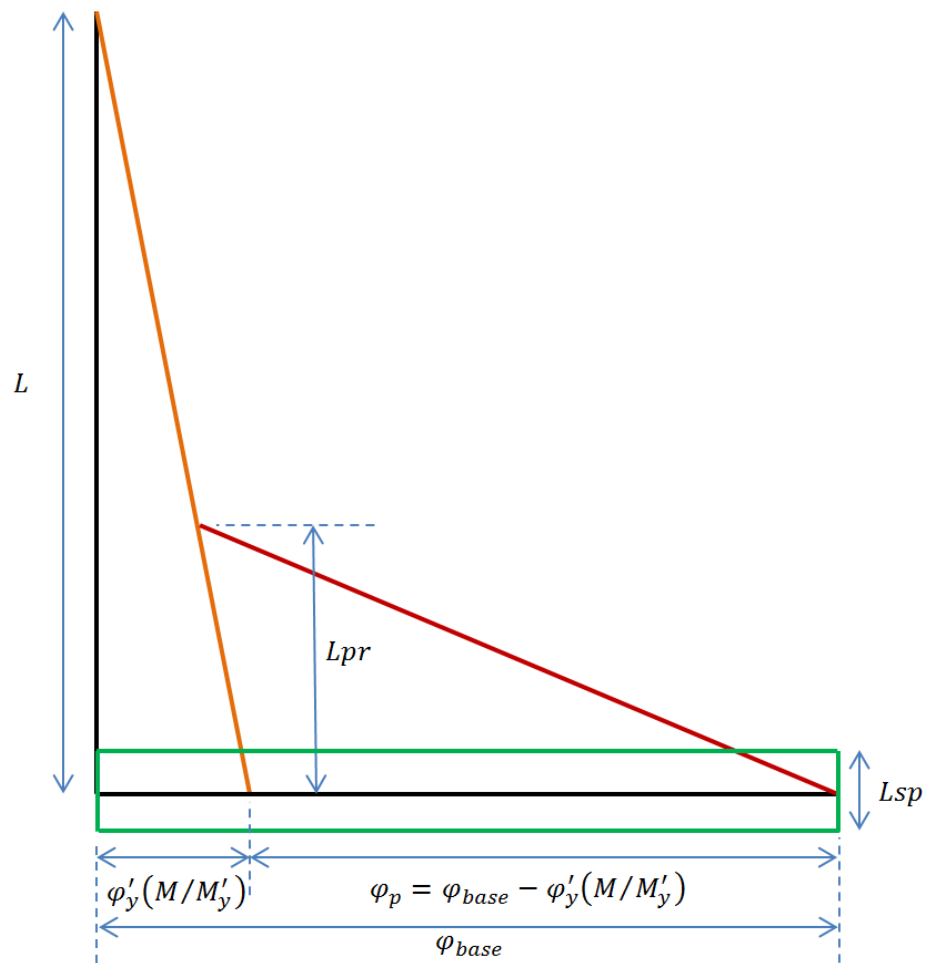
Figure 8.9 Modified Plastic Hinge Method for a Column in Single Bending

Predictions for the peak tensile strain before bar buckling, Eqn 8.1 are translated to top column displacements using monotonic section analysis in a script named Cumbia and Eqn 8.2 through Eqn 8.11. Specifically, the tensile triangular plastic hinge length, Lpr_t from Eqn 8.10, is employed to translate a tensile strain to a top column displacement. The result of this analysis appears in Figure 8.10 and Figure 8.11. Introduction of the Modified Plastic Hinge Method adds conservatism, with fewer specimens experiencing bar buckling at the Eqn 8.1 strain. As discussed previously, this additional conservatism is less than would be induced if the plastic hinge method from Priestly, Calvi, and Kowalsky (2007) were used instead.

$$mean\left(\frac{\Delta^{bb}_{Meausred} \ at \ \varepsilon s^{bb}_{Meausred}}{\Delta_{Cumbia} \ at \ \varepsilon s^{bb}_{Eqn \ 8.1} \ with \ Modified \ Lpr \ Method}\right) = 1.17 \ and \ COV = 0.157$$
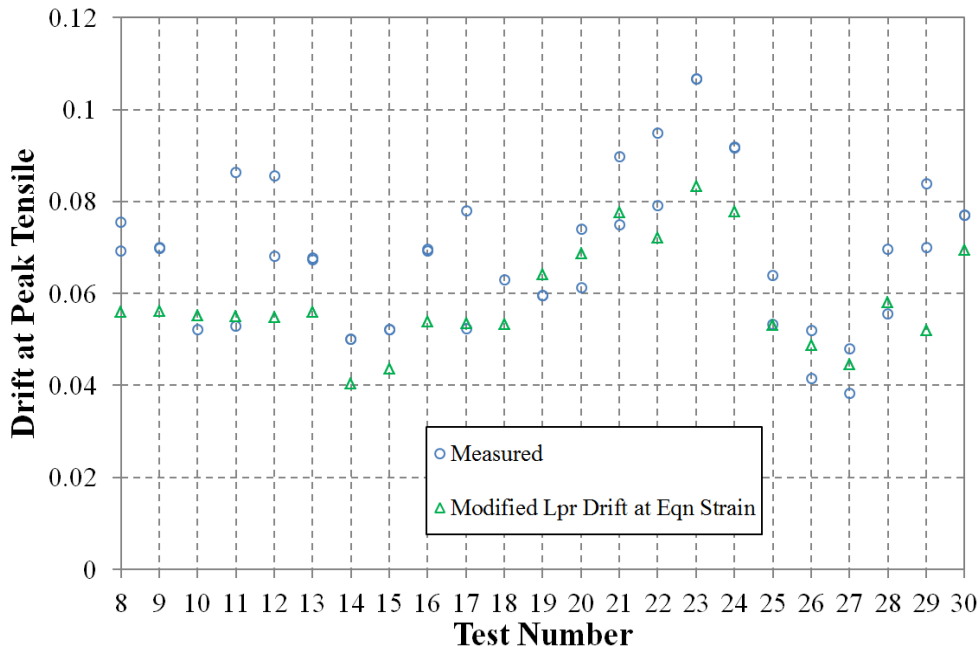
Figure 8.10 Graph of Measured Peak Tensile Drift and Result of $\Delta_{Cumbia} \ at \ \varepsilon s^{bb}_{Eqn \ 8.1}$
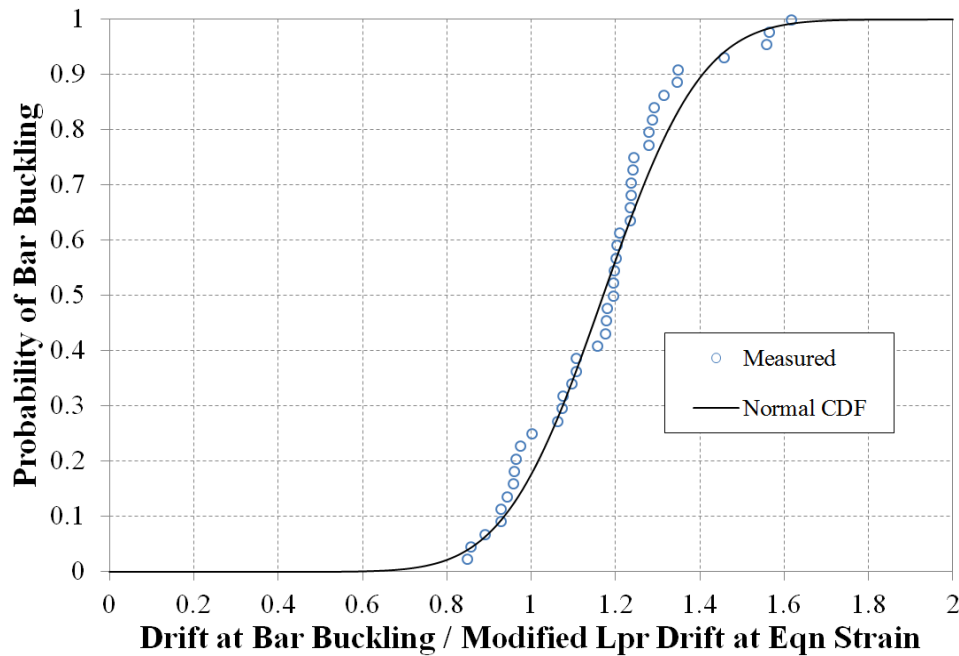
Figure 8.11 Cumulative Probability Distribution for $Drift_{bb}$ at $\varepsilon s_{Eqn\ 8.1}^{bb}$ (x-axis represents demand / calculation)

8.6   Berry (2006) Statistical Drift-Based Bar Buckling Model for Circular Bridge Columns

Analytical studies by Berry (2006) utilized a database of experimentally tested bridge columns with defined material, geometric, and reinforcing properties, with reported bar buckling observations.   The dataset, in Table 8.3, is a subset of the Column Structural Performance Database <www.ce.washington.edu/~peera1>. The dataset in Table 8.3 is more specific to bridge columns than the generalized circular column dataset presented in Berry and Eberhard (2005). Berry (2006) devised a statistical drift-based bar buckling model, Eqn 8.12, to fit the bridge column dataset.

It is important to note that low cycle fatigue load history tests by Kunnath et al. (1997) specimens A4, A5, and A6 were excluded from the formulation of Eqn 8.12. These load

histories are more severe than traditional symmetric three-cycle-set deformation histories which include a gradual ramp up of aptitude with three cycles at a given level of displacement. The low cycle fatigue load histories consisted of repeated cycling at a given displacement amplitude until bar buckling was observed. Alternatively, the peak excursion style load histories of Moyer and Kowalsky (2001) specimens No. 2, 3, and 4 were included in the dataset. These load histories were devised to isolate specific influences of peak tensile strain on bar buckling and are, in general, less severe than a symmetric three-cycle-set load history employed in Moyer and Kowalsky (2001) Specimen No. 1. Future evaluation of the strain based bar buckling prediction in this report includes the entire dataset of Table 8.3, regardless of load history employed.

$$\frac{\Delta_{bb}^{calculated}}{L}(\%) = 3.25\left(1 + 150\frac{\rho_{eff}d_{bl}}{D}\right)\left(1 - \frac{P}{f_c'A_g}\right)\left(1 + \frac{L}{10D}\right)$$
 from Berry (2006)   Eqn 8.12

$\rho_{eff} = \rho_s f_{yh}/f_c'$ Parameter termed the effective confinement ratio.

$$mean\left(\frac{\Delta_{bb}^{measured}}{\Delta_{bb}^{calc}}\right) = 1.01 \; and \; COV = 24.7$$
 For the Berry (2006) Circular Bridge Column Dataset
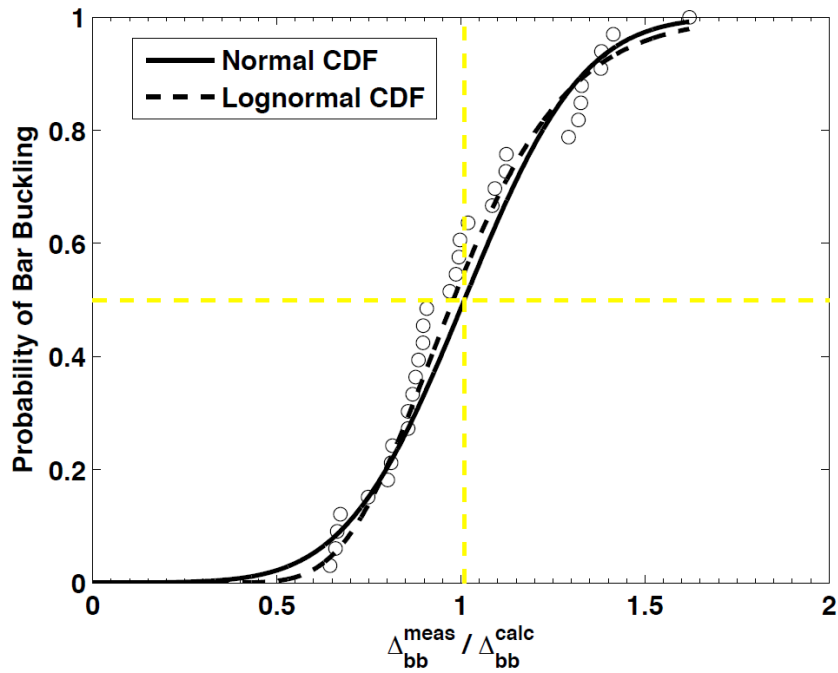
Figure 8.12 Berry (2006) Evaluation of Eqn 8.12 for the Berry (2006) Circular Bridge Column Dataset

8.7 Berry (2006) Bar Buckling Model Applied to the Goodnight et al. Dataset

Experiments within the Goodnight et al. dataset fall within the range of applicability of the Berry (2006) drift-based bar buckling model, Eqn 8.12. The accuracy of Eqn 8.12 in predicting bar buckling observations in the Goodnight et al. dataset is shown in Figure 8.13 and Figure 8.14.

$$mean\left(\frac{\Delta_{bb}^{measured}}{\Delta_{bb}^{calc}}\right) = 0.92 \; and \; COV = 0.171$$

Berry (2006) Eqn 8.12 applied to Goodnight et al. dataset
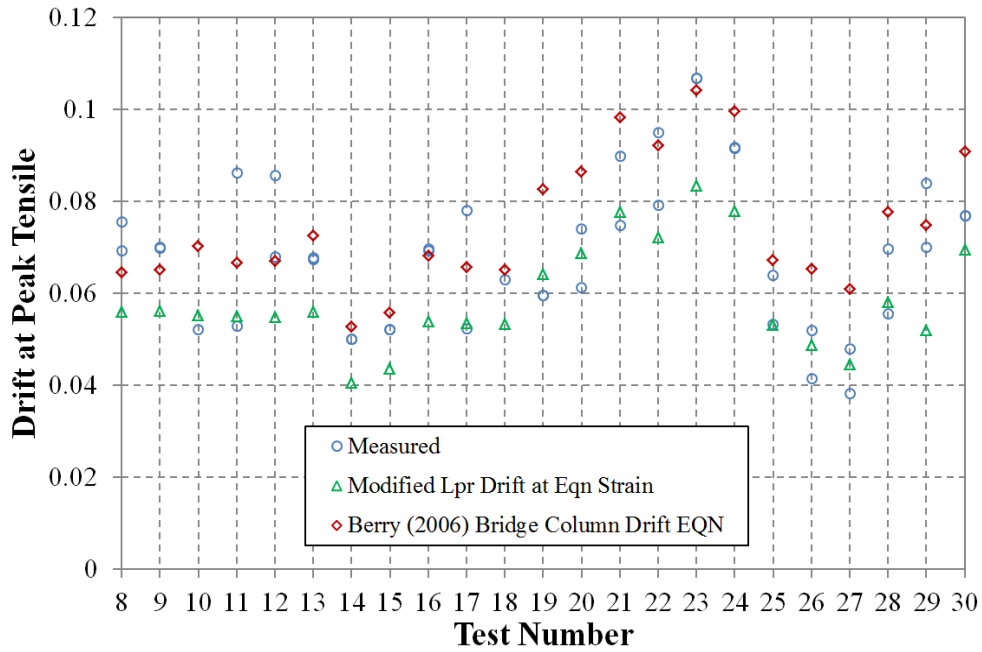
Figure 8.13 Graph of Measured Peak Tensile Drift and Result of Berry (2006) Eqn 8.12
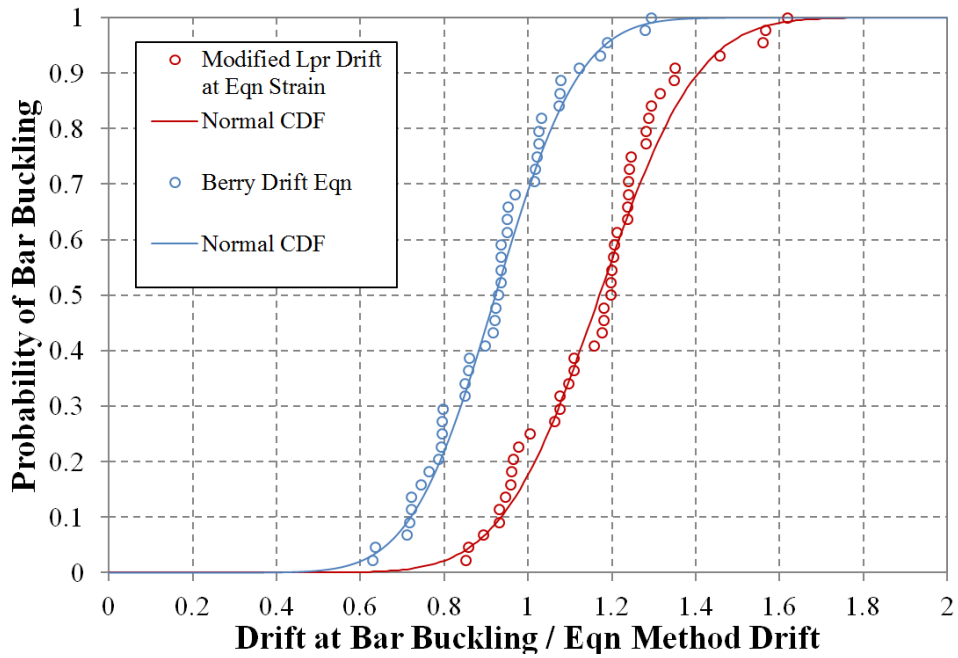
Figure 8.14 CDF for Berry (2006) Eqn 8.12 Applied to Goodnight et al. Dataset

8.8   Evaluation of Strain Based Bar Buckling Predictions for the Berry (2006) Dataset

Strain based predictions for bar buckling of individual tests within the Berry (2006) dataset, Table 8.3, were evaluated.   Reported material, geometric, and reinforcement properties of each experiment were used to run a moment-curvature analysis.   The peak tensile strain prior to bar buckling from Eqn 8.1 and its associated deformation from the Modified Plastic Hinge Method were compared to reported bar buckling observations.   The measured to predicted bar buckling displacement predictions using the Eqn 8.1 strain and Modified Plastic Hinge Method for experiments in the Berry (2006) dataset are shown in Figure 8.15 and Figure 8.17.   Measured to predicted bar buckling ratios for many of the Berry (2006) dataset experiments follow trends in the Goodnight et al. dataset, but some reported buckling observations occur at significantly larger deformations than the strain-based approach from Eqn 8.1 would predict.

Specific variables within the Berry (2006) dataset can account for some of the disparity in bar buckling predictions, Figure 8.15.   The severity of the imposed lateral displacement history can influence bar buckling.   Low cycle fatigue experiments by Kunnath et al. (1997), specimens A4, A5, and A6, have smaller displacements at bar buckling than the prediction. Alternatively, the peak excursion load histories of Moyer and Kowalsky (2001), specimens No. 2, 3, and 4, have larger displacements at bar buckling.   Earthquake load history tests by Kunnath et al (1997) specimens A7, A8, A9, A10, and A12 along with Goodnight et al. specimens 8, 10, 11, 12, 17, and 18 are included in their respective datasets.

Scaled specimens by Lehman et al. (1998) and Calderone et al. (2000) utilized smooth spirals with a yield stress which exceeded the upper bound yield stress for the A706 steel designation (78ksi).   A comparison of the stress-strain response of spiral reinforcement from Lehman et al. (1998) and Goodnight et al. (material from Tests 25-30) appears in Figure 8.16.   The stability of spiral layers confining the core concrete and restraining longitudinal bars from buckling is influenced by this change in behavior.   In general, experiments from

Lehman et al. (1998) and Calderone et al. (2000) had bar buckling observations at displacements which exceed the strain based prediction.

The influence of individual variables on the accuracy of strain based bar buckling displacements for the combined Goodnight and Berry (2006) datasets appears in Figure 8.18. Column aspect ratio and the ratio of spiral spacing to longitudinal bar diameter appear to be the only variables which show a trend regarding the accuracy of the strain-based approach.

$$mean\left(\frac{\Delta^{bb}_{Meausred}\ for\ the\ Combined\ Dataset}{\Delta_{Cumbia}\ at\ \varepsilon s^{bb}_{EQN1}\ with\ Modified\ Lpr\ \ Method}\right) = 1.21\ and\ COV = 0.227$$
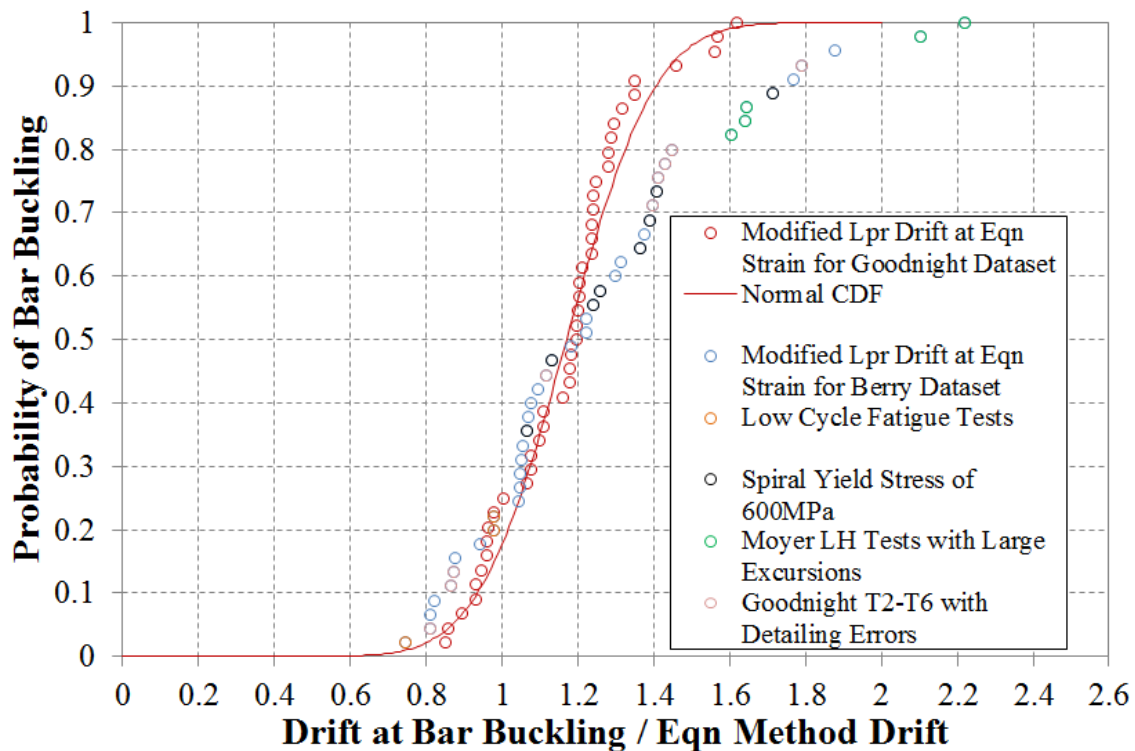
Figure 8.15 Cumulative Probability Distribution for Strain Based Bar Buckling Applied to Berry (2006) Dataset with Influence of Specific Test Variables
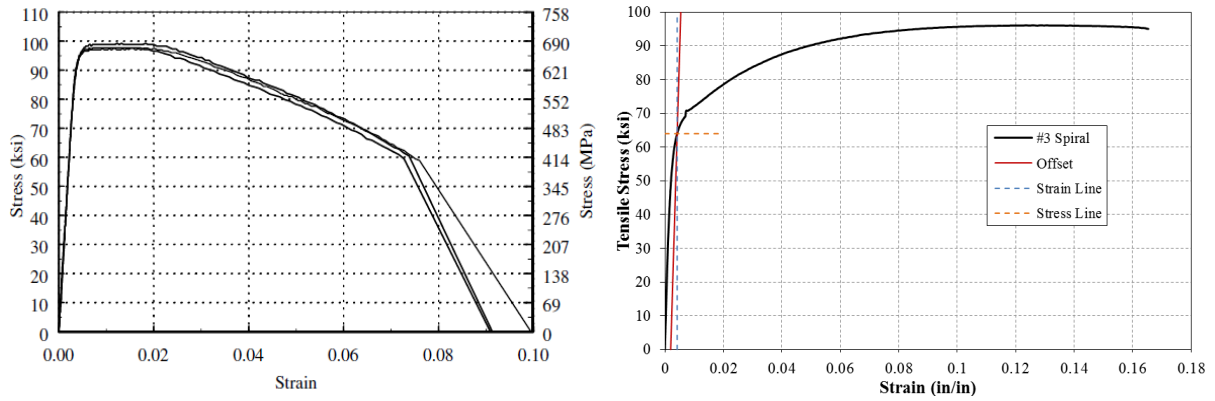
Figure 8.16 (Left) Spiral Stress-Strain Response Reported in Lehman et al. (1998) and Similar Characteristics in Spirals from Calderone et al. (2000); (Right) Sample Spiral Tensile Test Result for Specimens 25-30 of Goodnight et al.
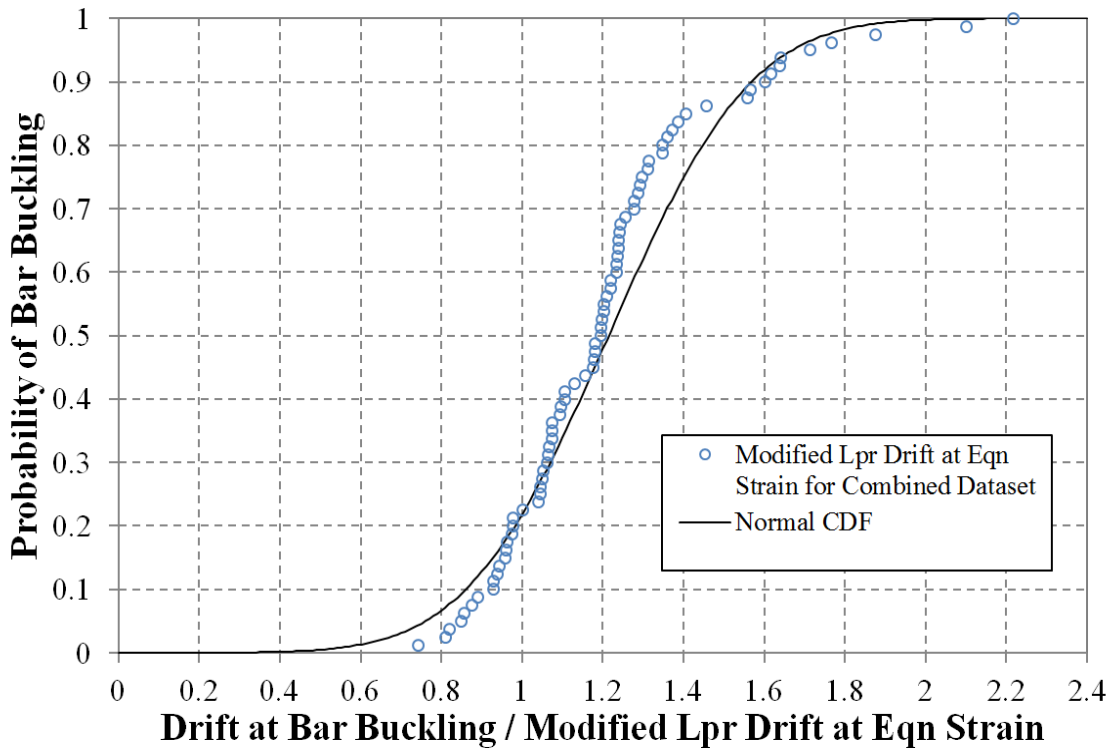
Figure 8.17 CDF for Strain Based Bar Buckling Eqn 8.1 for the Combined Dataset
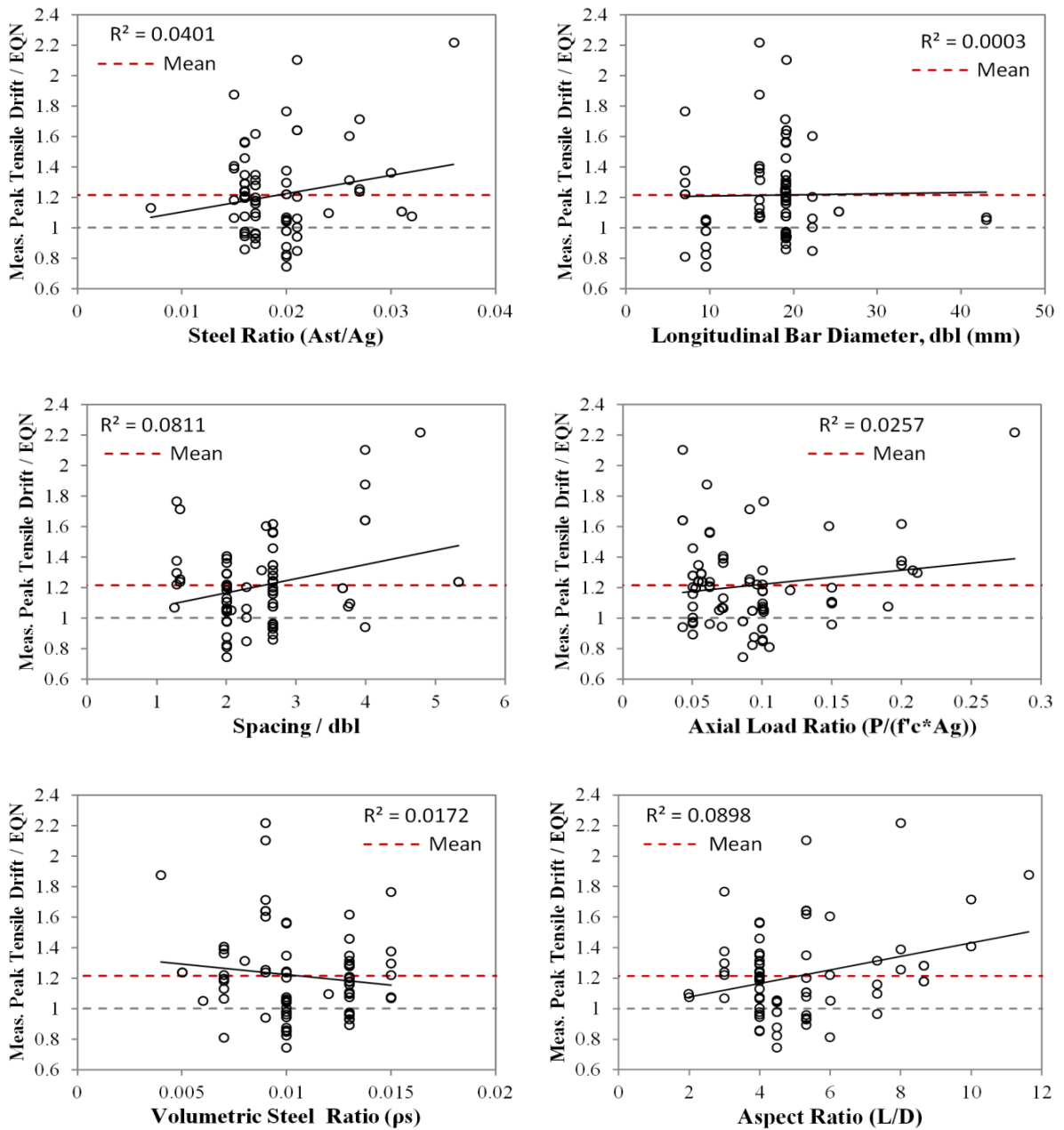
Figure 8.18 Sensitivity of Strain Based Bar Buckling Eqn 8.1 to Individual Variables in the Combined Dataset

8.9 Drift Based Approach Considering Combined Berry (2006) and Goodnight et al. Datasets

Since material strains are not available for tests in the Berry (2006) dataset, an equation with parameters designed to fit both datasets can only be created on the basis of drift. The strain based approach in Eqn 8.1 utilizes the same variables as the drift based Berry (2006) Eqn 8.12, with the exception of L/D which is only needed to evaluate the drift. Also, $\rho_s f_{yh}/E_s$ was found to more adequately describe the effect of transverse steel on bar buckling in the Goodnight et al. dataset when compared to $\rho_s f_{yh}/f_c'$ employed by Berry (2006).   Both were considered in the formulation of the drift-based equation for the combined dataset, and $\rho_s f_{yh}/E_s$ provided a more accurate result. The proposed Eqn 8.13 can be used to evaluate the peak tensile displacement before bar buckling is expected to occur upon reversal of loading in a cyclic deformation history. It is important to note that lateral displacement history influences bar buckling, and that this equation is formed without consideration of the varying load histories utilized in each experiment. The influence of individual variables on the accuracy of Eqn 8.13 applied to the combined Goodnight and Berry (2006) datasets appears in Figure 8.20. A graphical comparison of the accuracy of the three predictive bar buckling methods appears in Figure 8.19 in the form of a cumulative probability distribution.

$$\frac{\Delta_{bb}^{calculated}}{L}(\%) = 0.9 - 3.13\frac{P}{f_{ce}'A_g} + 142000\rho_s\frac{f_{yhe}}{E_s} + 0.45\frac{L}{D} \quad \begin{array}{l}\text{for Combined}\\ \text{Dataset}\end{array} \qquad \text{Eqn 8.13}$$

$$mean\left(\frac{\Delta_{bb}^{measured}}{\Delta_{bb}^{calc}}\right) = 1.09 \; and \; COV = 0.241 \quad \begin{array}{l}\text{for Combined Berry (2006) and}\\ \text{Goodnight et al. Dataset}\end{array}$$
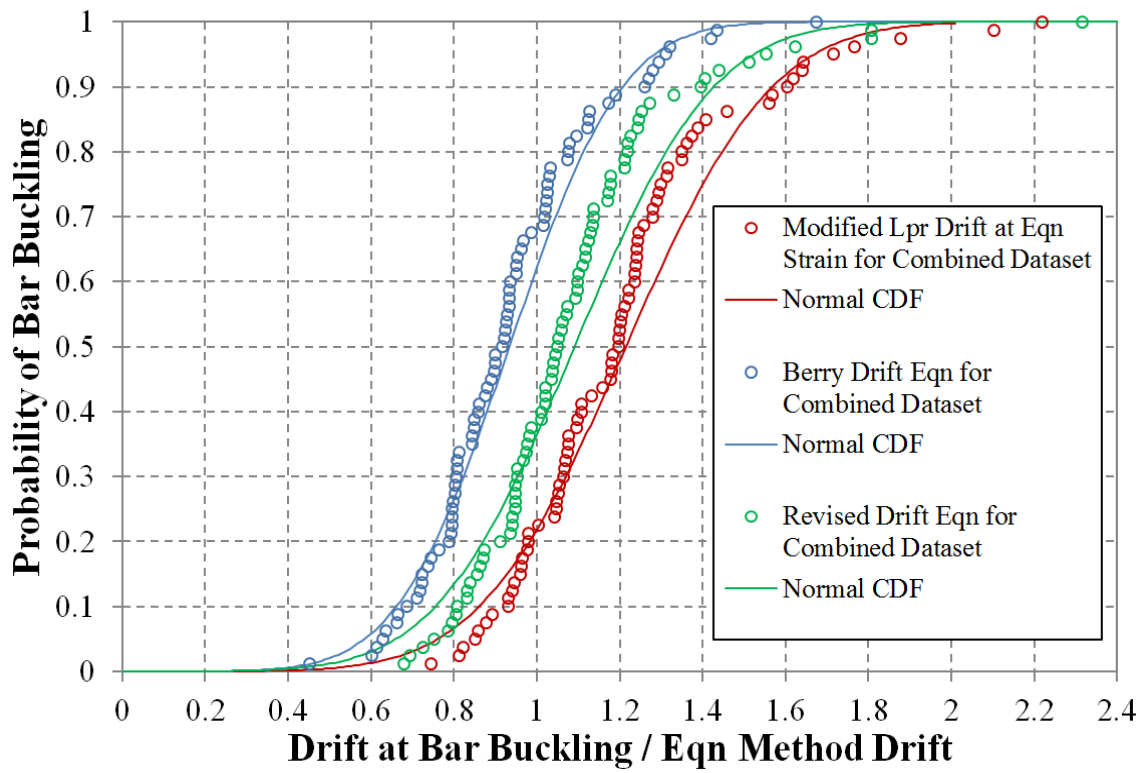
Figure 8.19 Cumulative Probability Distribution for Drift-Based Equation for Combined Dataset Compared to Berry (2006) and Strain-Based Approaches
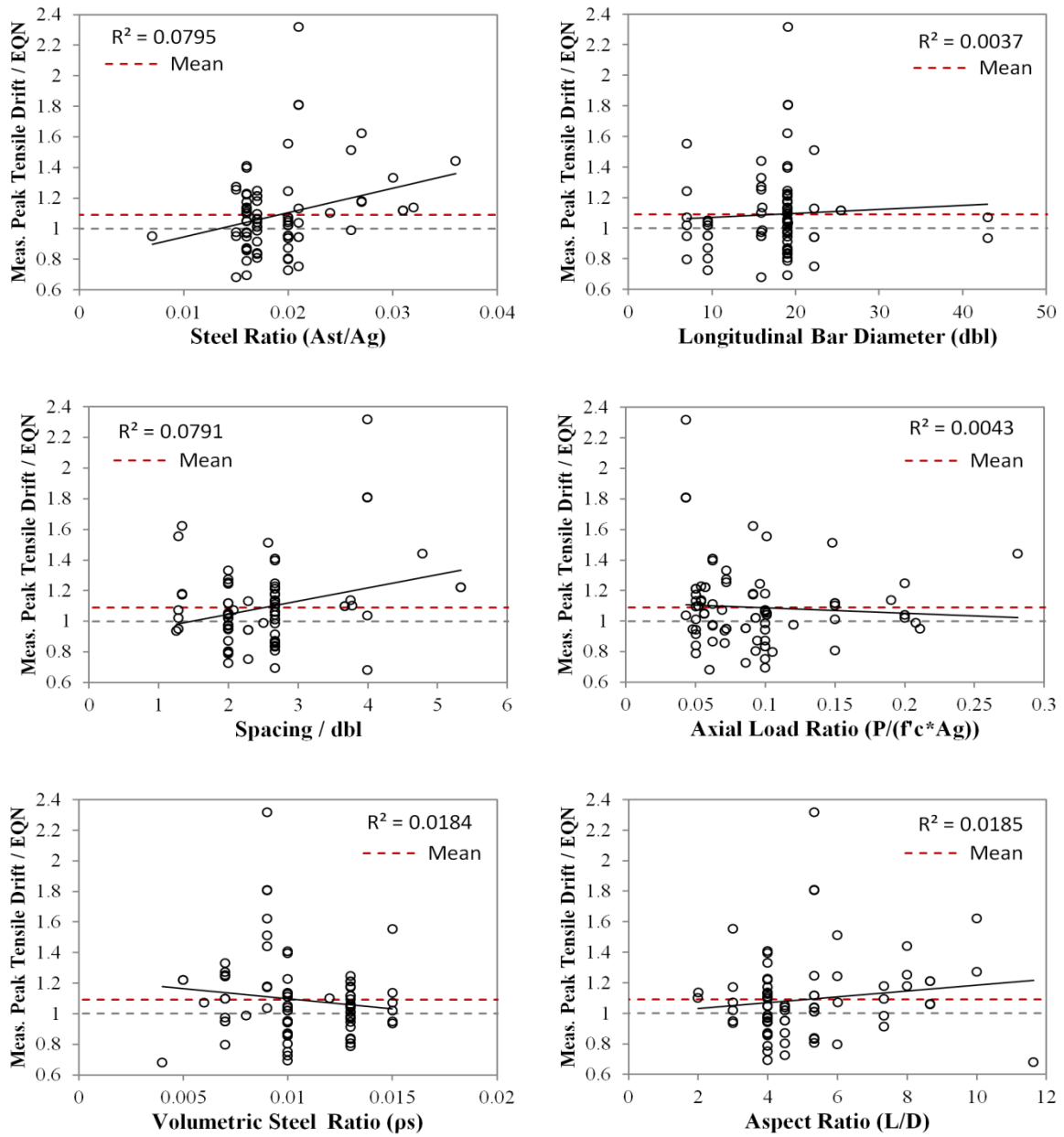
Figure 8.20 Sensitivity of Eqn 8.13 to Individual Variables in the Combined Dataset

8.10 Feng (2013) Bar Buckling Strain Limit Expressions from Finite Element Analysis

Feng (2013) proposed a series of equations to describe bar buckling behavior observed in finite element analysis. The analysis model, Figure 8.21, considered an extreme fiber longitudinal bar with realistic boundary conditions. The influence of the following behaviors were included in the analysis: (1) dilation of core concrete under compression, (2) restraint provided by individual spiral layers which can go inelastic, and (3) development of the longitudinal bar into the adjoining member. Specific strain histories were applied to the longitudinal bar to evaluate the influence of peak tension strain and prior compressive strains on bar buckling behavior. This behavior, once quantified, was used to create the multi-linear regression Eqn 8.14 through Eqn 8.18 to predict the peak tensile strain prior to bar buckling upon reversal of load.   In the expression, ε_t and ε_c are the tensile and compressive longitudinal bar strains (both taken as positive), d_{bl} and d_h are the longitudinal and transverse steel bar diameters, and s is the centerline spacing of transverse steel.
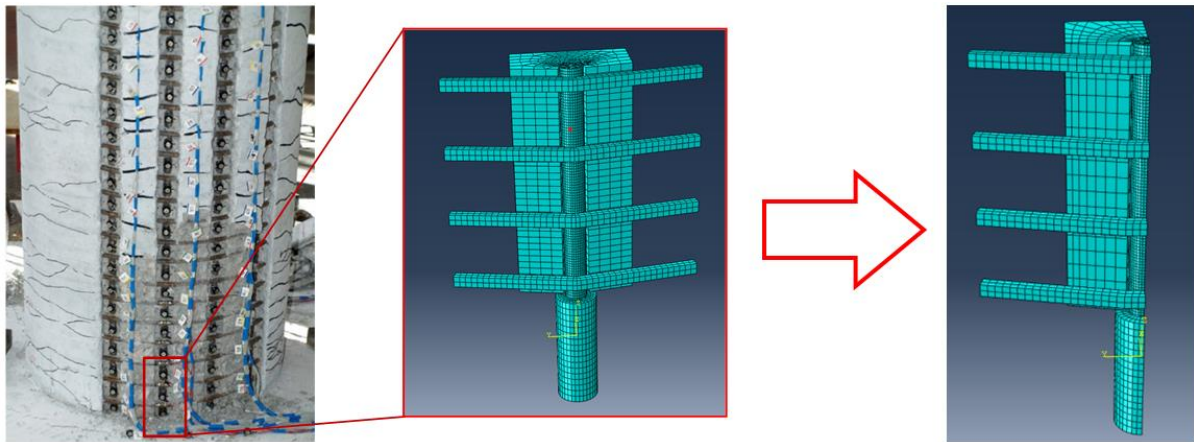
Figure 8.21 Feng (2013) Finite Element Model Geometry for Critical Region of Extreme Fiber Bar with Realistic Boundary Conditions

An evaluation of the Feng (2013) method applied to Test 9 from Goodnight et al. appears in Figure 8.22. The bar buckling prediction is defined as the intersection of the multi-linear regression and the tensile-compressive bar strain relationship from moment-curvature analysis. The tensile and compressive longitudinal bar strains are evaluated at each level of curvature in the section analysis. The tension and compression strain couple at the intersection point represents a compression cycle followed by a tension cycle to the same level of displacement, which would induce bar buckling upon subsequent reversal of load. The Priestley, Calvi, and Kowalsky (2007) hinge method is used to translate the curvature at the intersection point strain to member deformation, Figure 8.23. If the displacement amplitudes or the strain history is known, the model can be used to evaluate the influence of previous load history on bar buckling. However, this was not done for bar buckling predictions in this study, since the load history is not known in the design of new structures.

$$\varepsilon_t = \frac{-15\left(\varepsilon_c - \dfrac{0.0205}{\sqrt[3]{\dfrac{s}{d_{bl}}} - 1}\right)}{\left(\dfrac{d_{bl}}{d_h} - 1\right)^2} \qquad \text{Eqn 8.14}$$

$$\varepsilon_t \geq -1.7\frac{s}{d_{bl}}\sqrt{\frac{d_h}{d_{bl}}}\varepsilon_c + 0.045\sqrt{\frac{s}{d_{bl}}} \qquad \text{Eqn 8.15}$$

$$\varepsilon_t \leq 0.09, \qquad if \ \frac{s}{d_{bl}} < 3 \qquad \text{Eqn 8.16}$$

$$\varepsilon_t \leq 0.06, \qquad if \ \frac{s}{d_{bl}} > 4 \qquad \text{Eqn 8.17}$$

$$\varepsilon_t \leq 0.09 - 0.03\left(\frac{s}{d_{bl}} - 3\right), \qquad if \ 3 < \frac{s}{d_{bl}} < 4 \qquad \text{Eqn 8.18}$$
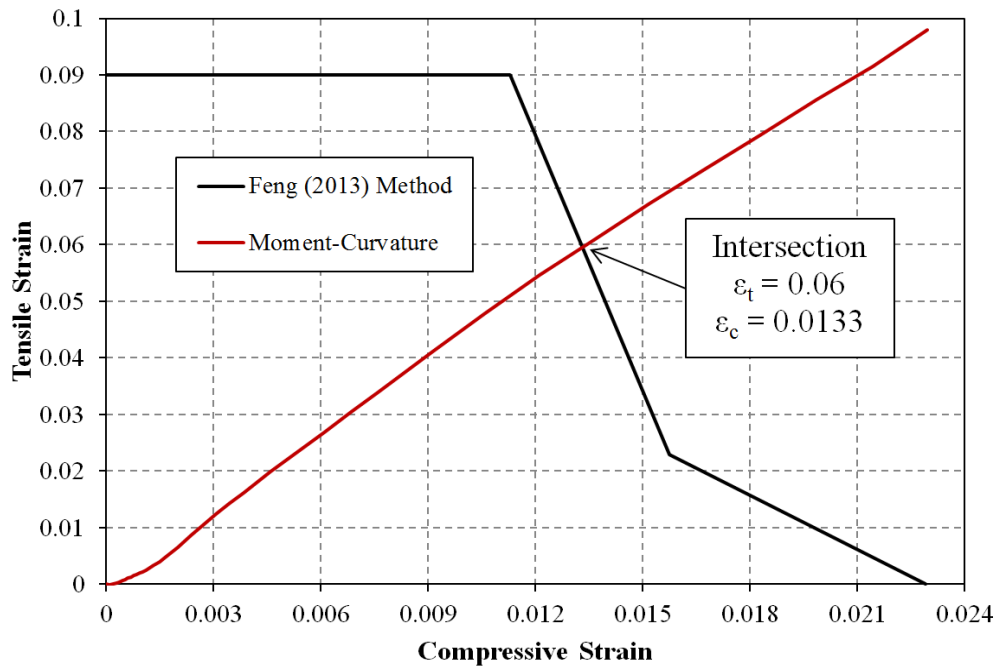
Figure 8.22 Feng (2013) Method Applied to Test 9 from Goodnight et al.
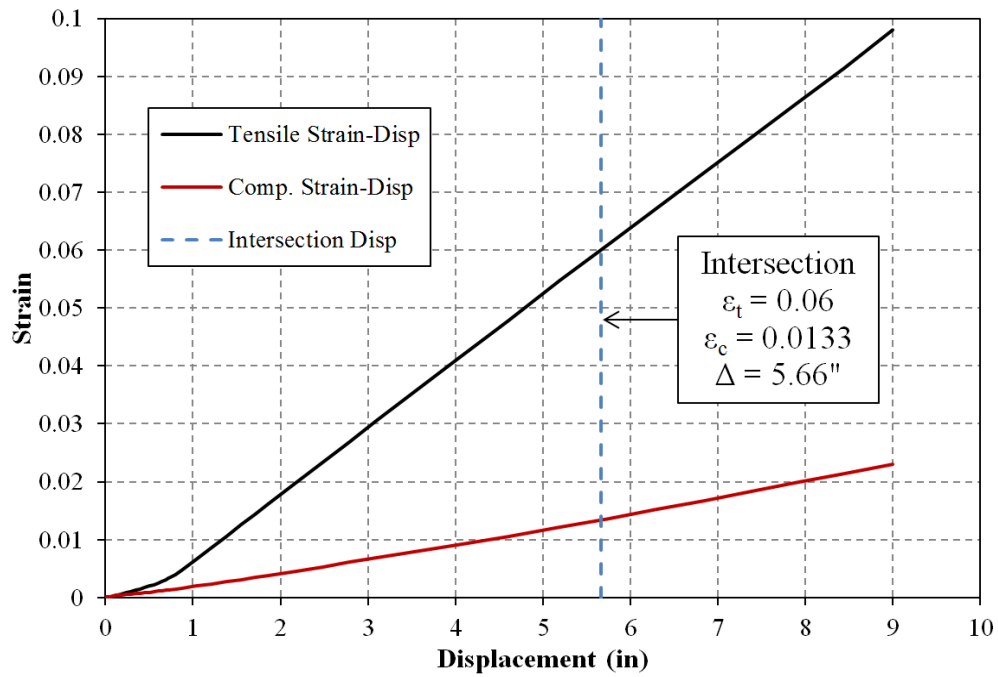
Figure 8.23 Bar Buckling at Intersection Point using PCK (2007) Hinge Length

The predicted peak tension strains which result when the Feng (2013) method is applied to Tests 8-30 of the Goodnight et al. dataset appear in Figure 8.24. For now, consider only the data points which evaluate the peak tension strain according to the tension-compression strain relationship evaluated at the same curvature and displacement, which is consistent with the PCK (2007) plastic hinge method. The peak tension strains predicted by this method exceed those measured in the tests. The Goodnight et al. (2014) modified hinge method, Figure 8.9 and Eqn 8.2 through Eqn 8.11, utilizes separate tensile and compressive hinge lengths to account for the influence of tension shift and moment gradient on the distribution of plastic curvature in columns. An adjustment to the tensile-compressive strain relationship in Figure 8.22 are necessary to account for the use of separate tensile and compressive hinge lengths. For Test 9, the extreme fiber bar tensile and compressive strain-displacement relationships are evaluated using the modified hinge method in Figure 8.25. A linear regression is used to compute the tensile and compressive strains at the same level of displacement, Figure 8.26. In comparison, this approach produces lower peak tension strains prior to bar buckling, which reflects the difference in the tensile-strain displacement relationships for the two hinge methods. To reinforce this point, the tensile strain-displacement relationship for Test 9 appears in Figure 8.27 with a monotonic prediction using the two plastic hinge methods.

The multi-linear regression approach from Feng (2013), combined with the strain-displacement relationships from the modified plastic hinge method, produced predicted peak tension strains prior to bar buckling which more closely resemble those measured in the Goodnight et al. dataset, Figure 8.24. This approach produces peak tensile strains which resemble those predicted from the statistical strain-based bar buckling approach from Eqn 8.1. The cumulative probability distribution for the ratio of the measured peak tension strain prior to bar buckling to the predicted value appears in Figure 8.28. This figure illustrates the non-conservatism in applying the Feng (2013) method with the PCK (2007) hinge method to predict peak tension strains measured in the Goodnight et al. dataset. The accuracy of these three methods in predicting the peak tension strain prior to bar buckling in the Goodnight et al. dataset is shown below. Ideally, a predictive equation would have a mean value of one

and minimize the coefficient of variation, resulting in a near vertical line at one in the cumulative probability distribution. This would also minimize the root mean squared error, which can be used to compare the accuracy of the three bar buckling strain predictions.

Mean, Coefficient of Variation, and Root Mean Squared Error

$$mean\left(\frac{\varepsilon s_{Meausred}^{bb}}{\varepsilon s_{Eqn\ 8.1}^{bb}}\right) = 1.05, COV = 0.199, RMSE = 0.188$$

$$mean\left(\frac{\varepsilon s_{Meausred}^{bb}}{\varepsilon s_{Feng\ (2013)}^{bb}\ with\ PCK\ (2007)\ Lp}\right) = 0.81, COV = 0.224, RMSE = 0.387$$

$$mean\left(\frac{\varepsilon s_{Meausred}^{bb}}{\varepsilon s_{Feng\ (2013)}^{bb}\ with\ Modified\ Lpr\ Method}\right) = 1.11, COV = 0.216, RMSE = 0.190$$

In the following section, the computed deformation at the predicted peak tensile strains are compared to the measured displacement prior to bar buckling in the Goodnight et al. dataset. The measured peak tensile drift sustained before bar buckling for columns in the Goodnight et al. dataset is compared to the predicted bar buckling drift using the following methods: [1] strain-based Eqn 8.1 with the modified plastic hinge method, [2] drift-based Eqn 8.13 with coefficients based on the combined dataset, [3] Berry (2006) drift-based Eqn 8.12, [4] Feng (2013) multi-linear regression with the PCK (2007) hinge method, and [5] Feng (2013) method with strain-displacement relationships from the modified hinge method. A test by test comparison of the result of these four methods and the measured peak tensile drift prior to bar buckling is shown in Figure 8.29. The cumulative probability distribution for the (Measured / Predicted) peak tension drift for the four methods appears in Figure 8.30. These figures as well as the summary statistics listed below indicate that the drift-based Eqn 8.13 and the Feng (2013) approach with the PCK (2007) Lp hinge method produce the most accurate results.

$$(1) \; mean\left(\frac{\Delta^{bb}_{Meausred} \; at \; \varepsilon s^{bb}_{Meausred}}{\Delta_{Cumbia} \; at \; \varepsilon s^{bb}_{Eqn \; 8.1} \; with \; Modified \; Lpr}\right) = 1.17, COV = 0.157, RMSE = 0.185$$

$$(2) \; mean\left(\frac{(\Delta/L)^{bb}_{Meausred}}{(\Delta/L)^{bb}_{Combined \; Dataset \; Eqn \; 8.13}}\right) = 1.04, COV = 0.158, RMSE = 0.164$$

$$(3) \; mean\left(\frac{(\Delta/L)^{bb}_{Meausred}}{(\Delta/L)^{bb}_{Berry \; (2006) \; Eqn \; 8.12}}\right) = 0.92, COV = 0.171, RMSE = 0.225$$

$$(4) \; mean\left(\frac{\Delta^{bb}_{Meausred} \; at \; \varepsilon s^{bb}_{Meausred}}{\Delta_{Cumbia} \; at \; \varepsilon s^{bb}_{Feng \; (2013)} \; with \; PCK \; (2007) \; Lp}\right) = 1.04, COV = 0.176, RMSE = 0.170$$

$$(5) \; mean\left(\frac{\Delta^{bb}_{Meausred} \; at \; \varepsilon s^{bb}_{Meausred}}{\Delta_{Cumbia} \; at \; \varepsilon s^{bb}_{Feng \; (2013)} \; with \; Modified \; Lpr}\right) = 1.23, COV = 0.165, RMSE = 0.212$$

As discussed previously, both plastic hinge methods induce conservatism when translating the measured peak tension strains to predicted displacements. The modified plastic hinge method reduces this conservatism significantly. The unconservative peak tensile strain predictions from the Feng (2013) method with the strain-displacement relationship from moment-curvature analysis appear to be balanced by the conservatism in the strain-displacement relationships from the PCK (2007) hinge method. Larger tension strains are predicted than those measured in the test, and the strain-displacement relationship predicts that these values would occur at lower levels of deformation than would occur with the measured tensile strain-displacement relationship.

By comparison, the methods which produced more accurate peak tensile strain predictions suffer from the induced conservatism when translating these tensile strains to lateral displacements, even when using the modified plastic hinge method which more closely resembles the measured strain-displacement relationship. As shown in Figure 8.24,

the strain-based Eqn 8.1 model combined with the modified hinge method and the Feng (2013) approach with the strain-displacement relationships from the modified hinge method produced the most accurate peak tensile strain predictions.   These methods, however, produce conservative peak tensile displacement predictions due to smaller level of, but still present, conservatism from the modified plastic hinge method.   The drift-based Eqn 8.13 does not need a plastic hinge method, since it is a direct calculation rather than a translation of a strain to displacement.
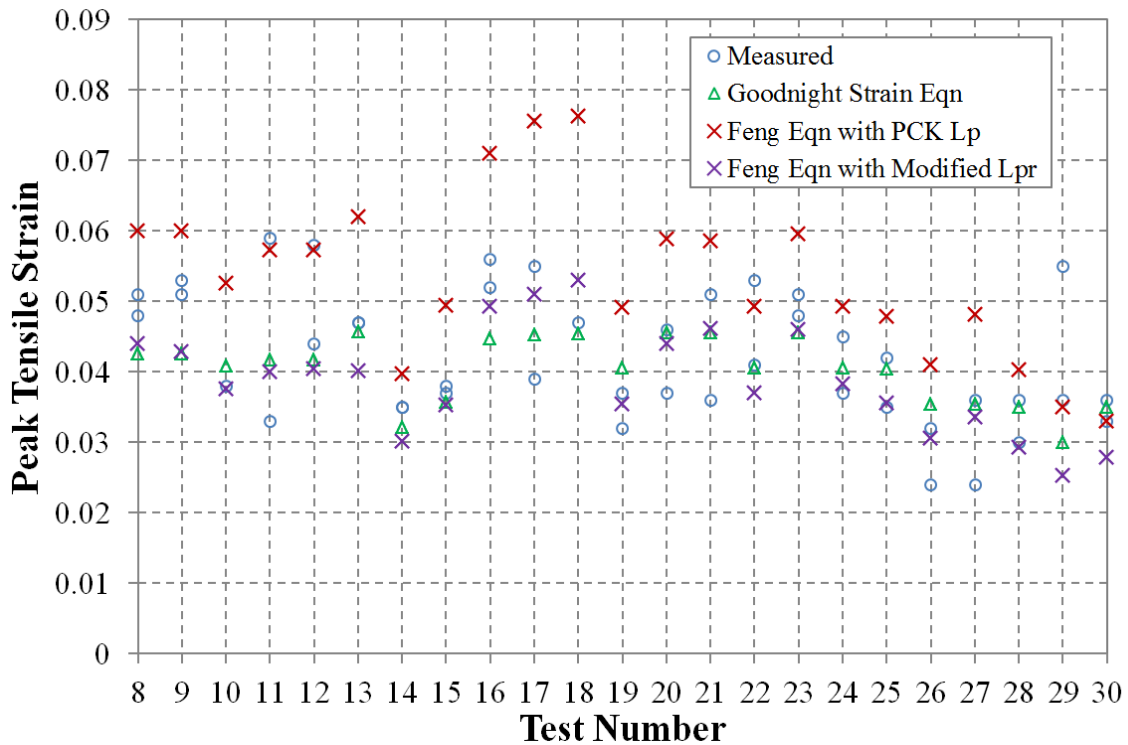
Figure 8.24 Comparison of Measured Peak Tensile Strains Prior to Bar Buckling and Result of Feng (2013) Method
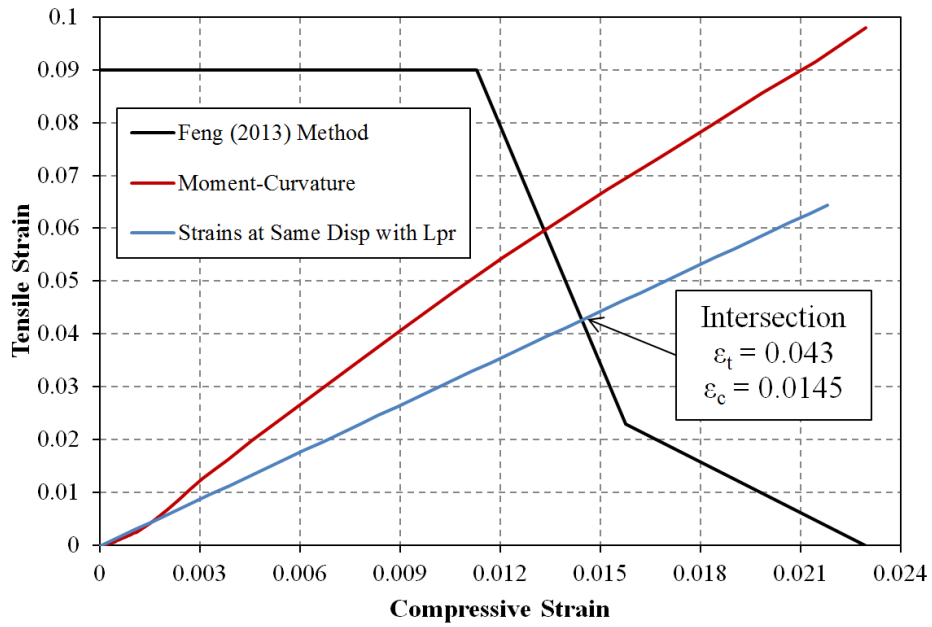
Figure 8.25 Tensile and Compressive Stain Relationship at Same Displacement, Consistent with Separate Goodnight et al. Lpr Hinge Lengths
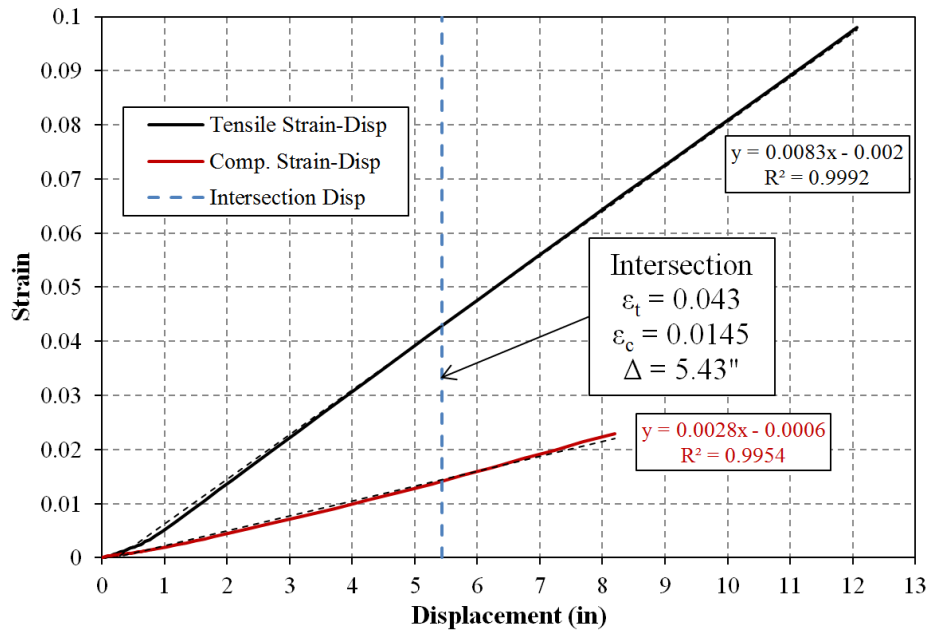
Figure 8.26 Bar Buckling at Intersection Point using Goodnight et al. (2014) Hinge Length Expressions
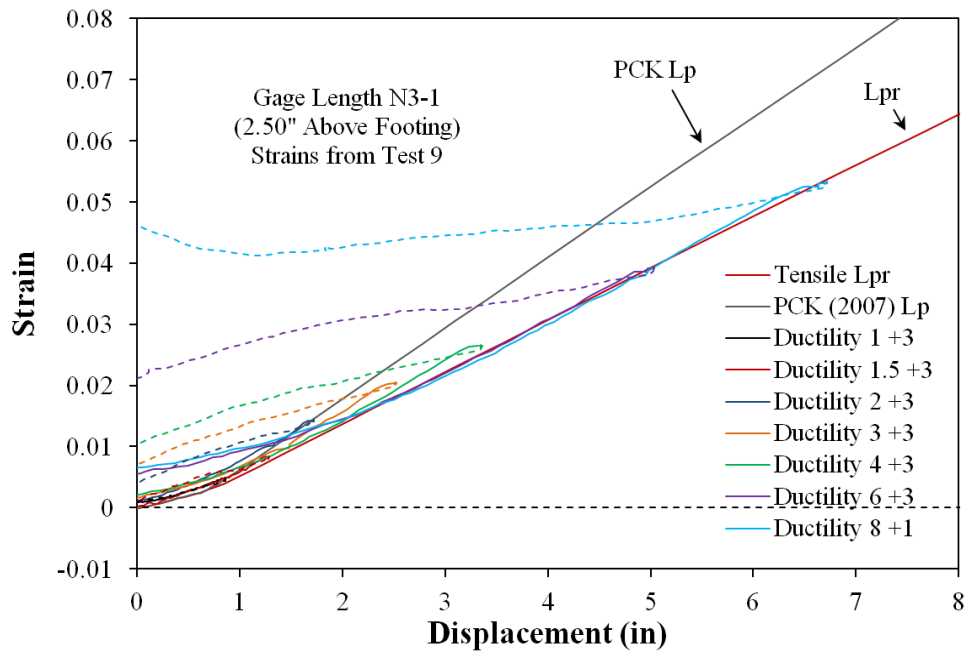
Figure 8.27 Tensile Strain-Displacement for Test 9 with Moment-Curvature Prediction
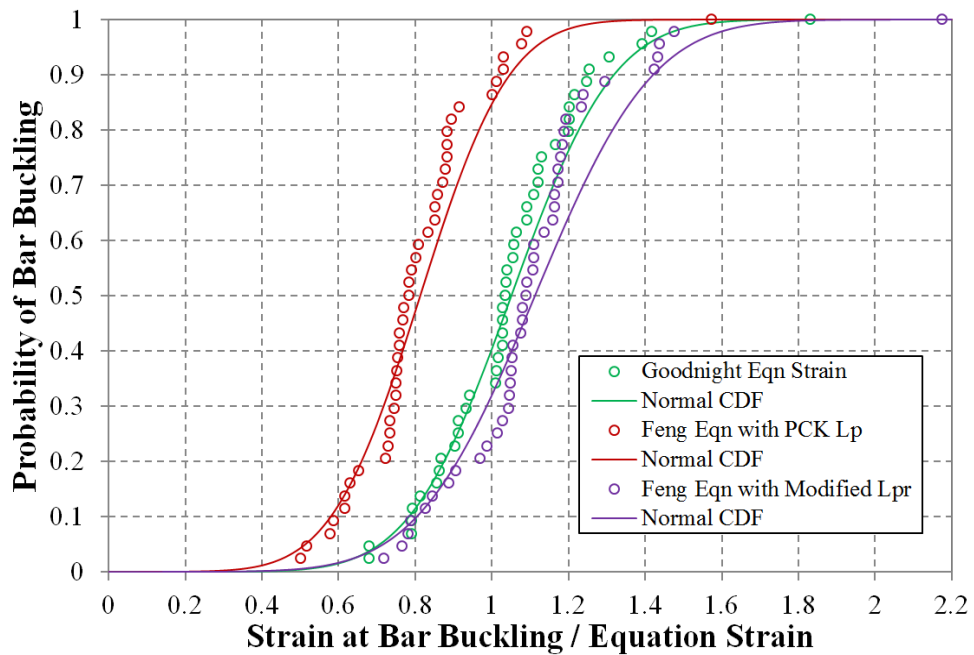
Figure 8.28 Cumulative Probability Distribution for the (Measured / Predicted) Peak Tension Strains Prior to Bar Buckling in the Goodnight et al. Dataset
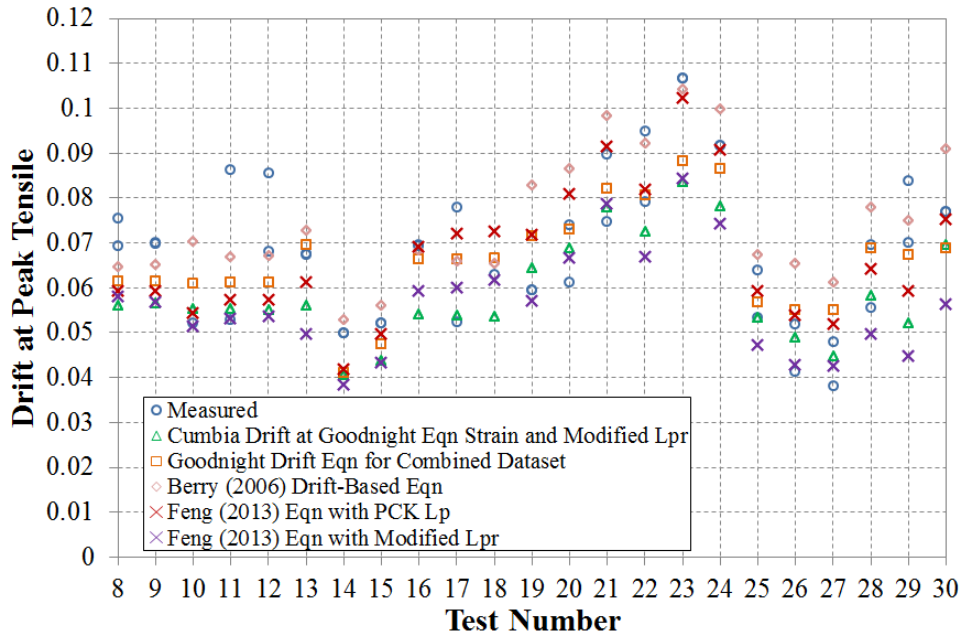
Figure 8.29 Comparison of Measured Peak Tensile Displacement Prior to Bar Buckling and Result of Feng (2013) Method
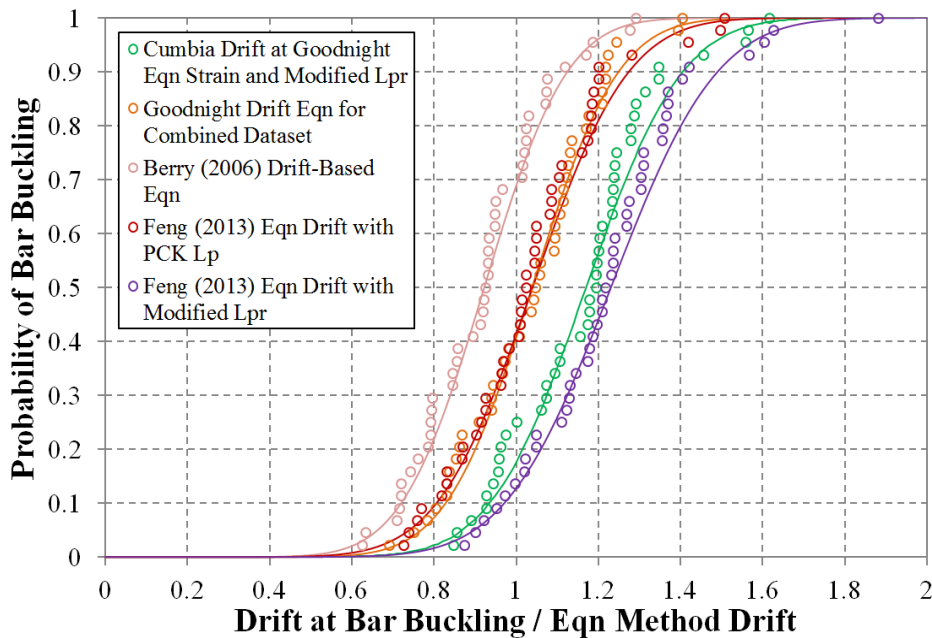
Figure 8.30 Cumulative Probability Distribution for the (Measured / Predicted) Peak Tension Displacement Prior to Bar Buckling in the Goodnight et al. Dataset

8.11 Bar Buckling Predictions for the Combined Berry (2006) and Goodnight et al. Dataset

In the following section, the accuracy of predicting the peak tensile displacement prior to bar buckling after reversal of load for columns in the combined Berry (2006) and Goodnight et al. datasets is explored. The Berry (2006) dataset contained 36 modernly detailed bridge columns which had reported bar buckling observations in literature, Table 8.3.   The Goodnight et al. dataset included 23 columns with 44 extreme fiber bar buckling observations, Table 8.2. The 23 specimens are from Tests 8-30 which were constructed at NCSU and utilized the Optotrak instrumentation method with direct application of target markers to the surface of longitudinal bars. For this combined dataset, bar buckling predictions were made with the following techniques: (1) peak tension strain from Eqn 8.1 translated to a displacement using the modified hinge method, (2) Berry (2006) drift-based bar buckling Eqn 8.12, (3) drift-based Eqn 8.13 with coefficients fit to the combined dataset, (4) Feng (2013) multi-linear regression with the PCK (2007) hinge method, and (5) Feng (2013) approach with strain-displacement relationships from the modified hinge method. A comparison of the accuracy of these methods appears in Figure 8.31, and in the statistics below.

Mean, Coefficient of Variation, and Root Mean Squared Error

$$(1)\ mean\left(\frac{\Delta_{Meausred}^{bb}\ in\ Combined\ Dataset}{\Delta_{Cumbia}\ at\ \varepsilon s_{\text{Eqn 8.1}}^{bb}\ with\ Modified\ Lpr}\right) = 1.21, COV = 0.227, RMSE = 0.223$$

$$(2)\ mean\left(\frac{(\Delta/L)_{Meausred}^{bb}\ in\ Combined\ Dataset}{(\Delta/L)_{Berry\ (2006)\ \text{Eqn 8.12}}^{bb}}\right) = 0.93, COV = 0.228, RMSE = 0.286$$

$$(3)\ mean\left(\frac{(\Delta/L)_{Meausred}^{bb}\ in\ Combined\ Dataset}{(\Delta/L)_{Combined\ Dataset\ \text{Eqn 8.13}}^{bb}}\right) = 1.09, COV = 0.241, RMSE = 0.200$$

$$(4)\ mean\left(\frac{\Delta^{bb}_{Meausred}\ in\ Combined\ Dataset}{\Delta_{Cumbia}\ at\ \varepsilon s^{bb}_{Feng\ (2013)}\ with\ PCK\ (2007)\ Lp}\right) = 1.12, COV = 0.234, RMSE = 0.202$$

$$(5)\ mean\left(\frac{\Delta^{bb}_{Meausred}\ in\ Combined\ Dataset}{\Delta_{Cumbia}\ at\ \varepsilon s^{bb}_{Feng\ (2013)}\ with\ Modified\ Lpr}\right) = 1.29, COV = 0.267, RMSE = 0.251$$
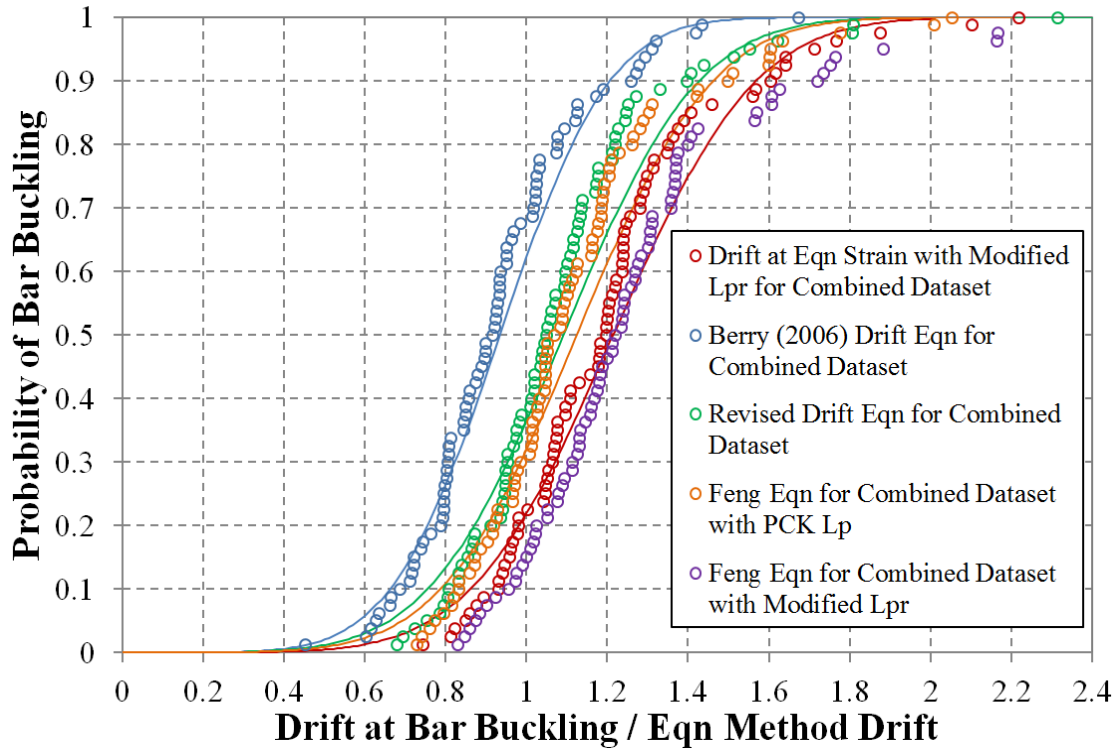
Figure 8.31 Cumulative Probability Distribution for the (Measured / Predicted) Peak Tension Displacement Prior to Bar Buckling in the Combined Berry (2006) and Goodnight et al. Dataset

8.12 Evaluation for Full Scale Column Experiments by Cheok and Stone (1989)

Cheok and Stone (1989) tested two full-scale, circular, spirally reinforced columns with constant axial load and applied quasi-static cyclic lateral displacement history. The performance of the two full-scale columns was later compared to 1/6 scale model tests. The first column, NIST Full Scale Flexure in Figure 8.32, had a 5ft diameter, 30ft cantilever length, longitudinal steel content of 2%, volumetric steel ratio of 0.6%, and a constant axial load of 6.9%. The second column, NIST Full Scale Shear in Figure 8.33, had a 5ft diameter, 15ft cantilever length, longitudinal steel content of 2%, volumetric steel ratio of 1.5%, and a constant axial load of 7.1%.

Additional information required for moment-curvature and strain-displacement predictions for the two columns appears in Figure 8.32 and Figure 8.33. The left table contains information utilized in the moment-curvature analysis, including the integrated PCK (2007) plastic hinge and strain penetration lengths. The middle table contains data used to compute the strain-displacement response using the tensile and compressive modified plastic hinge lengths (Lpr_t and Lpr_c) from Eqn 8.2 through Eqn 8.11. The right table includes reported damage observations and bar buckling predictions from the following methods: [1] Goodnight Eqn 8.1 bar buckling strain and the modified hinge method for strain-displacement, [2] Goodnight Eqn 8.1 bar buckling strain and the PCK (2007) hinge method, [3] Goodnight Eqn 8.13 bar buckling drift expression with coefficients for the combined dataset, [4] Berry (2006) Eqn 8.12 bar buckling drift, [5] Feng (2013) multi-linear regression with PCK (2007) strain-displacement, and [6] Feng (2013) multi-linear regression with the modified hinge method strain-displacement.

For the NIST Full Scale Flexure column, bar buckling was observed after reversal from 538mm. As summarized in the table, the predictive techniques produced the following result: (1) 511.4mm, (2) 431.7mm, (3) 501.8mm, (4) 598.1mm, (5) 488.3mm, and (6) 499.7mm.

Cheok and Stone (1989) NIST, Full Scale Flexure
Diameter: 1520.0 mm
Cover to Longitudinal Bars: 66.7 mm
Number of Longitudinal Bars: 25
Diameter of Longitudinal Bars: 43.0 mm
Diameter of Transverse Steel: 15.9 mm
Spacing of Transverse Steel: 89.0 mm
Axial Load: 4450.00 kN
Concrete Compressive Strength: 35.80 MPa
Long Steel Yielding Stress: 475.00 MPa
Long Steel Max. Stress: 665.00 MPa
Transverse Steel Yielding Stress: 493.00 MPa
Member Length: 9140.0 mm
Single Bending, Uniaxial
PCK (2007) Plastic Hinge Length: 1181 mm
PCK (2007) Strain Penetration Length: 449 mm
Longitudinal Steel Ratio: 0.020
Transverse Steel Ratio: 0.006
Axial Load Ratio: 0.069

Strain-Displacement Input Values		
fyh	493	MPa
fy	475	MPa
fu	665	MPa
f'c	35.8	MPa
dbl	43	mm
ρl	0.02	
ρs	0.006	
P/(f'c*Ag)	0.069	
Length	9140	mm
Dia	1520	mm
Lsp	288.07	mm
k	0.08	PCK eqn
Lpr.comp	1462.4	mm
Lpr.tension	2602.4	mm
φy'	2.66E-06	1/mm
My'	8963.59	kN*m

Reported Damage Observations	
Conc. Crushing	179 mm
Sig. Spalling	269 mm
Bar Buckling (bb)	538 mm
Bar Fracture	538 mm
Spiral Fracture	538 mm

Goodnight, Strain Based Bar Buckling	
εs bb	0.0335
Δbb, Lpr	511.4 mm
Δbb, Lp	431.7 mm
Goodnight, Drift Based Bar Buckling	
Δbb	501.8 mm
Berry (2006), Drift Based Bar Buckling	
Δbb	598.1 mm
Feng (2013), with PCK (2007) Strain-Disp	
εs bb, Lp	0.0385
Δbb, Lp	488.3 mm
Feng (2013), with Modified Lpr Strain-Disp	
εs bb, Lpr	0.0326
Δbb, Lpr	499.7 mm
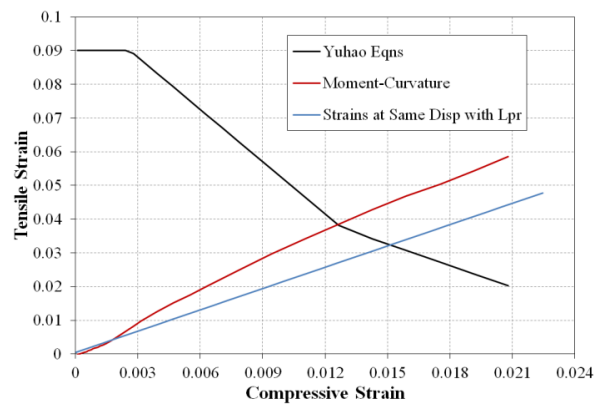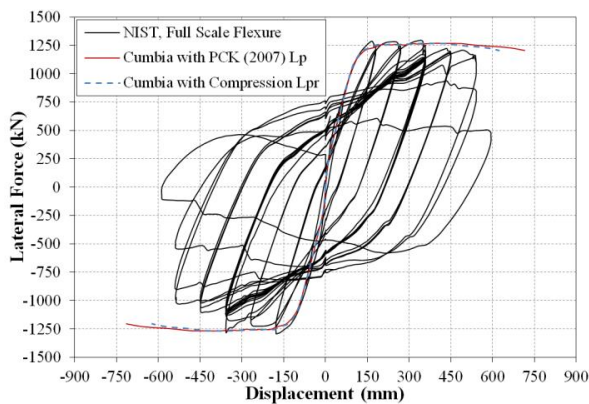
Figure 8.32 Bar Buckling Predictions Applied to NIST, Full Scale Flexure Specimen from Cheok and Stone (1989), Note: The Force-Deformation Predictions Include P-Delta Effects

For the NIST Full Scale Shear column, bar buckling was observed after reversal from 285mm. As summarized in the table, the predictive techniques produced the following result: (1) 266.7mm, (2) 209.6mm, (3) 304.5mm, (4) 324.3mm, (5) 350.2mm, and (6) 332.2mm.

Cheok and Stone (1989) NIST, Full Scale Shear
Diameter: 1520.0 mm
Cover to Longitudinal Bars: 69.8 mm
Number of Longitudinal Bars: 25
Diameter of Longitudinal Bars: 43.0 mm
Diameter of Transverse Steel: 19.1 mm
Spacing of Transverse Steel: 54.0 mm
Axial Load: 4450.00 kN
Concrete Compressive Strength: 34.30 MPa
Long Steel Yielding Stress: 475.00 MPa
Long Steel Max. Stress: 665.00 MPa
Transverse Steel Yielding Stress: 435.00 MPa
Member Length: 4570.0 mm
Single Bending, Uniaxial
PCK (2007) Plastic Hinge Length: 899 mm
PCK (2007) Strain Penetration Length: 449 mm
Longitudinal Steel Ratio: 0.020
Transverse Steel Ratio: 0.015
Axial Load Ratio: 0.071

Strain-Displacement Input Values		
fyh	435	MPa
fy	475	MPa
fu	665	MPa
f'c	34.3	MPa
dbl	43	mm
ρl	0.02	
ρs	0.015	
P/(f'c*Ag)	0.071	
Length	4570	mm
Dia	1520	mm
Lsp	392.85	mm
k	0.08	PCK eqn
Lpr.comp	731.2	mm
Lpr.tension	1871.2	mm
φy'	2.69E-06	1/mm
My'	8906.96	kN*m

Reported Damage Observations		
Conc. Crushing	N/A	mm
Sig. Spalling	142	mm
Bar Buckling (bb)	285	mm ←
Bar Fracture	356	mm
Spiral Fracture	356	mm

Goodnight, Strain Based Bar Buckling		
εs bb	0.0457	
Δbb, Lpr	266.7	mm ←
Δbb, Lp	209.6	mm
Goodnight, Drift Based Bar Buckling		
Δbb	304.5	mm ←
Berry (2006), Drift Based Bar Buckling		
Δbb	324.3	mm
Feng (2013), with PCK (2007) Strain-Disp		
εs bb, Lp	0.079	
Δbb, Lp	350.2	mm ←
Feng (2013), with Modified Lpr Strain-Disp		
εs bb, Lpr	0.0575	
Δbb, Lpr	332.2	mm ←
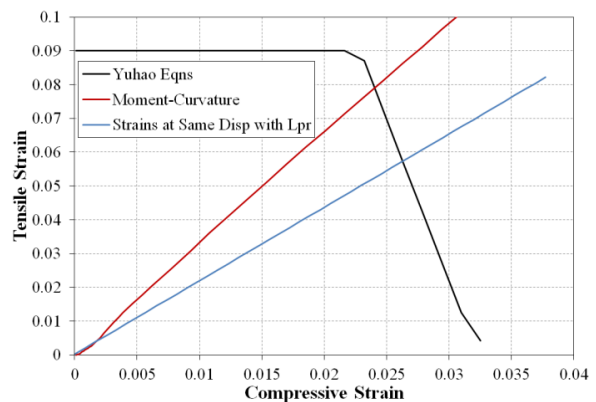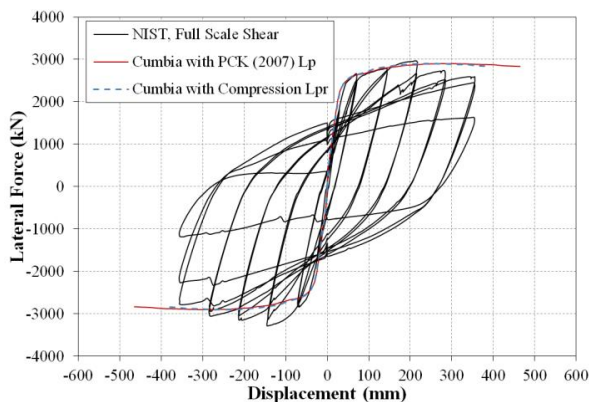
Figure 8.33 Bar Buckling Predictions Applied to NIST, Full Scale Shear Specimen from Cheok and Stone (1989), Note: The Force-Deformation Predictions Include P-Delta Effects

8.13 Compressive Strain at Cover Concrete Crushing

For Tests 8-30, the measured compressive strains in the extreme fiber bars at the peak of the cycles where cover concrete crushing was observed were used to develop two empirical expressions. The first, Eqn 8.19, is a single value expression developed based on minimizing the sum of squared error between the prediction and the measured strain. The observed cover crushing behavior was found to be influenced by the amount of confinement steel provided in the column, as shown in Figure 8.34. Columns with additional confinement steel had larger measured compressive strains at the peak of the cycle where cover crushing was observed. This relationship was used to formulate a second empirical expression to predict the compressive strain at cover concrete crushing, Eqn 8.20. The results of the two equations are compared with the measured compressive strains at the peak of the cycle were cover concrete crushing was observed in Figure 8.35.

Tests within the Goodnight et al. dataset may not be the best gage for assessing limit states related to the cover concrete due to the blockouts installed during construction for instrumentation with the Optotrak system. For columns with the full cover blockout the first sign of concrete flaking in the compression zone was taken as the cover concrete crushing observation.   The current serviceability concrete compressive strain of 0.004 is still recommended for the design of new structures, since inevitably the measured compressive strain at the peak of a cycle exceeds the raw value which initiated the cover crushing.

$$\varepsilon_{crushing}^{cover} = 0.00475$$

Compression Strain at Cover Crushing which Minimizes the Sum of Squared Error in Prediction

Eqn 8.19

$$\varepsilon_{crushing}^{cover} = 197\rho_s \frac{f_{yhe}}{E_s}$$

Compression Strain at Cover Crushing in Terms of Transverse Volumetric Steel Ratio

Eqn 8.20
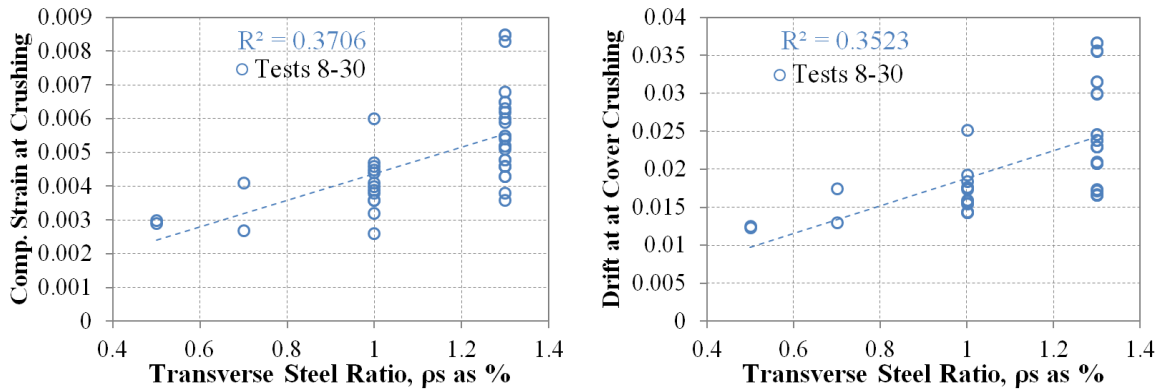
Figure 8.34 Trans. Steel and Peak Comp. Strain and Drift at Cover Concrete Crushing
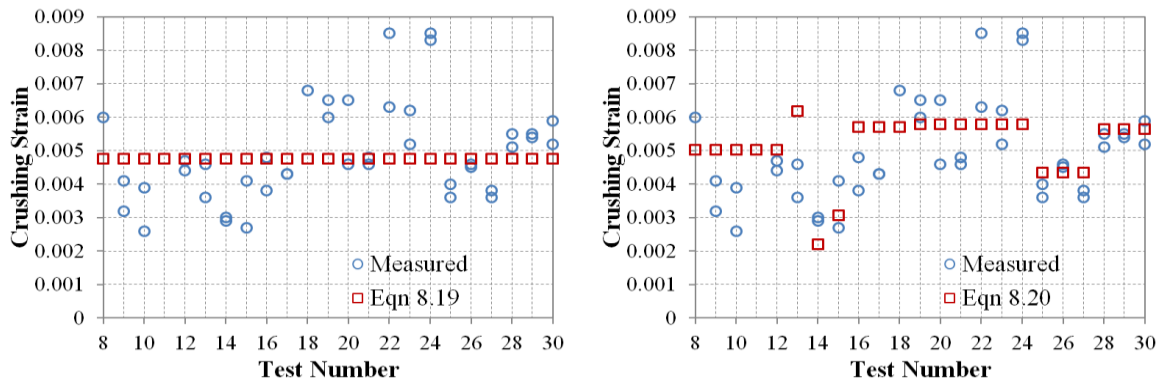
Figure 8.35 Result of Compression Strain at Cover Crushing Eqns 8.19 and 8.20

8.14 Compressive Strain at Spiral Yielding in Confinement Regions of the Column

The current damage control concrete compressive strain limit is defined by the Mander et al. (1988) ultimate concrete compression strain. This expression was developed based on an energy balance between the core concrete dilation and the confinement provided by the transverse steel for a column subjected to uniform compression. Comparatively little is known about the relationship between compressive demand and confinement in inelastic flexural members such as bridge columns which have a strain gradient and a fanned

compressive strut pattern emanating from the compressive toe region of the column. Experimental results within the Goodnight et al dataset imply that after initial yielding of the confinement steel, localization of compressive demand can occur over several spiral layers. Measured compressive strains in this region have exceeded the Mander et al. (1988) ultimate concrete compressive strain without resulting in fracture of confinement steel. For many of these tests, measurable deformation could be observed in the recorded longitudinal and spiral strain hysteresis prior to the visible bar buckling observation. The distribution of spiral strains measured both around the circumference of the column and over multiple layers was found to impact the observed bar buckling behavior. Localized spiral demands led to increased levels of measured compressive strain and early buckling of longitudinal reinforcement.

Since the stiffness of the transverse reinforcement restraining the bar from buckling is linked to its degree of inelasticity, perhaps an intermediate limit state of initial spiral yield in the confinement region is needed. Initial spiral yield is termed as an intermediate limit state because it marks the point where localization of compressive demand begins. This localization led to measurable deformation prior to visible bar buckling. An understanding of the variables which influence the initial yielding behavior is helpful. Higher levels longitudinal steel content resulted in lower compressive strains measured at the peak of the cycle where transverse steel in the confinement region initially yielded, Figure 8.36. The additional restraint demands required to maintain stability of the longitudinal reinforcement reduces the available component left over for core concrete confinement. The spiral yielding observation occurred at higher values of measured compressive strain for experiments with larger transverse steel yield stress, Figure 8.36. The measured spiral yielding behavior was expected to be influenced the same variables which impact confinement. Nether transverse volumetric steel ratio or the magnitude of the computed Mander (1988) ultimate concrete compressive strain influenced the measured spiral yielding behavior is Tests 8-30, Figure 8.37. On average, the initial spiral yielding observation was observed at 75% of the computed Mander (1988) ultimate concrete compressive strain.

Two empirical equations were made to predict the compressive strain at spiral yielding, Eqn 8.21 and Eqn 8.22. The first, Eqn 8.21, is a single valued expression formulated based on minimizing the sum of squared error between the prediction and measured result. The second expression, Eqn 8.22, was created in the same manner, but includes the influence of steel content and spiral yield stress which were found to influence the measured behavior. A comparison of the results for these two equations is shown graphically in Figure 8.38. Alternatively, the accuracy of Eqn 8.22 in predicting the measured compressive strains at the peak of the cycle where spiral yielding was observed can be viewed using a cumulative probability distribution in Figure 8.39. The mean and coefficient of variation for this strain comparison appears below. The compressive strains at spiral yield from Eqn 8.22 were translated to lateral displacements using the compressive strain-displacement relationship from the Modified Lpr Plastic Hinge Method. The cumulative probability distribution in Figure 8.40 cam be used to gage the accuracy and conservatism of displacements evaluated at the Eqn 8.22 spiral yield strain. A measured to predicted displacement ratio lower than one implies that the mean value for the computed spiral yield displacements is conservative.

$$\varepsilon_{yielding}^{spiral} = 0.0124 \qquad \text{Compression Strain at Spiral Yielding} \qquad \text{Eqn 8.21}$$

$$\varepsilon_{yielding}^{spiral} = 0.009 - 0.3\frac{A_{st}}{A_g} + 3.9\frac{f_{yhe}}{E_s} \quad \text{Compression Strain at Spiral Yielding} \qquad \text{Eqn 8.22}$$

$$mean\left(\frac{\varepsilon_{Meausred}^{spiral\ yield}\ in\ Goodnight\ et\ al.\ Dataset}{\varepsilon s_{Eqn\ 8.22}^{spiral\ yield}}\right) = 1.06, COV = 0.167$$

$$mean\left(\frac{\Delta_{Meausred}^{spiral\ yield}\ in\ Goodnight\ et\ al.\ Dataset}{\Delta_{Cumbia}\ at\ \varepsilon s_{Eqn\ 8.22}^{spiral\ yield}\ with\ Modified\ Lpr}\right) = 0.94, COV = 0.186$$
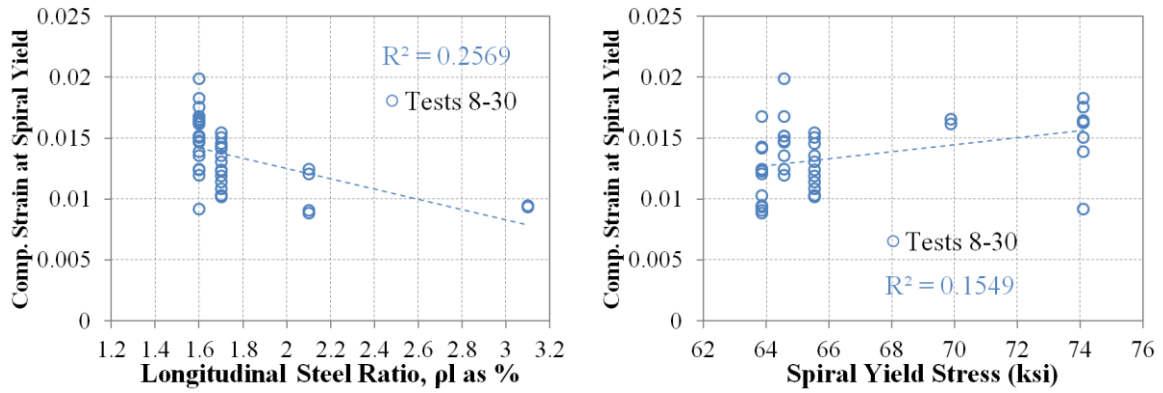
Figure 8.36 Impact of Long. Steel and Spiral Strength on Comp. Strain at Spiral Yield
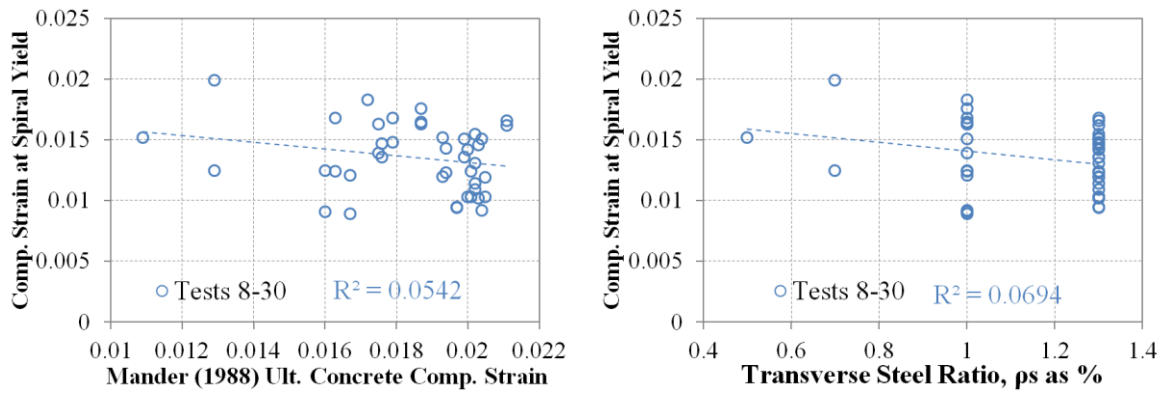
Figure 8.37 Impact of Mander εcu and Trans. Steel on Comp. Strain at Spiral Yield
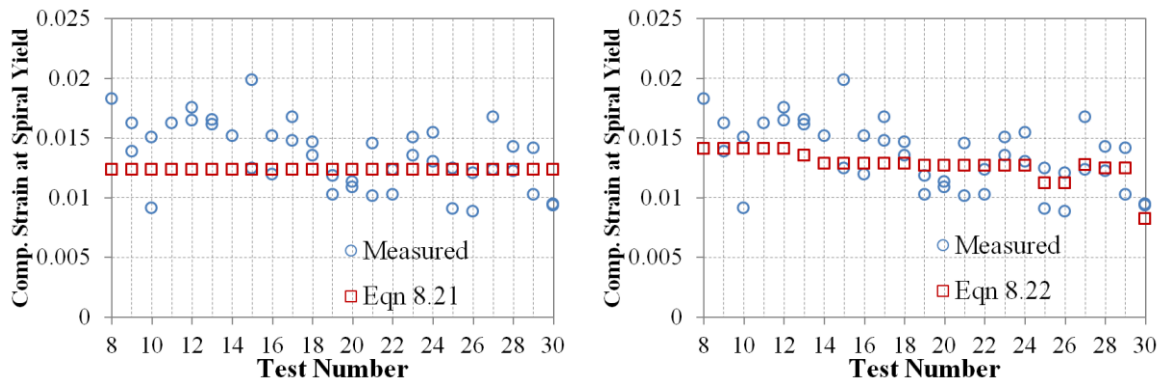
Figure 8.38 Result of Compression Strain at Spiral Yield Eqn 8.21 and Eqn 8.22
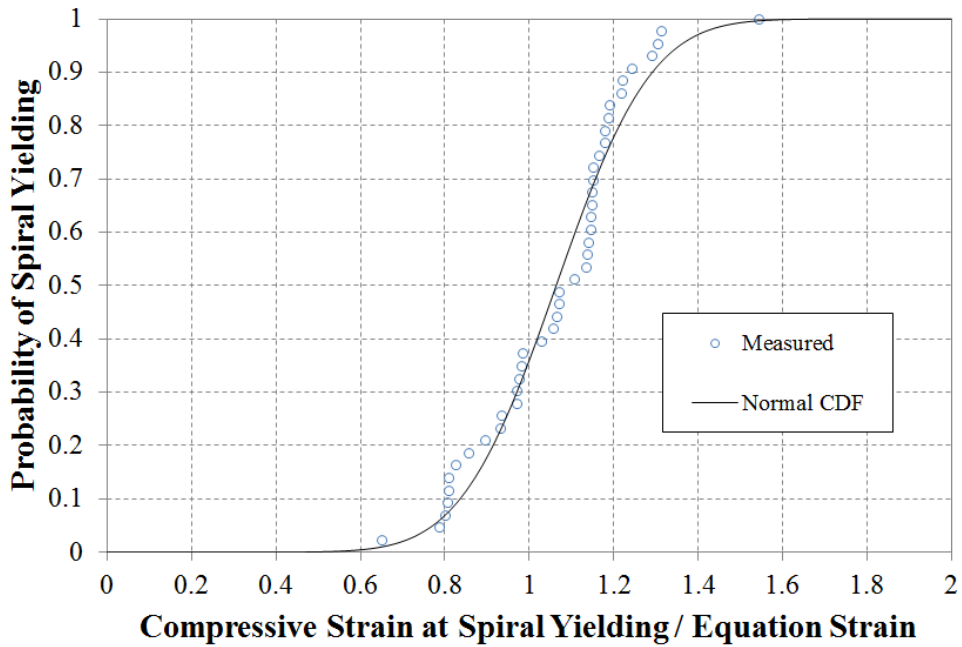
Figure 8.39 CDF for Comp. Strain at Spiral Yield Eqn 8.22 for Goodnight Dataset
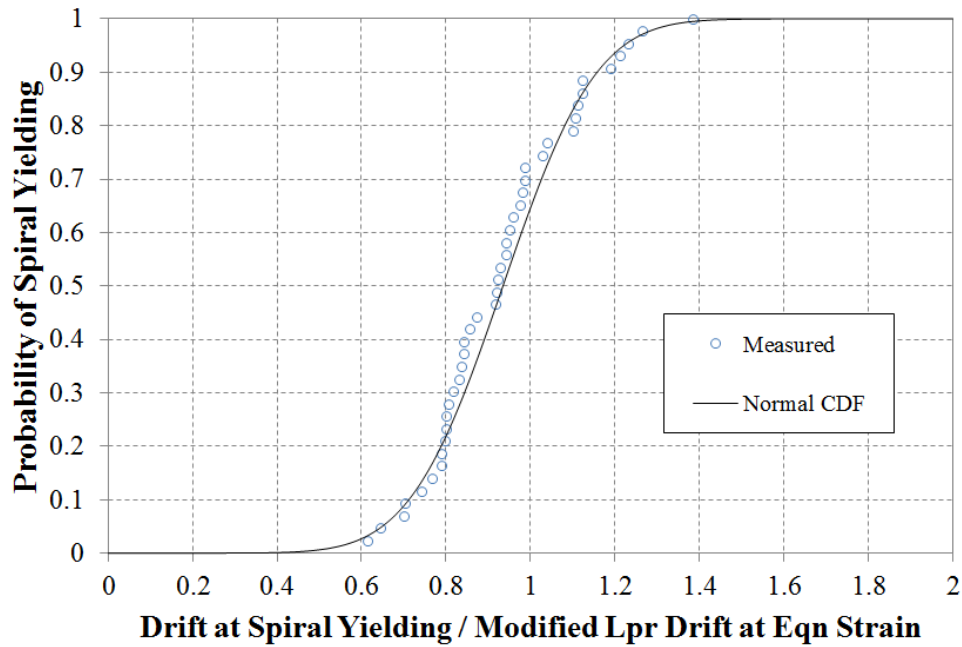
Figure 8.40 CDF for Modified Lpr Drift at Eqn 8.22 Strain for Goodnight Dataset

8.15 Residual Crack Widths

The current serviceability steel tensile strain limit of $\varepsilon_s = 0.015$ represents the tensile strain at the peak of a given cycle that is expected to result in 1mm residual crack widths measured at zero lateral force. The residual crack width of 1 mm represents the limit at which epoxy injection may be needed to prevent corrosion of internal reinforcing steel. Residual crack widths were not directly measured in experiments from the Goodnight et al. dataset. A process through which the measured peak crack widths of a given cycle were used to approximate the residual crack widths using the measure extreme fiber reinforcement strains is described below. It is important to note that this process was only utilized in Tests 8-18, which had the vertical cover concrete blockout strips over extreme fiber reinforcement. Tests 19-30 had a full cover concrete blockout, which prevented accurate measurements of crack widths.

The measured peak tensile strains and their associated measured crack widths at cycle peaks prior to the cover concrete crushing observation in Tests 8-18 are shown in Figure 8.41. The residual tension strain was taken as the strain measured in the extreme fiber bar at zero displacement during the reversal from a cycle peak. The relationship between measured peak and residual tension strains appears in the right half of Figure 8.41. If the ratio of the peak tension strain to the residual tension strain is assumed to be the same as the ratio between the peak crack width and the residual crack width, then the residual crack widths can be computed. The resulting relationship between peak tension strain and computed residual crack widths appear in the left half of Figure 8.42. Using this method, the computed residual crack widths never exceed the threshold value of 1mm which was taken as the steel tensile serviceability limit state. Further measurements of crack widths were prevented by cover concrete crushing on each side of the specimen before the computed residual crack widths reached 1 mm. A residual crack width of 0.5 mm would be expected to occur after reversal from a peak tensile strain of 0.015, based on the linear relationship presented in Figure 8.42.
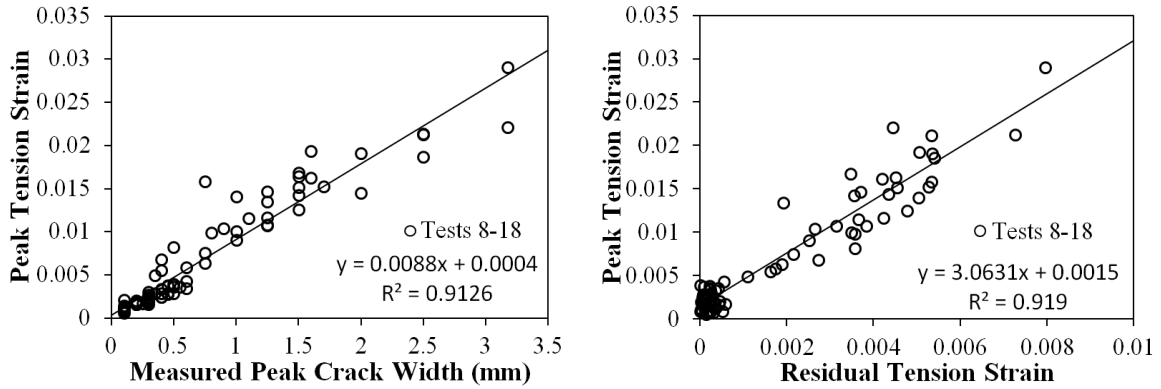
Figure 8.41 Peak Tension Strains and (Left) Peak Crack Width or (Right) Residual Crack Width Measured at Zero Displacement during the Following Reversal
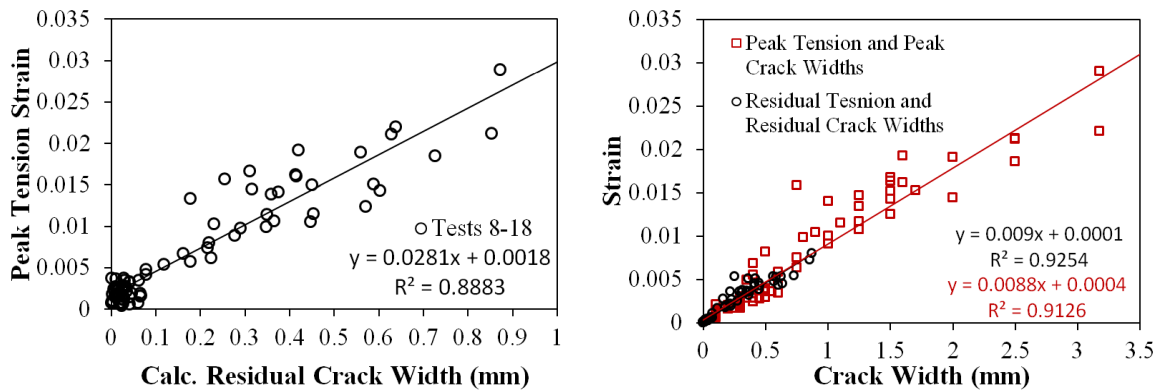
Figure 8.42 (Left) Peak Tensile Strains and Calculated Residual Crack Widths, (Right) Comparison of Peak Tensile and Crack Width to Residual Tensile and Crack Width

8.16 Conclusion

To satisfy the aims of performance based design, levels of damage which interrupt the serviceability of the structure or require more invasive repair techniques must be related to engineering criteria. For reinforced concrete flexural members such as bridge columns, concrete compressive and steel tensile strain limits are very good indicators of damage. An experimental study was carried out to assess the performance of thirty circular, well-confined, bridge columns with varying lateral displacement history, transverse reinforcement detailing, axial load, aspect ratio, and longitudinal steel content. A key feature of the experiments is the high fidelity strain data obtained through the use of an optical 3D position measurement system. Previous performance strain limit recommendations from Kowalsky (2000) have been revisited in light of the data collected in the experiments.

Serviceability limit states represent the point at which repair is necessary, interrupting the serviceability of the structure, but not posing a safety concern. The current serviceability concrete compressive strain limit of $\varepsilon_c = 0.004$ was found to be conservative, but is ultimately recommended since the measured compressive strains at cover concrete crushing come from the peak of the cycle where cover crushing was observed. Within the Goodnight et al. dataset, larger measure compressive strain at cover crushing were observed in columns with higher levels of confinement steel. The current serviceability steel tensile strain limit of $\varepsilon_s = 0.015$ represents the tensile strain at the peak of a given cycle that is expected to result in 1 mm residual crack widths measured at zero lateral force. The residual crack width of 1 mm represents the limit at which epoxy injection may be needed to prevent corrosion of internal reinforcing steel. Although residual crack widths were not directly measured in experiments from the Goodnight et al. dataset, approximations for the residual crack widths were made based on the measured peak crack widths and recorded bar strains. For columns in the Goodnight et al. dataset, the calculated residual crack widths never exceeded 1 mm before cover concrete crushing occurred, preventing further crack width measurements. Ultimately no further recommendations on the serviceability steel tensile strain limit are

provided beyond the observation that the current value is conservative when compared to the dataset.

Experimental results within the Goodnight et al dataset suggest that after initial yielding of the confinement steel, localization of compressive demand can occur over several spiral layers. Measured compressive strains in this region have exceeded the Mander et al. (1988) ultimate concrete compressive strain without resulting in fracture of confinement steel. For many of these tests, measurable deformation could be observed in the recorded longitudinal and spiral strain hysteresis prior to the visible bar buckling observation. Currently there is not an intermediate strain limit between serviceability and damage control which is related to a change in compressive behavior that results due to confinement steel entering the inelastic range. To gain a better understanding of the behavior, trends were analyzed in measured compressive strains at the initial spiral yield observation in the Goodnight et al. dataset. Specimens with higher levels of longitudinal steel content had smaller measured compressive strains at the spiral yielding observation since a larger component of its capacity was utilized for bar restraint. An empirical expression for intermediate concrete compressive strain limit related to initial yielding of confinement steel was developed, Eqn 8.22. This expression provided a mean measured/predicted compression steel at spiral yield of 1.06 with a coefficient of variation of 0.167. When converted to lateral displacements using the compressive strain-displacement relationship for the Modified Lpr Hinge Method, the resulting mean measured/predicted displacement was 0.94 with a coefficient of variation of 0.186.

The damage control limit state represents the limit of economical repair, where past this point repair may be uneconomical or unfeasible. The current damage control concrete compressive strain limit is defined by the Mander et al. (1988) ultimate concrete compression strain. This expression was developed based on an energy balance between the core concrete dilation and the confinement provided by the transverse steel for a column subjected to uniform compression. In the Goodnight et al. dataset, severe yielding of the transverse steel resulted in localized compressive demand. In this region, measured compressive strains have

exceeded the Mander et al. (1988) ultimate concrete compressive strain without resulting in confinement steel fracture as the energy balance approach would imply. The current damage control concrete compressive strain limit is still recommended because it is related to significant levels of damage in the core concrete which would coincide with observed measureable deformation and potential buckling of reinforcing bars.

The current damage control steel tensile strain limit of $\varepsilon_s = 0.06$ is related to the peak tensile strain that is expected to initiate bar buckling in longitudinal reinforcement upon reversal of load. Measured peak tensile strains prior to bar buckling in the Goodnight et al. dataset suggest that this value is too large. An empirical expression for the peak tensile strain prior to bar buckling, Eqn 8.1, was formulated based on measured trends in the dataset. Additional confinement steel increased the measured tensile strains prior to bar buckling while higher axial load ratio reduced the peak tensile strain in the dataset. For columns in the Goodnight et al dataset, Eqn 8.1 produced a mean measured/predicted peak tensile strain of 1.05 with a coefficient of variation of 0.199. When the result of Eqn 8.1 is translated to a top column displacement using the tensile-strain displacement relationship from the Modified Lpr Hinge Method produced a mean measured/predicted displacement of 1.17 with a coefficient of variation of 0.157.

Berry (2006) utilized a subset of the PEER Column Performance Dataset to make an empirical drift-based expression to predict the peak drift prior to bar buckling, Eqn 8.12. The bridge column dataset utilized by Berry (2006) appears in Table 8.3. When the Berry (2006) Eqn 8.12 is applied to the Goodnight et al. dataset, the resulting mean measured/predicted displacement at bar buckling is 0.92 with a coefficient of variation of 0.171.

Feng (2013) proposed a series of equations to describe bar buckling behavior observed in finite element analysis. The influence of the following behaviors were included in the analysis: (1) dilation of core concrete under compression, (2) restraint provided by individual spiral layers which can go inelastic, and (3) development of the longitudinal bar into the adjoining member. The analysis resulted in a multi-linear regression model, Eqn 8.14 through Eqn 8.18, which forms a boundary for tensile versus compressive strain relationship.

Bar buckling strains predicted using this method were unconservative. The method resulted in a mean measured/predicted peak tensile strain proceeding bar buckling of 0.81 with a coefficient of variation of 0.224. This unconservative peak tensile strain when combined with the conservative tensile-strain displacement relationship from the Priestley, Calvi, and Kowalsky (2007) plastic hinge method resulted in accurate peak displacements proceeding bar buckling.

Finally, all of the predictive bar buckling methods previously described where employed to predict bar buckling in bridge columns from the Berry (2006) dataset. It became apparent that a drift-based empirical expression, similar to the original expression derived by Berry (2006), could be developed utilizing the combined dataset including the experiments from Goodnight et al. The resulting empirical drift-based bar buckling expression, Eqn 8.13, produced a mean measured/predicted drift prior to bar buckling in the combined dataset of 1.09 and coefficient of variation of 0.241. This was the most accurate predictive method for bath buckling in the combined dataset, but this is since the same dataset was used to find the empirical parameters. The strain-based bar buckling expression, Eqn 8.1, combined with the tensile strain-displacement relationships from the Modified Lpr Hinge Method produced a mean measured/predicted bar buckling displacement of 1.21 with a coefficient of variation of 0.227. Finally the Feng (2013) multi-linear regression method utilizing strain-displacement relationships from the PCK (2007) Lp Hinge Method produced a mean measured/predicted displacement proceeding bar buckling of 1.12 and a coefficient of variation of 0.234. Of the methods studied, these three bar buckling methods produced the most accurate results. While the drift-based approach is the easiest to employ in design, it is also limited to specific column configurations. The strain-based approaches do not suffer from this limitation, but require appropriate equivalent curvature distributions for the respective methods.

Chapter 9: Design Recommendations for Limit State Displacements

9.1   Performance Strain Limits

To satisfy the aims of performance based design, levels of damage which interrupt the serviceability of the structure or require more invasive repair techniques must be related to engineering criteria. Cover concrete crushing and residual crack widths exceeding 1mm represent serviceability limit states, which when exceeded require repair. Longitudinal bar buckling and significant damage to the core concrete represent damage control limit states which represent the limit of economical repair. The ultimate limit state is characterized by fracture of previously buckled reinforcement or rupture of confinement steel. The first occurrence of these limit states in a column test by Goodnight et al. is shown in Figure 9.1.
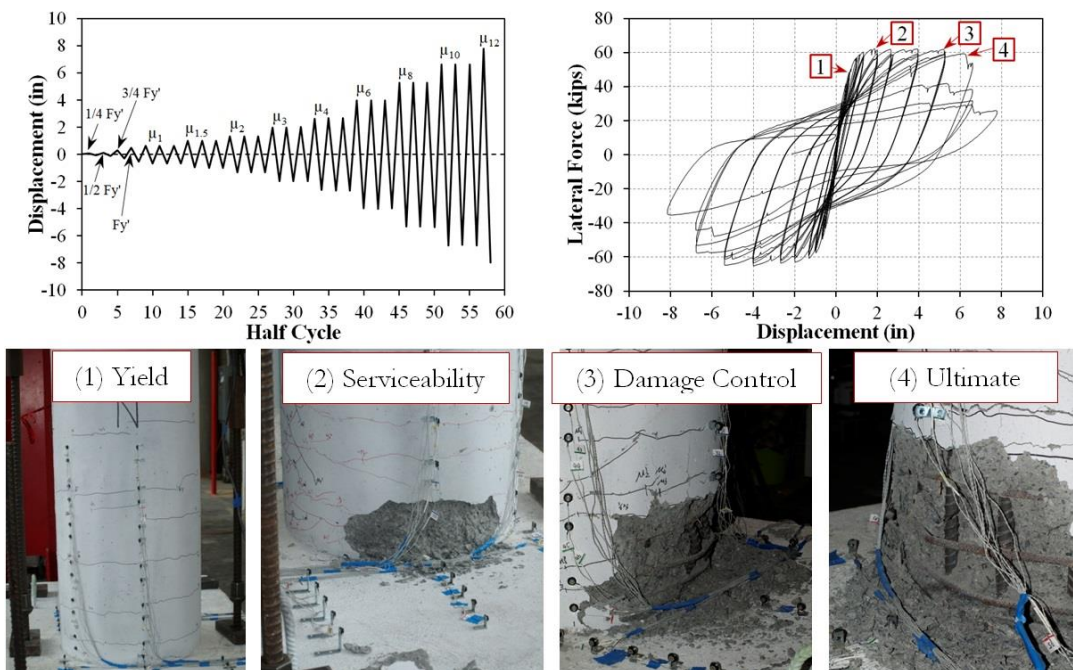
Figure 9.1 Displacement History, Hysteretic Response, and Performance Limit States

9.1.1 Serviceability Limit States

When exceeded, serviceability limit states represent the point at which repair is necessary, interrupting the serviceability of the structure, but not posing a safety concern. The serviceability limit states are characterized by crushing of cover concrete or residual crack widths which exceed 1mm, both should be repaired to prevent corrosion of internal reinforcing steel.

Cover Concrete Crushing:

$$\varepsilon_c = 0.004$$ Concrete compression strain related to crushing of the cover concrete. Evaluated at the extreme compression fiber.   Eqn 9.1

Residual Crack Widths (1 mm):

$$\varepsilon_s = 0.015$$ Steel tensile strain limit related to residual crack widths which exceed 1 mm. Evaluated at the location of extreme longitudinal reinforcing bar.   Eqn 9.2

9.1.2 Intermediate Compressive Limit State

Currently there is not an intermediate strain limit between serviceability and damage control which is related to a change in compressive behavior that results due to confinement steel yielding. Experimental results suggest that localization of compressive demand can occur in regions with inelastic transverse steel. This localization can lead to compression strains which exceed predictions utilizing moment-curvature analysis and an equivalent curvature distribution. Furthermore, inelastic transverse steel restraint resulted in measurable outward deformation of longitudinal reinforcement prior to visible bar buckling observations.

Initial Yielding of Confinement Steel:

$$\varepsilon_c = 0.009 - 0.3\frac{A_{st}}{A_g} + 3.9\frac{f_{yhe}}{E_s}$$
Concrete compression strain at initial yield of confinement steel. Evaluated at the centerline of the transverse steel, i.e. the concrete core.

Eqn 9.3

9.1.3 Damage Control Limit States

The damage control limit state represents the limit of economical repair, where past this point repair may be uneconomical or unfeasible. The current damage control concrete compressive strain limit is defined by the Mander et al. (1988) ultimate concrete compression strain. While the intermediate compressive limit state was related to initial yielding of confinement steel, the damage control limit state is a reasonable approximation to compressive strain levels which influence the ability of the transverse steel to restrain longitudinal bars from buckling.

Bar buckling was observed to occur after reversal from a peak tensile strain while the bar is under net elongation, but compressive stress. Although prior compression is important to describing the restraint provided by transverse steel, expressions developed based on the peak tension strain or drift measured before bar buckling upon reversal of load were found to produce the most accurate predictions. Furthermore, higher levels of tensile strain reduce the tangent modulus of the reinforcing during the subsequent stress reversal. Sufficient confinement steel should be provided such that the Mander (1988) Ultimate Concrete Compressive Strain exceeds the compressive strain at the bar buckling displacement. For new design, the strain-based Eqn 9.5 or the drift-based Eqn 9.6 can be used to evaluate the peak displacement at which bar buckling is expected to occur after reversal during a cyclic load history. The parameters in these expressions are known or may be reasonably approximated at the onset of design, and later confirmed after finalizing the transverse steel detailing.

Ultimate Concrete Compressive Strain:

Mander (1988) ε_{cu}

Ultimate Concrete
Compressive Strain

Concrete compression strain related to limit of economical repair of core concrete. Evaluated at the centerline of the transverse steel. For a typical $\rho_s = \frac{4A_{sp}}{D's} = 1\%$, the computed Mander (1988) $\varepsilon_{cu} \approx 0.018$.

Eqn 9.4

Strain-Based Bar Buckling:

$$\varepsilon_s = 0.03 + 700\rho_s \frac{f_{yhe}}{E_s} - 0.1\frac{P}{f'_{ce}A_g}$$

Peak Tension Strain Prior to Bar Buckling. Evaluated at the location of extreme longitudinal reinforcing bar.

Eqn 9.5

$$\rho_s = \frac{4A_{sp}}{D'S}$$ Transverse Volumetric Steel Ratio, influences confinement and bar restraint.

f_{yhe}/E_s Inelastic Transverse steel is less effective at restraining longitudinal bars.

$P/f'_{ce}A_g$ Axial Load Ratio expressed as a decimal rather than a percent.

Drift-Based Bar Buckling:

In the following expression, L is the length from the column base to the point of contraflexure and D is the diameter of the cross section. The result of the expression is the drift as a percent in which bar buckling would be expected to occur during the subsequent reversal in a cyclic load history.

$$\frac{\Delta}{L}(\%) = 0.9 - 3.13\frac{P}{f'_{ce}A_g} + 142000\rho_s\frac{f_{yhe}}{E_s} + 0.45\frac{L}{D}$$ Drift at Bar Buckling   Eqn 9.6

Feng (2013) Bar Buckling Model:

Feng (2013) proposed a series of equations to describe bar buckling behavior observed in finite element analysis. The resulting bar buckling model consists of a series of three equations (Eqn 9.7 through Eqn 9.11) which form a border between tension and compression strain couples, which when exceeded produce bar buckling. In the expression, ε_t and ε_c are the tensile and compressive longitudinal bar strains (both taken as positive), d_{bl} and d_h are the longitudinal and transverse steel bar diameters, and s is the centerline spacing of transverse steel.

The bar buckling prediction is defined as the intersection of the multi-linear regression and the tensile-compressive bar strain relationship from moment-curvature analysis, Figure 9.2. The tension and compression strain couple at the intersection point represents a compression cycle followed by a tension cycle to the same level of displacement, which would induce bar buckling upon subsequent reversal of load. The Priestley, Calvi, and Kowalsky (2007) plastic hinge method is used to translate the intersection point strain to curvatures and finally member deformation. When compared to the Goodnight et al. dataset, the predicted tensile strains at a bar buckling are unconservative, but when combined with the conservative tensile strain-displacement relationship of the PCK (2007) plastic hinge method, the resulting bar buckling displacement is improved.

$$\varepsilon_t = \frac{-15\left(\varepsilon_c - \frac{0.0205}{\sqrt[3]{\frac{s}{d_{bl}}-1}}\right)}{\left(\frac{d_{bl}}{d_h}-1\right)^2} \qquad\qquad \text{Eqn 9.7}$$

$$\varepsilon_t \geq -1.7\frac{s}{d_{bl}}\sqrt{\frac{d_h}{d_{bl}}}\varepsilon_c + 0.045\sqrt{\frac{s}{d_{bl}}} \qquad\qquad \text{Eqn 9.8}$$

$$\varepsilon_t \leq 0.09, \quad if \ \frac{s}{d_{bl}} < 3 \qquad\qquad\qquad \text{Eqn 9.9}$$

$$\varepsilon_t \leq 0.06, \quad if \ \frac{s}{d_{bl}} > 4 \qquad\qquad\qquad \text{Eqn 9.10}$$

$$\varepsilon_t \leq 0.09 - 0.03\left(\frac{s}{d_{bl}} - 3\right), \quad if \ 3 < \frac{s}{d_{bl}} < 4 \qquad\qquad \text{Eqn 9.11}$$
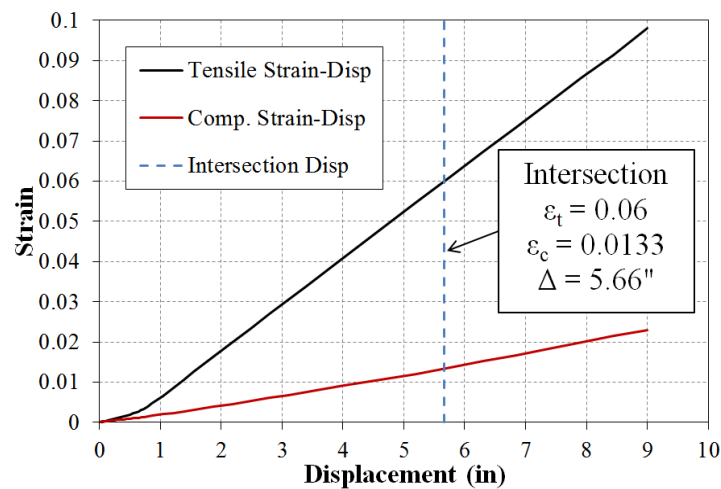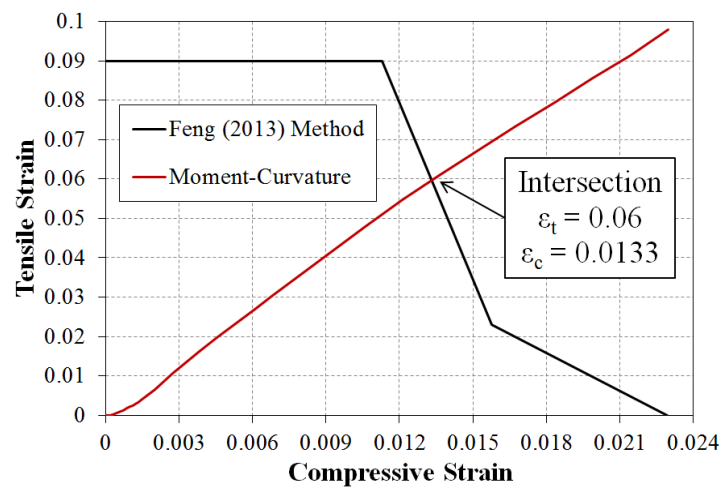
Figure 9.2 (Left) Feng (2013) Method with Tension/Compression Bar Strains from Moment-Curvature Analysis and (Right) Bar Buckling at Intersection Point using PCK (2007) Hinge Length

9.2 Modified Plastic Hinge Method

The Modified Plastic Hinge Method was developed to improve the accuracy of strain-displacement predictions necessary for successful implementation of strain-based limit states. Equivalent curvature distributions for the Modified Plastic Hinge Method appear in Figure 9.3 for a fixed-fixed column in double bending and a fixed-free column in single bending. The key aspects of the proposed Modified Plastic Hinge Model which differentiate it from the current method recommended in Priestley, Calvi, and Kowalsky (2007) include: (1) a decoupling of column flexure and strain penetration deformation components, (2) a linear plastic curvature distribution which emulates the measured curvature profiles, and (3) separate plastic hinge lengths for tensile and compressive strain-displacement predictions.

In the experiments, the measured extent of plasticity was found to increase due to the combined effects of moment gradient and tension shift. The proposed tension hinge length, Lpr_t Eqn 9.14, was calibrated to match the upper bound of the measured spread of palsticity in each test. The proposed compressive hinge length, Lpr_c Eqn 9.15, only contains a term related to the moment gradient effect. Expressions for the elastic and plastic column flexural displacement for both single and double bending were derived. Expressions which describe the additional column deformation due to strain penetration of reinforcement into the adjoining member were derived based on the measured fixed-end rotations. Part of this was the formulation of a new equivalent strain penetration length L_{sp} Eqn 9.12.

Elastic displacements are computed when the base section curvature is either at or below the first yield curvature, ϕ_y'. The elastic displacement of a column in single bending is calculated using Eqn 9.16 through Eqn 9.18. The elastic displacement of a column in double bending is computed using Eqn 9.19 through Eqn 9.21. The elastic displacement is the addition of elastic column flexural, strain penetration, and shear deformations.   Shear displacements were negligible for columns in the Goodnight et al. dataset, therefore no further guidance is provided.

Inelastic displacements are computed when the base section curvature exceeds the first yield curvature, ϕ_y'. To account for additional elastic flexibility of the column, the first yield displacement is multiplied by the ratio of the current base section moment to the moment at first yield of longitudinal reinforcement, M/M_y'. The plastic curvature at the base section is obtained by subtracting the elastic curvature from the base section curvature, $\phi_p = \phi_{base} - \phi_y'(M/M_y')$. For translation of a tensile strain limit to a lateral displacement, the tensile triangular plastic hinge length should be used, Lpr_t Eqn 9.14. If instead, a compressive strain limit is translated to a later displacement, the compressive triangular plastic hinge length should be employed, Lpr_c Eqn 9.15. Expressions needed to compute the inelastic displacement of a column in single bending are shown in Eqn 9.22 through Eqn 9.26. Expressions needed to compute the inelastic displacement of a column in double bending appear in Eqn 9.27 through Eqn 9.31. The inelastic flexural displacement is the sum of the elastic column flexural, plastic column flexural, strain penetration, and shear deformations.

List of Selected Terminology:

$L = $ Length of the Column

$D = $ Column Diameter

$L_c = $ Length to the Point of Contraflexure, ($L_c = L/2$ for a Column in Double Bending)

$k = $ Moment Gradient Coefficient of Plastic Hinge Length Expression

$M_y' \; and \; \phi_y' = $ Moment and Curvature at First Yield of Longitudinal Reinforcement

$M = $ Column Base-Section Moment

$\phi_p = \phi_{base} - \phi_y' \, M/M_y' = $ Plastic Curvature at the base Section

$\Delta_e \; and \; \Delta_p = $ Elastic and Plastic Column Flexural Displacement

Δ_{shear} = Column Shear Displacement

Lpr_t = Tension Hinge Length Based on Triangular Distribution

Lpr_c = Compression Hinge Length Based on Triangular Distribution

Δ_{sp} = Column Displacement Attributable to Strain Penetration of Reinforcement

L_{sp} = Equivalent Strain Penetration Length

f_{ye} and f_{ue} = Yield and Ultimate Stress of Longitudinal Steel with Expected Properties

f'_{ce} = Unconfined Column Concrete Compressive Strength with Expected Properties

f'_{ce_f} = Concrete Compressive Strength of the Adjoining Member

d_{bl} = Diameter of the Longitudinal Reinforcement and Column Axial Load

P = Column Compressive Axial Load
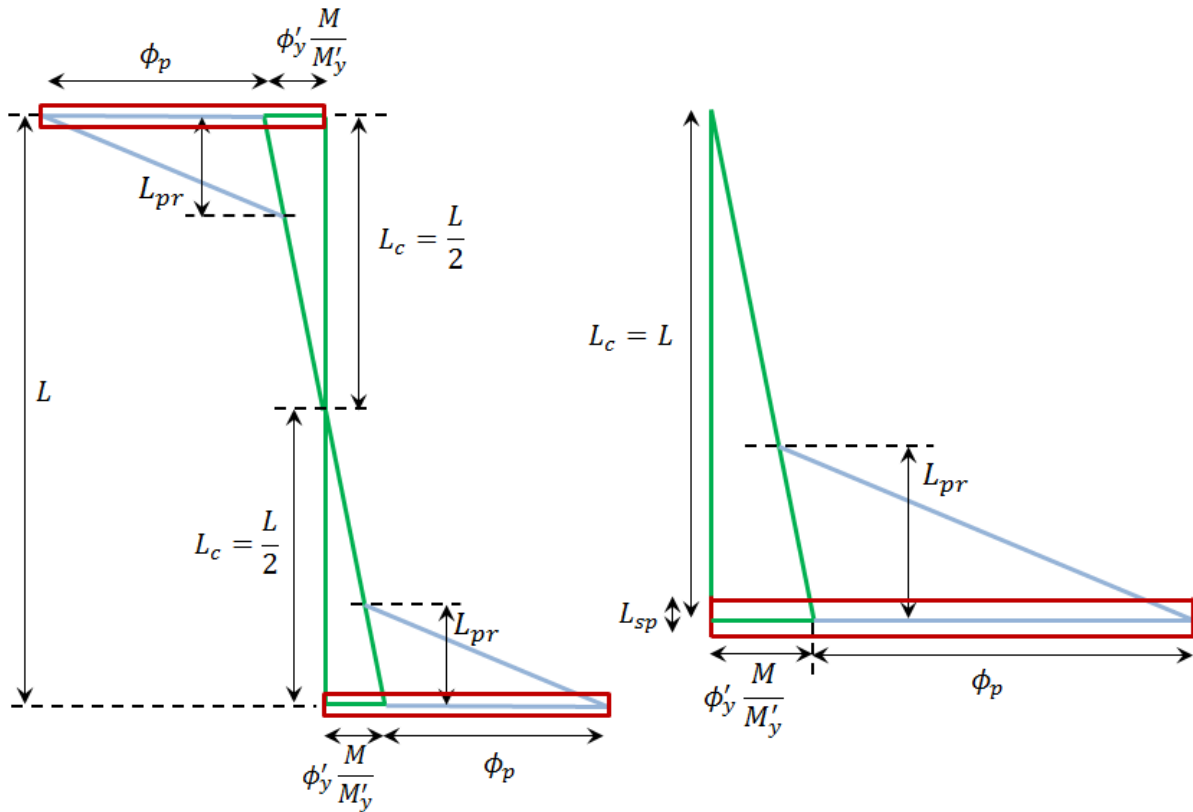
Figure 9.3 Equivalent Curvature Profiles for the Modified Plastic Hinge Method, (Left) Column in Double Bending and (Right) Column in Single Bending
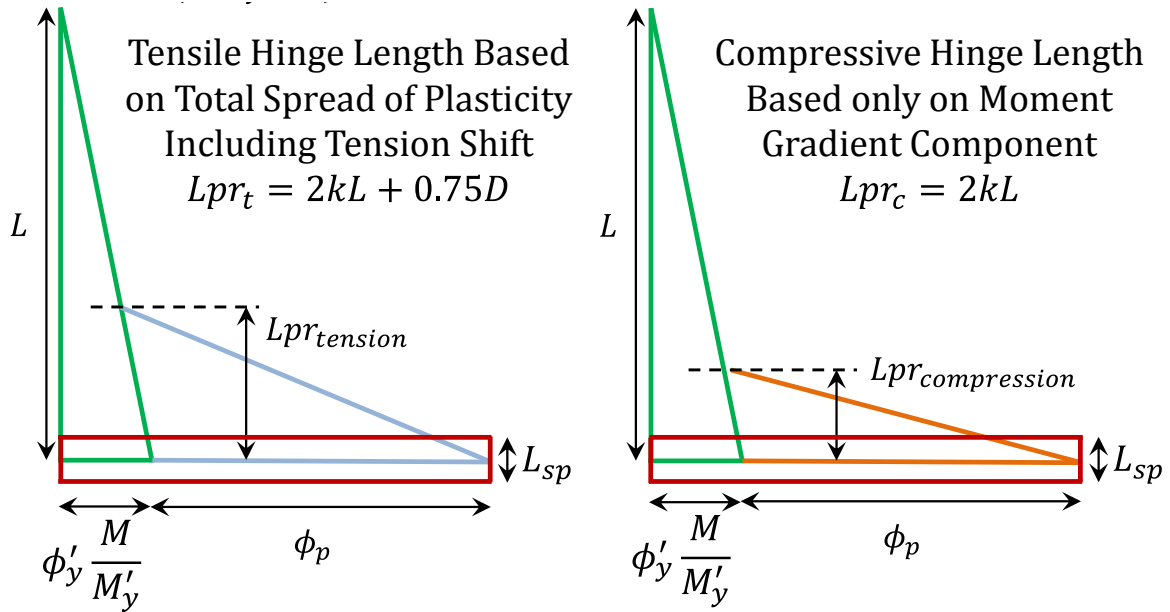
Figure 9.4 Separate Tensile and Compressive Triangular Plastic Hinge Lengths Utilized for Tensile and Compressive Strain-Displacement Respectively

9.2.1 Strain Penetration Length and Tension/Comp. Plastic Hinge Lengths

$$L_{sp} = U\left(1 - \frac{P}{f'_{ce}A_g} - \frac{L_c}{16D}\right)\frac{f_{ye}d_{bl}}{\sqrt{f'_{ce_f}}} \qquad U = 0.4 \text{ for ksi and } 0.152 \text{ for MPa units} \qquad \text{Eqn 9.12}$$

$$k = 0.2\left(\frac{f_u}{f_y} - 1\right) \le 0.08 \qquad \begin{array}{l}\text{Same Definition of k as Priestley,} \\ \text{Calvi, and Kowalsky (2007)}\end{array} \qquad \text{Eqn 9.13}$$

$$Lpr_t = 2kL_c + 0.75D \qquad \text{Tension Hinge Length Based on Triangular Dist.} \qquad \text{Eqn 9.14}$$

$$Lpr_c = 2kL_c \qquad \text{Compression Hinge Length Based on Triangular Distribution} \qquad \text{Eqn 9.15}$$

9.2.2   Elastic Displacements for a Column in Single Bending

$$\Delta_e = \phi_{base}L^2/3 \qquad \text{(Single) Elastic Flexural Displacement before First Yield} \qquad \text{Eqn 9.16}$$

$$\Delta_{sp} = L_{sp}\phi_{base}L \qquad \text{Displacement due to Strain Penetration} \qquad \text{Eqn 9.17}$$

$$\Delta_T = \left(\Delta_e + \Delta_{sp} + \Delta_{shear}\right) \qquad \text{Total Top Column Displacement} \qquad \text{Eqn 9.18}$$

9.2.3   Elastic Displacements for a Column in Double Bending

$$\Delta_e = \phi_{base}L^2/6 \qquad \text{(Double) Elastic Flexural Disp. before First Yield} \qquad \text{Eqn 9.19}$$

$$\Delta_{sp} = L_{sp}\phi_{base}L \qquad \text{Displacement due to Strain Penetration} \qquad \text{Eqn 9.20}$$

$$\Delta_T = \left(\Delta_e + \Delta_{sp} + \Delta_{shear}\right) \qquad \text{Total Top Column Displacement} \qquad \text{Eqn 9.21}$$

9.2.4 Inelastic Displacements for a Column in Single Bending

$\Delta_e = \phi'_y\left(M/M'_y\right)L^2/3$ (Single) Elastic Flexural Disp. after First Yield   Eqn 9.22

$\phi_p = \phi_{base} - \phi'_y\left(M/M'_y\right)$ Plastic Curvature at the Base Section   Eqn 9.23

$\Delta_p = \phi_p\left(L_{pr}/2\right)\left[L - L_{pr}/3\right]$ (Single) Plastic Disp. for Triangular Plastic Curvature Distribution   Eqn 9.24

$\Delta_{sp} = L_{sp}\phi_{base}L$ Displacement due to Strain Penetration   Eqn 9.25

$\Delta_T = \left(\Delta_e + \Delta_{sp} + \Delta_p + \Delta_{shear}\right)$ Total Top Column Displacement   Eqn 9.26

9.2.5 Inelastic Displacements for a Column in Double Bending

$\Delta_e = \phi'_y\left(M/M'_y\right)L^2/6$ (Double) Elastic Flexural Disp. after First Yield   Eqn 9.27

$\phi_p = \phi_{base} - \phi'_y\left(M/M'_y\right)$ Plastic Curvature at the Base Section   Eqn 9.28

$\Delta_p = \phi_p\left(L_{pr}/2\right)\left[L - 2\,L_{pr}/3\right]$ (Double) Plastic Disp. for Triangular Plastic Curvature Distribution   Eqn 9.29

$\Delta_{sp} = L_{sp}\phi_{base}L$ Displacement due to Strain Penetration   Eqn 9.30

$\Delta_T = \left(\Delta_e + \Delta_{sp} + \Delta_p + \Delta_{shear}\right)$ Total Top Column Displacement   Eqn 9.31

Chapter 10: Future Research on the Effects of Seismic Load Path

10.1 Problem Statement

Seismic bridge design practice utilizes the simplifying assumption of unidirectional response, which results in consideration of orthogonal directions of loading on an individual basis. Typically, for bridges, the two directions are transverse and longitudinal to the direction of traffic (for a straight bridge). Such a division is usually employed for assessing demand and capacity, and would be appropriate if the two directions of loading were uncoupled from each other.

Prior research at NCSU investigated the impact of loading history on the unidirectional response of RC bridge columns, leading towards recommendations on strain limits and plastic hinge lengths which consider the impacts of real seismic loading. The next step in this progression is to consider the impact of multi-directional loading path on these recommendations. It is possible that multi-directional loading, even for circular columns, could lead to adjustments to unidirectional strain limits proposed for design, as well as the manner in which those strain limits are converted to design displacements via the plastic hinge method for member deformations.

10.2 Background

Bridge columns are designed as ductile elements which form plastic hinges to dissipate energy in a seismic event. The goal of performance based seismic engineering is to design structures to achieve a predictable level of performance under a specific earthquake hazard within definable levels of reliability, as defined by the Structural Engineering Association of California (SEAOC 1999). To satisfy the aims of performance based design, levels of damage which interrupt the serviceability of the structure or require more invasive repair

techniques must be related to engineering criteria. For reinforced concrete flexural members such as bridge columns, concrete compressive and steel tensile strain limits are good indicators of damage.

Serviceability limit states such as concrete cover crushing or residual crack widths exceeding 1mm may occur during smaller, more frequent earthquakes (Priestley et al. (1996)). While the serviceability limit states do not pose a safety concern, the hinge regions must be repaired to prevent corrosion of internal reinforcing steel. At higher ductility demands produced by larger less frequent earthquakes, reinforcing bar buckling may lead to permanent elongation in the transverse steel, which diminishes its effectiveness in confining the concrete core. Bar buckling and significant damage to the core concrete represent the damage control limit states, which when exceeded lead to significant repair costs (Priestley et al. (1996)). Furthermore, rupture of previously buckled bars during subsequent cycles of loading leads to rapid strength loss. The life safety or collapse prevention limit state is characterized by fracture of previously buckled bars. A summary of damage observations from a reinforced concrete bridge column tested at NCSU by Goodnight et al. (2014) appears in Figure 10.1.

Performance based seismic engineering requires accurate limit state-based engineering demand parameters, such as material strains, and an accurate method of relating these quantities to a capacity measure in design, such as member deformation. In the following section, advancements in strain limit-based displacement predictions are summarized for the current AKDOT sponsored project (Goodnight et al. (2014)). The experimental portion of the research program is complete and design recommendations are being finalized for the AKDOT. Finally, the importance of considering bi-directional displacement history is evaluated based on specific observations reported in literature.
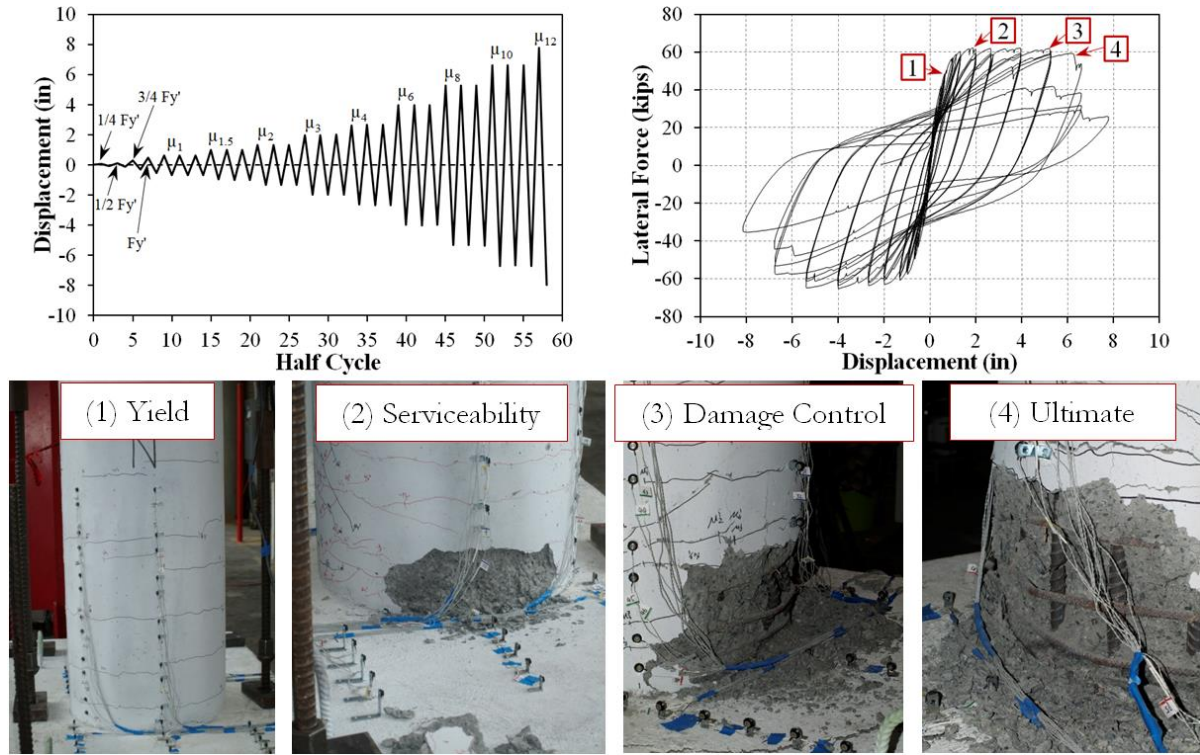
Figure 10.1 Goodnight et al. (2014). Bridge Column Uniaxial Displacement History, Hysteretic Response, and Photos at (1) Yield, (2) Cover Crushing, (3) Long. Bar Buckling, (4) Long. Bar Fracture

While the progression of damage in flexural bridge columns has been investigated in the past for both uniaxial and biaxial deformation demands, traditional methods of deriving material strains from measured curvatures do not asses strains at the locations of interest, namely the longitudinal reinforcement and core concrete. These methods utilize an array of linear potentiometers placed on the ends of threaded rods embedded in the core concrete to calculate changes in displacement outside of the cover concrete. A new instrumentation technique was devised to overcome this limitation. Goodnight et al. (2014) investigated the impact of unidirectional-lateral displacement history and design variables on the material strain limits and the relationship between strain and displacement for circular reinforced

concrete columns.   To date, all thirty experiments have been completed and design recommendations are being finalized for AKDOT.

The specimen was designed to represent a single degree of freedom bridge column subjected to lateral and axial load, Figure 10.2. The test specimen consists of a footing, column, and loading cap. The footing is a capacity protected member which secures the specimen to the lab strong floor using post tensioned bars. A 200kip hydraulic actuator, with a 40in stroke capacity, applies lateral load to the loading cap of the specimen. A spreader beam, two hydraulic jacks, and a load cell are placed above the loading cap to apply a constant axial compressive load. The top column displacement was obtained through a string potentiometer placed at the center of the lateral load. The experimental program utilized multiple Optotrak Certus HD 3D position monitors developed by Northern Digital Inc. The position monitors track the locations of the target markers in 3D space, returning X-Y-Z spatial coordinates with an accuracy of 0.1mm and with a resolution of 0.01mm.

A technique of applying target markers to longitudinal and transverse reinforcement, Figure 10.2, was utilized in the plastic hinge region. Strains are computed by dividing the change in three dimensional distance between two adjacent target markers by the original unloaded gage length. Both transverse and longitudinal steel was instrumented to measure the interaction between core concrete confinement and longitudinal bar restraint demands in spiral layers leading up to visible bar buckling. Closely spaced transverse steel restrains the dilation of core concrete under compressive demands, improving its strength and deformation capacity. These spiral layers locally support the longitudinal bar, reducing its unbraced length, which delays the onset of bar buckling. Large compressive cycles can yield the transverse steel, reducing its effectiveness as a boundary condition restraining the longitudinal bar from buckling. Longitudinal bars are prone to buckling during reversals from peak tensile strains, while the cracks are still open, and they are the sole source of compression zone stability. This behavior is observable in the measured longitudinal and overlaying spiral strain hysteresis, Figure 10.3, in the region where outward bar buckling was observed just above the footing-column interface. Some small level of outward deformation

prior to visible bar buckling is observable in the longitudinal and transverse steel hysteresis during the first two pull cycles to -6.6". Upon visible bar buckling, a significant deviation in both hystereses is noted, confirming the observation.
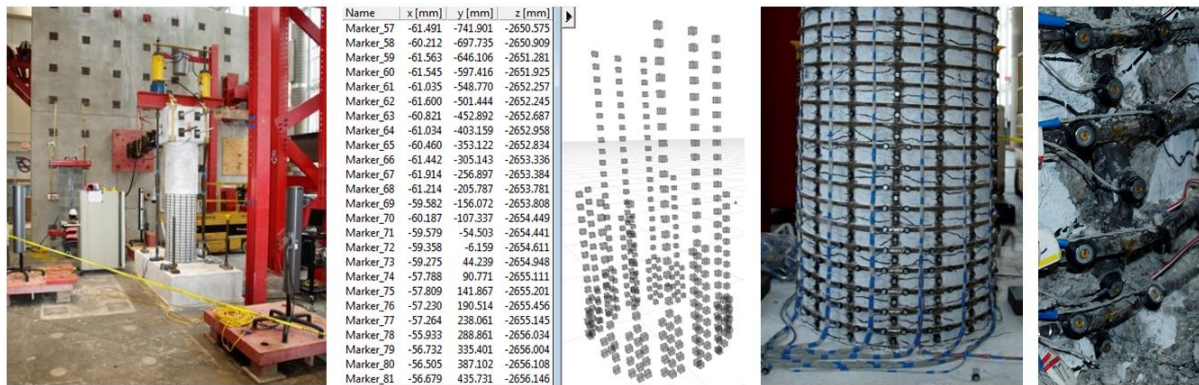
Figure 10.2 Optotrak Instrumentation Technique Applied to Columns in Goodnight et al. (2014). Target Markers Monitor Longitudinal and Transverse Reinforcement Strains in the Column Hinge Regions.
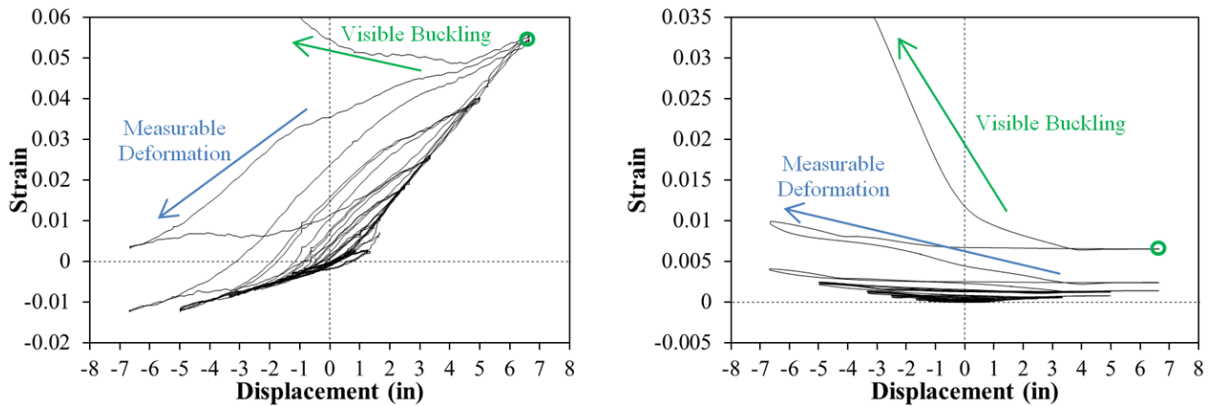
Figure 10.3 Goodnight et al. (2014) Test 16. [Left] Longitudinal Steel Strain Hysteresis and [Right] Spiral Strain Hysteresis for the Layer over the Outward Buckled Region of the Longitudinal Bar

The instrumentation technique proved pivotal in improving the accuracy of strain-limit based displacement predictions. The data was used to calculate material strains, curvature distributions, and fixed end rotations due to strain penetration of reinforcement into the footing. The decoupling of column flexural displacements from fixed-end rotations due to strain penetration, along with an understanding of the spread of plasticity, allowed for creation of a new equivalent curvature distribution. In design, there are two main techniques to assess the member displacement at a given material strain level: (1) monotonic moment-curvature analysis paired with an equivalent curvature distribution and (2) cyclic fiber analysis paired with an element representation of the beam or column. In the following section, the predictive capabilities of these two methods are evaluated along with the design recommendations from Goodnight et al. (2014).

For this comparison, the monotonic section analysis from a script developed at NCSU called Cumbia (2007) is translated into member response using the plastic hinge method presented in Priestley, Calvi, and Kowalsky (2007) and the modified NCSU hinge method proposed by Goodnight et al. (2014), Figure 10.5. In both methods, the elastic and plastic curvature distributions are separated into equivalent simplified shapes to facilitate design. The PCK (2007) hinge method utilizes a constant plastic hinge length which includes the influence of strain penetration.   Independent measurement of deformation components allowed for a decoupling of strain penetration and column flexure in the NCSU hinge method. Furthermore, the shape and size of the plastic hinge length are now related to physical quantities which reflect the measured extent of plastic curvatures, Figure 10.4. The total spread of plasticity in RC bridge columns is due to the combined effects of moment gradient and tension shift. Tension shift concentrates compressive strains near the footing-column interface while fanning tension strains above the footing following the inclined flexural-shear crack distribution. Moment gradient spreads plasticity in accordance with the increase in moment higher above the footing when the base-section moment exceeds the nominal value. Tension strains were found to be influenced by the combined effect of moment gradient and tension shift, while compressive strains are more closely related to only the moment gradient component. Separate expressions for tensile and compressive plastic

hinge lengths were devised to improve both the tensile and compressive strain-displacement predictions of the equivalent curvature distribution. In Figure 10.6, the strain-displacement predictions for the two hinge methods are compared to the measured response on an extreme fiber bar instrumented in a cyclic column test from Goodnight et al. (2014). The NCSU hinge method shows improvement, but both methods fail to account for the localization of compressive strains once severe transverse steel yielding has occurred.

Monotonic section analysis and an equivalent curvature distribution allow for an accurate prediction of the backbone curve of cyclic response, but if the actual cyclic response is required, then cyclic fiber analysis paired with an element representation of the beam or column is needed. The cyclic displacement history from the experiment was recreated using a combination of two elements in OpenSees: (1) a beam with hinges element to model the column flexural deformations and (2) a zero length strain penetration element to model the fixed end rotations due to strain penetration. The beam with hinges element, developed by Scott and Fenves (2006), is a force-based beam-column element with a plastic hinge integration method. The zero length strain penetration element, developed by Zhao and Sritharan (2007), models the fixed-end rotations attributable to strain penetration of longitudinal reinforcement into the footing. Response predictions for the two analysis methods appear in Figure 10.7. The predicted tensile strains from OpenSees exceeded the measured response with the plastic hinge length from PCK (2007). The hinge length in OpenSees was changed to 1.2*Lp from PCK (2007) to match the measured tensile strain displacement relationship in Figure 10.7. Manually changing the plastic hinge length to match tensile response leads to an under prediction of the compressive strain-displacement relationship for the peak compressive gage length, leading to different hinge lengths which are proposed based on the NCSU equivalent curvature distribution.
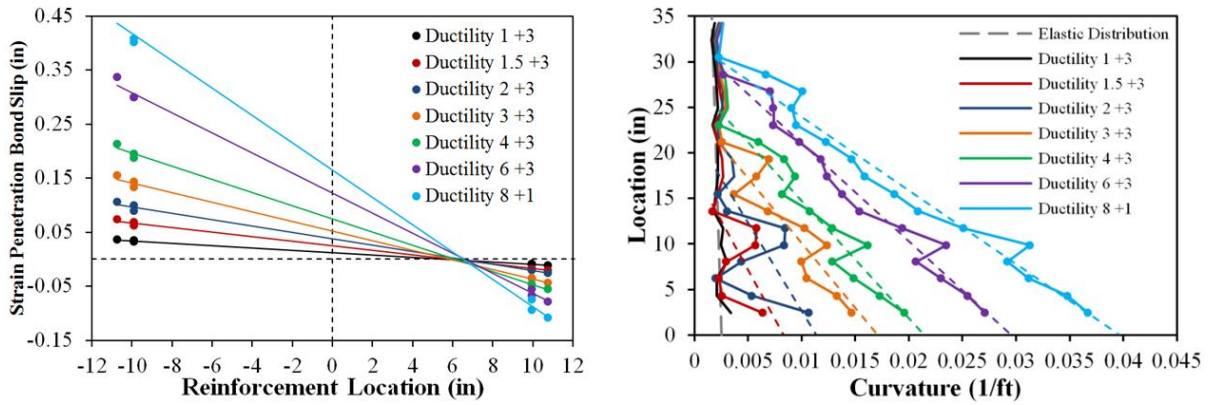
Figure 10.4 Goodnight et al. (2014) Test 9. [Left] Measured Fixed-End Rotation due to Strain Penetration of Longitudinal Reinforcement into the Footing and [Right] Curvature Distribution with Linear Dashed Plastic Curvature Regression Lines
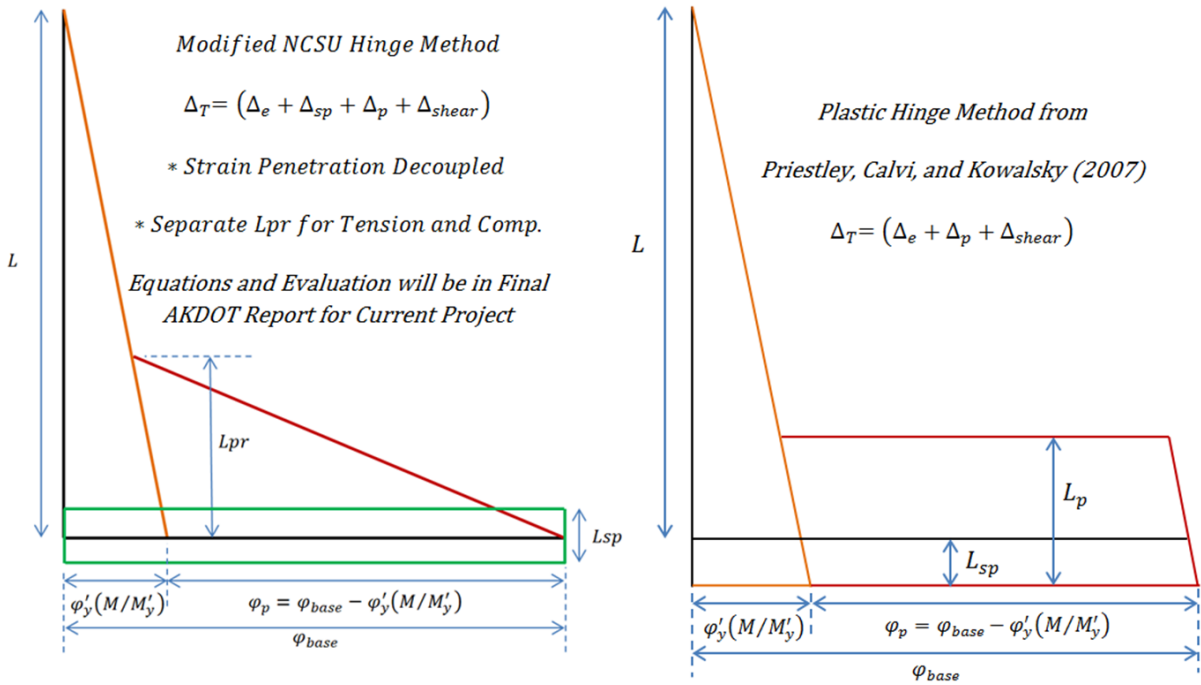
Figure 10.5 [Left] Proposed NCSU Plastic Hinge Method from Goodnight et al. (2014) and [Right] PCK (2007) Method
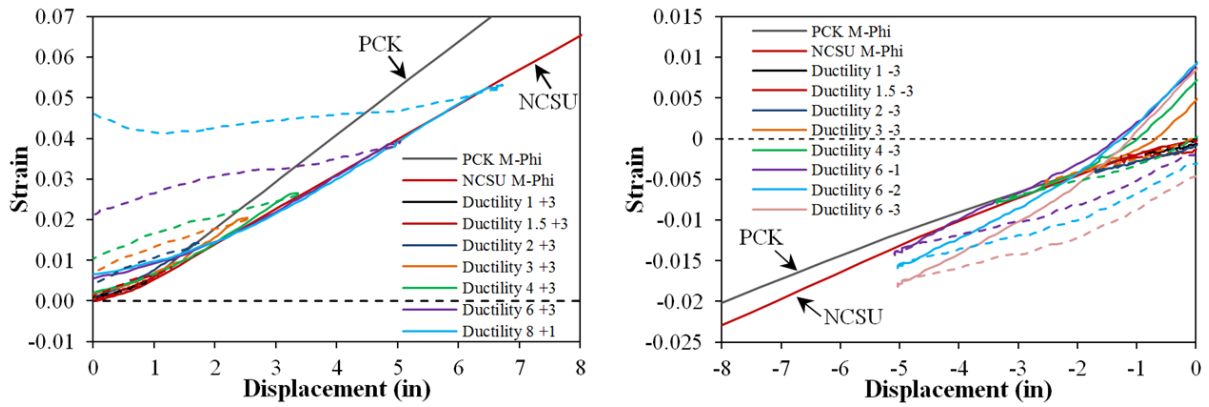
Figure 10.6 Goodnight et al. (2014) Test 9. Strain-Displacement Relationships and Moment Curvature Predictions with PCK and NCSU Plastic Hinge Methods
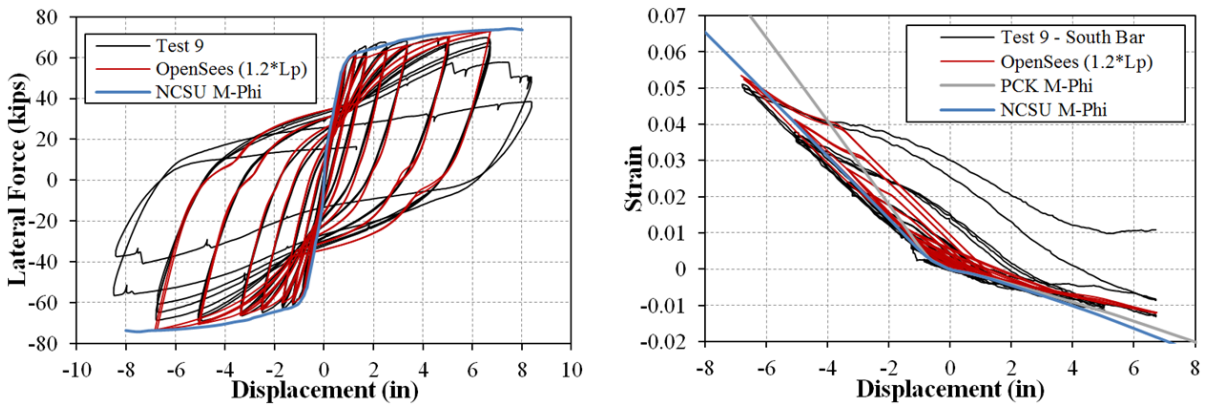
Figure 10.7 Goodnight et al. (2014) Test 9. Member Response Prediction with Cyclic Fiber Model and Monotonic Section Analysis

10.3 Brief Load Path Literature Review

In a seismic event, bridge columns undergo demands in the longitudinal and transverse directions simultaneously, which produce a two-dimensional displacement path.   Past experimental studies on biaxial bending with either constant or variable axial load provide insight into their effect on member behavior.

10.3.1 Yuk-Lung Wong, T. Paulay, and M. J. Nigel Priestley (1993). "Response of Circular Reinforced Concrete Columns to Multi-Directional Seismic Attack"

Sixteen circular shear-dominated columns were tested with different biaxial displacement histories, volumetric steel ratios, and levels of applied constant axial load. The purpose of the research was to determine the influence of biaxial loading on the "concrete component" of shear resistance. Short circular columns were tested with a 400mm diameter, an aspect ratio of 2, and a steel content of 3.2%. Axial loads of 0, 19 or 39% were utilized. Transverse volumetric steel ranged between 0.39 and 2.46%. Four displacement patterns were considered, Type u, b, s, and r in Figure 10.8. The uniaxial 'u' pattern had five cycles at a given amplitude before increasing to a larger displacement ductility level. Biaxial 'b' and 's' patterns had two cycles at each amplitude before ramping up the displacement. Due to the bidirectional nature of the load history this resulted in four complete reversals at each displacement level. The multi-directional 'r' pattern was used to simulate a displacement path originating from NLTHA of a column under earthquake excitation.

Wong et al. (1993) concluded that biaxial response reduced the deformation capacity by one ductility level when compared to a nominally identical column subjected to uniaxial response. Furthermore, Wong et al. (1993) conclude that there was not a clear difference in results of the two b- and s-type laboratory biaxial displacement patterns. The following observation is of significance to bar buckling, "For columns reinforced with similar spiral steel content, the commencement of spiral yielding was consistently observed at lower ductilities when more severe displacement orbits were imposed." On the topic of load path

effects, Wong et al. (1993) note, "The difference in the response of columns with identical properties subjected to simple biaxial b-type displacement patterns or to more sophisticated s-type patterns was small enough to be disregarded in design. Moreover, the performance of the unit tested with the realistic earthquake simulating random biaxial displacement pattern was found to be better than its companion unit under b-type displacement history. These suggest that if biaxial seismic effects are to be studied further, test using biaxial b-type (orthogonal) displacement paths should be sufficient."
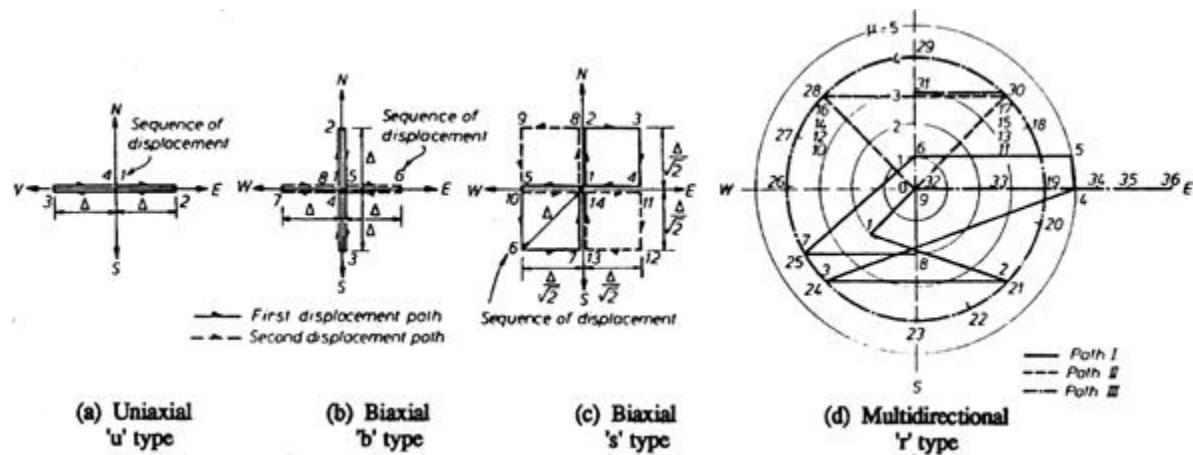
Figure 10.8 Wong et al. (1993), Lateral Displacement Histories

10.3.2 E. Osorio, J.M. Bairán, and A.R. Marí (2012).   "Effects of Biaxial Shear Loading on the Seismic Response of RC Columns"

Two nominally identical circular columns were tested, one subjected to uniaxial and the other biaxial loading. The specimens were designed for flexural-shear failure. The 350mm diameter circular specimens had 2.5% longitudinal steel, 0.5% transverse volumetric steel, a constant 20% axial load, and an aspect ratio of 4.3. A clover leaf style lateral displacement history utilized in the biaxial test, Figure 10.9. Two complete cycles at a given displacement amplitude were conducted for the bidirectional tests. Strain gages were applied in each quadrant for the first three spiral layers. The location of these strain gages directly overlaid

the extreme fiber reinforcing bars subjected to the peak excursions. The reported transverse steel strain hysteresis for bidirectional and unidirectional loading appears in Figure 10.9. Although the shape of the measured response is similar, the biaxial loading resulted in an additional accumulation of hoop strain during repeated cycles at displacement amplitude of 27mm. This additional hoop strain can reduce its ability to restrain longitudinal bars from buckling as well as influence confinement effects. The reported observations indicate that this spike in measured hoop strains coincided with visible bar buckling. In comparison, bar buckling was reported one displacement amplitude larger in the uniaxial test. Osorio et al. (2012) note, "Results show that biaxial shear loading affects the shear mechanisms, producing larger transversal strains for the same load intensity and lower crack angles." It is still important to note that the displacement amplitudes are small, and the level of confinement/restraint is low in the shear dominated columns.
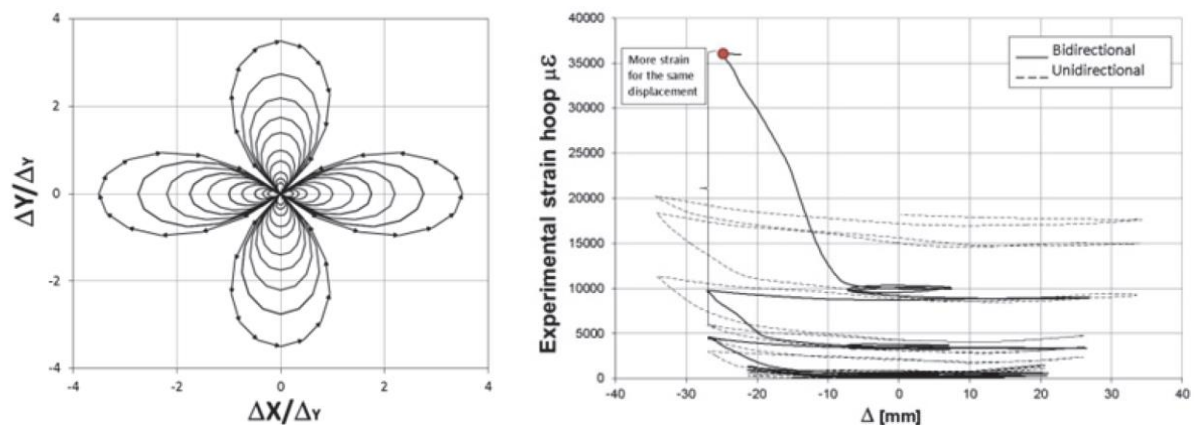
Figure 10.9 Osorio et al. (2012), [Left] Biaxial Displacement History and [Right] Measured Hoop Strains for Uniaxial and Biaxial Displacement Patterns

10.3.3 Kazuhiro Tsuno and Robert Park (2004). "Experimental Study of Reinforced Concrete Bridge Piers Subjected to Bi-Directional Quasi-Static Loading"

The study considered four rectangular bridge columns subjected to different bidirectional load paths, and one repeat load history for a fifth column with a lower concrete strength. The specimens were 550mm square with and aspect ratio of 4.1, a steel content of 1.2%, a volumetric steel ratio of 1%, and a constant axial load equivalent to 4.4%. The first specimen, S1, was subjected to a symmetric uniaxial two-cycle-set load history which served as a baseline for comparison to biaxial tests. Specimen S2 was subjected to the exact opposite of the load history used for S1, with the high ductility cycles occurring first followed by a gradual decrease in ductility. Specimen S3 utilized a bi-directional orthogonal symmetric two cycle set load history, Figure 10.10. Four total cycles were conducted at each ductility level, two in the E-W direction followed by two in the N-S direction. Specimen S4 utilized a bi-directional s-shape load history, Figure 10.11. Two complete orbital paths (1-16) were completed at each ductility level. The fifth column had reduced concrete strength and was subjected to the same uniaxial load history as S1.

Tsuno and Park (2004) reported that reinforcement buckled at $\mu_{\Delta 8}$ and ruptured at $\mu_{\Delta 12}$ during the uniaxial two-cycle-set load history of S1. Spiral fracture was reported during $\mu_{\Delta 10}$. In specimen S2, bar buckling was reported during the reversal from the first cycle of $\mu_{\Delta 12}$ before the specimen reached zero displacement. Again, this was an inverse of the two-cycle-set load history which began with high ductility reversals. For bi-directional load history of specimen S3, bar buckling was reported during $\mu_{\Delta 6}$ and bar fracture during $\mu_{\Delta 8}$. For bi-directional load history of specimen S4, bar buckling was reported during $\mu_{\Delta 6}$ and bar fracture during $\mu_{\Delta 8}$. The fifth specimen, with weaker concrete and a uniaxial two-cycle-set load history had reported bar buckling during $\mu_{\Delta 6}$ and bar fracture during $\mu_{\Delta 10}$.

Tsuno and Park (2004) utilized an array of linear potentiometers to monitor curvature distributions in the main orthogonal directions of the load histories. Cross section curvature

profiles obtained from the potentiometers were used to calculate an equivalent rectangular plastic hinge length Lp. Lp is the length over which plastic curvatures are assumed to remain constant, and in their formulation it includes the strain penetration component. A sample curvature profile for specimen S1, and the resulting Lp values for all of the experiments is shown in Figure 10.12. Tsuno and Park (2004) provide a summary of observations related to the influence of bi-directional loading on curvature profiles and computed plastic hinge lengths, which are repeated below.

"1. The plastic hinge zone length Lp tends to be stable at around the theoretical values after some cyclic loadings and is not affected by bi-directional loading. The plastic hinge zone length is shorter than the theoretical values until the displacement ductility factor μ_Δ reaches around 4. The concrete strength of a column might affect the plastic hinge zone length Lp. No significant difference in the Lp-μ_Δ relationship was observed between tests S1-S4, which suggests that Lp is not affected by bi-directional loading after some cycles of loading.

2. If an extremely large displacement, such as $\mu_{\Delta 12}$, for the specimens used in this research is applied to a column at the early stage of cyclic loading, it may lead to the buckling of main-bars and confinement failure with only small energy dissipation. However, as long as the displacement amplitude in the cyclic loading starts at a small level and increases step-by-step, like the standard loading pattern suggested by Park, the energy dissipation capacity of a column until the ultimate state is the same for both uni-directional and bi-directional loading.

3. The maximum displacement of a column when it reaches the ultimate state in a bi-directional cyclic loading, is smaller than that of the same column subjected to the standard uni-directional loading pattern suggested by Park."

(a) Loading pattern for Specimen-3:
Loading cycle for East-West direction

(b) Loading pattern for Specimen-3:
Loading cycle for North-South direction

(c) Loading pattern for Specimen-3:
Loading orbit at the top of the spec
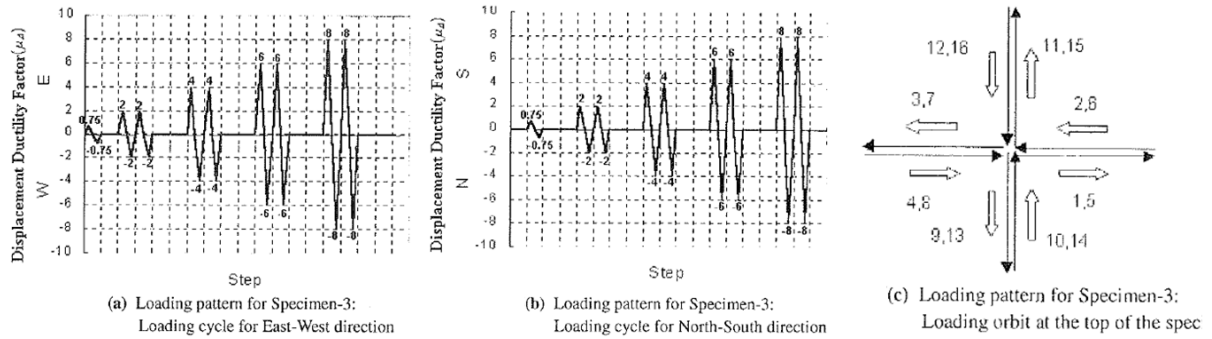
Figure 10.10 Tsuno and Park (2004). Bi-Directional Load History for Specimen S3

(a) Loading pattern for Specimen-4:
Loading pattern for East-West direction

(b) Loading pattern for Specimen-4:
Loading pattern for North-South direction

(c) Loading pattern for Specimen-4:
Loading orbit at the top of the spec
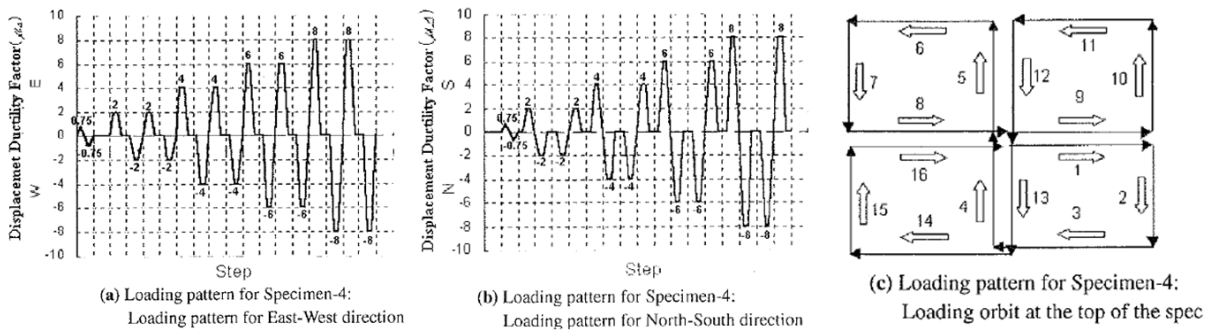
Figure 10.11 Tsuno and Park (2004). Bi-Directional Load History for Specimen S4

Curvature Distribution of Specimen-1

Plastic Hinge Zone Length Obtained in Tests
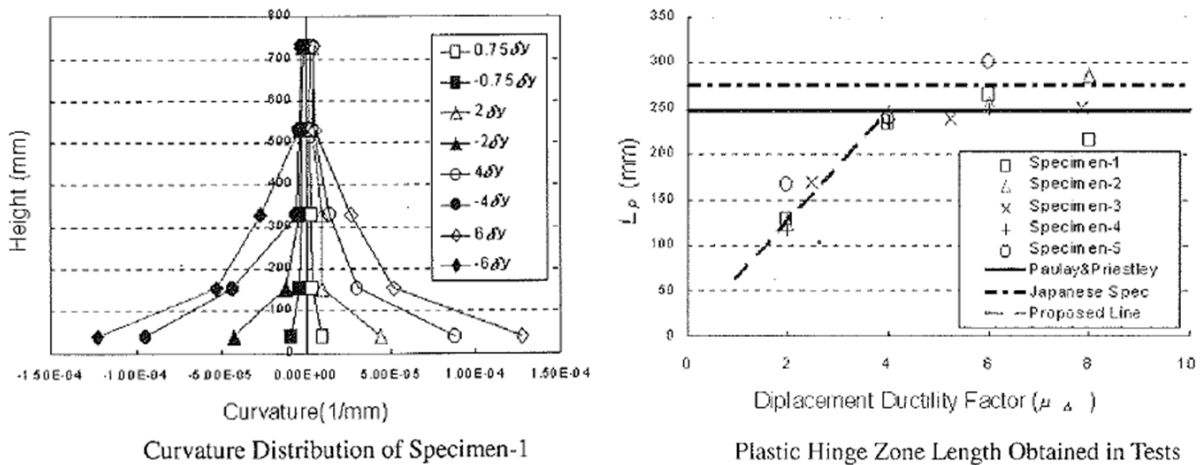
Figure 10.12 Tsuno and Park (2004) Calculated Lp Values from Measured Curvature Profiles

10.3.4 Stathis N. Bousias, Guido Verzeletti, Michael N. Fardis, Eugenio Gutierrez (1995). "Load Path Effects in Column Biaxial Bending with Axial Force"

The research focused on the effect of three dimensional load path, including a mixture of displacement and force controlled lateral input as well as varying axial load for square columns. The columns were 250mm square and an aspect ratio of six. The cross section had 8, 16mm bars uniformly distributed around the perimeter and a double 8mm diameter hoop arrangement with 70mm spacing. The load histories utilized in the experiments are shown in Figure 10.13. Load histories S0, S1, S2, S5, S6, S7, and S8 utilized constant axial force and varying imposed lateral displacement history. Specimens S3 and S4 had a mixture of force control and displacement controlled loading histories in the orthogonal directions and a constant axial force. Test units S9, S10, and S11 had varying lateral and axial loading history. The load histories were devised to evaluate specific characteristics unique to bidirectional loading.

Bousias et al. (1995) note the following regarding the influence of load path, "The strong coupling between the two transverse directions produced an apparent reduction of strength and stiffness in each of the two transverse directions considered separately, but also increased the hysteretic energy dissipation. This increase is manifested by the larger width of the hysteresis loops in a transverse direction in the presence of a nonzero force or deflection in the orthogonal direction, as compared with the cases of cyclic uniaxial bending. Moreover, biaxial force paths are rotated with respect to the biaxial deflection paths in the sense in which these are traced, so that the vector resultant of transverse displacements always lags behind the vector resultant of transverse forces."

Test Specimen (1)	f$_c'$ (MPa) (2)	N/A$_c$f$_c'$ (3)	Load Path (4)
S0	30.75	0.16	
S1	29.0	0.12	δx / δy
S2	31.1	0.15	δy / δx
S3	29.9	0.17	δx / Fy
S4	27.7	0.15	δx / Fy
S5	33.1	0.12	δy / δx
S6	25.7	0.10	δy / δx
S7	28.1	0.12	Expanding
S8	25.4	0.11	Shrinking
S9	23.9	0.03/0.15	Circle δy / δx
S10	28.5	0 - 0.28	N / Fx
S11	35.4	0 - 0.27	N / Fy / δx
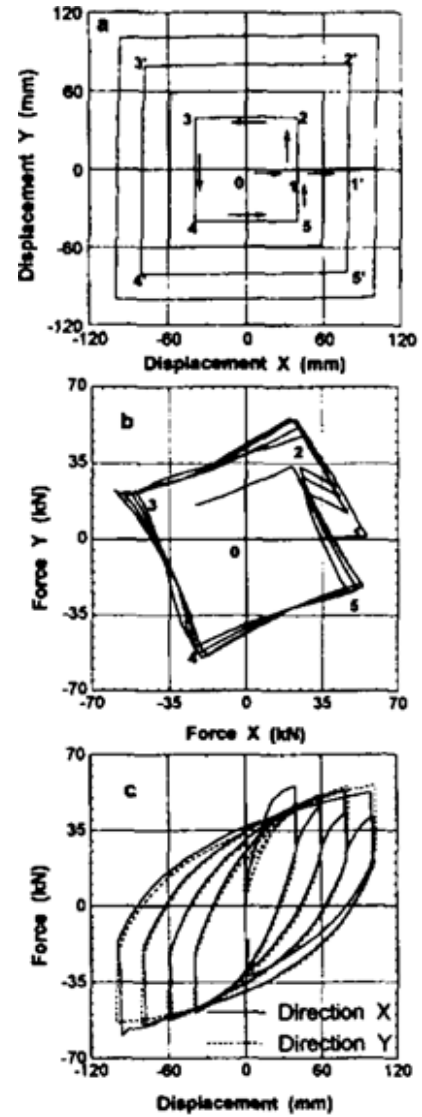
Figure 10.13 [Left] Load Histories Utilized in Bousias et al. (1995) and [Right] Selected Test S7 from Bousias et al. (1995) which Demonstrates Lag of Force Resultant behind Disp. Resultant

10.4 Study Objectives

The objective of the research described in this research is to determine the impact of a 2-dimensional loading path on the definition of displacement-based performance limit states and the relationship between strain and displacement (i.e., plastic hinges). The specific issues with regard to load path are the impact of multi-directional loading on: (1) Accumulation of strain in reinforcing steel; (2) Uni-directional design (which is the normal practice); and (3) Crack formation and the plastic hinge length method for member deformations.

10.5 Research Plan

10.5.1 Task One: Detailed Literature Review

As previously noted, the research team has been studying the issue of loading history and its impact on the relationship between strain and displacement and strain limits themselves. As part of that work, a more accurate model for plastic hinge lengths in concrete bridge columns has been developed, along with a simple method for accurately predicting the force-displacement response of a column considering column flexure and strain penetration. This was possible due to the fidelity of the data that was obtained through the use of a 3D non-contact position measurement system, as well as by detailed fiber modeling of RC columns. As part of that work, a detailed literature review was conducted on the impact of load history (which will not be repeated here). In addition, pilot analytical studies were undertaken to assess the impact of loading path on the recommendations developed as part of that research. The literature review will focus on past studies on load path and its possible impacts on performance-based design. This will include an examination of different loading protocols, as well as real bi-directional EQ load histories.

10.5.2 Task Two: Load Path Analysis

Accurate fiber models capable of predicting force deformation response and local strain information were developed as part of the load history research previously conducted at NCSU. Examples of this are shown in Figure 10.14 for strain and force versus deformation response. As part of this task, the load path analysis conducted during the load history research project will be extended.
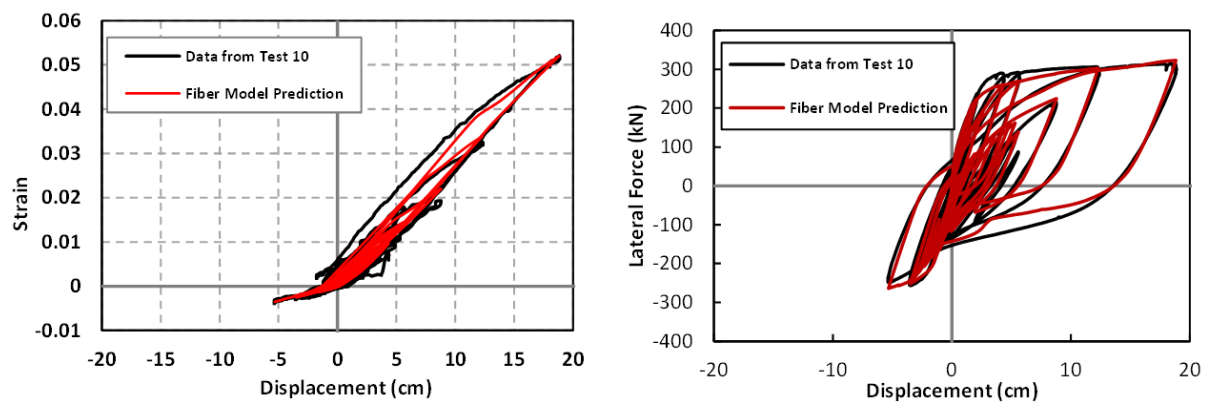
Figure 10.14 Analytical and Experimental Comparison for (Left) Strain Hysteresis and (Right) Force-Displacement Curve

10.5.3 Task Three: Experimental Studies on Columns

The experimental work will involve a series of 12 circular bridge columns, each subjected to bi-directional loading and constant axial force. The dimensions of the cross section, length of the member, and reinforcement detailing mirror previously tested specimens from Goodnight et al. (2014). The uniaxial response of similarly detailed columns serves as the basis of comparison for the proposed experiments. Other variables that will be considered include longitudinal steel ratio, transverse steel detailing, and axial load ratio. The proposed test setup is shown in Figure 10.15. The lateral load will be applied by two

hydraulic actuators, which form a 45-45-90 triangle in the X-Y plane with initially concentric lines of action. The input displacement control and post-processing of the actuator loads is defined based on the initial and deformed geometry of the setup. Through geometry, each actuator load is resolved into the X and Y components, which in turn is used to compute the resultant force on the column. A constant vertical load is maintained by a single hydraulic jack placed above the specimen which post tensions a 1 ¾" Dywidag bar located within a 3" PVC duct at the center of the cross-section. A 10"x10"x8" pocket at the bottom of the footing-column joint provides a reaction for the axial load bar.

The bi-directional loading paths will be prescribed in some cases and earthquake time history based in others, Figure 10.16. The Type-B and Type-S load paths serve as a two-dimensional extension of the symmetric-three-cycle set load history employed in Goodnight et al. (2014), Figure 10.1. The Type-B load path, Figure 10.16, consists of a reversal in the y-direction 1-4 followed by a reversal in the x-direction 5-8. The Type-S load path follows the double figure eight path 1-16 in Figure 10.16. The Type-S load history still contains defined reversals to evaluate the damage induced by the prior cycle while providing some out of plane deformation demands. The load paths induced by earthquakes are more random in nature in both path and sequence of displacement amplitudes. The load path for earthquake records will come from time history analysis of the bridge column under orthogonal directions of seismic input. The shape of the load path will be simplified into straight line approximations along the displacement orbit, so that it can be used in the lab as a displacement controlled loading procedure. Regardless of which load history is used, the test will begin in the same format. A single Type-B reversal will be completed in the following fractions of the analytical first yield force: ¼, ½, ¾, and F_y'. The recorded first yield displacements in each of the principle directions, N-S-E-W, will be averaged to find the experimental first yield displacement. The experimental first yield displacement is multiplied by the ratio of the nominal to the first yield moment to determine the equivalent yield displacement, $\mu_{\Delta 1} = \Delta_y'(M_n/M_y')$. The Type-B and Type-S load paths then resume with two complete reversals at each of the following displacement amplitudes: $\mu_{\Delta 1}$, $\mu_{\Delta 1.5}$, $\mu_{\Delta 2}$, $\mu_{\Delta 3}$, $\mu_{\Delta 4}$, $\mu_{\Delta 5}$, $\mu_{\Delta 6}$, $\mu_{\Delta 7}$, etc. until failure is observed.

The proposed test matrix for the 12 bi-directional load path columns is shown in Table 10.1. The geometry and reinforcement was selected to mirror that of previous uniaxial tests by Goodnight et al. (2014), shown in Table 10.2. That way, a separate uniaxial load history experiment may not be necessary to compare to the results of the biaxial tests. Although it is unlikely, if the material properties of the reinforcement vary significantly from prior experiments, Tests 5, 6, and 9 may be replaced by uniaxial load histories. Two longitudinal steel ratios will be evaluated in the test matrix, 1.6% and 2.1%. Similarly, two transverse volumetric steel ratios are included, 0.7% and 1%. The majority of the tests will have a constant level of applied axial load equivalent to $P/(f_c' A_g) \approx 9\%$, depending on the concrete compressive strength. The detailing was chosen to be representative of the well-detailed bridge columns with a flexural failure mode dictated by fracture of previously buckled longitudinal bars. The ranges of variables in the test matrix were selected to measure their influence of the observed failure mode. The specimens will be constructed at the NCSU lab and will utilize the same three-dimensional position monitoring system employed during Goodnight et al. (2014), Figure 10.2.
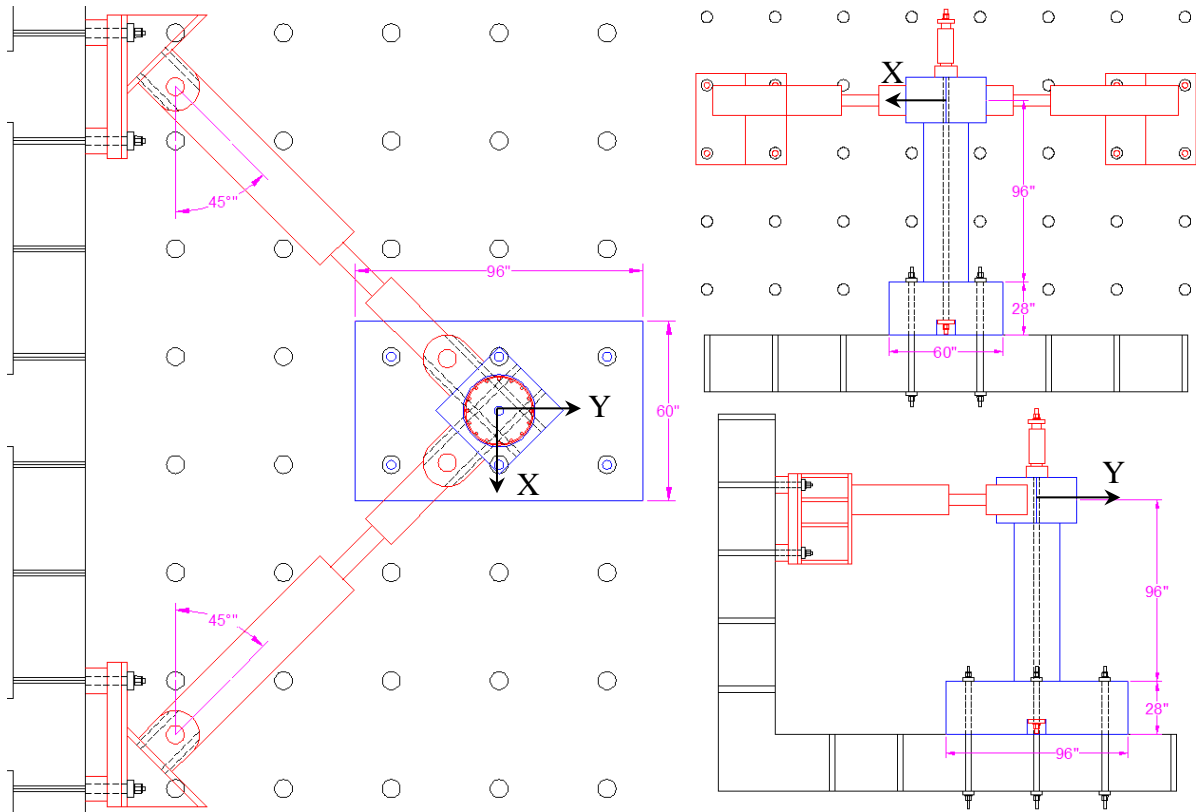
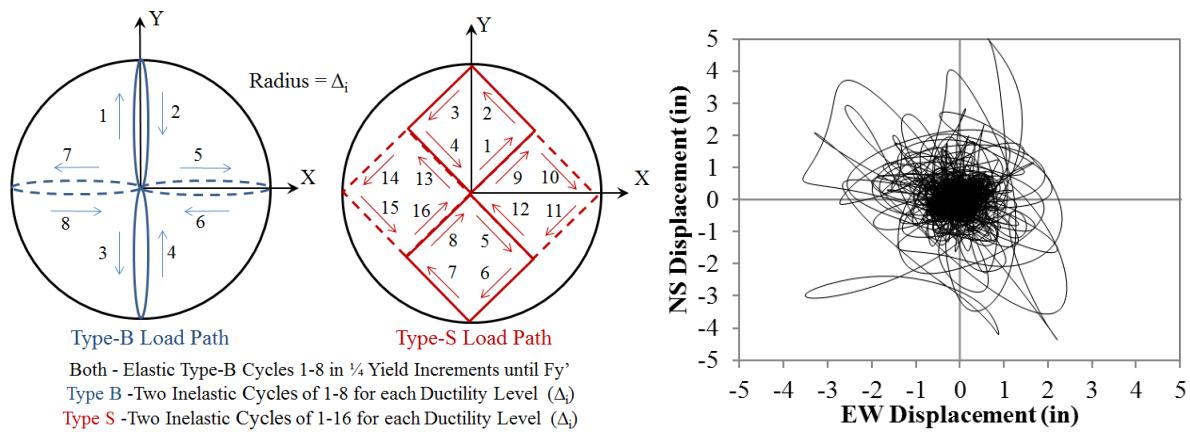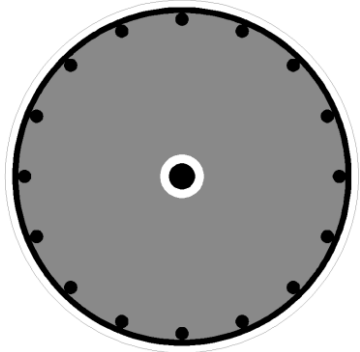**Figure 10.15 Sample Test Setup and Positioning on the Lab Strong Wall and Floor**

Figure 10.16 (Left) Prescribed Load History and (Right) Load History from Japan Earthquake 2011

Table 10.1 Proposed Test Configurations

Test	Load Path	Long. Steel	Trans. Steel	Axial	Cross Section Details
1	Type-B	16 #7 (2.1%)	#3@2" (1%)	9%	24in Dia. and 8ft Length
2	Type-S	16 #7 (2.1%)	#3@2" (1%)	9%	0.5in Cover to Outside of Spiral
3	Type-B	16 #7 (2.1%)	#3@2.75" (.7%)	9%	3in Dia. PVC Duct at Center for
4	Type-S	16 #7 (2.1%)	#3@2.75" (.7%)	9%	1 ¾" Dia. Dywidag Axial Bar
5	Type-S	16 #7 (2.1%)	#3@2" (1%)	4%	
6	Type-S	16 #7 (2.1%)	#3@2.75" (.7%)	4%	
7	Type-B	16 #6 (1.6%)	#3@2" (1%)	9%	
8	Type-S	16 #6 (1.6%)	#3@2" (1%)	9%	
9	ACI374	16 #6 (1.6%)	#3@2" (1%)	9%	
10	EQ2	16 #6 (1.6%)	#3@2" (1%)	9%	
11	EQ3	16 #6 (1.6%)	#3@2" (1%)	9%	
12	EQ4	16 #6 (1.6%)	#3@2" (1%)	9%	

Table 10.2 Uniaxial Experiments from Goodnight et al. (2014) Serve as Comparison

Test	Load Path	Long. Steel	Trans. Steel	Axial
9	3-Cycle-Set	16 #6 (1.6%)	#3@2" (1%)	5.4%
8	Chile (2010)	16 #6 (1.6%)	#3@2" (1%)	5.4%
10	Chichi (1999)	16 #6 (1.6%)	#3@2" (1%)	7.1%
11	Kobe (1995)	16 #6 (1.6%)	#3@2" (1%)	6.2%
12	Japan (2011)	16 #6 (1.6%)	#3@2" (1%)	6.2%
13	3-Cycle-Set	16#6 (1.6%)	#4@2.75" (1.3%)	6.2%
14	3-Cycle-Set	16#6 (1.6%)	#3@4" (0.5%)	5.7%
15	3-Cycle-Set	16#6 (1.6%)	#3@2.75" (0.7%)	5.2%
16	3-Cycle-Set	16#6 (1.6%)	#3@1.5" (1.3%)	5.6%
17	Chile (1985)	16#6 (1.6%)	#3@1.5" (1.3%)	5%
18	Darfield (2010)	16#6 (1.6%)	#3@1.5" (1.3%)	4.8%
25	3-Cycle-Set	16 #7 (2.1%)	#3@2" (1%)	5%
26	3-Cycle-Set	16 #7 (2.1%)	#3@2" (1%)	10%
27	3-Cycle-Set	16 #6 (1.6%)	#3@2" (1%)	10%

10.5.4 Task Four: Analysis of Data and Model Calibration

The experimental data will serve multiple purposes. First, it will provide information that may be directly used as design recommendations (for example, strain limits). It also will provide data for model calibration that is then used for the studies described below (such as for plastic hinge length and location).

10.5.5 Task Five: Recommendations

The previous load history research project has developed recommendations for strain limits at key performance limit states as well as more accurate models for correlating strains to displacement that are consistent with the measured data. Based on the work of the load path project, it is the hope that the recommendations from the previous study (Goodnight et al., 2014; Feng et al. 2014a, b, c) will either be confirmed, or modified to consider load path effects. In addition, this work will provide recommendations on how best to establish uni-directional target displacements that consider the impacts of 2D load path. These recommendations, which will be based on 2D nonlinear time history analysis, will likely take the form of amplification of the uni-directional target displacement to account for multi-directional loading.

REFERENCES

Berry, M. P. and Eberhard, M. O. (2005). "Practical Performance Model for Bar Buckling." *Journal of Structural Engineering* 131(7), 1060-1070.

Bousias, S. N., Verzeletti, G., Fardis, M. N., Gutierrez, E. (1995). "Load-Path Effects in Column Biaxial Bending with Axial Force." *Journal of Engineering Mechanics* 121(5), 596-605.

Cheok, G. S. and Stone, W. C. (1986) "Behavior of 1/6-Scale Model Bridge Columns Subjected to Inelastic Loading, NBSIR 86-3494. U.S. National Institute of Standards and Technology, Gaithersburg, MD.

Dwairi, W., Kowalsky, M. J., and Nau, J. M., (2007). "Equivalent Viscous Damping in Support of Direct Displacement-Based Design." *Journal of Earthquake Engineering*, 11(4), 512-530.

Dutta, A., Mander, J. B., and Kokorina, T., "Retrofit for Control and Reparability of Damage." *Earthquake Spectra* 15(4), 657-679.

Esmaeily, A. and Xiao, Y. (2005). "Behavior of Reinforced Concrete Columns Under Variable Axial Loads: Analysis." *ACI Structural Journal* 102(5), 736-744.

Esmaeily, A., Xiao, Y., (2002). "Seismic Behavior of Bridge Columns Subjected to Various Loading Patterns", Pacific Earthquake Engineering Research Center, PEER 2002/15, pp. 321.

Feng, Y, Kowalsky, M.J., and Nau, J. (2014a). "Finite Element Method to Predict Bar Buckling in RC Structures" *ASCE Journal of Structural Engineering*. In Press.

Feng, Y, Kowalsky, M.J., and Nau, J. (2014b). "Fiber-Based Modeling of Circular Reinforced Concrete Bridge Columns" *Journal of Earthquake Engineering*. In Press.

Feng, Y, Kowalsky, M.J., and Nau, J. (2014c). "Development of a model to predict reinforcing bar buckling in RC bridge columns including the effect of load history" Submitted to *ASCE Journal of Structural Engineering*.

Freytag, D. (2006). "Bar buckling in reinforced concrete bridge columns." Master's thesis, University of Washington, Seattle, WA.

Goodnight, J.C., Kowalsky, M.J., and Nau, J.M. (2013). "Effect of Load History on Performance Limit States of Circular Bridge Columns." *Journal of Bridge Engineering.* 18 (12): 1383-1396 pp.

Grant, D. N., Blandon, C. A., and Priestley, M. J. N. (2005). "Modelling Inelastic Response in Direct Displacement-Based Design." Report 2005/03, IUSS Press, Pavia, 104pp.

Henry, L. and Mahin (1999). Study of Buckling of Longitudinal Bars in Reinforced Concrete Bridge Columns. Report to the California Dept. of Transportation

Hines, E. M. and Seible F. (2001) Experimental Spread of Plasticity in Reinforced Concrete Bridge Piers. Structural Systems Research Project 2001/08, University of California, San Diego, La Jolla, California, 196 pp.

Hines, E.M., Restrepo, J.I., and Seible, F. (2004). "Force-Displacement Characterization of Well Confined Bridge Piers." *ACI Structural Journal* 101(4), 537-548.

Hose, Y. D., Seible, F., and Priestley, M. J. N. (1997). Strategic Relocation of Plastic Hinges in Bridge Columns, Structural Systems Research Project, 97/05. University of California, San Diego.

Jacobsen, L. S., (1960). "Damping in Composite Structures." Proceedings, 2nd World Conference on Earthquake Engineering, Vol. 2, Tokyo and Kyoto, Japan, 1029-1044.

King, D. J, Priestley, M. J. N., and Park, R. (1986). "Computer Programs for Concrete Column Design." Research Report 86/12, Department of Civil Engineering, University of Canterbury, New Zealand.

Kowalsky, M. J, Priestley, M. J. N., Seible, F. (1999). "Shear and Flexural Behavior of Lightweight Concrete Bridge Columns in Seismic Regions." *ACI Structural Journal*

Kowalsky, M. J. (2000). "Deformation Limit States for Circular Reinforced Concrete Bridge Columns." *Journal of Structural Engineering* 126(8), 869-878.

Kunnath, S., El-Bahy, A., Taylor, A., and Stone, W. (1997). "Cumulative Seismic Damage of Reinforced Concrete Bridge Piers." Technical Rep. NCEER-97-0006, National Center of Earthquake Engineering Research, Buffalo, NY.

Lehman, D. E. and Moehle, J. P. (2000). "Seismic Performance of Well-Confined Concrete Bridge Columns." PEER 1998/01, Pacific Earthquake Engineering Research Center, Berkeley, CA.

Mander, J. B., Priestley, M. J. N., and Park R. (1988). "Theoretical Stress-Strain Model for Confined Concrete." *ASCE Journal of Structural Engineering* 114(8), 1804-1826.

Montejo, L. A. and Kowalsky, M. J. (2007). "CUMBIA – Set of Codes for the Analysis of Reinforced Concrete Members." Technical Report No. IS-07-01, North Carolina State University, Raleigh, NC.

Moyer, M. J. and Kowalsky, M. J. (2003). "Influence of Tension Strain on Buckling of Reinforcement in Concrete Columns." *ACI Structural Journal* 100(1), 75-85.

Northern Digital Inc. "OPTOTRAK Certus HD Dynamic Measuring Machine." Products, <http://www.ndigital.com/industrial/certushd.php> (Jan. 14, 2013)

OpenSees – Open System for Earthquake Engineering Simulation. University of California. Version 2.4.2. <opensees.berkely.edu> (Oct. 25, 2013)

Osorio, E., Bairán, J.M., and Marí, A.R. (2012) "Effects of Biaxial Shear Loading on the Seismic Response of RC Columns." Proceedings of the 15th World Conference on Earthquake Engineering. Lisbon, Portugal.

Priestley, M. J. N., Seible, F., and Calvi, G. M. (1996). Seismic Design and Retrofit of Bridges. John Wiley & Sons, New York.

Priestley, M. J. N., Calvi, G. M., and Kowalsky, M. J. (2007). "Displacement-Based Seismic Design of Structures." IUSS Press, Pavia, Italy.

Restrepo-Posada, J. I., Dodd, L. L., Park, R., Cooke, N. (1994). "Variables Affecting Cyclic Behavior of Reinforcing Steel." *Journal of Structural Engineering* 120(11), 3178-3196.

Rodriguez, M. E., Botero, J. C., Villia, J. (1999). "Cyclic Stress-Strain Behavior of Reinforcing Steel Including Effect of Buckling." *Journal of Structural Engineering* 125(6), 605-612.

Scott, M. H. and Fenves, G. L.(2006) "Plastic Hinge Integration Methods for Force-Based Beam-Column Elements." *Journal of Structural Engineering* 132 (2), 244-252.

SEAOC (1999). "Recommended Lateral Force Requirements and Commentary (7th Edition)." Structural Engineers Association of California, Seismology Committee: Sacramento, CA.

Stone, W. C. and Cheok, G. S. (1989). Inelastic Behavior of Full-Scale Bridge Columns Subjected to Cyclic Loading, NIST Building Science Series 166. U.S. National Institute of Standards and Technology, Gaithersburg, MD.

Syntzirma, D. V., Pantazopoulou, S. J., Aschheim, M. (2010). Load-History Effects on Deformation Capacity of Flexural Members Limited by Bar Buckling. *Journal of Structural Engineering* 136:1, 1-11.

Tsuno, K. and Park, R. (2004). "Experimental Study of Reinforced Concrete Bridge Piers Subjected to Bi-Directional Quasi-Static Loading." *Journal of Structural Eng./Eathquake Eng. JSCE.* 21 (1): 11-26 pp.

Vu, N. D., Priestley, M. J. N., Seible, F., and Benzoni, G. (1998). Seismic Response of Well Confined Circular Reinforced Concrete Columns with Low Aspect Ratios, 97/05. Proc., 5th Caltrans Seismic Research Workshop, Sacramento, California.

Wong Y., Paulay, T., Priestley M. J. N., (1993). "Response of Circular Reinforced Concrete Columns to Multi-Directional Seismic Attack." *ACI Structural Journal* 90(2), 180-191.

Zhao, J. and Sritharan, S. (2007). "Modeling of Strain Penetration Effects in Fiber-Based Analysis of Reinforced Concrete Structures." *ACI Structural Journal.* 104(2), 133-141.